Enhancing Water Quality through Adsorptive Removal of Contaminants of Emerging Concern using Bio-based Engineered Adsorbents: Modeling and Toxicological Evaluation

A thesis submitted in partial fulfillment of the

requirements for the degree of

DOCTOR OF PHILOSOPHY

by

VISHNU PRIYAN V

(196106029)

Under the supervision of

Dr. Selvaraju Narayanasamy

Department of Biosciences and Bioengineering

Indian Institute of Technology Guwahati

Assam

January 2024

This thesis is dedicated to My Family and Friends

INDIAN INSTITUTE OF TECHNOLOGY GUWAHATI

DEPARTMENT OF BIOSCIENCES AND BIOENGINEERING

GUWAHATI-781039

DECLARATION

I, hereby declare that the matter embodied in this thesis entitled "**Enhancing Water Quality through Adsorptive Removal of Contaminants of Emerging Concern using Bio-based Engineered Adsorbents: Modeling and Toxicological Evaluation**" is the result of investigations carried out by me under the supervision of **Dr. Selvaraju Narayanasamy**, Department of Biosciences and Bioengineering, Indian Institute of Technology Guwahati, Guwahati, India for the award of the degree of Doctor of Philosophy. This work has not been submitted elsewhere for any degree, diploma, associateship, or membership etc. of any Institute or University to the best of my knowledge and belief.

IIT Guwahati — VISHNU PRIYAN V

January 2024 — Roll No. 196106029

INDIAN INSTITUTE OF TECHNOLOGY GUWAHATI
DEPARTMENT OF BIOSCIENCES AND BIOENGINEERING
GUWAHATI-781039

Dr. Selvaraju Narayanasamy
Associate Professor
Department of Biosciences and Bioengineering

Tel. No.: +91-361-2583210
Fax No.: +91-361-2582249
E-mail: selva@iitg.ac.in

CERTIFICATE

This is to certify that the thesis entitled "**Enhancing Water Quality through Adsorptive Removal of Contaminants of Emerging Concern using Bio-based Engineered Adsorbents: Modeling and Toxicological Evaluation**" being submitted to the **Indian Institute of Technology Guwahati** by **VISHNU PRIYAN V** for the award of the degree of **Doctor of Philosophy** in **Biosciences and Bioengineering,** is a bonafide record of research work carried out by him. The contents of this thesis have not been submitted to any other University or Institute for the award of any degree or diploma.

IIT Guwahati

January 2024

Dr. Selvaraju Narayanasamy

(Thesis supervisor)

ACKNOWLEDGEMENT

Undertaking this Ph.D has been a truly life-changing experience for me and it would not have been possible to do without the support and guidance that I received from many people.

First and foremost, I thank my supervisor, **Dr. Selvaraju Narayanasamy**, Associate Professor, Department of Biosciences and Bioengineering, Indian Institute of Technology Guwahati for accepting me into his group. During my tenure, he contributed to a rewarding research experience by giving me intellectual freedom in my work, supporting my attendance at various conferences, engaging me in new ideas, and demanding a high quality of work in all my endeavours.

I would also like to thank my doctoral committee, chairperson **Prof. Senthilkumar Sivaprakasam** and members **Prof. Vaibhav V. Goud**, **Dr. Rajkumar P. Thummer** for their constructive criticism and valuable insights. Their feedback helped me to refine my research and ensured that my thesis met the highest standards of academic excellence.

I owe my gratitude to former HOD **Prof. Latha Rangan** for her administrative capability. I would like to thank the present HOD **Prof. Rakhi Chaturvedi** for providing departmental facilities. I am grateful to the staff and faculty of **Department of Biosciences and Bioengineering**, who provided a stimulating and supportive research environment. Their dedication in teaching and research inspired me to pursue my own scholarly interests and helped me to develop important skills and competencies.

I would like to acknowledge the financial support provided by **Ministry of Education (MOE, Government of India)**. Their support allowed me to focus on my research and to pursue my academic goals without the burden of financial stress.

I am grateful for the instrumentation facilities provided by **Central Instrument Facility (CIF)**, **Department Central Instrument Facility (DCIF, BSBE)**, other departments and their technical team. I would like to express my gratitude to all of the research scholars from the Department of Biosciences and Bioengineering as well as from all of the other departments, centres and schools at IIT Guwahati.

I would want to express my heartfelt gratitude to my institute, **IIT Guwahati**, a lovely campus surrounded by wonderful natural scenery for giving me the chance to engage in this excellent academic experience with top-notch facilities.

I will take this opportunity to express my gratitude to all my past and present lab members of the **Biochemical and Environmental Engineering Lab**. My special thanks to my seniors **Dr. Chandi Patra** and **Dr. Tasrin Shahnaz** for their endless help and support

throughout my Ph.D journey and particularly for guiding me in paper publications. I extend my gratitude to my lab fellow **Mr. Ajit Kumar** for helping me in various projects and dedicating his valuable time to carry out scanning electron microscopy of my samples. I express my sincere thanks to my lab juniors (**Mr. Ragavan C., Ms. Sandhya S., Mr. Harish Kumar R., Mr. Jyoti Prakash Ray., Ms. Jothika J., Mr. Mohammed Askkar Deen F., Mr. Ajithkumar V., Ms. Debanjana Ghosh, Ms. Anushka Singh**) for their valuable discussion and help provided during my tenure. I am extending my warm thanks to **Mr. Jeevanantham Sathasivam** for his motivation and support during hard days of research. Every result described in this thesis was accomplished with the help and support of fellow lab mates and collaborators. I am thankful to **Mr. Nitesh Kumar** for his countless support, extending his helping hand during my hectic research work. I would also like to extend my deepest gratitude to all the previous M. Tech students **Mr. Rishabh Gupta, Ms. Anjali J., Mr. Nirvesh Patel, Mr. Bedadeep D**, and current M. Tech student **Ms. Pavithra P**. I extend my gratefulness to **Ms. Ghurupreya Ramesh** for helping me in various research activities and giving me support during the final days of my Ph.D. Their support and help have been integral in coming up with many new ideas and solving various problems that I faced during my research tenure. I would like to express my gratitude to my friends, who provided bond, encouragement, and a sense of camaraderie throughout my time as a Ph.D student. Their insights and perspectives enriched my research and made the experience of doctoral study more enjoyable.

My grateful and deepest gratitude to my family **Appa,** and **Amma** for their unconditional love, support, patience, motivation, and blessings to carry out my Ph.D. I am thankful to my brother and sister **Mr. Naveen Varadharaj** and **Mrs. Kanagathara Gowthaman** who supported me morally during my hard days of Ph.D tenure. I thank all my relatives for their blessings in this journey. I express my sincere thanks to all my friends for their unconditional love and support throughout my journey.

Finally, I would like to express my gratitude to all those who have contributed to my academic journey in ways both large and small. Whether through their expertise, encouragement, or simply their presence, they have all played a role in shaping me into the scholar and person I am today.

Above all, I am grateful to God for finding me capable of fulfilling this extremely difficult task and providing me continuous motivation, positive energy and support. I am thankful to God for blessing me with the completion of Doctoral work.

VISHNU PRIYAN V

TABLE OF CONTENTS

ABSTRACT

Rapid industrialization and urbanization cause tremendous stress on the natural resources which leads to severe ecological impacts, amongst water is the foremost concern that can be easily polluted by contaminants of emerging concern (CECs) including pharmaceuticals, pesticides, herbicides, personal care products, endocrine disrupting compounds, illicit drugs, food additives, hydrocarbons, metabolites, microplastics, etc. CECs typically are not regulated under current environmental laws because of their occurrence in lower or negligible concentrations. However, the persistence and/or pseudo-persistence nature of these pollutants could cause various environmental and health impacts on water ecosystems and living beings. Thereby, sequestration of these contaminants from the water systems is mandatory. Inspite of various treatment methods, adsorption is the prominent approach for the sequestration of these contaminants due to its efficiency at lower pollutant concentration, easy implementation, cost-effective, selectivity, economic feasibility and potential to meet environmental sustainability without secondary pollution.

Precursor selection and modification of the adsorbents/biosorbents are the crucial factor that leads the efficiency of the adsorption process for diverse selective target pollutants. The primary aspect of this thesis work focuses on the development of the bio-based engineered adsorbents from the natural derivatives including agricultural byproducts and biopolymers. Difficulty in recovery of adsorbents after the treatment and limited surface functionality are the major drawbacks of adsorbent which limits the adsorption process applicability for selective targeted pollutants. These limitations can be overwhelmed by development of magnetic adsorbents through iron oxide nanoparticles impregnation and oxidative treatment of adsorbents. Optimization of process parameters such as pH, adsorbent/biosorbent dosage, initial pollutant concentration, contact time and temperature conveys suitable conditions for the sequestration of targeted pollutants. The second major

component of this thesis includes the toxicological evaluation before and after treatment using various model organisms to assess the safety and efficacy of the adsorption process. Further, this thesis work aims to bridge the gap between laboratory-scale studies and practical applications by considering real-time factors via reusability and column studies. Thereby, this research findings contributes to the theoretical understanding of various CECs adsorption process and provides practical insights into the feasibility and sustainability of employing bio-based engineered adsorbents for large-scale water treatment. The findings of this thesis are expected to have significant implications for water quality management, environmental sustainability and may create a path for regulation of various persistent toxic pollutants in water ecosystems.

ABBREVIATIONS & NOMENCLATURES

AC	Activated Carbon
AES	Atomic Emission Spectroscopy
AFM	Atomic Force Microscopy
AOPs	Advanced Oxidation Process
ASPs	Activated Sludge Process
BAC	Biological Activated Carbon
BF	Basic Fuchsin
BOD	Biochemical Oxygen Demand
BPA	Bisphenol A
C_0/C_t	Ratio of influent to an effluent concentration
CAC	Commercial activated carbon
Cd	Cadmium
Ce	Cerium
Ce^{3+}	Cerium (III) ions
CECs	Contaminants of Emerging Concern
cm	Centimeter
Co	Cobalt
COD	Chemical Oxygen Demand
CPCB	Central Pollution Control Board
CR	Congo Red
Cr	Chromium
CSNP	Corn starch nanoparticles
CSR	Corn starch raw
Cu	Copper
CWs	Constructed Wetlands
DCF	Diclofenac
DR	Dubinin Radushkevich
EC_{50}	Half maximal Effective Concentration
EDCs	Endocrine disruptors
EDX	Energy Dispersive X-ray Spectroscopy
EPA	Environmental Protection Agency

F	Flow rate
Fe_3O_4-NP	Iron oxide Nanoparticles
$FeCl_3.6H_2O$	Ferric Chloride hexahydrate
FESEM	Field Emission Scanning Electron Microscopy
$FeSO_4.7H_2O$	Ferrous Sulfate heptahydrate
FETEM	Field Emission Transmission Electron Microscopy
FTIR	Fourier-Transform Infrared Spectroscopy
FWAs	Fluorescent Whitening Agents
g	Gram
h	Hours
H_2O_2	Hydrogen peroxide
HCl	Hydrochloric acid
IBU	Ibuprofen
J	Joule
K	Kelvin
k_1	Pseudo-first-order rate constant
k_2	Pseudo-second-order rate constant
k_{AB}	Adams-Bohart kinetics constant
K_F	Freundlich isotherm constant
K_{ID}	Intraparticle diffusion rate constant
K_J	Jovanovic isotherm constant
K_L	Langmuir isotherm constant
K_T	Equilibrium binding constant
k_{TH}	Thomas model constant
k_{YN}	Yoon-Nelson rate constant
L	Litre
LC_{50}	Half maximal Lethal Concentration
M	Molar (concentration)
m	meter
MBRs	Membrane Bioreactors
MCAC	Fe_3O_4/CAC nanocomposite
mg	Milligram

mL	Milliliter
mm	Millimeter
Mn	Manganese
mol	Mole
MSD	Magnetic Sawdust
MSDAA	Magnetic Sawdust After Adsorption
mtotal	Total amount of dye introduced into the column
N	Normal (concentration)
N_{AB}	Saturation constant
NaOH	Sodium Hydroxide
NAWQA	National Water-Quality Assessment
ng	Nanogram
NH_3	Ammonia
Ni	Nickel
nm	Nanometer
NTU	Nephelometric Turbidity Unit
OBC	Oxidant-modified biochar
OECD	Organization for Economic Co-operation and Development
•OH	Hydroxyl radicals
OVAT	One-variable-at-a-time
PAHs	Polycyclic Aromatic Hydrocarbons
Pb	Lead
$Pb(NO_3)_2$	Lead nitrate
PCBs	Poly Chlorinated Biphenyls
PCPs	Personal Care Products
PFAS	Poly Fluoro Alkyl Substances
PFO	Pseudo-first-order
ppm	parts per million
PSO	Pseudo-second-order
Q_0	Adsorption/Biosorption capacity
q_e	Equilibrium biosorption capacity
q_t	Biosorption capacity at time

R	Universal gas constant
REE	Rare Earth Element
rpm	Rotations per minute
RS	Raman Spectroscopy
SD	Sawdust
SUL	Sulfamethoxazole
T	Temperature
TDS	Total Dissolved Solids
TGA	Thermo Gravimetric Analysis
t_{total}	Total time for column saturation
u	Superficial velocity
UNICEF	United Nations International Children's Emergency Fund
USGS	US Geological Survey
UV	Ultraviolet
UV-LEDs	Ultraviolet light-emitting diodes
V_{eff}	Volume of the effluent
Vis	Visible
VM	*Vigna mungo*
VOCs	Volatile Organic Compounds
VR	*Vigna radiata*
VSM	Vibrating Sample Magnetometer
WHO	World Health Organization
XRD	X-ray powder Diffraction
Y%	Percentage removal of adsorbate in packed bed column
z	Bed height of the adsorbent
Zn	Zinc
β	Activity coefficient
ΔG	Change in Gibbs free energy
ΔH	Change in Enthalpy
ΔS	Change in Entropy
µg	Microgram
µs	Microsecond

LIST OF TABLES

Appendix

LIST OF FIGURES

Chapter 1

General Introduction and Theoretical Background

1.1. Background

Water is an essential substance for various life forms on earth and is a significant asset for human development. Rapid industrialization and urbanization lead to tremendous stress on natural resources causing severe ecological impacts, with water being one of the major concerns. Out of the total water content available on the earth, nearly 2.5% is freshwater. From this, only 0.007% is accessible for the population of 6.8 billion (Li et al., 2023; Vishnu Priyan et al., 2021). Due to the tremendous development of the world's population over the last century, the need for fresh and drinkable water has skyrocketed. According to a recent, 2.3 billion people live in water-stressed nations, with 733 million living in high and critically water-stressed countries. According to a recent UNICEF estimate, 1.42 billion people, including 450 million children, live in high or extremely high-water insecurity areas. Every year, 1.5 million children under the age of five die because of water-related illnesses throughout the world (UNICEF, 2021). According to the World Economic Forum, 4,00,000 people die in India each year from drinking unclean water. The contaminants of emerging concern (CECs), which include a wide range of pollutants including pharmaceuticals, pesticides, dyes, heavy metals, herbicides, personal care products, endocrine disrupting compounds, hydrocarbons, metabolites, microplastics, etc., may contaminate the water bodies causing various toxic effects (Rout et al., 2021). An essential humanitarian fundamental is to access clean water at a cheap economic cost, which is the greatest challenge for this global scenario.

This thesis contains various biosorbents/adsorbents that could effectively remove contaminants of emerging concern (CECs), including pharmaceuticals, endocrine disruptors, rare earth elements, heavy metals, and dyes with high removal efficiency have been proposed. This work will mainly be focused on the synthesis, characterization, and application required for wastewater remediation. Engineered adsorbents, which are exposed to individualized improvisation during synthesis and have increased physicochemical features, might be a potential long-term option for environmental clean-up.

1.2. Contaminants of Emerging Concern (CECs)

Contaminants of Emerging Concern (CECs), also known as Emerging Contaminants (ECs), are a term used by the Environmental Protection Agency (EPA) and water quality

professionals to describe various chemicals and other substances that have been detected in water bodies, may cause ecological or human health effects, and for which scientific understanding of potential risks is evolving. CECs typically are not regulated under current environmental laws. CECs include various types of manufactured chemicals and substances, as well as naturally occurring substances, which may be found in lakes, rivers, and streams, and may have a detrimental effect on living organisms (Kim et al., 2018; Salimi et al., 2017).

The potential range of CECs includes:

- Pharmaceuticals
- Polycyclic aromatic hydrocarbons (PAHs)
- Pesticides
- Rare earth elements and Heavy metals,
- Microplastics
- Phthalates
- Personal care products
- UV filters and flame retardants
- Disinfection by-products
- Dyes
- Endocrine disruptors
- Persistent Organic Pollutants

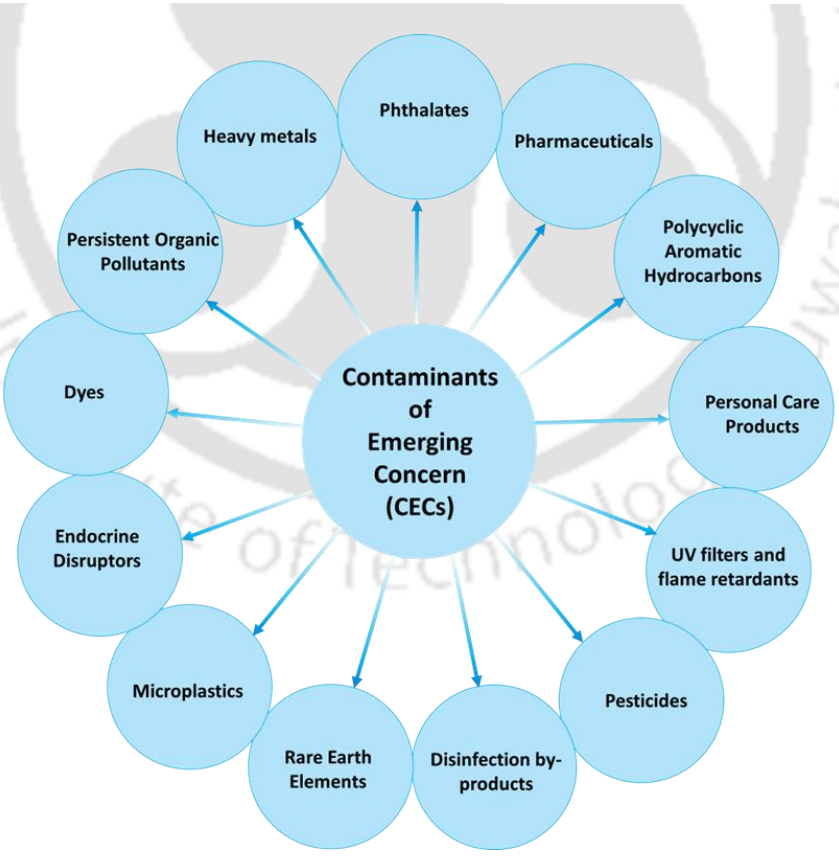

Fig. 1.1. *Various Contaminants of Emerging Concern*

1.2.1. Pharmaceuticals

Pharmaceuticals are a class of contaminants of emerging concern that are increasingly being used in human and veterinary medicine. They include compounds like steroids, antibiotics, analgesics, legal and illicit drugs, beta-blockers, etc. Their specific mechanism of action causes their persistence in the human and animal body. Various pharmaceutical compounds have been spotted in sediments, effluents, drinking, and natural and ground waters. These compounds are intended to boost soil bacteria to produce antibiotic-resistant genes. More than 160 distinct pharmaceuticals have already been found in aquatic systems at concentrations between ng/L and µg/L levels (Osuoha et al., 2023). Ibuprofen was found to be 19.2 µg/L in surface water according to research by Madikizela and Ncube (2020), however 1.38 µg/L of the same CEC was found in wastewater according to Matongo et al. (2015) (Madikizela et al., 2020; Matongo et al., 2015). Acetaminophen and amoxicillin ranged from 0.0058 to 1.23 µg/L in both surface water and ocean. Moreover, Amdany et al. (2014) reported that the concentrations of Naproxen, Ibuprofen, and Triclosan in wastewater ranged from 10.7 to 127.7 µg/L (Amdany et al., 2014). The list of CECs in pharmaceuticals and their characteristics is given in the Table 1.1.

Table 1.1. *Pharmaceuticals and their structures*

Pharmaceutical type	Emerging Contaminants	Molecular Formula	Structure
Analgesics and anti-inflammatories	Codeine	$C_{18}H_{21}NO_3$	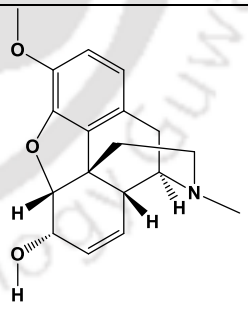
	Antipyrine	$C_{11}H_{12}N_2O$	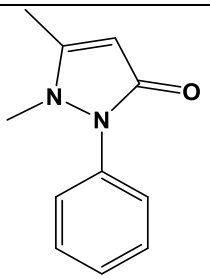

	Diclofenac	$C_{14}H_{11}Cl_2NO_2$	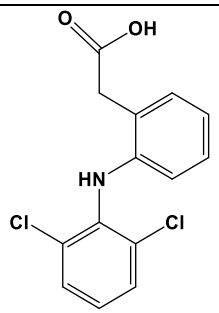
	Naproxen	$C_{14}H_{14}O_3$	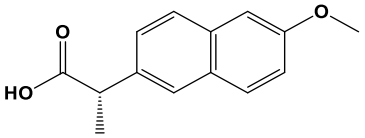
	Ketoprofen	$C_{16}H_{14}O_3$	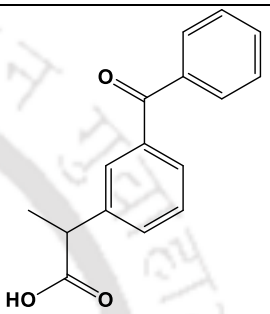
	Ibuprofen	$C_{13}H_{18}O_2$	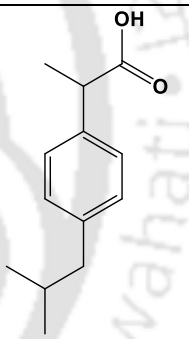
	Acetaminophen	$C_8H_9NO_2$	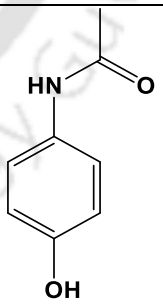
Antibiotics	Metronidazole	$C_6H_9N_3O_3$	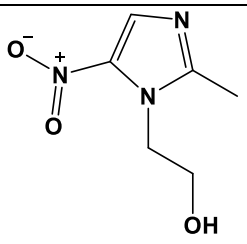

	Azithromycin	$C_{38}H_{72}N_2O_{12}$	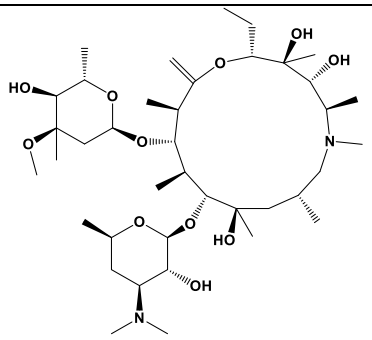
	Amoxicillin	$C_{16}H_{19}N_3O_5S$	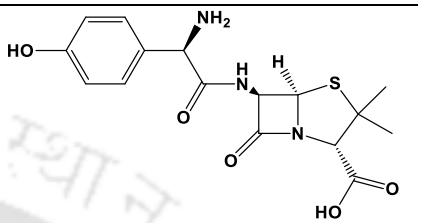
	Sulfamethoxazole	$C_{10}H_{11}N_3O_3S$	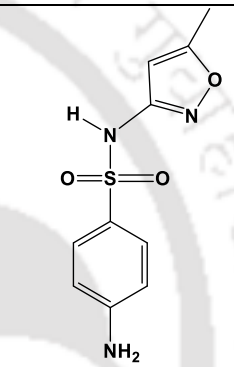
	Trimethoprim	$C_{14}H_{18}N_4O_3$	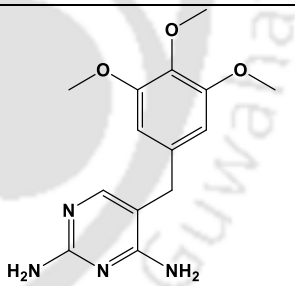
	Flumequine	$C_{14}H_{12}FNO_3$	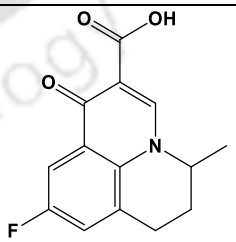
Psychiatric drugs	Salbutamol	$C_{13}H_{21}NO_3$	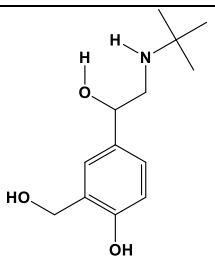

	Diazepam	$C_{16}H_{13}ClN_2O$	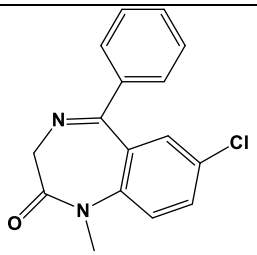
	Primidone	$C_{12}H_{14}N_2O_2$	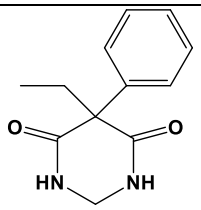
	Carbamazepine	$C_{15}H_{12}N_2O$	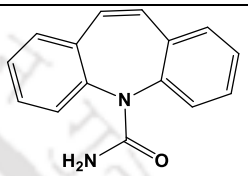
β-blockers	Sotalol	$C_{12}H_{20}N_2O_3S$	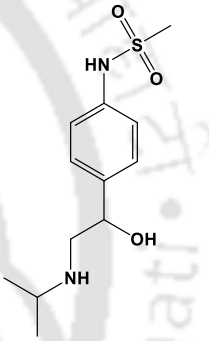
	Metoprolol	$C_{15}H_{25}NO_3$	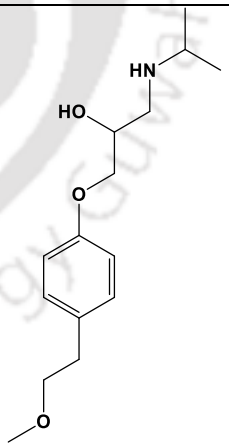
	Propranolol	$C_{16}H_{21}NO_2$	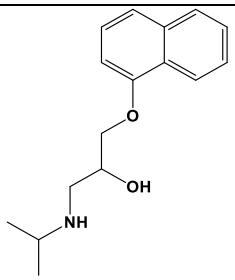

	Atenolol	$C_{14}H_{22}N_2O_3$	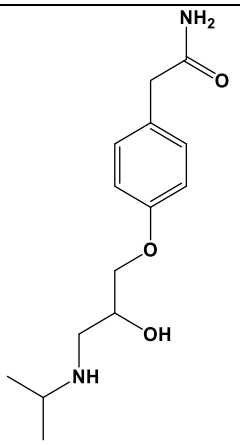

1.2.2. Personal care products

Personal care products are the collection of everyday household chemicals that are used for different purposes such as beauty, health, and cleaning. They also include various cosmetic items, perfumes, personal and skin care items. The use of skincare and personal care products is widespread, and as a result, very large amounts of these products' waste are regularly released into the environment.

The majority of these personal care products are bioactive and are classed according to their ability for retention and bioaccumulation, endangering the environment and the general populace (Balakrishna et al., 2023; Emnet et al., 2020; Roh and Cheng, 2022). Around 15,000 tonnes and 227,000–454,000 kg of triclosan and triclocarban are manufactured globally each year, according to estimates (Chen et al., 2013). The usual concentrations of triclocarban and triclosan in products sourced from European nations are 0.2% and 0.3%, respectively (Lehutso et al., 2017).

The list of CECs in personal care products and their properties is given in the Table 1.2.

Table 1.2. *Personal care products and their structures*

Personal Care Product type	Emerging Contaminants	Molecular formula	Structure
UV filters	Benzimidazole	$C_7H_6N_2$	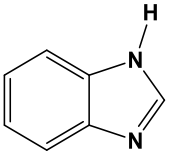

	Dibenzoyl methane	$C_{15}H_{12}O_2$	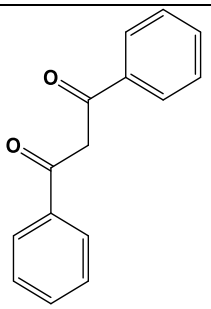
	Benzophenone	$C_{13}H_{10}O$	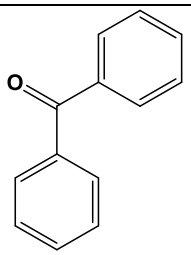
	p-Aminobenzoate	$C_7H_6NO_2$	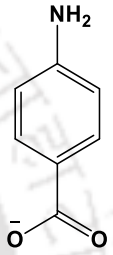
Disinfectants	Triclosan	$C_{12}H_7Cl_3O_2$	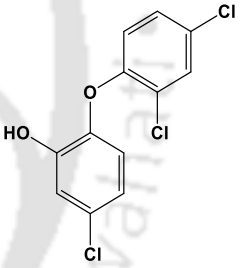
	Triclocarban	$C_{13}H_9Cl_3N_2O$	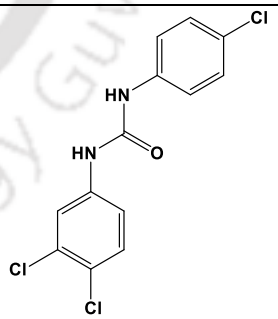
Fragrances	Galaxolide	$C_{18}H_{26}O$	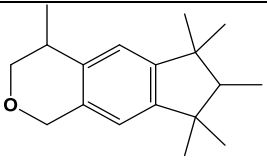

	Tonalide	$C_{18}H_{26}O$	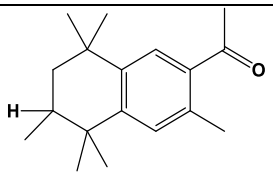
	Celestolide	$C_{17}H_{24}O$	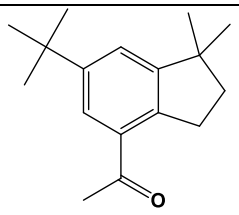
	Phantolide	$C_{17}H_{24}O$	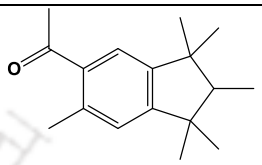
Preservatives	Diethyl phthalate	$C_{12}H_{14}O_4$	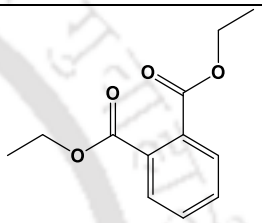
	Chloroxylenol	C_8H_9ClO	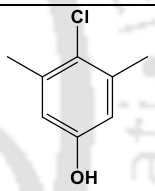
	Methylisothiazolone	C_4H_5NOS	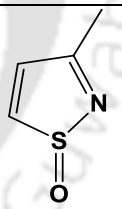
	Butylparaben	$C_{11}H_{14}O_3$	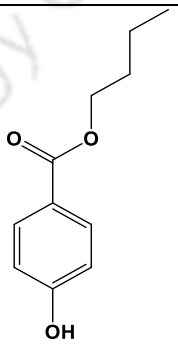

1.2.3. Pesticides

Pesticides are a broad category of substances with physiochemical properties that may be used to control or stop the spread of dangerous insects, weeds, and germs like microorganisms. Herbicides, fungicides, insecticides, and bactericides are the different categories of pesticides. Although they help prevent pests, they may also be hazardous to people and other living things. More than 95% of pesticides reach water sources causing various effects on the ecosystem.

US Geological Survey (USGS) reported the ten most frequently detected anthropogenic contaminants on surface water, of which eight are pesticides. Based on the National Water-Quality Assessment (NAWQA), pesticides are found more often in surface waters than groundwater (Frîncu, 2021). Rivers are also becoming highly polluted by industrial, agricultural, mining, and urban wastewaters, leading to increased levels of pesticides from agricultural and landscaping origins (Saleh et al., 2020).

A list of emerging pesticide contaminants and their structures are listed in the Table 1.3.

Table 1.3. *Pesticide contaminants and their structures*

Pesticide type	Emerging Contaminants	Molecular Formula	Structure
Insecticide	Endosulfan	$C_9H_6Cl_6O_3S$	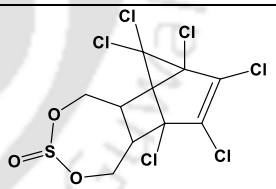
	Diazinon	$C_{12}H_{21}N_2O_3PS$	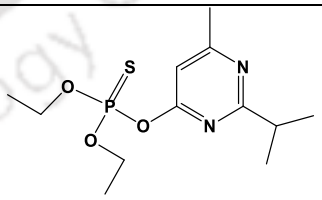
	Chlorpyrifos	$C_9H_{11}Cl_3NO_3PS$	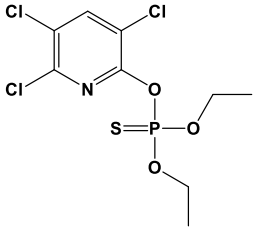

	Deltamethrin	$C_{22}H_{19}Br_2NO_3$	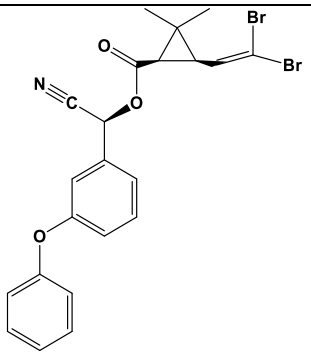
	Atrazine	$C_8H_{14}ClN_5$	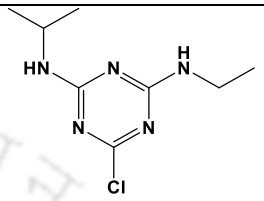
Herbicide	Alachlor	$C_{14}H_{20}ClNO_2$	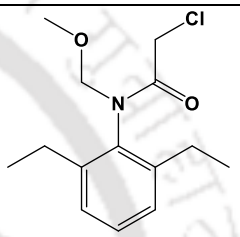
	Dimethenamid	$C_{12}H_{18}ClNO_2S$	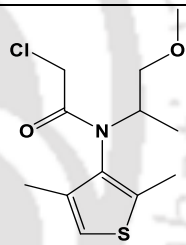
	Hexachlorbenzene	C_6Cl_6	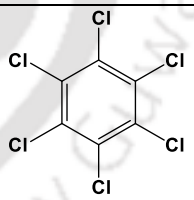
Fungicide	Edifenphos	$C_{14}H_{15}O_2PS_2$	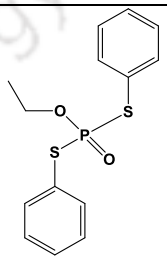
	Dichloran	$C_{13}H_{18}Cl_5NO_7P_2S$	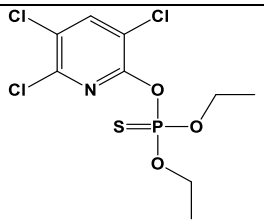

Bactericide	Triclosan	$C_{12}H_7Cl_3O_2$	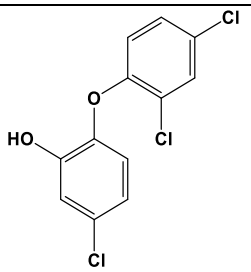
	Oxytetracycline	$C_{22}H_{24}N_2O_9$	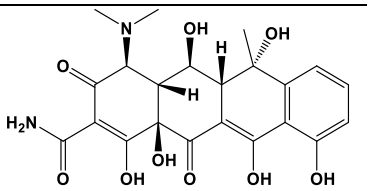

1.2.4. Endocrine disruptors

EDCs are synthetic chemicals ingested into the body that can either copy or obstruct hormones and affect the body's normal functioning. According to Environmental Protection Agency (EPA), EDCs are external agents that interfere with the formation, release, transport, attachment, activity, or displacement of the body's natural hormones that maintain homeostasis, development, reproduction, and behavior. Human activities and industries discharge natural and synthetic EDCs into the water bodies through sewage treatment systems before finally going to soil, surface, and groundwater. The EDCs were found in wastewater at low concentrations (ng/L or µg/L). These substances are concerning due to the unknown long-term exposure and adverse effects on humans (Gogoi et al., 2018; Kasonga et al., 2021).

A list of endocrine disruptors and their structures are listed in the Table 1.4.

Table 1.4. *Endocrine disruptors and their structures*

Endocrine disruptors	Molecular formula	Structure
Bisphenol A (BPA)	$C_{15}H_{16}O_2$	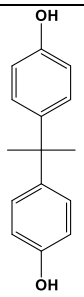

1,4-Dioxin	$C_4H_4O_2$	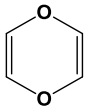
Phthalates	$C_8H_4O_4^{-2}$	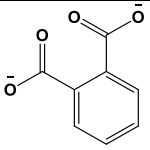
Polybrominated diphenyl ether	$C_{34}H_{26}Br_4N_4O_8$	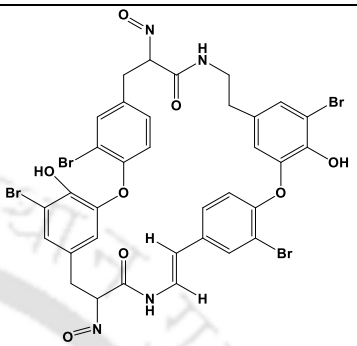

1.2.5. Dyes

Dyes are synthetic or natural substances that are commonly used to impart color to various products, such as textiles, paper, plastics, and cosmetics. However, some dyes have been identified as contaminants of emerging concern due to their potential adverse effects on human health and the environment (Jeyabalan et al., 2023). Dyes as contaminants of emerging concern include:

Azo dyes: Azo dyes are a type of synthetic dye that are commonly used in the textile industry. Some azo dyes have been found to be carcinogenic or mutagenic, and can also cause skin irritation and respiratory problems (Dutta et al., 2021).

Anthraquinone dyes: Anthraquinone dyes are used in the production of textiles, paper, and plastics. These dyes have been found to be toxic to aquatic organisms and can bioaccumulate in the food chain.

Phthalocyanine dyes: Phthalocyanine dyes are used in the production of inks, paints, and plastics. These dyes have been found to be toxic to aquatic organisms and can also have adverse effects on human health, including reproductive and developmental toxicity.

Triphenylmethane dyes: Triphenylmethane dyes are used in the production of textiles, paper, and plastics. Some of these dyes have been found to be carcinogenic or mutagenic, and can also cause skin irritation and respiratory problems.

Fluorescent whitening agents (FWAs): FWAs are used in a wide range of products, including textiles, paper, and detergents, to make them appear brighter. Some FWAs have been found to be toxic to aquatic organisms and can bioaccumulate in the food chain (Wang et al., 2024).

1.2.6. Rare earth elements (REEs)

Rare earth elements (REEs) are a group of 17 metallic elements that have a wide range of applications in various industries, including electronics, energy, and defence. REEs includes the lanthanide series (lanthanum, cerium, praseodymium, neodymium, promethium, europium, gadolinium, terbium, dysprosium, holmium, erbium, thulium, ytterbium, and lutetium) as well as scandium and yttrium (Moldoveanu and Papangelakis, 2012). While REEs are essential for modern technology, their increasing use has also led to their presence in the environment as contaminants of emerging concern. The primary source of REE contamination is from mining and processing operations, where the extraction of these elements from ore can release them into the environment. REEs can also be found in consumer products, such as electronics and batteries, which can end up in landfills or the ocean, leading to their accumulation in soil and water (Anastopoulos et al., 2016).

1.3. Sources of CECs

The major sources of emerging contaminants are personal care products, surfactants, artificial sweeteners, pharmaceuticals, hormones, fertilizer, antibiotics, per fluorinated compounds, flame retardants, cushions of foam, cleaning solvents, ointments, clothing adhesives, cosmetics, sun protection, packaged food, and beauty care (Khan et al., 2022). There are numerous sources of CECs that can enter the environment, including:

1.3.1. Wastewater treatment plants

Many CECs are found in municipal wastewater, which is often released into rivers, lakes, and oceans. Wastewater treatment plants are not designed to remove these compounds, and they can persist in the environment. Some of the CECs commonly found in wastewater include pharmaceuticals, personal care products, and industrial chemicals. Pharmaceuticals are a major source of CECs in wastewater. These compounds can enter the environment through excretion, disposal of unused medication, and improper disposal of expired

medication. Personal care products, such as cosmetics and fragrances, can also enter the environment through domestic wastewater (Rout et al., 2021).

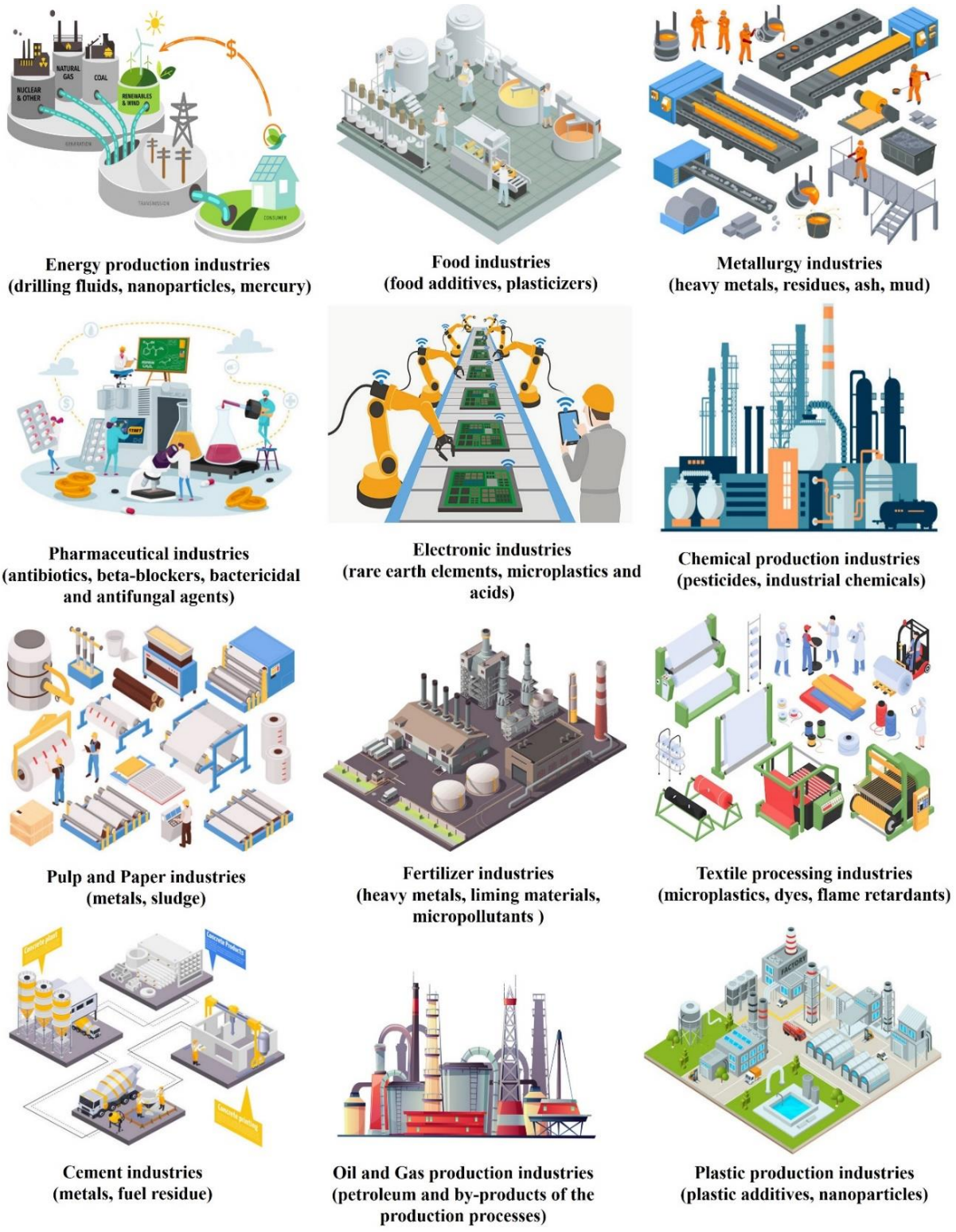

Fig. 1.2. *Different industrial sources of CECs*

1.3.2. Human excretion

Human excretion is the primary source of pharmaceuticals in the environment. When humans consume pharmaceuticals, some of the drugs are not fully metabolized and are excreted in urine and faeces. These compounds then enter the wastewater stream and can be transported to surface water and groundwater sources.

1.3.3. Production and processing industries

Many industrial processes can release CECs into the environment. Chemical manufacturing, oil and gas production, and mining are just a few examples of industries that can contribute to the release of CECs. Many chemicals used in manufacturing are persistent and can accumulate in the environment over time. Some of the CECs commonly found in industrial wastewater include flame retardants, phthalates, and per- and polyfluoroalkyl substances (PFAS). Flame retardants are chemicals that are added to products such as electronics, furniture, and textiles to reduce the risk of fire. These chemicals can enter the environment through various routes, including leaching from products, disposal of products in landfills, and incineration. Per- and Polyfluoroalkyl Substances (PFAS) are a group of chemicals that are widely used in various industrial and consumer products, including firefighting foam, food packaging, and non-stick cookware. These chemicals can enter the environment through various routes, including industrial discharges, landfills, and atmospheric deposition (Rahman et al., 2014). Oil and gas production is another significant source of CECs. The extraction, refining, and transportation of oil and gas can release a wide range of contaminants into the environment, including benzene, toluene, and heavy metals (Richardson and Kimura, 2017).

1.3.4. Agricultural practices

Pesticides and herbicides used in agriculture also contribute to the release of CECs into the environment. These compounds can enter the environment via including runoff from agricultural fields, urban runoff, and disposal of unused pesticides or leaching into groundwater. Some of the CECs commonly found in agricultural runoff include atrazine, glyphosate, and 2,4-D. Drift is another pathway for pesticides to enter the environment. When pesticides are sprayed, some of the chemicals can be carried by wind and contaminate nearby areas, including surface water sources and neighbouring crops (Panthi et al., 2019).

1.3.5. Consumer products

Consumer products can be a source of CECs in the environment. These products can contain a wide range of chemicals, including volatile organic compounds (VOCs), and nanoparticles. Some of the VOCs commonly found in cleaning products include formaldehyde, benzene, and toluene which are released into water bodies through anthropogenic activities. Nanoparticles are ultra-small particles that are commonly used in consumer products such as sunscreens, cosmetics, and electronics. These particles can enter the ecosystem through different routes, including wastewater discharges, landfills, and atmospheric deposition.

1.3.6. Plastics

Microplastics are a relatively new source of CECs in the environment. These tiny particles are less than 5mm in size and can come from a variety of sources, including cosmetics, clothing, and plastic debris. Microplastics can enter the environment through wastewater and bottled drinking water.

1.3.7. Sewage overflow

Sewage overflow is also a source of Personal Care Products (PCPs) in the environment. When the capacity of the sewage system is exceeded, raw sewage can overflow and enter surface water and groundwater sources. This overflow can contain high concentrations of PCPs, which can potentially harm aquatic organisms and impact human health.

1.4. Adverse effects of CECs

CECs can have adverse effects on living organisms, including humans, wildlife, and aquatic organisms. These effects can range from acute toxicity to chronic exposure, and they can affect multiple organ systems and functions. Below are some of the adverse effects of CECs on living organisms:

1.4.1. Endocrine disruption

CECs such as pharmaceuticals, personal care products, and industrial chemicals can interfere with the endocrine system in animals and humans. Endocrine disruptors can mimic or interfere with the normal function of hormones, which can cause developmental and reproductive abnormalities, tumours, and other health problems. Some examples of

endocrine-disrupting CECs include bisphenol A (BPA), phthalates, and triclosan (Nika et al., 2020; Panthi et al., 2019).

1.4.2. Antibiotic resistance

Overuse and misuse of antibiotics in both human medicine and agriculture have contributed to the development of antibiotic resistance in bacteria. The presence of antibiotic residues in the environment can also select for antibiotic-resistant bacteria, leading to the spread of antibiotic resistance. This can make infections harder to treat, and in severe cases, can lead to untreatable infections and increased mortality rates (Wang et al., 2020).

1.4.3. Cancer

Exposure to certain CECs has been linked to the development of cancer in humans and animals. For example, exposure to polycyclic aromatic hydrocarbons (PAHs) has been linked to lung, skin, and bladder cancer, while exposure to benzene has been linked to leukaemia.

1.4.4. Developmental and reproductive abnormalities

Exposure to certain CECs during critical periods of development can cause developmental and reproductive abnormalities in humans and animals. For example, exposure to phthalates during pregnancy has been linked to adverse reproductive outcomes, such as decreased sperm count and quality, and increased risk of birth defects.

1.4.5. Neurological effects

Exposure to some CECs has been linked to neurological effects in both humans and animals. For example, exposure to lead can cause cognitive and behavioural problems in children, while exposure to mercury can cause developmental delays and neurological problems (Nilsen et al., 2019).

1.4.6. Immune system suppression

Exposure to certain CECs can suppress the immune system, making animals and humans more susceptible to infections and diseases. For example, exposure to polychlorinated biphenyls (PCBs) has been linked to immune system suppression in animals.

1.4.7. Disruption of aquatic ecosystems

CECs can also have adverse effects on aquatic organisms and ecosystems. For example, exposure to pesticides and herbicides can kill aquatic organisms, while exposure to pharmaceuticals and personal care products can alter the behavior and physiology of fish and other aquatic organisms.

1.5. Treatment methods for removing CECs

Removing CECs from water can be challenging, as many traditional water treatment methods are not designed to target these specific contaminants. However, there are several emerging technologies and treatment methods that show promise for removing CECs from water.

1.5.1. Advanced Oxidation Processes (AOPs)

AOPs are a group of water treatment methods that use powerful oxidants, such as hydrogen peroxide and ozone, to break down and eliminate organic contaminants in water. Highly reactive oxygen species will be produced during this process which attacks the organic compounds in the water by either direct electrophilic attack by means of molecular ozone or indirect attack through hydroxyl radicals (•OH). In recent years, several studies have evaluated the effectiveness of AOPs for removing CECs from water sources (Marican and Durán-Lara, 2018; Wang and Zhuan, 2020).

1.5.2. Membrane filtration

Membrane filtration technologies, such as reverse osmosis and nanofiltration, are highly effective in removing CECs from water. These technologies use a semi-permeable membrane to separate and remove contaminants from water, and can remove a wide range of CECs, including pharmaceuticals and endocrine-disrupting compounds. Membrane technology suitable for CECs is problematic because of the diverse physicochemical properties of materials and the wide range of parameters to combine for separation enhancement (Heo et al., 2020). Appropriate separation mechanisms and target pollutants narrow the choices of the membrane. Moreover, modifying the membrane surface with a target compound may improve the separation efficiency.

1.5.3. Biological treatment

Several biological treatment processes including activated sludge process (ASPs), microalgae-based treatments, biological activated carbon (BAC), and membrane bioreactors (MBRs) have exhibited effective removal for various CECs. Biological treatment methods, such as bioreactors and constructed wetlands (CWs), use microorganisms to break down and eliminate contaminants in water (Huang et al., 2018). Biological treatment can be effective in removing CECs, such as pharmaceuticals and hormones, from wastewater. BAC is effective in removing various analgesics, antibiotics, and pesticides. MBRs have shown better removal of PCPs, EDCs, and betablockers compared with CWs (Navaratna et al., 2016; Zhao et al., 2017). However, these available treatment processes have certain limitations, such as long retention time, membrane fouling, large area requirement, poor removal of some CECs, and final disposal of the sludge that contains CECs.

1.5.4. Ozonation

Ozonation is a water treatment method that uses ozone gas to disinfect water and remove organic contaminants. Ozone can break down a wide range of CECs, including pharmaceuticals, personal care products, and endocrine-disrupting compounds. Interestingly, ozone can undergo autocatalysis assisted decomposition as the rate increases with increased pH and forms non-selective and highly reactive hydroxyl radicals, which can act on a wide range of contaminants. Catalytic ozonation utilizes catalysts to improve the decomposition of ozone and enhanced the production of hydroxyl radicals, which can overcome some disadvantages of ozonation. Both homogeneous and heterogeneous catalytic ozonation processes have been used in water treatment. However, owing to the possible secondary pollution caused by the dissolved metal ions in homogeneous catalytic ozonation, the heterogeneous catalytic ozonation process is more promising (Ghanbarlou et al., 2020; Pérez-Lucas et al., 2020).

1.5.5. Ultraviolet (UV) treatment

UV treatment uses high-energy UV light to disinfect water and eliminate contaminants. UV treatment has been shown to be effective in removing CECs, such as pharmaceuticals and personal care products, from water. However, the efficiency of UV treatment depends on

several factors, including the intensity of the UV radiation, the water quality parameters, and the type of reactor used. There are several types of UV reactors used for water treatment, including low-pressure mercury lamps, medium-pressure mercury lamps, and UV-LEDs (Lindsey et al., 2018). Each type of reactor has its own advantages and limitations. The combination of UV treatment with hydrogen peroxide, known as the UV/H_2O_2 process, is a particularly effective method for removing emerging contaminants. However, the UV/H_2O_2 process can also lead to the formation of disinfection by products, which can be harmful to human health. It offers several advantages over other treatment methods, including energy efficiency, low chemical consumption, and environmentally friendly (Lee et al., 2017). However, the efficiency of UV treatment is influenced by several factors, including water quality parameters, UV dose, and the type of reactor used. Further research is needed to optimize the UV treatment process for specific contaminants and water quality parameters.

1.5.6. Adsorption

Adsorption is a commonly used method for removing emerging contaminants from water, and can be used in both drinking water and wastewater treatment applications. Adsorption works by attracting contaminants to the surface of a solid material, called an adsorbent. The most commonly used adsorbents for removing emerging contaminants are activated carbon, zeolites, and graphene-based materials. Activated carbon is the most widely used adsorbent due to its high surface area, pore structure, and availability. However, zeolites and graphene-based materials have shown promising results in recent studies. The efficiency of adsorption depends on several factors, including the properties of the adsorbent, the concentration and type of contaminants, and the pH and temperature of the water. The adsorption capacity of an adsorbent is influenced by its surface area, pore structure, and surface chemistry. The type of contaminant also affects the adsorption efficiency, as some contaminants are more easily adsorbed than others. The pH and temperature of the water can also affect the adsorption efficiency, as changes in these parameters can alter the surface chemistry of the adsorbent and the properties of the contaminants.

It is important to note that each of these treatment methods has its own advantages and limitations, and may not be equally effective for all types of CECs or water sources. Additionally, implementing these technologies can be costly and may require specialized expertise. Therefore, continued research and development of emerging technologies and

treatment methods is necessary to effectively remove CECs from water and protect public health and the environment.

1.6. Why adsorption as a promising treatment method for CECs removal?

Adsorption is a water treatment technology that involves the attachment or adhesion of CECs onto the surface of a solid material, known as the adsorbent. Compared to other treatment techniques, adsorption has several advantages that make it an effective option for the removal of CECs (Fig. 1.3).

Selectivity: Adsorption is a selective process that can target specific CECs in water, while leaving other harmless compounds intact. This is especially important when dealing with low concentrations of CECs or when other chemicals are present.

Wide range of CEC removal: Adsorption can remove a wide range of CECs from water, including pharmaceuticals, personal care products, and endocrine-disrupting compounds, among others. This makes it a versatile treatment option for the removal of various types of CECs.

High removal efficiency: Adsorption can achieve high removal efficiencies of up to 99%, making it a highly effective treatment option for removing CECs from water.

Cost-effective: Adsorption is often less expensive than other treatment technologies, as it requires less energy and chemicals. Adsorbents can be easily regenerated and reused, which further reduces the cost of the treatment process.

Easy implementation: Adsorption is a simple and easy-to-implement water treatment technology. It can be easily scaled up or down depending on the size of the treatment plant, and requires minimal operator training.

Compatibility with other treatment techniques: Adsorption can be used in combination with other water treatment techniques, such as advanced oxidation processes (AOPs) and membrane filtration, to enhance the overall efficiency of the treatment process.

Environmental sustainability: Adsorption is an environmentally sustainable treatment technology that produces very less or no waste, and can be operated using renewable energy sources, such as solar or wind power. Reusability of adsorbent can lead to zero-waste disposal.

In conclusion, adsorption is an effective and cost-efficient water treatment technology that offers several advantages over other treatment techniques for the removal of contaminants of emerging concern (CECs). Its selectivity, wide range of CEC removal, high removal efficiency, cost-effectiveness, easy implementation, compatibility with other treatment techniques, and environmental sustainability make it an attractive option for the removal of CECs from water (Dai et al., 2019; Pai et al., 2020).

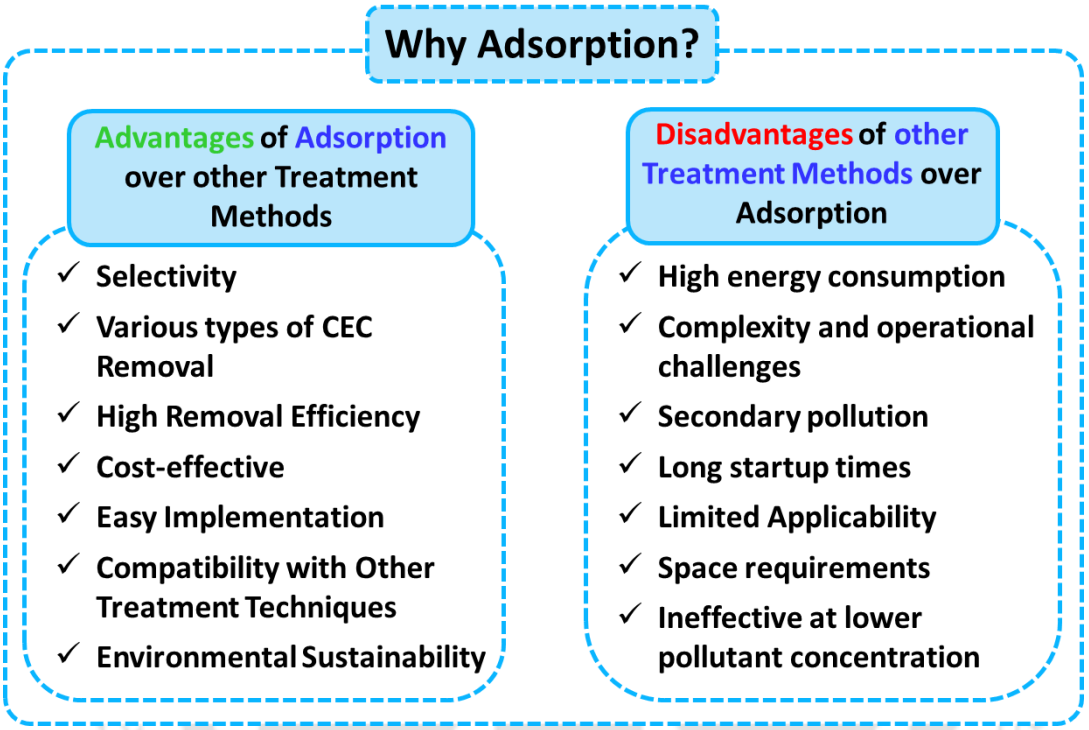

Fig. 1.3. *Advantages of adsorption and disadvantages of other treatment methods*

1.7. Theoretical aspects

1.7.1. Isotherm models

Isotherm refers to the relationship between the equilibrium adsorbate concentrations in the liquid-phase and the equilibrium adsorption amount on the solid-phase at a certain temperature. Various isotherm models with their linear and non-linear equations were tabulated in the Table A1.

1.7.1.1. Langmuir isotherm model

The Langmuir isotherm model assumes that adsorption occurs through a reversible process in which the pollutant molecules attach to the surface of the adsorbent via weak chemical bonds. The Langmuir model also assumes that the surface of the adsorbent is homogeneous,

and that the adsorption of one molecule does not affect the adsorption of another molecule. The Langmuir isotherm model is often used to analyze data from batch adsorption experiments, in which a fixed amount of adsorbent is exposed to a range of pollutant concentrations. The Langmuir isotherm model has several limitations, including the assumption of a homogeneous surface, the assumption of a fixed number of adsorption sites, and the assumption of reversible adsorption. However, the Langmuir isotherm model is a useful tool for understanding the adsorption of pollutants onto solid surfaces and for designing adsorption systems for pollution control (Guo et al., 2019; Langmuir, 1918).

1.7.1.2. Freundlich isotherm model

The Freundlich isotherm model is another commonly used model to describe the adsorption of pollutants onto solid surfaces. Unlike the Langmuir isotherm model, the Freundlich model does not assume a homogeneous surface or a fixed number of identical adsorption sites. Instead, it assumes that the adsorption occurs on a heterogeneous surface with a range of adsorption energies. The Freundlich model assumes that the amount of pollutant adsorbed increases with increasing concentration, but at a decreasing rate. This reflects the fact that as more pollutant molecules are adsorbed onto the surface, the available adsorption sites become more limited, and the energy required to adsorb additional molecules increases.

The Freundlich isotherm model has several advantages over the Langmuir isotherm model, including its ability to account for the heterogeneity of the adsorption surface and the non-reversible nature of adsorption. However, it is important to note that the Freundlich model also has limitations, including its inability to account for saturation effects and its sensitivity to changes in the adsorbent surface properties (Freundlich, 1907; Zaheer et al., 2019).

1.7.1.3. Dubinin Radushkevich (DR) isotherm model

The Dubinin Radushkevich (DR) isotherm model is another commonly used model to describe the adsorption of pollutants onto solid surfaces. The DR model assumes that the adsorption occurs on a heterogeneous surface with a range of adsorption energies, similar to the Freundlich model. However, it also takes into account the variation of the adsorption potential with the degree of surface coverage. The DR model assumes that the adsorption potential decreases as the degree of surface coverage increases, due to the increasing

competition between adsorbate molecules for available adsorption sites (Dubinin, 1947). This results in a characteristic downward curvature in the DR isotherm plot.

The DR isotherm model has several advantages over the Langmuir and Freundlich models, including its ability to account for the variation of the adsorption potential with the degree of surface coverage and the heterogeneity of the adsorption surface. However, it also has limitations, including its inability to account for the effects of surface diffusion and pore size distribution on the adsorption process (Chabani et al., 2006).

1.7.1.4. Temkin isotherm model

The Temkin isotherm model is another commonly used model to describe the adsorption of pollutants onto solid surfaces. The Temkin model assumes that the adsorption occurs on a homogeneous surface with a uniform distribution of adsorption energies (Temkin, 1940). The Temkin model assumes that the heat of adsorption decreases linearly with coverage due to adsorbate-adsorbate interactions on the surface, resulting in a decrease in the adsorption energy for each additional adsorbate.

The Temkin isotherm model has several advantages over the Langmuir and Freundlich models, including its ability to account for adsorbate-adsorbate interactions on the surface and the effect of temperature on the adsorption process. However, it also has limitations, including its inability to account for the effects of surface heterogeneity and pore size distribution on the adsorption process (Yang, 1993).

1.7.1.5. Jovanovic isotherm model

The Jovanovic isotherm model is a relatively new model that has been proposed to describe the adsorption of pollutants onto solid surfaces. This model assumes that the adsorption of pollutants occurs on a heterogeneous surface with a range of adsorption energies, similar to the Freundlich model.

The Jovanovic model assumes that the adsorption potential decreases as the concentration of the pollutant increases, due to the increasing competition between adsorbate molecules for available adsorption sites. The Jovanovic isotherm model has some advantages over other models, including its ability to account for both surface heterogeneity and the competition between adsorbate molecules for available adsorption sites. However, it is a relatively new model and has not been extensively validated or compared to other models

in the literature. More research is needed to determine the effectiveness and limitations of the Jovanovic isotherm model for different types of adsorption systems (Chu et al., 2023).

1.7.2. Kinetic models

The adsorption kinetic study provides information of the adsorption rate, the performance of the adsorbent used, and the mass transfer mechanisms. Knowing the adsorption kinetic is essential for the design of the adsorption systems. Various kinetic models with their equations were tabulated in the Table A2.

1.7.2.1. Pseudo-first-order model

Pseudo-first-order assumes of the rate of number of filled adsorption sites to unfilled sites in most biosorption process, this model is not significant for whole contact time, and it suits for the biosorption process only at the initial stage. As the pollutant is adsorbed onto the surface, the number of unoccupied sites decreases, causing the rate of adsorption to slow down. It is important to note that the pseudo-first-order kinetics model assumes that the concentration of the pollutant in the surrounding solution remains constant throughout the adsorption process, which may not always be the case in real-world situations. Additionally, the model may not accurately describe the adsorption behavior of all pollutants and surfaces (Wang and Guo, 2020).

1.7.2.2. Pseudo-second-order model

Pseudo-second-order model states about the behavior of the biosorption process for the entire time. In this model it is assumed that due to the sharing of electrons between the adsorbate and adsorbent which involves some valence forces considered to be the rate limiting step. Unlike the pseudo-first-order model, the pseudo-second-order model does not assume that the concentration of the pollutant in the surrounding solution remains constant throughout the adsorption process. This makes it a more accurate model for describing real-world situations where the concentration of the pollutant may change over time. However, it is important to note that the pseudo-second-order kinetics model may not accurately describe the adsorption behavior of all solutes and surfaces. Other factors such as temperature, pH, and the presence of other compounds can also affect the adsorption process. Therefore, it is important to use caution when applying this model and to validate its assumptions with experimental data (El-Khaiary et al., 2010).

1.7.2.3. Elovich kinetic model

The Elovich kinetic model is a commonly used model to describe the adsorption mechanism of pollutants onto surfaces. It assumes that the adsorption process occurs through two steps: (1) a surface reaction that is relatively fast and (2) a diffusion step that is slower. It is useful for describing the complex adsorption process that involves both surface reactions and diffusion, and can provide insight into the mechanisms underlying the adsorption process. It is useful for providing insight into the underlying mechanisms of the adsorption process and can be used to predict the behavior of the adsorption system over time (Wu et al., 2009).

1.7.2.4. Intra-particle diffusion model

The intra-particle diffusion model is a commonly used kinetic model for describing the adsorption of solutes onto solid surfaces. It assumes that the adsorption process occurs through several steps, including (1) transport of solute molecules from the bulk solution to the external surface of the adsorbent, (2) diffusion of solute molecules through the pores of the adsorbent, and (3) adsorption of solute molecules onto the surface of the adsorbent. The intra-particle diffusion model is often used to describe the adsorption behavior of solutes onto porous materials, such as activated carbon or zeolites. It is useful for providing insight into the mechanisms underlying the adsorption process (Wang and Guo, 2022).

1.7.3. Thermodynamic analysis

Thermodynamic studies in adsorption are important for understanding the energy changes that occur during the adsorption process. These studies help to determine the feasibility and spontaneity of the adsorption process, and provide insight into the factors that influence the adsorption behavior. The thermodynamic parameters that are commonly studied in adsorption include the Gibbs free energy change (ΔG), the enthalpy change (ΔH), and the entropy change (ΔS). These parameters can be calculated using experimental data such as the adsorption isotherm and the temperature dependence of the adsorption process.

The Gibbs free energy change (ΔG) is an important parameter that determines the spontaneity of the adsorption process. Gibbs free energy (G) is a thermodynamic potential that measures the maximum useful work obtained from a system at constant temperature and pressure. If ΔG is negative, the adsorption process is thermodynamically favourable

and spontaneous. If ΔG is positive, the adsorption process is not favourable and non-spontaneous.

The enthalpy change (ΔH) is related to the heat absorbed or released during the adsorption process. It is a measure of the internal energy of a system plus the product of pressure and volume, which makes it particularly useful for systems under constant pressure conditions, such as most chemical reactions that occur in open containers. It provides information about the energy required for the adsorption process to occur. If ΔH is negative, the adsorption process is exothermic, and if it is positive, the adsorption process is endothermic.

The entropy change (ΔS) is related to the degree of disorder in the system during the adsorption process. It provides information about the change in the degree of freedom of the adsorbate and adsorbent. A high entropy implies a high degree of disorder, while a low entropy implies orderliness or organization. The concept of entropy change is crucial in understanding the spontaneity and direction of processes, particularly in chemical reactions and phase transitions. If ΔS is positive, the adsorption process is accompanied by an increase in the degree of disorder, which suggests that the adsorption process is more favourable at higher temperatures (Myers and Monson, 2014).

Thermodynamic studies in adsorption can be used to optimize the design and operation of adsorption systems, as well as to understand the fundamental mechanisms of the adsorption process. However, it is important to note that the thermodynamic parameters may be affected by experimental conditions such as the initial concentration of the adsorbate and the surface properties of the adsorbent, and thus caution must be taken when interpreting the results (REN et al., 2007).

1.7.4. Continuous column models

Continuous column models are commonly used to study the process of adsorption in industrial and laboratory settings. In these models, a fixed-bed column is packed with a solid adsorbent material, and a liquid or gas stream containing the target species to be adsorbed is passed through the column. These studies are used to determine the performance of the adsorbent material for removing pollutants from the water under different conditions.

The experimental setup typically involves measuring the influent and effluent concentrations of the pollutant, and monitoring the breakthrough curve, which is the time-dependent change in effluent concentration as the adsorbent becomes saturated with the pollutant. By analyzing the breakthrough curve data, various parameters such as the breakthrough time, the adsorption capacity, and the rate of adsorption can be determined (Bunluesin et al., 2007; Lim and Aris, 2014).

Continuous column studies can also be used to optimize the operating conditions for the adsorption process, such as the flow rate, bed height, and contact time. These studies can provide valuable information for designing and scaling up adsorption systems for the treatment of contaminated water.

1.7.4.1. Thomas model

The Thomas model is a mathematical model that is commonly used for column studies in adsorption processes. It is particularly useful for describing the adsorption of solutes from dilute solutions in continuous-flow systems. The model assumes that the adsorption of solutes occurs on a surface with a finite capacity, and that the driving force for adsorption is the concentration difference between the bulk liquid phase and the adsorbent surface (Soetaredjo et al., 2014). The equation can be mathematically represented as:

$$\ln\left(\frac{C_0}{C_t} - 1\right) = \frac{k_{TH} Q_0 w}{F} - k_{TH} C_0 t \qquad (1.1)$$

Where, k_{TH} (mL min^{-1} mg^{-1}) and Q_0 (mg g^{-1}) are the Thomas model constant and the adsorption capacity of adsorbent, respectively; F (mL min^{-1}) represents the flow rate of adsorbate in the column; w (g) is the weight of adsorbent in the fixed bed column; and C_0/C_t denotes the ratio of influent to an effluent concentration of adsorbate.

The Thomas model assumes that the adsorption process is controlled by two steps: transport of the solute from the bulk liquid phase to the adsorbent surface, and adsorption of the solute onto the surface. The model can be used to determine the breakthrough time, which is the time required for the effluent concentration of the solute to reach a certain level, as well as the rate of adsorption and the adsorption capacity of the adsorbent (Calero et al., 2009). Column studies using the Thomas model can be used to optimize the design and operation of adsorption systems, as well as to evaluate the performance of different types of adsorbents for the removal of pollutants from water. The model can be applied to a wide

range of solutes and adsorbents, and can provide valuable insights into the adsorption process.

1.7.4.2. Adams-Bohart model

The Adams-Bohart model is a mathematical model used to describe the behavior of a fixed-bed column during the adsorption of solutes from a fluid stream (Foroughi-dahr et al., 2016). This model is useful for predicting the breakthrough behavior of a fixed-bed adsorbent and can be used for design and optimization of adsorption systems. The linear expression can be presented mathematically as:

$$\ln\left(\frac{C_t}{C_0}\right) = k_{AB}C_0 t - \frac{k_{AB}N_{AB}z}{u} \qquad (1.2)$$

where C_0 (mg L^{-1}) and C_t (mg L^{-1}) are influent and effluent adsorbate concentrations, adsorbent bed height is z (cm); superficial velocity u (cm min^{-1}) that were derived by dividing flow rate of the column by the cross-sectional area of the bed. k_{AB} (L mg^{-1} min^{-1}) and N_{AB} (mg L^{-1}) are the kinetics constant and saturation constant.

The Adams-Bohart model assumes that the adsorption process is a combination of external mass transfer and intraparticle diffusion. The model assumes that the adsorption capacity of the bed is uniform throughout the bed and the rate of adsorption is proportional to the concentration difference between the bulk fluid and the adsorbent surface. The Adams-Bohart model is useful for determining the breakthrough time of the adsorption process, as well as the maximum adsorption capacity of the bed. It can also be used to optimize the design of the fixed-bed column, such as the bed height and diameter, flow rate, and adsorbent characteristics (Chu, 2020).

1.7.4.3. Yoon-Nelson model

The Yoon-Nelson model is used to simulate the behavior of particles in a packed column. In a packed column, particles are packed into a fixed bed and a fluid flow through the column, causing the particles to move and interact with each other. The Yoon-Nelson model considers the hydrodynamic interactions between the particles and the fluid, and is used to predict the motion and behavior of the particles in the column (Yu et al., 2015). Mathematical equation of this model is given below,

$$\ln\left(\frac{C_t}{C_0 - C_t}\right) = k_{y_N}t - k_{yN}\tau \qquad (1.3)$$

Here, k_{yN} (min^{-1}) and τ (min) are the rate constant and time needed for 50% adsorbate breakthrough respectively whereas t represents the processing time.

The Yoon-Nelson model is based on the concept of a two-phase flow, where the fluid is treated as one phase and the particles are treated as another phase. The model uses equations that describe the motion and behavior of the particles and the fluid, and includes terms that account for the interactions between the particles and the fluid. The Yoon-Nelson model is generally used in column studies, to predict the behavior of particles in a packed column under various operating conditions.

1.8. Problem statement and related objectives

Water pollution, because of rapid increase in the contaminants of emerging concern (CECs), such as pharmaceuticals, personal care products, heavy metals, and endocrine-disrupting compounds, in water sources poses a significant threat to the environment, living organisms, and public health. These CECs are persistent in aquatic environments because the conventional water treatment methods fail to eliminate them completely. To address this issue, there is a critical need for innovative and sustainable solutions. Adsorption via bio-based engineered adsorbents present a promising solution for the removal of CECs, due to their potential for tailored surface modifications and environmental sustainability. However, several knowledge gaps and challenges such as target specificity, interaction studies between adsorbate and adsorbent, absence of column studies, desorption and reusability studies hinder the widespread application of these adsorbents for CEC removal. This thesis aims to address these gaps by investigating the adsorption efficiency, mechanisms, and scalability of bio-based engineered adsorbents in the context of removing contaminants of emerging concern from aquatic systems. By elucidating these aspects, this thesis seeks to contribute to the development of effective and sustainable water treatment strategies for mitigating the impact of CECs on environmental and public health. So, based on the discussed problem statements the current research work has been designed with the following objectives:

1. *Synthesis and Characterization of engineered adsorbents from bio-based materials.*
2. *Optimization of adsorption parameters for maximum removal efficiency through batch studies.*

3. *Investigating the mechanisms and possible interactions via isotherm and kinetic modeling.*
4. *Performing regeneration studies to evaluate adsorbents' recyclability.*
5. *Examining the toxicity before and after adsorption process through Phyto, Microbial and Fish models.*
6. *Continuous packed bed column studies and real-time sample studies for industrial setup.*

Table 1.5. *Various adsorbents/biosorbents and the pollutants used in this thesis work*

Adsorbent/Biosorbent	Precursor material	Modification method	Pollutant	Environmental impacts of pollutants
Magnetic Sawdust (MSD)	Sawdust	Magnetization	Diclofenac (DCF)	• Mortality • Growth abnormalities • Cardiotoxicity • Neurotoxicity • Hepatotoxicity • Nephrotoxicity
Corn starch nanoparticles (CSNP)	Corn Starch	Acid hydrolysis	Ibuprofen (IBU)	• Gastric ulceration • Mucosal damages Dyspepsia • Bowel inflammation • Hinder postembryonic development among amphibians
			Sulfamethoxazole (SUL)	• Inhibits soil phosphatase activity • Thyroid gland follicular adenoma • Oxidative damage • Genotoxicity • Bioaccumulation in liver • Highly toxic to aquatic organisms
Fe_3O_4/CAC nanocomposite (MCAC)	Commercial Activated Carbon	Magnetization	Cerium (Ce)	• Irritation to the skin • Severe threat to liver • Carcinogenicity • Lung embolism

				• Negative influences on reproduction • Cellular damage
Fe_3O_4/AC nanocomposite	Biomass of *Prosopis juliflora*	Magnetization	Lead (Pb)	• Causes oxidative stress • Neurotoxicity • Hypertension • Cognitive deficits • Infertility • Gastrointestinal effects
			Congo red (CR)	• Hepatocarcinoma • Splenic sarcoma • Nuclear abnormalities • Chromosomal errors in mammalian cells • Platelet aggregation • Thrombocytopenia
Oxidant-modified biochar (OBC)	Sawdust	Oxidation	Basic fuchsin (BF)	• Carcinogenic and mutagenic effects • Headache • Muscle contraction • Gastrointestinal irritation • Nausea and vomiting

1.9. Outline of the thesis

Based on the above-discussed objectives the thesis work has been divided into the following 7 chapters.

Chapter-1: General introduction and theoretical background.

Chapter-2: Ecotoxicological assessment of micropollutant Diclofenac biosorption on Magnetic sawdust: Phyto, Microbial and Fish toxicity studies.

Chapter-3: Effective removal of Pharmaceutical Contaminants Ibuprofen and Sulfamethoxazole from water by Corn starch nanoparticles (CSNP): An ecotoxicological assessment.

Chapter-4: Development of Fe_3O_4/CAC nanocomposite for the effective removal of Contaminants of emerging concern (Ce^{3+}) from water: An ecotoxicological assessment.

Chapter-5: Toxicological assessment and adsorptive removal of Lead (Pb) and Congo Red (CR) from water by synthesized Iron oxide/Activated Carbon (Fe_3O_4/AC) nanocomposite.

Chapter-6: Synthesis, characterization, and application of oxidant-modified biochar prepared from saw-dust for sequestration of Basic Fuchsin: Isotherm, kinetics, column, and toxicity studies.

Chapter-7: Summary and overall conclusion

Chapter 2

Ecotoxicological Assessment of Micropollutant Diclofenac Biosorption on Magnetic Sawdust: Phyto, Microbial and Fish toxicity studies

The work embodied in this chapter is published in

Vishnu Priyan V., Shahnaz, T., Suganya, E., Sivaprakasam, S., Narayanasamy, S., 2020. Ecotoxicological assessment of micropollutant Diclofenac biosorption on magnetic sawdust: Phyto, Microbial and Fish toxicity studies. **Journal of Hazardous Materials**, 403,123532. https://doi.org/10.1016/j.jhazmat.2020.123532 **(Elsevier; SCI IF 2023: 13.6).**

Abstract

Diclofenac (DCF), a persistent pharmaceutical micropollutant which occurs in the ecosystems causing adverse effects on aquatic as well as terrestrial organisms. In this study, magnetic sawdust (MSD) was prepared using co-precipitation method for biosorptive removal of DCF from water. The MSD was characterized using various analytical techniques like microscopic and spectroscopic analysis. Vibrating sample magnetometer study confirms the ferromagnetic behavior of the biosorbent which is a key advantage in the separation of MSD after biosorption. The effect of experimental parameters was optimized in batch mode with evaluated maximum efficiency of 86.12% at pH 6.0, biosorbent dosage 0.025 g/L for 50 mg/L of DCF. Ecotoxicological assessment has been performed for the treated and untreated sample using plant seeds, microbes, and zebra fish to check the adverse effects of DCF on these organisms. Evaluation of toxicity studies revealed that inhibition concentration of DCF for various seeds (60.91 mg/L to 43.11 mg/L), *E. coli* (48.82 µg/mL) and *B. subtilis* (31.55 µg/mL). The lethal concentration of DCF on the *Danio rerio* was found to be 156.99 mg/L. In contrast, significant increase in both the concentration measures of DCF after biosorption was observed making this biosorbent a potent alternative to other available treatment measures.

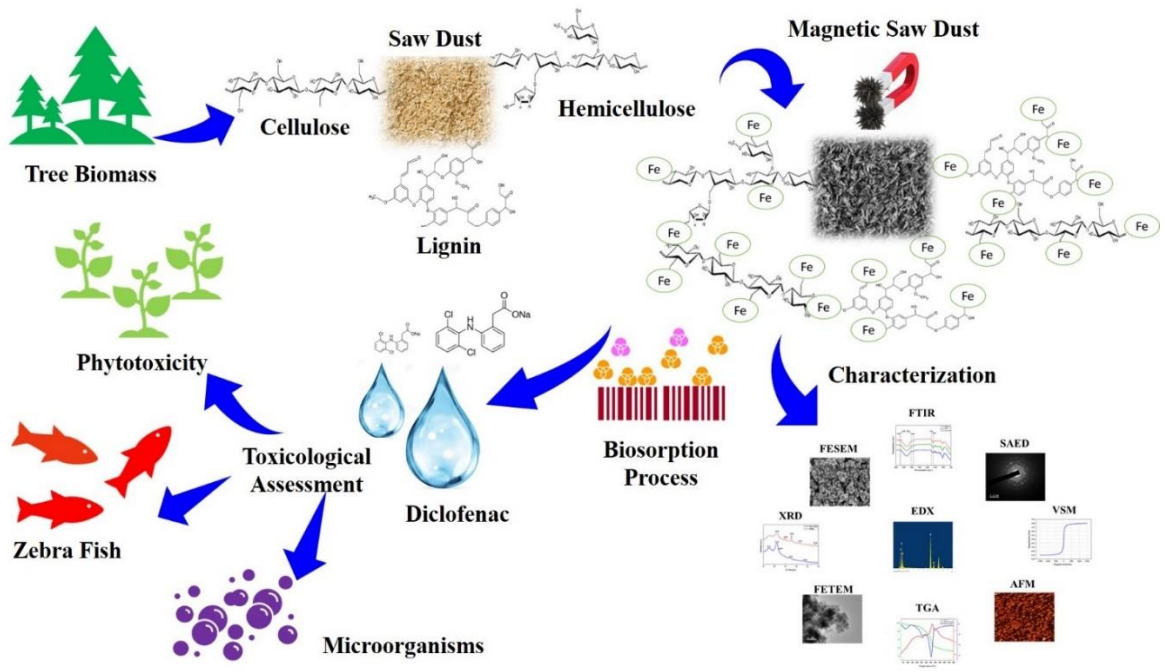

Graphical Abstract

2.1. Materials and methods

2.1.1. Chemicals and materials

Sawdust was collected from a sawmill in Guwahati, India. The sawdust was washed and made into magnetic sawdust using ferric chloride hexahydrate ($FeCl_3.6H_2O$), ferrous chloride tetrahydrate ($FeCl_2.4H_2O$), ammonia solution, and absolute ethanol (≥ 99.9%) were procured from HiMedia. Diclofenac sodium salt ($C_{14}H_{10}Cl_2NNaO_2$) which is used as a pollutant was obtained from Sigma-Aldrich. Sodium hydroxide (HiMedia) and hydrochloric acid (SRL) were used to adjust the pH of the mixture. All other chemicals used in this study were procured from HiMedia.

2.1.2. Preparation of magnetic sawdust (MSD)

The saw dust collected was washed with tap water and then with distilled water for several times until wash water becomes clear. Then the saw dust was dried at 70 °C for 36 h in the oven and grinded using a grinder. The powdered saw dust was then sieved (mesh size -150 BSS) and the sieved dust was stored for further use. To 200 mL of distilled water, 5.00 g of $FeCl_3.6H_2O$, and 2.50 g of $FeCl_2.4H_2O$ was added and stirred continuously in the magnetic stirrer until the chemicals completely dissolved in water. Then, to the solution 10.00 g of sieved saw dust was added and stirred at 80 °C for 15 h. Then 10% ammonia solution were added to the mixture drop-wise until the color of the mixture changes to bluish black, and stirred the mixture for 50 minutes at 60 °C. Then the suspension was filtered and washed with distilled water and ethyl alcohol for three times. Then the prepared magnetic sawdust was dried at 50 °C for 24 h in oven and stored in desiccator for further study.

2.1.3. Characterization of MSD

The morphology, topology and elemental analysis of the MSD was done using Field Emission Scanning Electron Microscopy (FESEM, Zeiss-Sigma 300), Field Emission Transmission Electron Microscopy coupled with EDX detector (FETEM, JEOL-2100F) and Atomic Force Microscopy (AFM, Oxford, Cypher).

The functional groups of MSD before and after biosorption were investigated using Fourier Transform Infrared Spectroscopy (Perkin Elmer, USA). The range of the spectra was from 400 to 4000 cm^{-1}. The thermal stability of the MSD was examined by thermogravimetric

analyzer (TGA, Netzsch-STA449F3A00). Crystallinity of the biosorbent was determined by using X-ray powder Diffraction (XRD, Rigaku, Micromax-007HF).

2.1.4. Batch biosorption experiments

The biosorption of DCF was investigated through batch studies under various initial concentrations. 50 mL of DCF solution was taken and stirred at 120 rpm on a shaking incubator. The effect of pH was studied in the range of 2.0-10.0. The pH of the solution was altered using 0.1M HCl or 0.1M NaOH solution. The effect of biosorbent dosage was determined using various amount of biosorbent ranging from 0.025-0.150 g/L. The effect of the initial concentration of DCF solution was investigated using various concentrations from (10 to 50 mg/L). The residual DCF concentration was determined using UV visible spectrophotometer at a wavelength of 276 nm.

The amount of DCF biosorbed per gram of MSD was calculated from the following equation

$$q_e = \frac{(C_0 - C_e)}{m} \times V \qquad (2.1)$$

The removal efficiency of DCF was determined by using following expression

$$Removal(\%) = \frac{C_0 - C_e}{C_0} \times 100 \qquad (2.2)$$

where q_e is the amount of DCF biosorbed at equilibrium time (mg/g), C_0 and C_e are the initial and equilibrium DCF concentrations (mg/L), V is the volume of DCF solution (L) and m is the mass of the biosorbent (g).

2.1.5. Phytotoxicity experiments

The phytotoxicity studies of DCF before biosorption and after treating with MSD was examined using *Vigna mungo* (black gram), *Macrotyloma uniflorum* (horse gram), *Cicer arietinum* (Bengal gram), *Vigna radiata* (green gram), *Pennisetum glaucum* (pearl millet) seeds. The phytotoxic experiments were carried out by Podio *et al* with modifications (Podio et al., 2020). These experiments were done at room temperature in Petri dishes. The phytotoxicity effect was measured in terms of germination rate of seeds, shoot length, and root length of seedlings after seven days. The seeds were sterilized to avoid fungal and yeast growth with 1% sodium hypochlorite solution for 10 minutes and washed 15 times with deionized water. Then the sterilized seeds were added to Petri dishes containing

distilled water as control, DCF solution before biosorption and after biosorption at various concentrations (10, 20, 30, 40 and 50 mg/L). The Petri dishes with seeds were incubated in dark for seven days, and checked the rate of germination and growth inhibition to determine phytotoxicity.

2.1.6. Microbial toxicity experiments

The DCF before and after biosorption were subjected to microbial toxicity test using *E. coli* and *B. subtilis* strains as model organisms. The toxicity studies on the model organisms were done in 96 well plate. *E. coli* and *B. subtilis* were cultured in Muller-Hinton broth media (37 °C, 24 h). Then 100 µL of the microorganism suspensions and 100 µL of DCF at various concentrations (10-50 µg/mL) were added to individual wells of the plate. Similarly, to 100 µL of microorganism suspension, 100 µL of treated DCF were added. Then the plates were incubated at 37 °C for 24 h. The control well contains only bacterial culture. After 24 h, optical density (OD) was measured at 600 nm and the growth inhibition was calculated (Wu et al., 2019).

2.1.7. Acute fish toxicity experiments

The acute toxicity of the zebra fish for 96 h on DCF solution before biosorption (untreated) and DCF solution after biosorption (treated) was done according to the Test Guideline No. 203, Fish acute toxicity testing of OECD. *Danio rerio* (zebra fish) were selected for each treatment with same size and age group. The untreated DCF solutions were prepared in the concentrations of 1, 5, 15, 30, 60, 90, 120, 150, 180, and 210 mg/L.

The parameters such as pH (6.5-7.5), oxygen concentration (>75% of air saturation), photoperiod (14:10, Light: Dark) and the temperature of 25 °C were maintained throughout the experiments. Totally, 22 treatments (11 each for DCF before and after biosorption) were done with 10 fishes for each treatment. The solution with 0 mg/L (no DCF) was taken as control and the remaining treatments with untreated DCF solution and treated DCF solution with the above-mentioned concentrations. After 96 h the total number of fish died in each treatment was recorded and the mortality % was calculated (Sotto et al., 2017) (Wu et al., 2019).

2.2. Results and discussion

2.2.1. Characterization of MSD

Field Emission Scanning Electron Microscopy, Field Emission Transmission Electron Microscopy and Atomic Force Microscopy were used to analyse morphology and topology of the MSD. The functional groups present in MSD were investigated using Fourier Transform Infrared Spectroscopy with spectra range 400 to 4000 cm^{-1}. Thermal stability and crystallinity of the biosorbent was determined by using thermogravimetric analyzer and X-ray powder Diffraction.

2.2.1.1. FESEM and FETEM analysis

The morphology of the surface of the MSD was examined using FESEM. The sawdust (Fig. 2.1 (a) and (b)) primarily comprised of 96.93% dry matter with extractible materials (7.30%), cellulose (57.60%) and lignin (28.10%) (Miao et al., 2017). The FESEM results revealed that the MSD forms aggregates and they are spherical in shape. These particles were observed clearly at high magnifications.

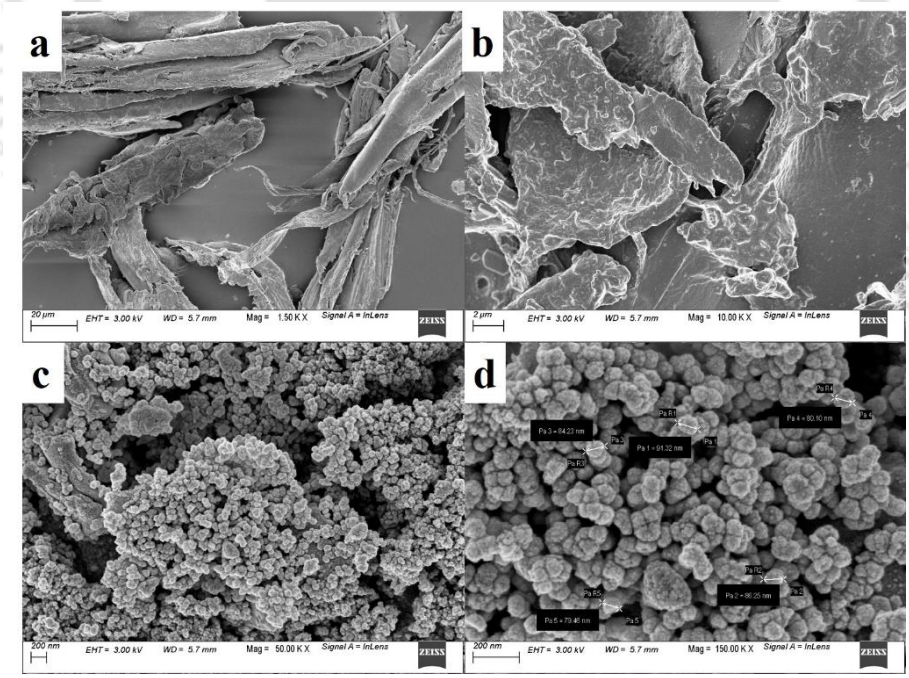

Fig. 2.1. *FESEM micrographs at different magnifications* ***a)*** *Sawdust (1.50 KX),* ***b)*** *Sawdust (10.00 KX),* ***c)*** *MSD (50.00 KX),* ***d)*** *MSD (150.00 KX)*

Fig. 2.1 (c) and (d) depicted that the MSD with a diameter of 30-100 nm and found to be non-homogeneous. FESEM results showed that the saw dust exhibits porous rough surface

and the particles with non-uniform size. Thus, making the saw dust magnetic which increases the surface to volume ratio providing large surface for biosorption process.

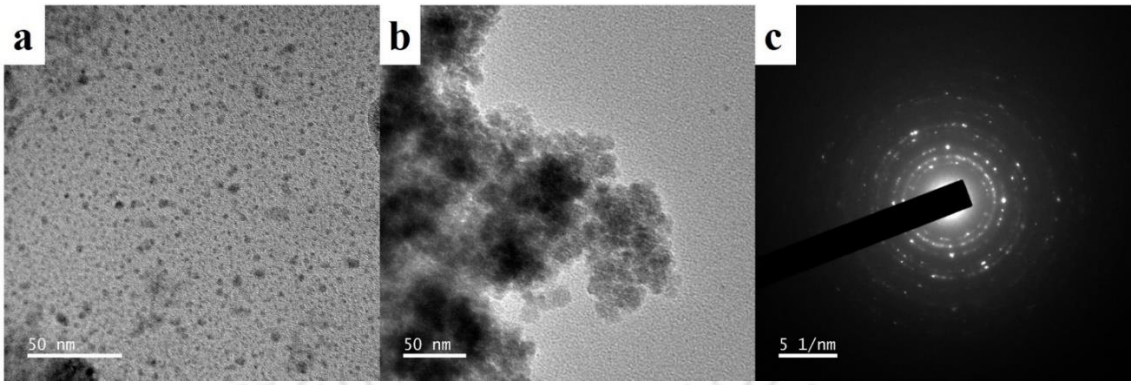

Fig. 2.2. *FETEM images (a) and (b) of MSD at different regions, c) SAED image of MSD*

Fig. 2.2 (a) and (b) showed the FETEM micrograph of MSD with average particle size less than 50 nm and forms clusters. Fig. 2.2 (c) illustrates the selected area electron diffraction (SAED) pattern of MSD which reveals that the biosorbent contains both crystalline and amorphous regions in it.

2.2.1.2. EDX analysis

The elemental characterization of the MSD was analyzed by using Energy Dispersive X-ray (EDX) analyzer, which was attached with a FETEM. The MSD (biosorbent) surface is exposed to an electron beam, which produces X-rays of precise wavelengths that are specific for each element. The electron beam moves across the MSD surface and produces distinguishing X-rays for each element.

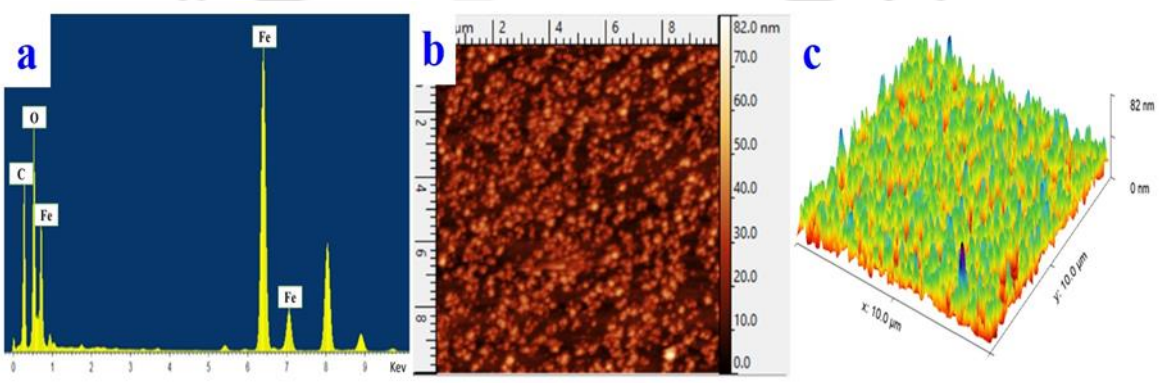

Fig. 2.3. a) *EDX image of Magnetic saw dust (MSD),* ***b)*** *AFM micrographs of MSD* ***b)*** *2-Dimensional and* ***c)*** *3-Dimensional image*

Fig. 2.3 (a) showed the EDX spectrum of the MSD and the results showed that the presence of carbon (C), oxygen (O), and iron (Fe). The weight percentage of the carbon is about 22.23% indicates that MSD consists of organic molecules made up of carbon. Oxygen (24.43%) is observed which represents the presence of hemicellulose and lignin. The amount of Fe is maximum (53.34%) which was due to the magnetic nature of MSD.

2.2.1.3. AFM analysis

The physical picture of MSD surface is given by AFM. The different characteristics such as size, surface roughness, shape can be determined by AFM. Fig. 2.3 (b) and (c) represents the 2D and 3D micrographs of AFM of MSD. The nodules are represented by bright peaks and the pores are seen as dark depressions. From the Fig. 2.3 (c) it is observed that the nodules are not merged and they have clear peaks. The height difference was found to be 82 nm. The various roughness parameters of biodegradable saw dust were found to be R_a (12.65), R_y (126.52), R_z (70.93), R_{ms} (16.70) (Miao et al., 2017). The values for roughness and some parameters were given in the Table 2.1.

Table 2.1. *AFM roughness parameters for MSD*

Roughness Parameters		**Values**
Roughness average	(R_a)	7.11303 nm
Root mean square roughness	(R_q)	8.57411 nm
Maximum height of the roughness	(R_t)	39.7740 nm
Maximum roughness valley depth	(R_v)	17.7741 nm
Maximum roughness peak height	(R_p)	21.9999 nm
Average maximum height of the roughness	(R_z)	35.2501 nm
Skewness	(R_{sk})	0.28532
Kurtosis	(R_{ku})	2.36417
Waviness average	(W_a)	3.13292 nm

The adsorption of the biosorbate into biosorbent can be influenced by the topography of the material surfaces. The surface roughness increases the maximum density attainable in the biosorbent. By increasing the roughness of the surface, it leads to increase in the process of the adsorption of DCF on the MSD.

2.2.1.4. Thermal stability analysis

The thermal stability of the MSD was determined by using TGA and DSC. Fig. 2.4 (a) depicts the TGA/DSC thermograms of the MSD. In TGA, heat is used to induce the reaction and changes the physical properties of the material. The mass change was due to oxidation, dehydration and decomposition of the MSD with the temperature and the time. DSC shows the melting point and polymorphic state of MSD. Fig. 2.4 (a) revealed that a broad exotherm was found at 265 °C and an endotherm at 365 °C. As the temperature increases from 50 °C to 220 °C, there is a weight loss of 9% weight in MSD due to the evaporation of water molecules from MSD. Due to pyrolysis of hemicellulose, cellulose and lignin, thermal degradation occurs sharply at 220 °C. The thermal decomposition takes place till 600 °C and the weight loss of MSD was found to be 68%. This proves that MSD have high thermal stability. DTG curve showed that MSD have multiple decomposition step with peak temperatures at 355 °C, 265 °C and 75 °C respectively.

2.2.1.5. FTIR analysis

Fig. 2.4 (b) explains the FTIR spectra of saw dust, MSD before and after biosorption. The broad and intense peak was seen in the spectra between 3700-3040 cm^{-1} which was due to the stretching of O-H vibrations of components present in saw dust, MSD, MSD after adsorption (MSDAA). The short weak peak was seen at 2941 cm^{-1} which corresponds to the stretching vibrations of C-H present in the alkyl groups (mostly methyl) of saw dust. The peak (weak) at 1730 cm^{-1} of the spectra denotes the C=O vibration due to the carbonyl groups present in hemicellulose of saw dust (Ghasemi and Gholami, 2016). Similar type of peaks was observed around 1739 cm^{-1} due to carbonyl stretching vibration (Gan et al., 2016). The medium peak at 1640 cm^{-1} is assigned to C=C stretching vibrations.

The peak about 1560 cm^{-1} was attributed by aromatic vibration (stretching) of saw dust, MSD due to the presence of lignin in them. There observed a weak peak at 560 cm^{-1} which was due to the vibration of Fe-O bond of magnetic saw dust. Due to the C-H deformation of alkyl and alkoxy groups the weak peak is observed around 1425 cm^{-1}(Nagy et al., 2014). The peaks around 1300-1110 cm^{-1} attributed to C-O stretching. The peak around 3750 cm^{-1} was due to the NH_2 group present in the saw dust (Zhu et al., 2019).

The peak shift in the fingerprint region of the FTIR spectra confirms the successful binding of DCF on the surface of MSD. It is seen that OH-bending vibration standing for phenolic

hydroxyl group shifted from 1344 cm^{-1} to 1327 cm^{-1}, this shift phenomenon is possibly due to electron donating effect from negative -COO- group of DCF. Electron donating effect supports H-bonding interaction of DCF with MSD. π-π interactions also takes part in biosorption as we see peak shifts and strength changes at the region of 1000-1650 cm^{-1}. π-π stacking interactions with phenyl cycle of DCF, electrostatic interaction and H-bonding interaction plays an important role and increases the affinity of MSD with DCF (Wu et al., 2020).

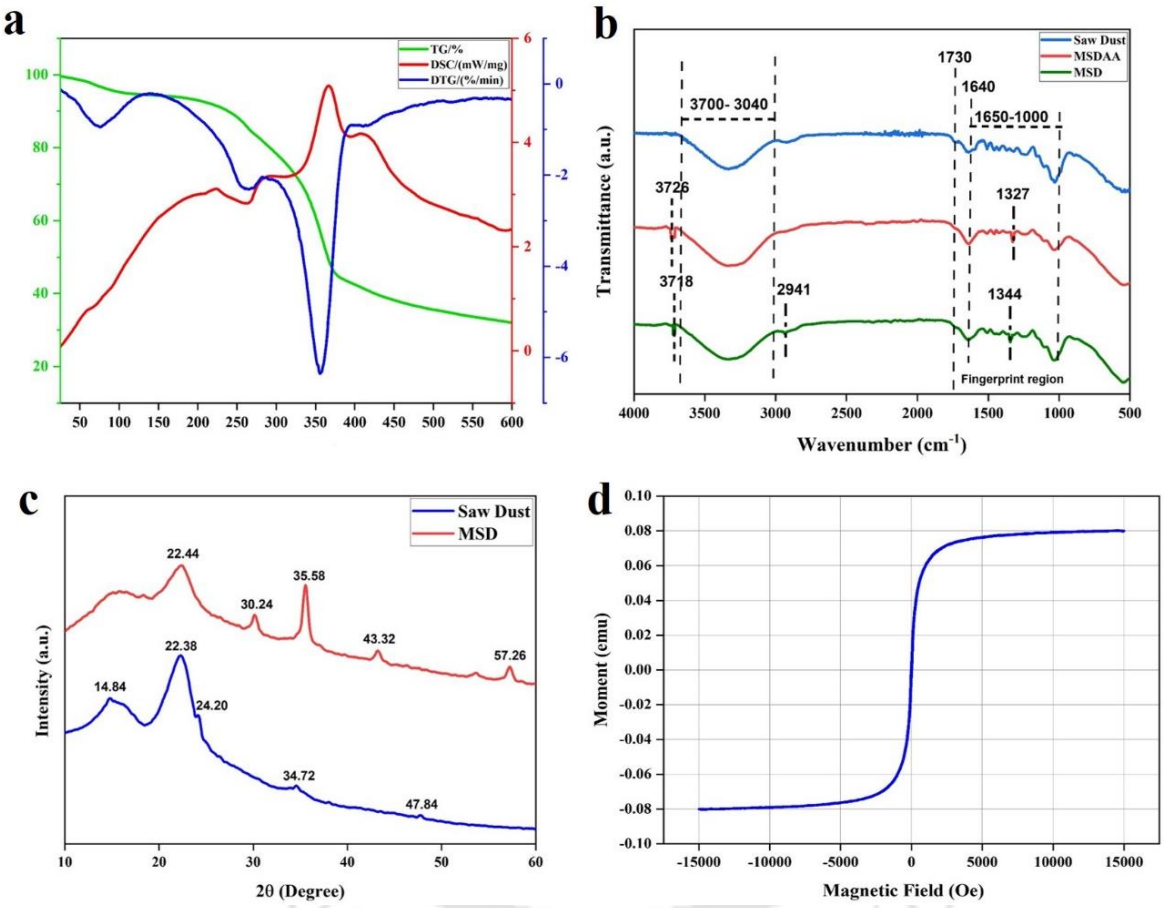

Fig. 2.4. a) *Thermogravimetric analysis (TGA) and differential scanning calorimetry (DSC) image of MSD,* ***b)*** *FTIR analysis of Sawdust, MSD, MSDAA showing different peaks for different functional groups,* ***c)*** *XRD analysis of Sawdust and MSD showing 2 theta peaks explaining crystallinity, and* ***d)*** *Vibrating sample magnetometer (VSM) analysis of MSD for evaluating the magnetic behaviour*

2.2.1.6. XRD analysis

The crystallinity and phase purity of the saw dust and MSD was determined by using XRD. The diffraction pattern (Fig. 2.4 (c)) of saw dust exhibited the peaks at 2 theta at about

14.84˚, 22.38˚, 24.20˚, 34.72˚, and 47.84˚. The peaks around 14.84˚ and 22.38˚ represents the characteristic peak of the cellulose present in the saw dust (Abdel-Salam et al., 2020). The diffraction pattern of MSD revealed the peaks at 2 thetas at 22.44˚, 30.24˚, 35.58˚, 43.32˚, and 57.26˚. The diffraction peak with maximum intensity proved that the crystallinity increases in the MSD structure on comparing to saw dust. The increase in crystallinity was due to the addition of $FeCl_2$ and $FeCl_3$ to make it magnetic (Cheng et al., 2012).

2.2.1.7. VSM analysis

Magnetization of magnetic saw dust was characterized by Vibrating Sample Magnetometer (VSM). Biosorbent with magnetic properties increases attention of many researchers due to their easy separation by applying magnetic field. Thus, it increases the operational cost and efficiency by magnetic separation. Magnetization can be measured as the function of temperature and magnetic field. Fig. 2.4 (d) shows the magnetization curve for the MSD at room temperature. The saw dust shows ferromagnetic behavior. The purpose of incorporating magnetism in the sample is the facilitation of easy separation after treating the pollutant, which also enables the sample to be reused after retrieving (Carvalho Costa et al., 2020).

2.2.2. Effect of various parameters on biosorption

2.2.2.1. Effect of pH on biosorption

The pH of the solution is the critical process parameter affecting the biosorption process. It influences both the biosorbate and biosorbent chemical properties in an aqueous solution. The effect of pH on biosorption of DCF onto the MSD was studied by changing the pH value from 2.0 to 10.0 at 298 K. The DCF biosorption on the MSD was mainly dependent on the pH of the solution (Fig. 2.5 (a)). With the increase in pH value the biosorption capacity towards the removal of DCF increases and then decreased after pH 7.0. The maximum removal efficiency of DCF was seen at pH 6.0. As the pH increases, the biosorption capacity of MSD towards DCF increased from 10.29 mg/g to 25.88 mg/g and gradually decreases to 17.20 mg/g at high pH 10.0. The efficiency of the DCF removal was increased from 34.31% to 86.27% as the pH of the solution increases and then it decreases to 57.35%. The pH of DCF solution has effect on both the ionization of the biosorbate and the surface charge of the biosorbent. There is an increase in the protonation effect due to

less pH, which increases the biosorption capacity. At lower pH (2.0-4.0), deprotonation occurs on the surface of MSD and there is no less interaction with DCF causes decreased biosorption (Patra et al., 2020).

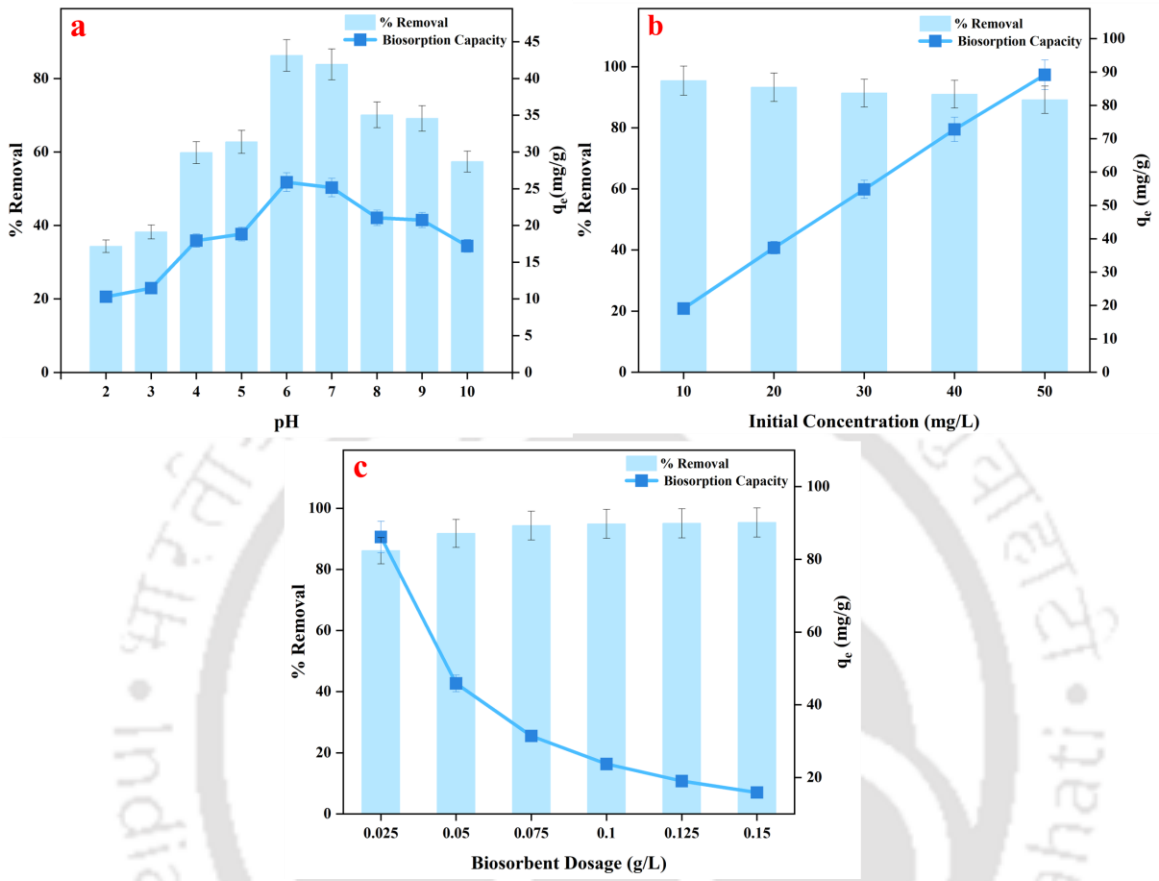

Fig. 2.5. a) *Effect of pH on biosorption of DCF by MSD at various pH ranging from pH 2.0-10.0,* ***b)*** *Effect of initial DCF concentration on biosorption of DCF by MSD at different concentrations of DCF ranging from 10-50 mg/L and* ***c)*** *Effect of biosorbent dosage on biosorption of DCF by MSD at different dosage of MSD ranging from 0.025 to 0.150 g/L*

2.2.2.2. Effect of initial DCF concentration on biosorption

The effect of initial concentration (Fig. 2.5 (b)) was studied using DCF concentration ranging from 10-50 mg/L, 298 K and the starting pH of 6.0. While initial DCF concentration was increased, there increases biosorption capacity from 19.08 mg/g to 89.16 mg/g and the efficiency of the removal was decreased from 95.41% to 89.16%. The dynamic interactions between the DCF solution and the MSD are affected by the initial DCF concentration. A sufficient biosorption environment was provided by high initial

concentration and the resilient adsorption driving force overcomes the mass transfer resistance between the biosorbate and the biosorbent (Shahnaz et al., 2020a). Higher DCF removal percentage was observed at a lower initial concentration of DCF solution and lower DCF removal efficacy was seen at higher initial DCF concentration. The lower removal efficiency was due to the presence of a large amount of DCF molecules than MSD, which tends to decrease in removal efficiency (Larous and Meniai, 2016)

2.2.2.3. Effect of biosorbent dosage on biosorption

The effect of adsorbent dosage was done using MSD of different dosage varying from 0.025 to 0.150 g/L, with a fixed initial DCF concentration of 50 mg/L, 298 K and pH 6.0. The effect of the biosorbent dosage was displayed in Fig. 2.5 (c). While increasing the dosage of biosorbent, there observed an increase in the removal efficiency from 86.12% to 95.31%. Whereas, the biosorption capacity was decreased from 86.12 mg/g to 15.88 mg/g by increasing the biosorbent dosage. The removal efficiency was increased by increasing the dosage of the biosorbent, which increases the active sites allowing more surface area of the biosorbent. The rise in a dosage leads to an increase in removal efficiency because biosorbate adheres to the biosorbent surface, which leads to strong interaction with active sites. When biosorbent dosage is decreased, the diffusion sites are fully exposed, leading to higher biosorption capacity (Shahnaz et al., 2020b).

2.2.3. Biosorption isotherms

The biosorption capacity of the MSD on biosorption DCF was investigated using adsorption isotherms such as Langmuir, Freundlich, Temkin, Dubinin-Radushkevich, and Jovanovic isotherm models (Fig. 2.6 (a)). The process parameters of various isotherms are shown in Table 2.2.

The monolayer biosorption onto the surface with finite number of biosorption sites were explained by Langmuir isotherm model. In this model, there is no transmigration of biosorbate in the biosorbent surface plane (Tomul et al., 2019). This model calculates the maximum biosorption capacity of the monolayer coverage. The value of Q_0 found to be 107.52 (mg/g). The value of separation factor R_L denotes the process nature of the biosorption. If the R_L value is (> 0 to < 1 represents favorable biosorption; > 1 corresponds to unfavorable biosorption; = 1 follows linear biosorption; = 0 represents irreversible biosorption). The R_L value is 0.0414, which represents favorable biosorption.

Table 2.2. *Various isotherm parameters of DCF biosorption onto MSD*

Isotherm Model	MSD
Langmuir Isotherm	
Q_0 (mg/g)	107.52
K_L (L/mg)	0.4626
R^2	0.9878
Freundlich Isotherm	
K_F (L/g)	31.024
n	1.5857
R^2	0.9978
Dubinin Radushkevich Isotherm	
β (mol^2/J^2)	0.0018
E (kJ/mol)	16.56
R^2	0.8606
Temkin Isotherm	
b_T (kJ/mol)	409.34
K_T (L/mg)	6.7115
R^2	0.9783
Jovanovic Isotherm	
q_m (mg/g)	22.334
K_J (L/g)	-0.0565
R^2	0.8595

The process of biosorption, which happens on a heterogeneous surface, was predicted using Freundlich isotherm. They also describe the exponential distribution of active centers and their energies with multilayer biosorption (Khandaker et al., 2020). The K_F and n values were found to be 31.024 (L/g) and 1.5857. The value for the coefficient of determination R^2 was found to be 0.9978. The value of R^2 was found to be more significant showing that the biosorption of DCF follows Freundlich isotherm.

Biosorption mechanism with Gaussian energy distribution onto heterogeneous surface was expressed by Dubinin-Radushkevich isotherm model. It is used to predict physical or chemical biosorption (Mate and Mishra, 2020). The value of β and q_m were 0.0018 (mol^2/J^2) and 69.819 (mg/g). The R^2 value found to be 0.8606. The E (apparent energy) value provides the mechanism of the biosorption. Physical biosorption is favorable when E value is between 1 and 16 kJ/mol and chemical biosorption is favorable for the E value more than 16 kJ/mol. The apparent energy for DCF biosorption was found to be 16.56 which shows that the process of biosorption is chemical.

The indirect interactions of biosorbate and biosorbent were given by the Temkin model. This model assumes that the surface increases with the linear decrease in the heat of biosorption. Temkin isotherm is valid only for a medium range of concentrations of biosorbate (Abutaleb et al., 2020). The values for b_T and K_T are 409.34 (kJ/mol) and 6.7115 (L/mg). The value of R^2 was found as 0.9783. The assumptions made in this model are like Langmuir isotherm. When maximum solute concentration reaches the saturation level, the biosorption is localized and mobilized. The values are 22.334 (mg/g) and -0.0565 (L/g). The R^2 value of Jovanovic isotherm was 0.8595.

2.2.4. Biosorption kinetics

Biosorption kinetics gives the information about the rate of biosorption (uptake of biosorbate on the biosorbent). To predict the kinetics of the biosorption process various kinetic models such as pseudo-first-order, pseudo-second-order, Elovich and intra-particle diffusion models were used (Fig. 2.6 (b)). Pseudo-first-order assumes of the rate of number of filled adsorption sites to unfilled sites in most biosorption process, this model is not significant for whole contact time, and it suits for the biosorption process only at the initial stage.

The q_e and k_1 values are found to be 49.468 (mg/g) and 0.0195 (min^{-1}). The calculated qe values are not significant with the values of experimental q_e due to limitations in the boundary layer control of the process. The correlation coefficient (R^2) was found to be 0.9492, which was comparatively low on comparison with intra-particle diffusion model. These values represent that the pseudo-first-order model is not suited for the biosorption of DCF on MSD.

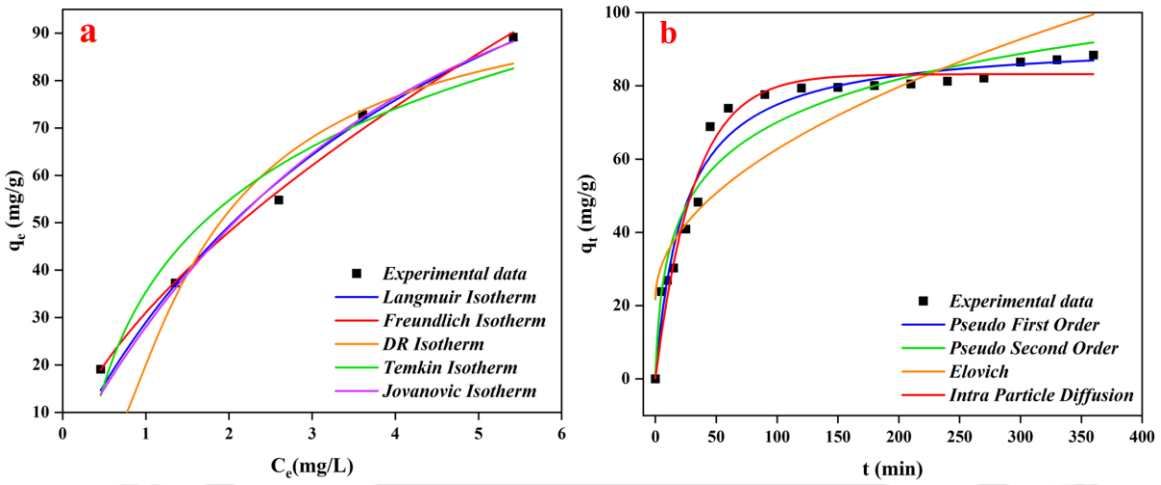

Fig. 2.6. a) *Various isotherm models for DCF biosorption and* ***b)*** *Various kinetic models for DCF biosorption*

Pseudo-second-order model states about the behavior of the biosorption process for the entire time. In this model it is assumed that due to the sharing of electrons between the DCF and MSD which involves some valence forces considered to be the rate limiting step. The calculated value of qe is 47.276 (mg/g) and k_2 is 0.0008 (g/mg min). The value of R^2 for pseudo-second-order was found to be 0.9101, which is very less as compared to other kinetic models.

The mechanism of the chemical biosorption is elucidated by Elovich kinetic model. This type of model is best suited for the materials with heterogenous surface. The values for the α and β is found to be 3.4236 (g/mg min) and 0.0913 (mg/g). The value of coefficient of correlation (R^2) shows that the process of biosorption of DCF on MSD is not significant to the Elovich kinetic model. The process of biosorption on the porous material can be of three stages namely, intra-particle diffusion, adsorption, and external mass diffusion. The rate controlling step that occurs in the process of biosorption was due to the diffusion of biosorbate on the biosorbent (Pholosi et al., 2020). The true rate controlling mechanism

involved in the biosorption process was predicted by intra-particle diffusion. The plot for DCF predicts that the diffusion of DCF on MSD surface layer may be the rate-controlling step of the biosorption process.

Table 2.3. *Different kinetic parameters of DCF biosorption onto MSD*

Kinetics	**MSD**
Pseudo-first-order model	
q_e (mg/g)	49.468
k_1 (1/min)	0.0195
R^2	0.9492
Pseudo-second-order model	
q_e (mg/g)	47.276
k_2 (g/mg min)	0.0008
R^2	0.9101
Elovich model	
α (g/mg min)	3.4236
β (mg/g)	0.0913
R^2	0.9137
Intra-particle diffusion	
k_i (mg/g min $^{1/2}$)	3.9606
d	0.2434
R^2	0.9515

The regression plot pass through the origin shows that the vital for the biosorption process is diffusion. From the Table 2.3 on observing the R^2 values, the biosorption of DCF on MSD follows the intra-particle diffusion kinetic model.

2.2.5. Phytotoxic studies

The phytotoxic effects of DCF before biosorption and after biosorption was investigated through seed germination (%) and inhibition of growth (%). The germination of the seeds decreases as the concentration of DCF increases. From the Fig. 2.7 (a) and (b) it is observed that the germination of seeds among all the control groups (without DCF) exhibit 100% of germination. At the concentration of 30 mg/L of DCF the germination % of black gram decreases to 96.66% and reduces till 80% for 50 mg/L. The germination of horse gram vigorously reduced as the DCF concentration increases. The germination of Bengal gram decreased from 100% to 86.66% (50 mg/L). Comparatively, green gram shows highest germination of seeds (90%) at 50 mg/L of DCF concentration. Pearl millet shows very less seed germination of about 70% at highest concentration.

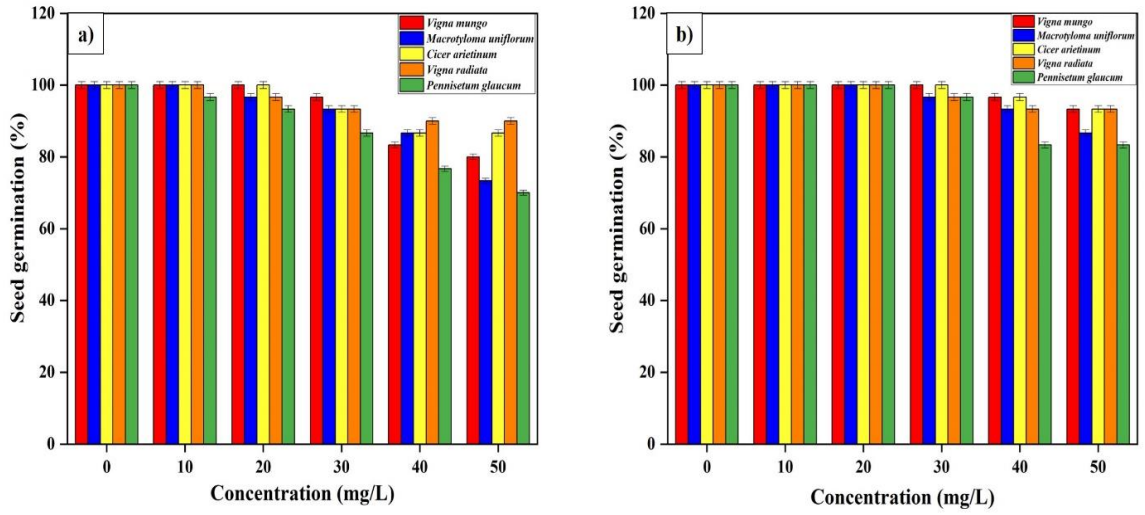

Fig. 2.7. *Seed germination (%) of Vigna mungo (black gram), Macrotyloma uniflorum (horse gram), Cicer arietinum (Bengal gram), Vigna radiata (green gram), Pennisetum glaucum (pearl millet) seeds at various concentrations of DCF.* ***a)*** *DCF before biosorption and* ***b)*** *DCF after biosorption*

Sousa et al. (2020) reported that on exposure of *Solanum lycopersicum* seeds to DCF there is no effect on germination of seeds, but the length of roots was decreased by 0.43-fold on 10 mg/ L of DCF compared to the length of untreated roots (Sousa et al., 2020). Exposure of 5 to 50 mg/L of pharmaceuticals to cucumber plants, shows burnt edges on the mature leaves due to the decrease in pigments responsible for photosynthesis (Sun et al., 2018).

After the biosorption process we can see that there is the drastic increase in the germination of seeds of all groups. The minimal germination rate increases to 93.33% for black gram from 80%. After the biosorption of DCF, we can observe there is an increase in germination of seeds (%) in all the groups. The increase in the germination was due to the removal of toxic micropollutant DCF from the water by MSD.

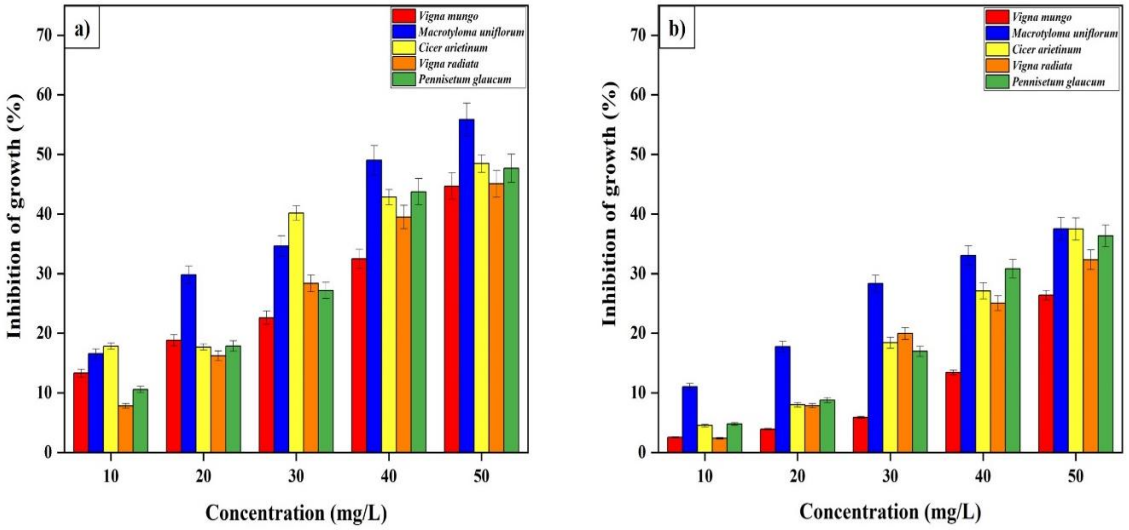

Fig. 2.8. *Inhibition of growth (%) of Vigna mungo (black gram), Macrotyloma uniflorum (horse gram), Cicer arietinum (Bengal gram), Vigna radiata (green gram), Pennisetum glaucum (pearl millet) seeds at various concentrations of DCF.* ***a)*** *DCF before biosorption and* ***b)*** *DCF after biosorption*

Fig. 2.8 (a) and (b) revealed the growth inhibition of different seeds on exposure to different concentrations of DCF before and after biosorption. The inhibition of seed growth takes place as the concentration dependent manner. As the concentration of DCF increased the growth of shoot and root of the seed gets decreased. The IC_{50} values of DCF for black gram, horse gram, Bengal gram, green gram, pearl millet was found to be 60.91 mg/L, 43.11 mg/L, 49.21 mg/L, 53.12 mg/L and 50.36 mg/L respectively.

The cellular and subcellular metabolic process of plants are adversely affected due to DCF, which induces the changes in their growth and development. Svobodníková et al. reported that the viability of BY-2 cells of *Nicotiana tobacum* decreased on treatment with DCF which induces oxidative stress triggering cell apoptosis (Svobodníková et al., 2019). Hájková et al. (2019) showed that DCF at acute concentrations influences the photosynthetic process of *Lemna minor* chloroplasts by inhibiting oxygen production and

growth of plants (Hájková et al., 2019). The concentration above the IC_{50} value leads to retardation of growth of shoot and root of the plants.

2.2.6. Microbial toxicity studies

The growth of microbes exposed to the untreated DCF solution and treated DCF solution after the biosorption process in 96-well plates expressed as % inhibition of bacterial growth (Fig. 2.9 (a) and (b)). The growth of *E. coli* and *B. subtilis* are affected adversely due to the untreated DCF solution. At the concentration of 50 µg/mL of untreated DCF solution, *E. coli* shows 66.46% of growth inhibition followed by 24.87%, 18.15%, 10.43% and 9.81% for the 40, 30, 20 and 10 µg/mL concentrations of untreated DCF solutions.

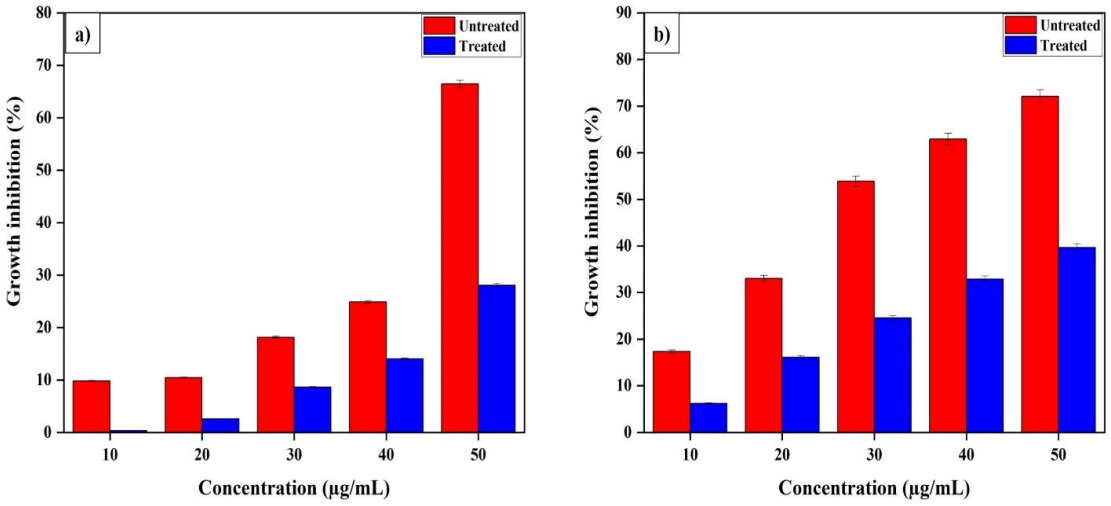

Fig. 2.9. *Growth inhibition (%) of microorganisms at various concentrations of DCF before and after biosorption.* ***a)*** *E. coli, and* ***b)*** *B. subtilis*

From the Fig. 2.9 (a) we can observe that as the concentration increases the percentage of growth inhibition also increases in concentration dependent manner. The treated DCF shows the maximum inhibition of 28.06% at the concentration of 50 µg/mL. Similarly, Fig. 2.9 (b) showed the growth inhibition of *B. subtilis* due to the untreated and treated DCF solutions. The untreated DCF solution shows highest inhibition activity about 72.05% at 50 µg/mL concentration, but the treated DCF solution shows only 39.66% inhibition to the growth of *B. subtilis* at the same concentration. The inhibitory concentration (IC_{50}) value for untreated DCF solution on *E. coli* and *B. subtilis* was found to be 48.82 µg/mL and 31.55 µg/mL. After the biosorption process, we can observe that there is a decrease in the growth inhibition due to the removal of DCF from the solution by MSD. After the treatment

process the IC_{50} value for *E. coli* and *B. subtilis* was found to be 88.73 µg/mL and 61.23 µg/mL which shows that the treatment process is effective and less toxic. Acute ecotoxicity experiments showed that the biotransformed product of DCF was less toxic to *Vibrio fischeri* on compared DCF parent compound (Stylianou et al., 2018).

2.2.7. Acute fish toxicity studies

In the present study the toxicity of the micropollutant DCF before and after treatment was evaluated on *Danio rerio* (zebra fish). The untreated DCF solution (before biosorption) showed high toxicity towards zebra fish than the treated DCF solution (after biosorption) with MSD. There is no death and abnormal behavior of zebra fish in the control groups. We observed some acute toxic symptoms like unusual swimming, staying at bottom and rapid tumbling in the treatment groups with the concentration above 120 mg/L. After 60 mg/L DCF concentration the mortality rate of zebra fish increases with the concentration of DCF solution in dependent manner (Fig. 2.10).

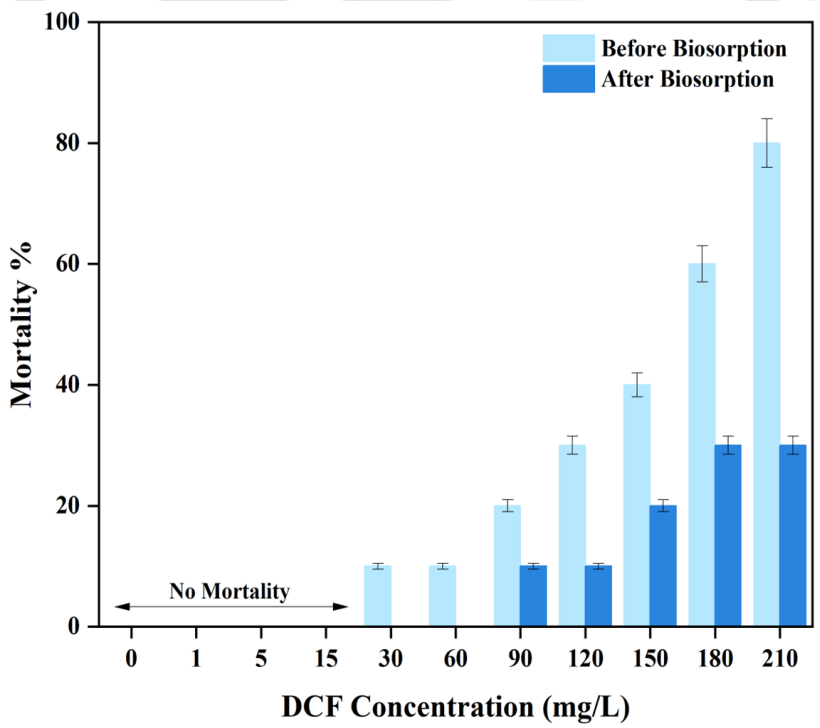

Fig. 2.10. *Mortality (%) of Danio rerio (zebra fish) to various concentrations of DCF before and after biosorption*

In the current study, after 96 h LC_{50} value of DCF on the *Danio rerio* was found to be 156.99 mg/L. The treated DCF solution by biosorbent shows the highest mortality rate of

30% at 210 mg/L concentration. The mortality % decreases to 30% on treatment of DCF solution with MSD. This shows that the effective removal of DCF from aqueous solution by MSD and the LC_{50} value for the treated DCF solution was found to be 340.73 mg/L which was double the concentration of LC_{50} of DCF before biosorption. Islas-Flores et al. (2013) reported that the EC_{50} value for DCF was about 71 mg/L for *Cyprinus carpio* (Islas-Flores et al., 2013).

The exposure for 72 h resulted in no observed effect concentration (NOEC) at 1.5 mg/L (van den Brandhof and Montforts, 2010). (Ribeiro et al., 2015) depicted that the hatching rate of *D. rerio* embryo decreases significantly when exposed to 12.5 mg/mL of DCF. (Praskova et al., 2014) reported that the juvenile *D. rerio* on exposed to DCF for 96 h showed LC_{50} value at the range of 156.80-176.40 mg/L which was more significant to our results and stated that the fishes in the test groups exposed to 2, 5, and 15 mg/L of DCF exhibited mortality rate less than 5%. They also reported that at 60 mg/L the mortality rate was 10% which was like our results. (Duarte et al., 2020) reported that on exposure of DCF to *Argyrosomus regius* showed that the oxidative stress is not enhanced in the liver, yet triggering rapid energy consumption in the muscles of fish.

2.3. Significant findings

In the present study MSD was prepared using co-precipitation of $FeCl_3.6H_2O$ and $FeCl_2.4H_2O$. The biosorbent characterized with FESEM, FETEM and AFM showed the nano sized MSD with spherical size ranging 5-90 nm. EDX analysis confirms the presence of iron on the MSD. X-Ray Diffraction pattern confirmed that the magnetized biosorbent has both crystalline and amorphous in nature with two distinct peaks for iron. The TGA study showed the multiple thermal decomposition step with three peak temperatures. Functional groups present were analyzed with FTIR. VSM analysis confirmed the ferromagnetism of the MSD. The conditions for maximum removal of DCF was optimized at pH 6.0, 50 mg/L initial DCF concentration and 0.025 g/L MSD with adsorption capacity 107.52 mg/g. The behavior of DCF and MSD were described by Freundlich isotherm and Intra particle diffusion kinetics. Ecotoxicological assessment for seed germination and growth inhibition %, two microbial strains for growth inhibition % and *Danio rerio* fish for mortality % at different concentration of DCF before and after biosorption with MSD were carried out to evaluate the lethal and inhibition concentration of the pollutant. This biosorbent showed an excellent efficiency for DCF adsorptive removal. These findings

implied feasibility of the preparation of MSD for the efficient removal of DCF and reduced toxicity of the treated DCF on model organisms that could be a potent alternative in wastewater treatment.

Chapter 3

Effective removal of Pharmaceutical Contaminants Ibuprofen and Sulfamethoxazole from water by Corn starch nanoparticles: An ecotoxicological assessment

The work embodied in this chapter is published in

Vishnu Priyan V. and Selvaraju Narayanasamy, 2022. Effective removal of Pharmaceutical Contaminants Ibuprofen and Sulfamethoxazole from water by Corn starch nanoparticles: An ecotoxicological assessment, **Environmental Toxicology and Pharmacology**, 103930. https://doi.org/10.1016/j.etap.2022.103930 **(Elsevier; SCI IF 2023: 4.3).**

Abstract

Pharmaceutical pollutants, a vital type of emerging contaminants, have attracted researchers to study their removal from water. In this research, Corn starch nanoparticles (CSNP) have been synthesized and characterized using various analytical techniques. The synthesized CSNP was used for the biosorption of two pharmaceutical drugs, ibuprofen (IBU) and sulfamethoxazole (SUL). The influence of various experimental conditions was optimized through batch study with the removal efficiency of 86.33% (IBU) and 85.80% (SUL) at pH 2.0 and 3.0, initial concentration of 10 mg/L, 0.01 g/L of CSNP dosage. The biosorption of IBU follows Temkin, and SUL follows Langmuir isotherm models. The toxicological assessment was performed using the seeds of *Vigna mungo* (VM) and *Vigna radiata* (VR) and zebrafish to evaluate the toxic effects of pollutants on these organisms. The LC_{50} of IBU and SUL on zebrafish before the biosorption process was 209.50 mg/L and 338.84 mg/L. Thus, CSNP is an efficient biosorbent for removing the pharmaceutical pollutants to protect ecological systems.

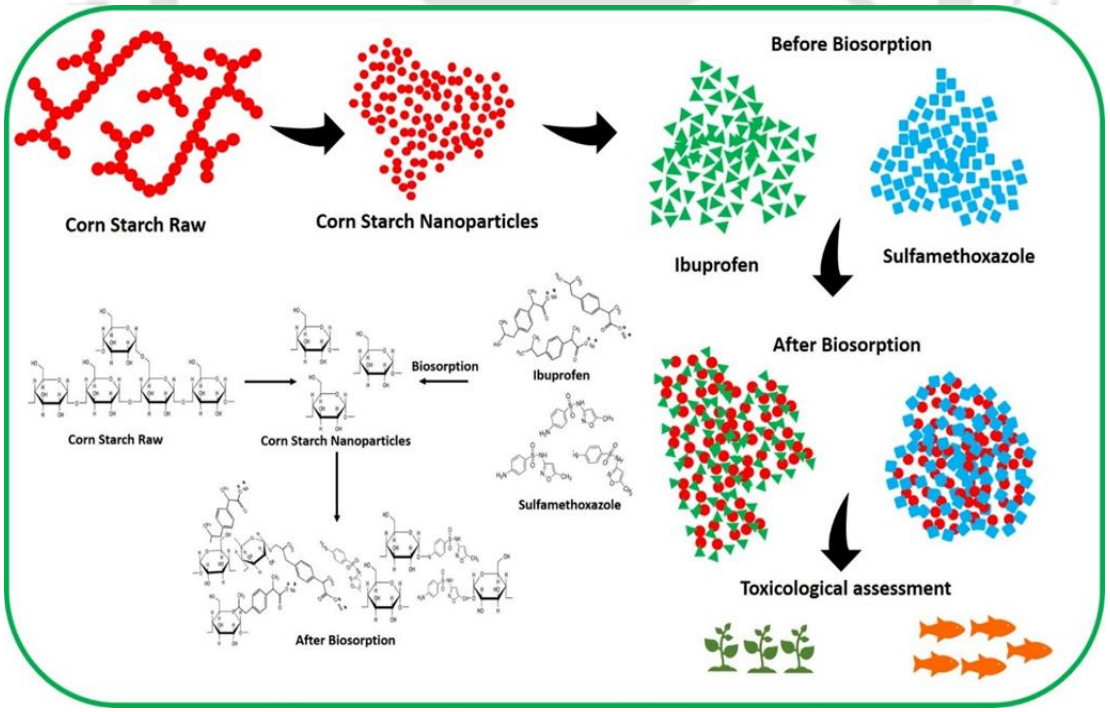

Graphical Abstract

3.1. Materials and methods

3.1.1. Chemicals

Certified analytical grade chemicals were used to prepare all chemical solutions. Starch nanoparticles were prepared using corn starch ($(C_6H_{10}O_5)_n$, RM198, Mol. Wt. $(162.14)_n$, HiMedia) and sulfuric acid (H_2SO_4, 98% pure/LR, Mol. Wt. 98.08, HiMedia). The pollutants ibuprofen ($C_{13}H_{17}O_2Na$, AR, Mol. Wt. 228.26, Sigma-Aldrich) and sulfamethoxazole ($C_{10}H_{11}N_3O_3S$, AR, Mol. Wt. 253.28, Sigma-Aldrich) was procured from Sigma-Aldrich. The pH was adjusted using hydrochloric acid (HCl, 99% pure, Mol. Wt. 36.46, SRL) and sodium hydroxide (NaOH, Hi-AR/ACS, Mol. Wt. 40, HiMedia).

3.1.2. Synthesis of Corn Starch nanoparticles (CSNP)

To prepare corn starch nanoparticles (CSNP), 50 g of corn starch was added in 500 mL of distilled water under continuous mechanical stirring at ambient temperature to get homogeneous mixture. Then 50 mL of concentrated sulfuric acid was added drop by drop to the starch solution and kept under vigorous stirring for 7 days. After seven days the solution was centrifuged at 12000 rpm for 15 minutes and the pellet was collected and washed with distilled water to get CSNP. These starch nanoparticles are dried in oven at 80 °C and stored for further use (Priyan et al., 2020; Varadharaj et al., 2020).

3.1.3. Characterization of CSNP

Various analytical techniques were used to characterize CSNP before and after biosorption of ibuprofen (IBU) and sulfamethoxazole (SUL) were tabulated in Table A3 (Appendix).

3.1.4. Biosorption experiments

Batch experiments were performed at various initial concentrations of IBU and SUL (10 to 60 mg/L), pH (2.0-9.0) and CSNP dosage (0.01-0.05 g/L). To perform batch experiments 30 mL of stock solution was taken and stirred at 150 rpm in a shaking incubator for 5 h. To optimize pH different pH stock solutions were taken and to optimize the CSNP dosage various amount of CSNP were used ranging from 0.01-0.05 g/L. The temperature was maintained at 308 K (35 °C) throughout the experiments. After biosorption the residual IBU and SUL concentration was determined from OD value taken using UV visible spectrophotometer at wavelength 222 nm for IBU and 270 nm for SUL (Vishnu Priyan et al., 2021).

The maximum biosorption capacity and removal efficiency of IBU and SUL biosorption was calculated from Table 3.1.

Table 3.1. *The maximum biosorption capacity and removal efficiency of IBU and SUL biosorption*

Parameters	Equation	Description	Equ. No.
Maximum biosorption capacity	$q_e = \frac{(C_0 - C_e)}{m} \times V$	**q_e** is the amount of IBU and SUL biosorbed at equilibrium time (mg/g),	(3.1)
Removal efficiency	$Removal\ (\%) = \frac{C_0 - C_e}{C_0} \times 100$	**C_0** and **C_e** are the initial and equilibrium IBU and SUL concentrations. (mg/L), **m** is the mass of the CSNP (g), **V** is the volume of IBU and SUL solution (L).	(3.2)

3.1.5. Phytotoxicity experiments

The seed toxicity studies on IBU and SUL before and after biosorption on CSNP was studied using the seeds of *Vigna* species (*Vigna mungo* (VM) and *Vigna radiata* (VR)). The seed toxicity experiments were done using the protocol of (Podio et al., 2020) with minor modifications. These experiments were carried out in Petri dishes in dark at room temperature.

The toxicological effects on these seeds were measured after seven days in terms of inhibition of seedling growth (%) and germination (%) of the seedlings. To avoid yeast and fungal contamination on seeds, the *Vigna* seeds were surface sterilized with 0.1% sodium hypochlorite solution and washed with deionized water for several times. The surface sterilized seeds were subjected to toxicity analysis by adding the seeds to the Petri dishes containing the IBU and SUL solutions before and after biosorption process. The pollutant solution was prepared in various concentrations (10, 30 and 50 mg/L) and distilled water is used as control. Then the seeds in Petri dishes were placed in dark for seven days. After seven days, the *Vigna mungo* and *Vigna radiata* seedlings were subjected to toxicity analysis.

3.1.6. Acute fish toxicity experiments

Acute fish toxicity studies were performed using Zebra fish (*Danio rerio*) as the model organism. This experiment was performed according to the OECD test guideline number 203. The experiments were done with fishes of same age and size. Different concentrations of IBU and SUL solutions (5, 10, 15, 30, 60, 120 mg/L) were prepared and used for this test. The oxygen concentration (>75%), pH (6.5-7.5), light period (14 h light: 10 h dark) and temperature (25 °C) were maintained constant throughout the tests. Ten healthy fishes were taken for each experiment with triplicates. The experiments were performed with IBU and SUL solutions with different concentrations before and after biosorption. The water without the pollutants was taken as control. At the end of 96 h total number of alive and dead fishes was recorded and the mortality percentage was calculated to determine the toxicity levels of IBU and SUL on zebra fish (Mishra and Mohanty, 2008; Sotto et al., 2017).

3.2. Results and discussion

3.2.1. Characterization of CSNP

3.2.1.1. Morphology and topology analysis

The surface morphologies of raw corn starch (CSR) and corn starch nanoparticles (CSNP) were examined through FESEM. The SEM micrographs (Fig. 3.1 (a) and (b)) revealed that the CSR granules were polygonal in shape with mean size of about 5-20 µm. Similar results have been reported by (Varadharaj et al., 2020). It was found that the synthesized CSNP was found to be spherical in shape with aggregation (Fig. 3.1 (c) and (d)). The starch nanoparticles were found to be non-homogeneous with average particle size less than 100 nm interconnected with each other. The topology of the CSNP was determined using FETEM revealing that the surface of the CSNP was eroded by sulfuric acid used for synthesis (Fig. 3.1 (e) and (f)). The action of sulfuric acid on CSR creates numerous pores on the surface of corn starch, which helps in biosorption of pollutants (Velásquez-Castillo et al., 2020). From the FETEM image (Fig. 3.1 (f)) the average size of CSNP was found to be 30 nm. The surface roughness of the synthesized CSNP was depicted through AFM. The different roughness parameters such as average roughness (R_a), RMS roughness (R_q), average maximum height of roughness (R_z), maximum roughness valley depth (R_v) and

maximum roughness peak height (R_p) were calculated and found to be 7.17 nm, 14.73 nm, 111.8 nm, 22.3 nm and 89.5 nm respectively (Miskeen et al., 2021).

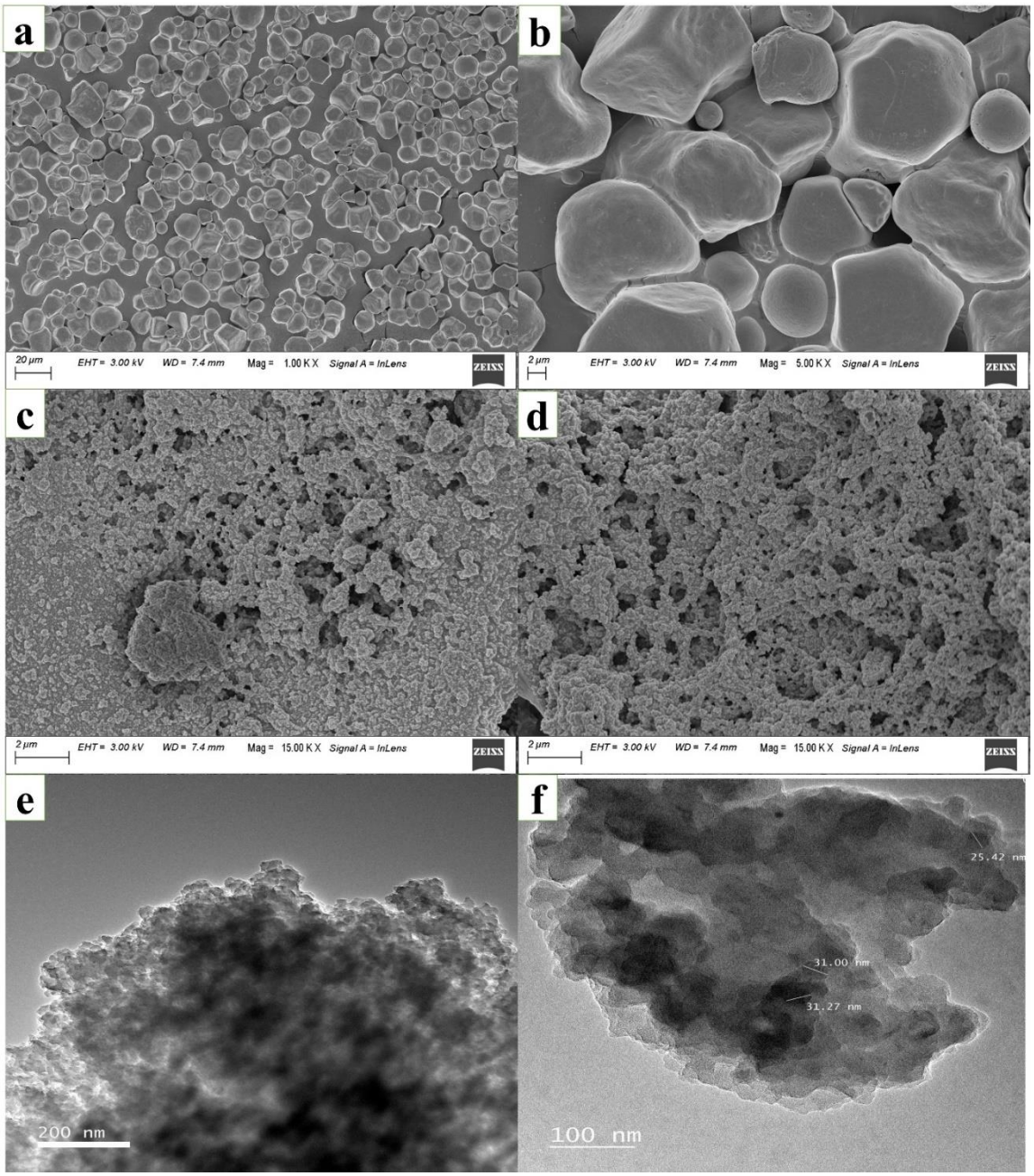

Fig. 3.1. *FESEM micrographs at different magnifications* ***a)*** *CSR (1.00 KX),* ***b)*** *CSR (5.00 KX),* ***c)*** *CSNP (15.00 KX),* ***d)*** *CSNP (15.00 KX) and* ***e*** *&* ***f)*** *FETEM image of CSNP*

3.2.1.2. EDX analysis

The elemental characterization of CSR, CSNP, CSNP-IBU and CSNP-SUL was examined using FESEM coupled energy dispersive X-ray spectroscopy (EDX). Characteristic X-rays

were produced by excitation of electrons through irradiation on the sample surface by charged particles of high energy. Elements such as carbon, oxygen, nitrogen, sulphur and sodium were found in the EDX spectra of CSR, CSNP, CSNP-IBU and CSNP-SUL. The weight percentage of carbon in CSR, CSNP, CSNP-IBU and CSNP-SUL was found to be 71.8 wt.%, 77.4 wt.%, 75.7 wt.% and 70.9 wt.%. It is seen that CSR (Fig. 3.2 (a)) consists of oxygen (26.8 wt.%) and nitrogen (1.4 wt.%). The presence of carbon in the samples was mainly due to the biological nature of the corn starch. The CSNP (Fig. 3.2 (b)) consists of oxygen (21.5 wt.%), nitrogen (0.6 wt.%) and sulphur (0.5 wt.%). The presence of sulphur was attributed due to the treatment of CSR with sulfuric acid. After the biosorption process the pollutants were adsorbed on CSNP.

The EDX spectra of CSNP-IBU (Fig. 3.2 (c)) showed the presence of oxygen (22.5 wt.%), nitrogen (1.2 wt.%), sodium (0.3 wt.%) and sulphur (0.3 wt.%). The presence of sodium in the EDX spectra of CSNP-IBU was due to the sodium salt of ibuprofen which is adsorbed on the CSNP. Elements such as oxygen (26.3 wt.%), nitrogen (2.6 wt.%) and sulphur (0.3 wt.%) were seen in the EDX spectra of CSNP-SUL (Fig. 3.2 (d)).

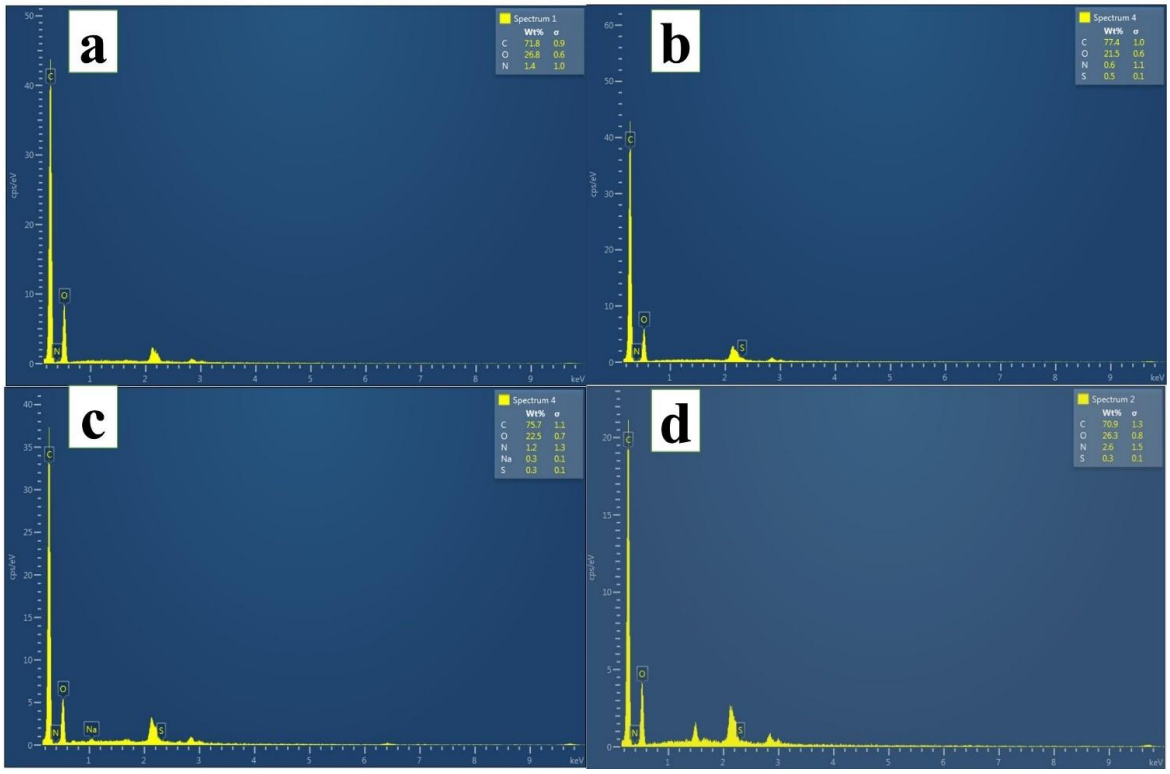

Fig. 3.2. *EDX spectra of,* ***a)*** *CSR,* ***b)*** *CSNP,* ***c)*** *CSNP-IBU and* ***d)*** *CSNP-SUL*

3.2.1.3. FTIR and Raman analysis

The functional groups present in the CSR, CSNP, CSNP-IBU, and CSNP-SUL were determined by using FTIR (400-4000 cm^{-1}) as shown in the (Fig. 3.3 (a)). In CSR spectra the broad peak at 3300 cm^{-1} was due to the OH stretching group of amylopectin of corn starch (Remanan and Zhu, 2021). In CSNP, due to oxidation, the -OH group of amylopectin reduces corresponding to the reduction of broad peak at 3300 cm^{-1}. A weak peak at 2926 cm^{-1} of CSR corresponds to the CH stretching of the alkane group, which has a peak shift from 2926 cm^{-1} to 2931 cm^{-1} after synthesizing starch nanoparticles (CSNP). The peak shift might be due to the acid hydrolysis of corn starch forming CSNP. The peak at 3748 cm^{-1} represents the NH stretching vibrations. The weak band at 1740 cm^{-1} in CSR corresponds to the carbonyl compound aldehyde present in the corn starch. After acid treatment we can observe a sharp peak shift for the aldehyde functional group to 1710 cm^{-1} in CSNP. The peak at 1640 cm^{-1} was due to ketones present in CSR, which shifted to 1610 cm^{-1} in CSNP because of the breakdown of starch units into glucose units exposing a greater number of ketone groups. On comparing the peaks between CSNP and CSNP-IBU, CSNP-SUL all the functional groups were similar and we can observe the peak at 531 cm^{-1} for CSNP after biosorption of pollutants. This was due to the biosorption of IBU and SUL on CSNP. The cis form of organic nitrites exhibits the peaks in the region 1625- 1610 cm^{-1} (Awokoya et al., 2021). The region between 850-620 cm^{-1} corresponds to the CH wag vibrations of CSNP, CSNP-IBU, and CSNP-SUL. The bands at 767, 706, 572, and 524 cm^{-1} were due to the amide group present in the sample (Guedidi et al., 2017).

The deformations in the structure of CSNP and their vibrational modes before and after the biosorption of pollutants were determined using Raman spectroscopy (Fig. 3.3 (b)). In CSR the band at 2911 cm^{-1} was due to the asymmetrical and symmetrical stretching of the CH group of amylopectin. It is seen that in CSNP the amylopectin region of corn starch was degraded by acid, and the peak shift was seen at 2564 and 2680 cm^{-1}. The similar peak was seen in CSNP-IBU and CSNP-SUL with peak shift. In the given Raman spectrum, the area between 1800 and 1200 cm^{-1} provides more detailed structural information (Wang et al., 2021). The peak at 1460, 1437, 1434, and 1441 cm^{-1} were due to the deformation of the CH_2 group of corn starch. Similar types of bands were seen in the Raman spectra of CSNP before and after biosorption of pollutants. The band represented the deformation of CCH stretching at 1330-1341 cm^{-1}. The peak at 786 cm^{-1} of CSR corresponds to the CC and CO

stretching of the glycosidic bond. In CSNP and CSNP-IBU, CSNP-SUL the band at 786 cm^{-1} was not there because the acid treatment leads to the breakage of glycosidic bonds. The vibrations between 900 cm^{-1} to 400 cm^{-1} were due to the deformation of the glycosidic bond, which is degraded due to the action of sulfuric acid. In CSR, the band at 478 cm^{-1} acts as the marker band to identify the presence of starch. This peak was not seen in other three spectra due to acid hydrolysis. All four spectra show similar bands at 900 – 1100 cm^{-1}, representing the vibrational modes of amylose and amylopectin present in the samples (Khedr et al., 2017; Priyan et al., 2020).

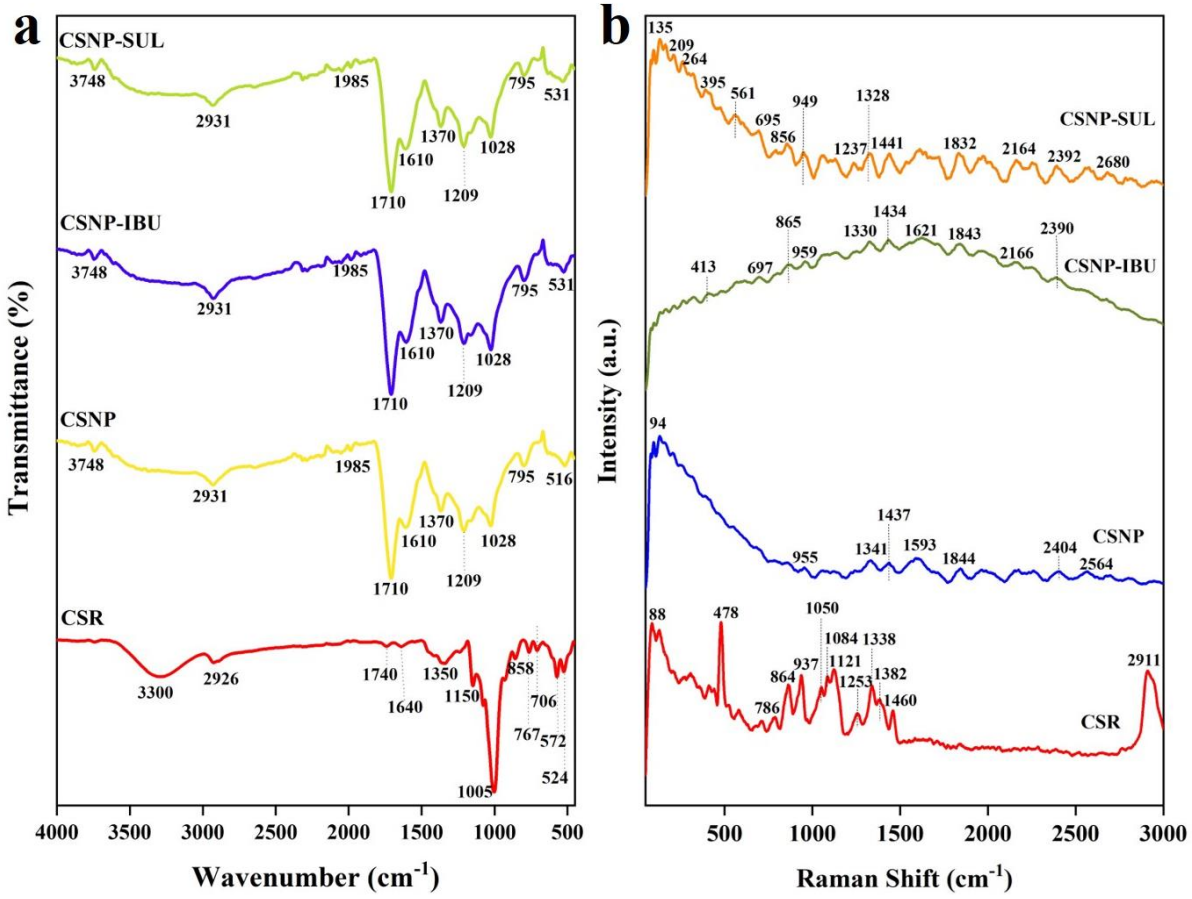

Fig. 3.3. a) *FTIR spectra of CSR, CSNP, CSNP-IBU and CSNP-SUL and* ***b)*** *Raman spectra of CSR, CSNP, CSNP-IBU and CSNP-SUL*

3.2.1.4. XRD analysis

The crystallinity of the CSR, CSNP, CSNP-IBU, CSNP-SUL were examined by XRD. The Fig. 3.4 illustrates the diffraction pattern exhibited by the samples, in which the peak at 2 theta about 15.02°, 17.04°, 18.02° and 23.04° represents the left handed double helical

structure present in the corn starch (Pan et al., 2021). We can observe the diffraction peak at 19.12° attributed to the left-handed single helix of the corn starch chain. After synthesis of CSNP the peaks at 15.02°, 17.04°, 19.12° and 23.04° are completely disappeared. The peak at 18.02° have some shift till 18.84° (CSNP and CSNP-IBU) and 19.78° (CSNP-SUL) with increasing in width of the peak.

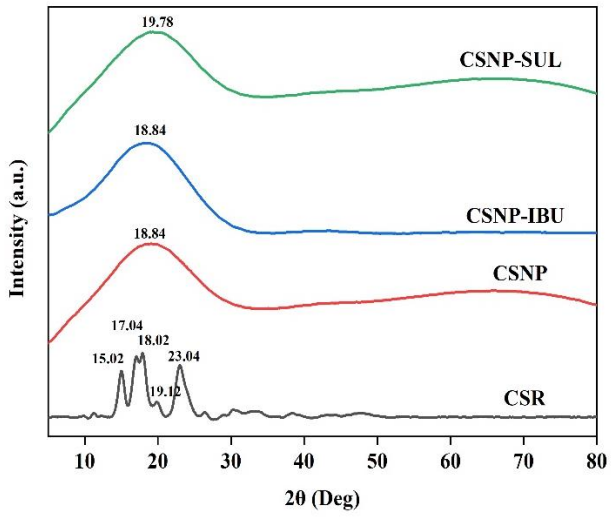

Fig. 3.4. *XRD analysis of CSR, CSNP, CSNP-IBU and CSNP-SUL showing 2 theta peaks explaining crystallinity*

3.2.2. Effect of various parameters on biosorption

3.2.2.1. Effect of pH on biosorption

A crucial parameter which influences chemical properties of sorbent and sorbate affecting the IBU and SUL biosorption on CSNP is pH of the solution. To know the influence of pH on IBU and SUL biosorption, different pH of the solutions (2.0-9.0) was taken (Fig. 3.6 (a)). The point of zero charge (PZC) of CSNP was determined in different pH using zeta potential and found to be 1.8. The pH below the pH PZC the surface of CSNP was positive and above the pH PZC the surface was found to be negative in nature. The behaviour of drugs at various pH was represented in the Fig. 3.5. The pKa value of IBU was found to be 4.91, in which the pH above the pKa value, IBU will exist in anionic form and below the pKa value it exists in cationic form (Oba et al., 2021). SUL molecules have both -NH_2 (amine) and -NH- (amide) groups showing two pKa values at 1.6 and 5.7. When the pH of the solution is less than 1.6 or higher than 5.7 SUL is positively or negatively charged promoting electrostatic interaction as a major role in the biosorption process (Ahsan et al.,

2018; Guo et al., 2019). At pH 2.0 the removal efficiency of IBU was high and found to be 57.09% and pH 3.0 favours high biosorption of SUL on CSNP with removal efficiency of 68.22%. The biosorption difference between IBU and SUL is about 11.13%. The removal efficiency of SUL is higher because of formation of hydrogen bonds between amine group of SUL and surface of CSNP. At pH 2.0 the CSNP surface was anionic and IBU was cationic promoting electrostatic attraction between CSNP and IBU molecules. At pH 3.0 the surface of CSNP was anionic and SUL exhibits zwitterion form possessing both equal positive and negative charges. So, the positive charge of SUL molecules gets attracted to the negative surface of CSNP promoting high biosorption. The decrease in the pH of the solution promotes the biosorption phenomenon. At high pH values, the OH- ions compete with the negatively charged pollutants to occupy the biosorption sites on CSNP. At low pH values the competition is reduced promoting high biosorption capacity.

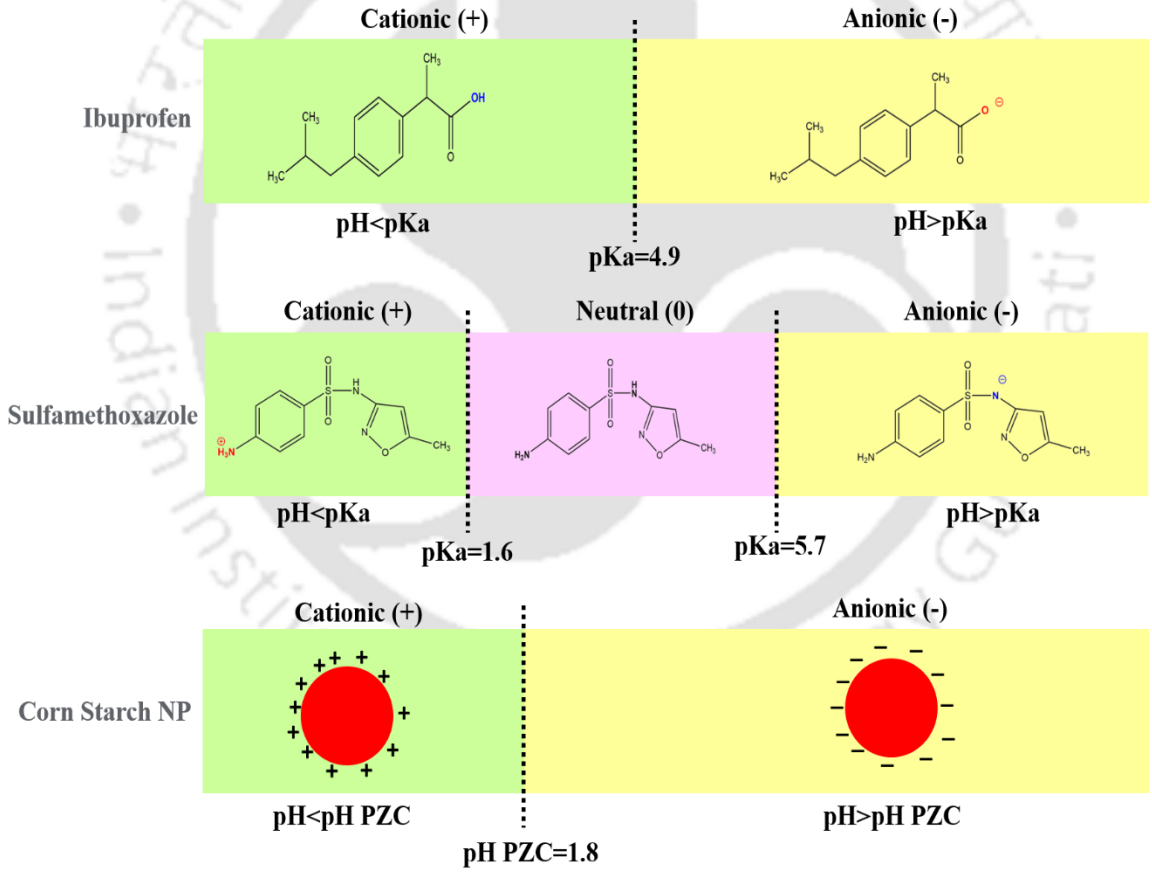

Fig. 3.5. *Scheme and charges of IBU, SUL and CSNP above and below the pKa values and pH PZC values. IBU is cationic when pKa is below 4.9 and anionic above 4.9. SUL is cationic below pKa 1.6, neutral between pKa 1.6-5.7 and anionic above 5.7. CSNP surface is cationic below pH PZC 1.8 and anionic above pH PZC 1.8*

3.2.2.2. Effect of initial IBU and SUL concentration

The influence of initial concentration on biosorption of IBU and SUL by CSNP (Fig. 3.6 (b)) was experimented using IBU and SUL solutions of various concentrations (10-60 mg/L) with pH 2.0 for IBU and pH 3.0 for SUL. As increase in the concentration of IBU and SUL solutions, we can observe the increase in the biosorption capacity from 20.56 mg/g to 65.48 mg/g for IBU biosorption and 20.50 mg/g to 82.21 mg/g for SUL biosorption. The efficiency of the removal percentage decreases as the concentration increases from 86.33% to 42.64% for IBU biosorption and 85.80% to 58.30% for SUL biosorption. The difference in the removal percentage between IBU and SUL is of 15.66%. Dynamic interactions between CSNP and pollutants (IBU and SUL) affects the initial concentration of the pollutant solutions (Shahnaz et al., 2021b). An adequate biosorption environment was found at high initial concentration of IBU, SUL solutions and a strong biosorption driving force between the CSNP and the pollutant overcomes the mass transfer resistance. Higher removal efficiency was found at 10 mg/L initial concentration of IBU and SUL. Lower removal efficiency was seen at 60 mg/L initial concentration of the adsorbate solutions. At 60 mg/L initial concentration the amount of IBU and SUL molecules are very high than the CSNP which tends to decrease in removal efficiency (Hoslett et al., 2020).

3.2.2.3. Effect of CSNP dosage

The effect of CSNP dosage on biosorption of IBU and SUL was done with various CSNP dosage ranging from 0.01 to 0.05 g/L with constant pH, temperature, and initial concentration. From the Fig. 3.6 (c) we can observe that if the CSNP dosage increases, the removal percentage also increases from 62.78% to 82.98% for IBU and 75.80% to 89.46% for SUL. The difference in the biosorption removal efficiency between IBU and SUL was about 6.48%. The SUL has maximum removal efficiency on comparing with IBU removal. But we can observe the decrease in the biosorption capacity from 98.00 mg/g to 25.90 mg/g for IBU and 116.75 mg/g to 27.56 mg/g for SUL biosorption. The removal efficiency of IBU and SUL increases when CSNP dosage increases as there are numerous active sites in CSNP which attracts more molecules of IBU and SUL. The attraction between CSNP and IBU, SUL leads to a very strong adsorbent/ adsorbate interactions promoting high removal percentage. At 0.01 g/L dosage the complete exposure of active sites leads to high biosorption capacity.

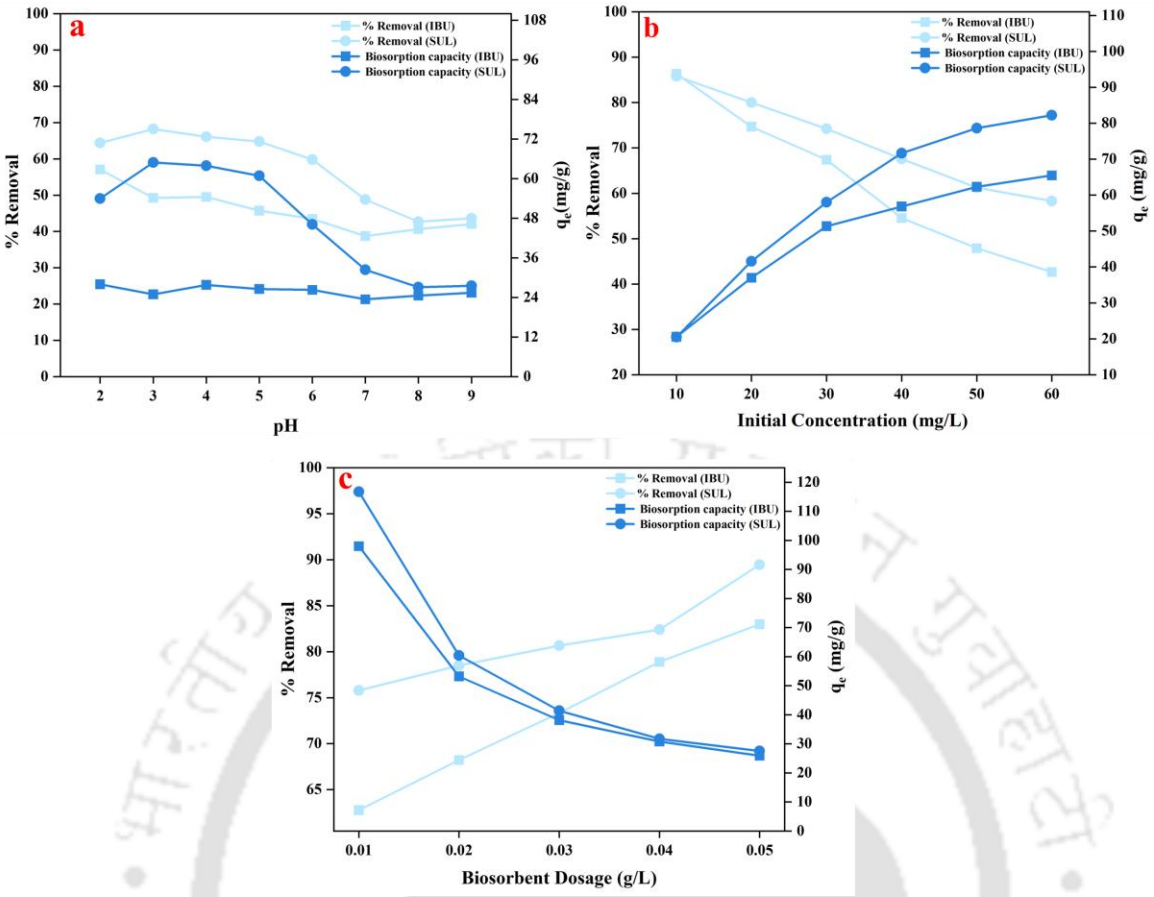

Fig. 3.6. a) *Effect of pH on biosorption of IBU and SUL by CNSP at various pH ranging from pH 2.0-9.0,* ***b)*** *Effect of initial IBU and SUL concentration on biosorption of IBU and SUL by CNSP at different concentrations of IBU and SUL ranging from 10-60 mg/L, and* ***c)*** *Effect of biosorbent dosage on biosorption of IBU and SUL by CNSP at different dosage of CSNP ranging from 0.01 to 0.05 g/L*

3.2.3. Biosorption isotherms

Biosorption isotherms are the theoretical graphs which represents the biosorption process as the function of an increase in adsorbate concentration at a constant temperature. The isotherm models (Table A1 (Appendix)) are used to determine the parameters like biosorption capacity, physical biosorption or chemical biosorption etc. The various biosorption process parameters of various isotherm models are shown in the Table 3.2. Isotherm models for IBU and SUL biosorption onto CSNP was shown in the Fig. 3.7 (a) and (b). Monolayer biosorption of IBU and SUL on the surface of CSNP was described by Langmuir isotherm (Hoslett et al., 2019). In Langmuir isotherm the CSNP have fixed number of sites for biosorption. The process of transmigration of SUL molecules on CSNP

surface plane is absent. The Q_0 of Langmuir model was found to be 65.3590 mg/g for IBU and 96.1538 mg/g for SUL biosorption. The K_L was found to be 0.3453 (L/mg) for IBU and 0.1980 (L/mg) for SUL. The R^2 value of SUL biosorption was 0.9984 which shows that SUL biosorption fit to Langmuir isotherm

Table 3.2. *Various isotherm parameters of IBU and SUL biosorption onto CSNP*

Isotherm Model	**IBU Biosorption**	**SUL Biosorption**
Langmuir Isotherm		
Q_0 (mg/g)	65.3590	96.1538
K_L (L/mg)	0.3453	0.1980
R^2	0.9860	0.9984
Freundlich Isotherm		
K_F (L/g)	20.1465	19.2841
n	2.8473	2.0635
R^2	0.9693	0.9774
Dubinin- Radushkevich Isotherm		
q_m (mg/g)	55.5001	69.0060
β (mol^2/J^2)	0.0045	0.0054
E (kJ/mol)	10.4720	9.5596
R^2	0.8578	0.8785
Temkin Isotherm		
b_T (kJ/mol)	188.2710	117.7760
K_T (L/mg)	3.3521	1.7541
R^2	0.9911	0.9968

Biosorption process of IBU and SUL on heterogeneous multilayer surface of CSNP was given by Freundlich isotherm model. It shows the exponential distribution of multilayer biosorption active centers with their energies. The values of exponent of Freundlich constant (n) were found to be 2.8473 for IBU and 2.0635 for SUL biosorption. The regression value (R^2) for IBU and SUL biosorption was found to be 0.9693 and 0.9774 respectively.

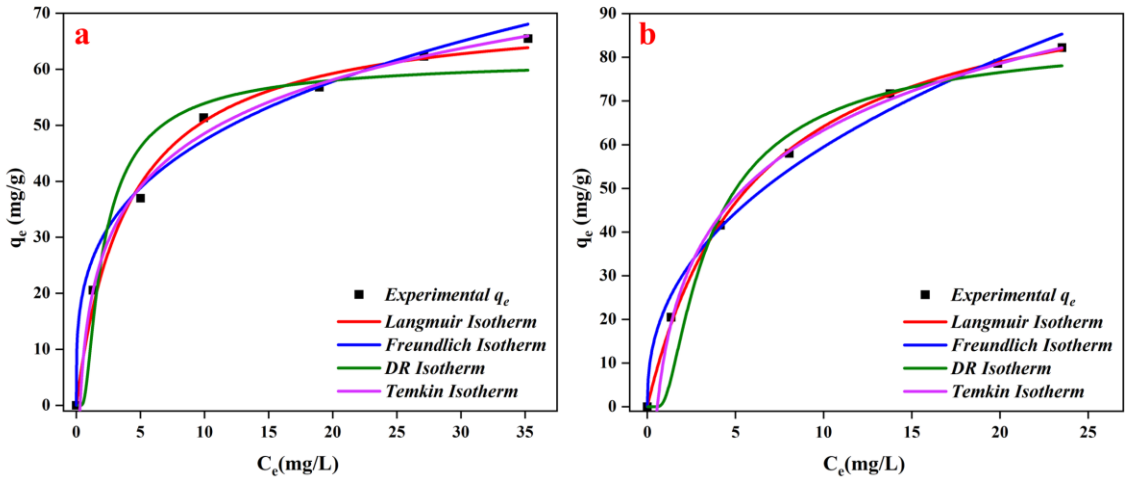

Fig. 3.7. *Isotherm models for* ***a)*** *IBU biosorption onto CSNP and* ***b)*** *SUL biosorption onto CSNP*

Mechanism of IBU and SUL biosorption process on CSNP heterogeneous surface with Gaussian energy distribution was explained by Dubinin-Radushkevich isotherm model. This model is best suited for intermediate range of IBU and SUL concentrations due to the exhibition of unrealistic asymptotic behavior (Khadir et al., 2020). Here the biosorption follows the pore filling mechanism and predicts whether the biosorption process is physical or chemical. The q_m and β for IBU biosorption was found to be 55.5001 mg/g and 0.0046 (mol^2/J^2) respectively. But for SUL biosorption the value of q_m was 69.0062 mg/g and β was 0.0055 mol^2/J^2. The apparent energy (E) for IBU and SUL biosorption was found to be 10.4720 and 9.5596 kJ/mol which favors theoretically chemical biosorption for both IBU and SUL (Hu and Zhang, 2019). The R^2 value was found to be 0.8578 (for IBU) and 0.8785 (for SUL) respectively. The indirect CSNP/IBU, SUL interactions were examined by Temkin isotherm model. This model assumes that there is a linear reduction in the heat of biosorption of IBU and SUL molecules as the surface increases. The value of b_T was found to be 188.2710 KJ/mol (IBU) and 117.7762 KJ/mol (SUL) biosorption process. The Temkin constant (K_T) was found to be 3.3521 L/mg and 1.7541 L/mg. The R^2 of IBU

biosorption was 0.9911 which shows that IBU biosorption fits the Temkin isotherm model (Vishnu Priyan et al., 2021).

3.2.4. Biosorption kinetics

Various biosorption kinetic models were used to investigate the rate of uptake of IBU and SUL on CSNP. The different kinetic models (Fig. 3.8 (a) and (b)), along with their non-linear mathematical equations, are given in the Table A2 (Appendix). The various kinetic parameters of these models were tabulated in the Table 3.3.

Table 3.3. *Different kinetic parameters of IBU and SUL biosorption onto CSNP*

Kinetics	**IBU Biosorption**	**SUL Biosorption**
Pseudo-first-order model		
q_e (mg/g)	40.8601	81.5455
k_1 (1/min)	0.0168	0.01884
R^2	0.8770	0.8438
Pseudo-second-order model		
q_e (mg/g)	49.0196	81.3008
k_2 (g/mg min)	0.0004	0.0001
R^2	0.9761	0.8539
Elovich model		
α (g/mg min)	3.3552	3.0025
β (mg/g)	0.1130	0.0813
R^2	0.9309	0.8310
Intra-particle diffusion		
k_i (mg/g min $^{1/2}$)	2.7588	4.0924
d	2.0656	4.7804
R^2	0.9481	0.9651

The pseudo-first-order (PFO) kinetic model assumes that the biosorption of IBU and SUL depends on the number of free active sites on CSNP and the concentration of IBU and SUL in the solution and on the surface of CSNP (Hoslett et al., 2021). The pseudo-first-order considers the rate of occupation of biosorption sites to be proportional to the number of unoccupied sites. This method is valid only at the initial stage of the biosorption process. For PFO, the R^2 and χ^2 value for IBU biosorption was found to be 0.9922 and 1.6517 respectively. For SUL biosorption the R^2 and χ^2 value was found to be 0.9829 and 7.7925.

The biosorption behavior of pollutants (IBU and SUL) on CSNP over the entire biosorption process was explained by pseudo-second-order (PSO) kinetic model. The rate-limiting step of PSO model is the chemisorption, involving interactions between the adsorbent and the adsorbate. The R^2 and χ^2 value for IBU biosorption was 0.9924 and 1.6000. For SUL biosorption the R^2 and χ^2 value was found to be 0.9870 and 5.9308. The Elovich model elucidates the nature of the chemical reaction between the pollutants (IBU and SUL) and the adsorbent (CSNP). This model is best fitted for the adsorbents with the heterogeneous surface. The alpha and beta value for IBU biosorption was found to be 1.2515 and 0.0728 respectively. For, SUL biosorption it was 0.6836 and 0.0304. The R^2 values of Elovich model is less than the R^2 values of PFO and PSO. Similarly, χ^2 values are higher than the χ^2 values of PFO and PSO, so Elovich model theoretically does not fit for IBU and SUL biosorption process.

Intraparticle Diffusion (IPD) model considers that there is mass transfer to the internal part of the CSNP, which occurs through the diffusion of the IBU and SUL molecules inside the pores of the CSNP. The R^2 for the IBU and SUL biosorption was found to be 0.9480 and 0.9651 respectively. On comparing the R^2 values (R^2(PSO) > R^2 (PFO) > R^2 (Elovich) > R^2 (IPD)) and χ^2 values (χ^2 (PSO) < χ^2 (PFO) < χ^2 (Elovich) < χ^2 (IPD)), it is observed that both IBU and SUL biosorption theoretically fits PSO kinetic model. Along with PSO kinetic model, other mechanisms like PFO and IPD takes place. At initial phase the biosorption process obeys PFO kinetic model as the initial concentration of the pollutant (IBU and SUL) in the solution is high leading to the boundary layer diffusion (Azizian, 2004). The second stage is the gradual biosorption stage, where intraparticle diffusion is rate controlling step (Rangabhashiyam and Selvaraju, 2015). In the final stage, IPD starts to slow down due to the low concentration of IBU and SUL in the solution promoting PSO kinetics (Shahnaz et al., 2021a).

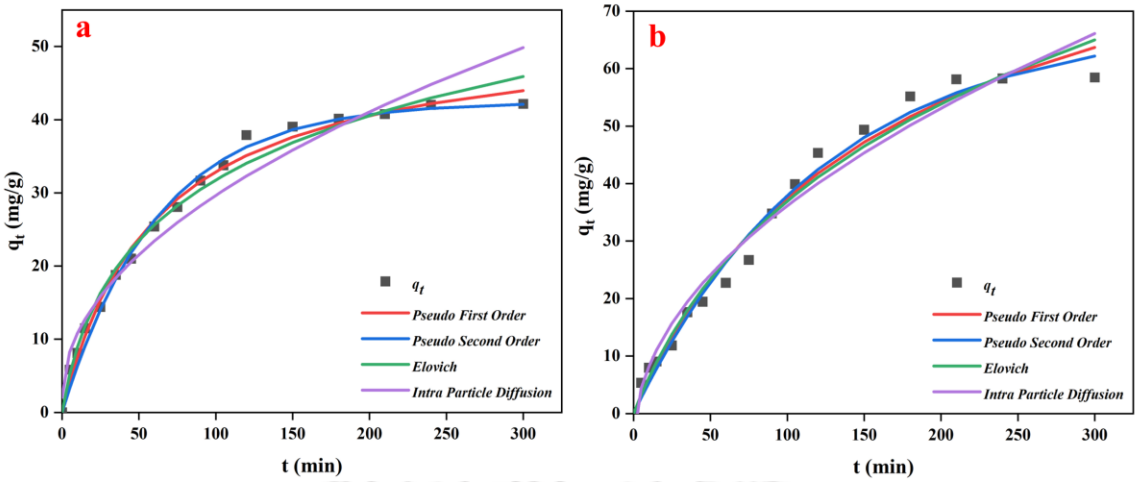

Fig. 3.8. *Various kinetic models* ***a)*** *IBU biosorption on CSNP and* ***b)*** *SUL biosorption on CSNP*

3.2.5. Phytotoxicity studies

The phytotoxic effects of IBU and SUL before and after biosorption on *Vigna mungo* (VM) and *Vigna radiata* (VR) seeds were examined through germination % of seedlings and inhibition of seedling growth (%). The Fig. 3.9 (a) and (b) shows that with the increase in IBU and SUL concentration, there is a decrease in the germination of seedlings. At 50 mg/L of IBU before biosorption, the seed germination % was 90% (VM) and 93.3% (VR). Due to the biosorption of IBU, the seed germination (%) increases to 100% for both VM and VR as the IBU molecules were adsorbed on CSNP. At 50 mg/L of SUL (before biosorption) VM and VR, the germination % was 93.3%, increasing to 96.6% after biosorption. (Sharma and Malan, 2017) investigated the effect of IBU on germination and growth of VR and reported that the maximum germination attained was 99.04%. Due to decline in the level of toxic metabolites, there is an increase in seed germination % of the seedlings.

The Fig. 3.9 (c) and (d) represents the growth inhibition of various seeds to various concentrations of IBU and SUL before and after biosorption. As the increase in time and concentration of IBU and SUL, the growth of the VM and VR seedlings decreases due to the inhibition of various metabolic activities. Before treatment of IBU with CSNP the inhibition % at 10, 30, 50 mg/L for VM was about 8.92%, 32.14%, 53.92% and for VR was 9.22%, 33.57% and 52.02% respectively. After treatment (after biosorption) the inhibition % decreases to 23.21% for VM and 24.72% for VR. Similarly, at 50 mg/L of SUL, the inhibition of growth (%) was about 46.78% (VM) and 48.70% (VR). After biosorption of

SUL by CSNP, we can observe that growth increases and the inhibition % decrease to 25% (VM) and 23.61% (VR), respectively. Pharmaceutical stress caused by IBU and SUL triggers an oxidative burst in mitochondrial and chloroplast compartments at the subcellular level through bioaccumulation of reactive oxygen species disrupting cell integrity by damaging proteins, DNA, and lipids leading to a decline in the growth of the seedlings (Wijaya et al., 2020).

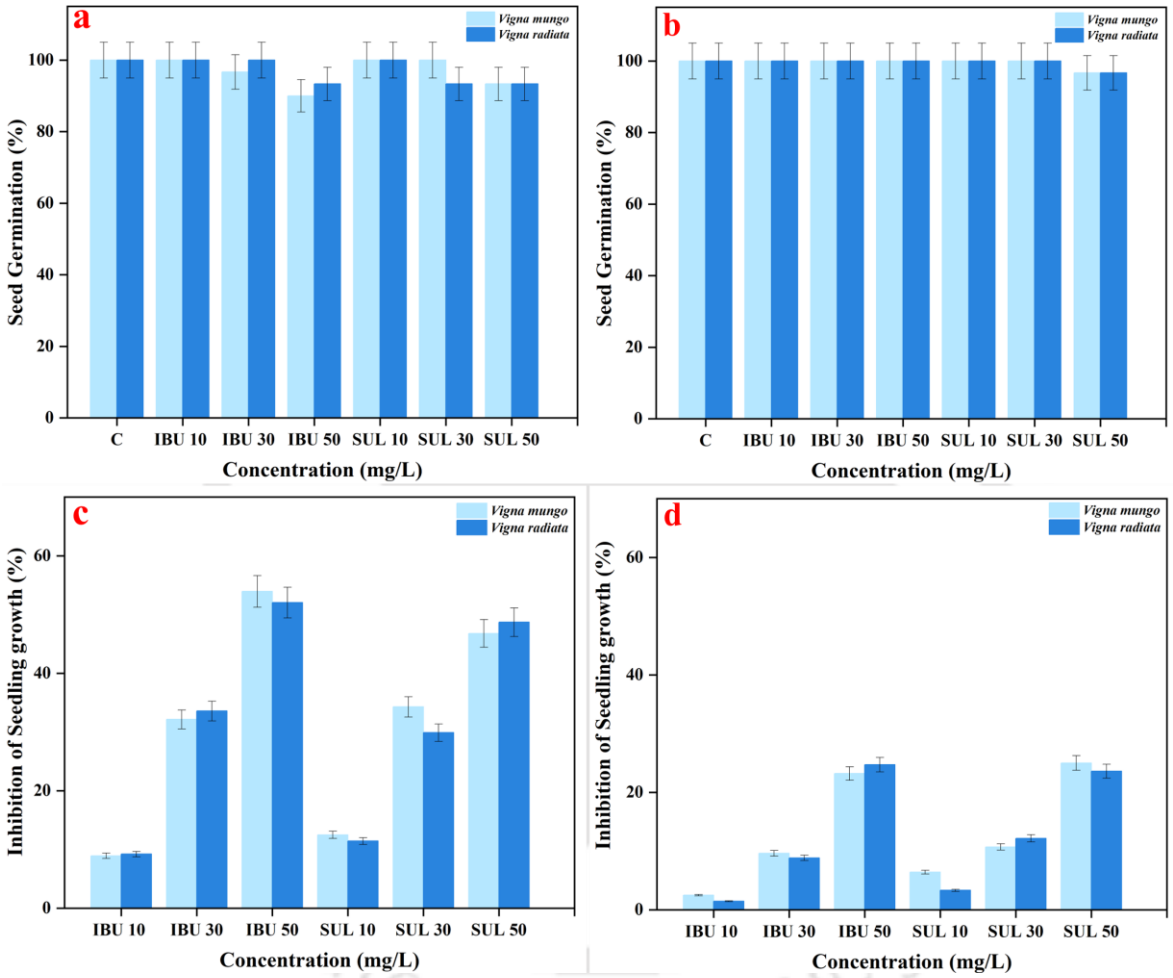

Fig. 3.9. a) *Seed germination (%) of Vigna mungo and Vigna radiata seeds at various concentrations of IBU and SUL before biosorption,* ***b)*** *Seed germination (%) of Vigna mungo and Vigna radiata seeds at various concentrations of IBU and SUL after biosorption* ***c)*** *Inhibition of growth (%) of Vigna mungo and Vigna radiata seeds at various concentrations of IBU and SUL before biosorption, and* ***d)*** *Inhibition of growth (%) of Vigna mungo and Vigna radiata seeds at various concentrations of IBU and SUL before biosorption*

3.2.6. Acute fish toxicity studies

In this present study the acute toxicological effects of two pharmaceutical drugs, IBU and SUL before and after biosorption on CSNP was investigated using zebra fish as model organism. It is observed that, the control group fishes were active and alive throughout the experimental study (Fig. 3.10). There is no abnormal behaviour of zebra fish in the control group. Various acute symptoms like fast tumbling, unusual swimming and staying at bottom were observed in the fishes treated with the pharmaceutical pollutant with concentration above 15 mg/L. The mortality percentage of the zebra fish increases as the IBU and SUL concentration increases, but there is no mortality till 15 mg/L.

The mortality percentage is depending on the concentration of the IBU and SUL solution. In the current study, the LC_{50} values were calculated for IBU and SUL, before and after biosorption process. After biosorption process the mortality percentage decreases due to biosorption of IBU and SUL on CSNP. We can observe that there is no death till 30 mg/L for both IBU and SUL.

Acute fish toxicity was performed for CSNP of different concentrations, including 50, 100, 150, 200, 1nd 250 mg/L, respectively. It was found that the control group fishes were active and alive throughout the experimental study. At 250 mg/L concentration of CSNP, the mortality % was found to be 3.33%, which might be due to the toxic effect of CSNP, which was treated with sulfuric acid. The LC_{50} values of IBU before and after biosorption on CSNP at 96 h was calculated as 209.50 mg/L and 1435.82 mg/L respectively. This confirms that CSNP removes IBU from the aqueous solution at highly efficient manner. (Mathias et al., 2018) investigated the various effects of IBU in environmental concentrations on Rhamdia quelen and found that IBU causes nephrotoxicity due to inhibition of renal carbonic anhydrase activity. The toxic effect of acute exposure of IBU on *Clarias gariepinus* was studied by (Ogueji et al., 2018) and found that 96 h LC_{50} of IBU was 0.38 mg/L. The LC_{50} values for SUL before and after biosorption after 96 h was found to be 338.84 and 1317.04 mg/L. The exposure of SUL on adult zebra fish triggers inflammatory cytokine expression and oxidative stress (Zhou et al., 2018).

Long term exposure of SUL on zebra fish leads to reduction in the body weight and affects its body system has been reported by (Yan et al., 2016). After biosorption the mortality percentage decreases from 67% to 33% for IBU and 53% to 27% for SUL respectively.

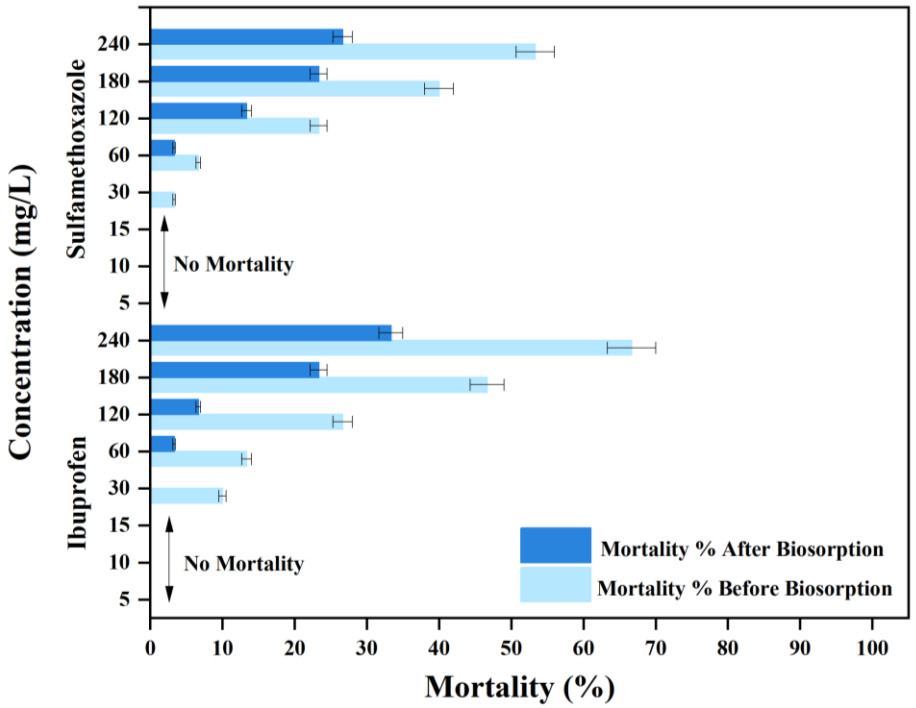

Fig. 3.10. *Mortality (%) of Danio rerio (zebra fish) to various concentrations of IBU and SUL before and after biosorption (experimental conditions: oxygen concentration (>75%), pH (6.5-7.5), light period (14 h light: 10 h dark) and temperature (25 °C))*

3.2.7. Proposed adsorption mechanism

The IBU and SUL adsorption onto CSNP depends on the CSNP solution's pH. The IBU and SUL adsorption process involves electrostatic interaction and hydrogen bonding (Fig. 3.11). The zero-point charge of CSNP was found to be 1.8. The pH below the pH PZC, the surface of CSNP was positive, and above the pH PZC, the surface was negative. The pKa value of IBU was found to be 4.91, in which the pH above the pKa value, IBU will exist in anionic form, and below the pKa value, it exists in cationic form. SUL molecules have both $-NH_2$ (amine) and -NH- (amide) groups showing two pKa values at 1.6 and 5.7. When the pH of the solution is less than 1.6 or higher than 5.7, SUL is positively or negatively charged, promoting electrostatic interaction. The maximum adsorption was seen at pH 2.0 for IBU and 3.0 for SUL, in which both the drug molecules possess positive and neutral charges. Due to their positive surface charges, IBU and SUL get attracted toward the negatively charged CSNP. Thus, the electrostatic interaction takes place between drug molecules and CSNP. In some cases, the surface of CSNP has -OH groups. The amine group in SUL forms a hydrogen bond with the surface -OH group of CSNP.

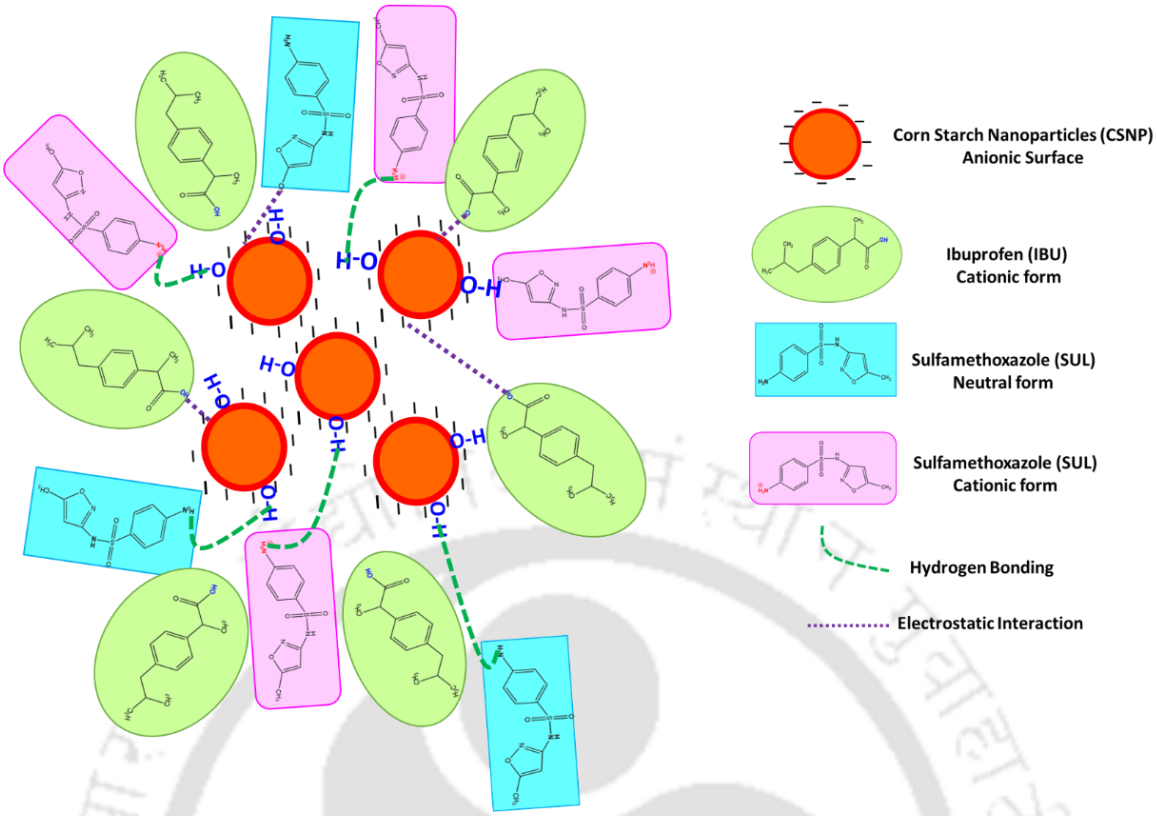

Fig. 3.11. *Proposed adsorption mechanism of IBU and SUL onto CSNP*

3.3. Significant findings

In the current research, the new low cost CSNP biosorbent was prepared using corn starch to remove two anionic pharmaceuticals ibuprofen and sulfamethoxazole. The synthesized CSNP was examined through various analytical techniques such as FESEM, FETEM, AFM, FTIR, XRD, Raman spectroscopy and EDX. The characterization results revealed that CSNP possess superior biosorption properties for the removal of IBU and SUL from aqueous solutions. The biosorption of IBU and SUL was controlled by various parameters such as pH of IBU and SUL solution, dosage of CSNP, initial concentration of IBU and SUL and contact time. The maximum removal efficiency of IBU was found at pH 2.0, initial concentration of 10 mg/L and 0.01 g/L of CSNP with removal efficiency of 86.33%. A high removal efficiency of 85.80% for SUL was observed at pH 3.0, 10 mg/L initial concentration and 0.01 g/L of CSNP dosage. The IBU and SUL biosorption follows Temkin and Langmuir isotherm models. Various kinetic models were analysed in which both IBU and SUL biosorption fits to PSO kinetic model. Seed toxicity studies revealed that before biosorption of IBU and SUL growth inhibition (%) and germination (%) decreases as the concentration of IBU and SUL increases. After biosorption seed germination drastically

increases upto 100% for both VM and VR respectively. Acute fish toxicity studies were performed in zebra fish at different concentrations of IBU and SUL before and after biosorption. Before biosorption the mortality rate increases to 67% and 53% for 240 mg/L of IBU and SUL (96 h). The LC_{50} of IBU and SUL on zebra fish before biosorption process was found to be 209.50 mg/L and 338.84 mg/L. These results inferred feasibility of CSNP preparation for the effective removal of IBU and SUL from aqueous solutions by reducing the toxicity levels.

Chapter 4

Development of Fe_3O_4/CAC nanocomposite for the effective removal of Contaminants of emerging concern (Ce^{3+}) from water: An ecotoxicological assessment

The work embodied in this chapter is published in

Vishnu Priyan V., Nitesh Kumar, Selvaraju Narayanasamy**,** 2021. Development of Fe_3O_4/CAC nanocomposite for the effective removal of contaminants of emerging concerns (Ce^{3+}) from water: An ecotoxicological assessment, **Environmental Pollution**, 285, 117326. https://doi.org/10.1016/j.envpol.2021.117326 **(Elsevier; SCI IF 2023: 8.9).**

Abstract

Contaminants of emerging concerns present in the ecosystems causes various adverse effects on all living organisms. In current study, removal of Ce^{3+} from water was performed using Fe_3O_4/CAC nanocomposite (MCAC) synthesized by co-precipitation technique. The synthesized MCAC was characterized using various analytical techniques. The magnetic behavior of the nanocomposite which is a crucial advantage in separation of MCAC after adsorption of Ce^{3+} from water was determined using vibrating sample magnetometer. MCAC was semicrystalline comprising both amorphous and crystalline regions with elements like C, O, Fe and N. The influence of process parameters was optimized through batch mode with the adsorption capacity of 86.206 mg/g. Ecotoxicological studies were performed using *Danio rerio* (Zebra fish) and seeds of *Vigna mungo* and *Vigna radiata* to assess the harmful effects of Ce^{3+} before and after adsorption process. The phytotoxicity studies on seeds revealed that inhibition of growth ranges from 50.39% to 12.55% (before adsorption) and 28.57% to 3.89% (after adsorption). After 96 h the LC_{50} value of Ce^{3+} on the *Danio rerio* was 2.44 mg/L. Thus, the current study investigated the effective removal of Ce^{3+} by MCAC and evaluates its ecotoxicological effects.

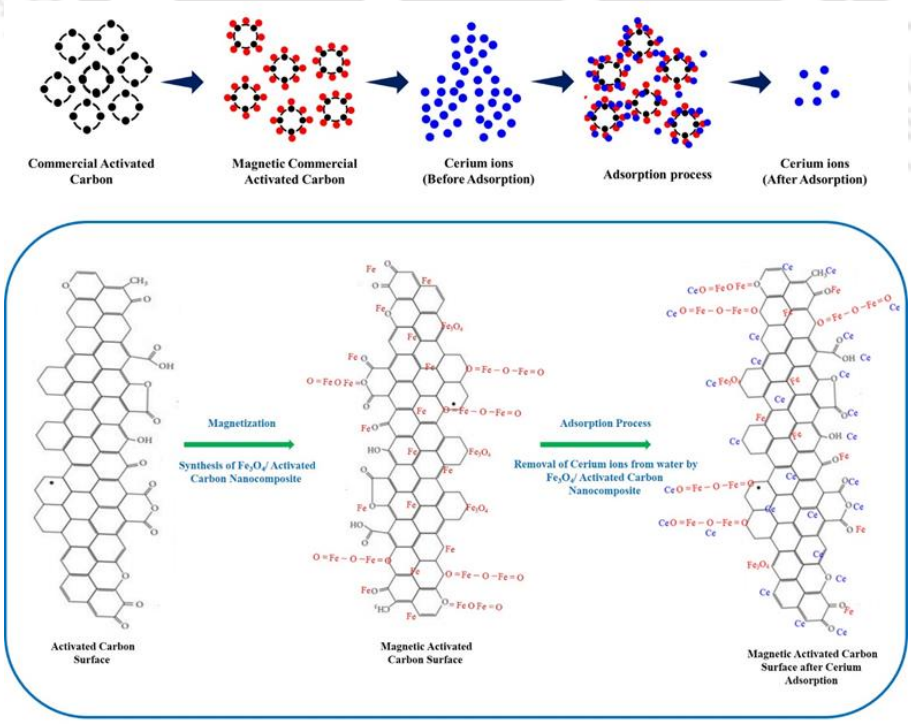

Graphical Abstract

4.1. Materials and methods

4.1.1. Chemicals and materials

All chemical solutions were prepared from certified lab grade chemicals. Cerium (III) chloride heptahydrate ($CeCl_3.7H_2O$, extrapure AR, Mol. Wt. 372.60) was used as the source of Ce (III) in the synthetic wastewater was procured from Sisco Research Laboratories, India. The activated carbon (Wellon, NSF/ANSI61- granular) used in this study was made up of coconut shell. Fe_3O_4/CAC nanocomposite was synthesised using Ferric chloride hexahydrate ($FeCl_3.6H_2O$, Hi-LR, Mol. Wt. 270.30), Ferrous sulphate heptahydrate ($FeSO_4.7H_2O$, Hi-LR, Mol. Wt. 278.01) were procured from HiMedia Laboratories, India. Ammonia solution (NH_4OH, extrapure AR, Mol. Wt. 35.05) was brought from Sisco Research Laboratories, India. Sodium hydroxide (NaOH, Hi-AR/ACS, Mol. Wt. 40, HiMedia) and hydrochloric acid (HCl, 99% pure, Mol. Wt. 36.46, SRL) were used to adjust the pH of the mixture.

4.1.2. Synthesis of MCAC (Fe_3O_4/CAC) nanocomposite

To synthesis MCAC, 1:2 molar ratio of $FeCl_3.6H_2O$ and $FeSO_4.7H_2O$ solutions were prepared in a beaker. To this mixture, 5 g of commercial activated carbon (CAC) was added under continuous vigorous stirring for 3 h. The temperature of the stirrer was maintained at 80 °C. Then, diluted ammonia solution was added to the mixture drop by drop by using a syringe. Then the reaction mixture was kept at 80 °C for another 1 h. Then, the synthesized MCAC nanocomposite was recovered by strong magnet and washed with ethanol/distilled water (2:1) to eliminate the unreacted materials from the MCAC. After washing, the obtained MCAC was dried in oven at 100 °C for 48 h and stored for further use as adsorbent (Takmil et al., 2020).

4.1.3. Characterization of MCAC

The detailed characterization of the MCAC before and after adsorption of Ce^{3+} were investigated through various analytical techniques as provided in the Table A3 (Appendix).

4.1.4. Ce^{3+} adsorption experiments

The adsorption of rare earth element Cerium (Ce^{3+}) by MCAC was performed in batch experiments under different Ce^{3+} initial concentrations (20 to 100 mg/L), pH (2.0-10.0) and MCAC dosage (0.02-0.12 g/L). 20 mL of Ce^{3+} stock solution was stirred at 150 rpm in a

shaking incubator. By using 0.1 M HCl or 0.1 M NaOH the pH of the mixture was adjusted. The temperature was maintained at 308 K throughout the experiments. After adsorption process, the residual Ce^{3+} concentration was determined using AES (446.021 nm).

The maximum adsorption capacity and removal efficiency of Ce^{3+} adsorption was calculated from Table 4.1.

Table 4.1. *The maximum adsorption capacity and removal efficiency of Ce^{3+} adsorption*

Parameters	Equation	Description	Equ. No.
Maximum adsorption capacity	$q_e = \frac{(C_0 - C_e)}{m} \times V$	**q_e** is the amount of Ce^{3+} adsorbed at equilibrium time (mg/g), **C_0** and **C_e** are the initial and equilibrium Ce^{3+} concentrations. (mg/L), **m** is the mass of the MCAC (g), **V** is the volume of Ce^{3+} solution (L).	(4.1)
Removal efficiency	$Removal\ (\%) = \frac{C_0 - C_e}{C_0} \times 100$		(4.2)

4.1.5. Phytotoxicity experiments

The phytotoxicity experiments of Ce^{3+} before and after adsorption on MCAC was performed in Petri dishes with seeds of various plant species using protocol of (Vishnu Priyan et al., 2021) with minor modifications. The plant species used in this experiment were *Vigna mungo* (VM) and *Vigna radiata* (VR). The experiment was performed at room temperature.

The effect of phytotoxicity was measured after seven days in terms of inhibition of growth (%) and seed germination (%) of the seedlings of *Vigna mungo* and *Vigna radiata*. The seeds of VM and VR were first washed with 1% sodium hypochlorite to evade yeast and fungal growth and then with deionized water for several times. The sterilized seeds of VM and VR were placed in the Petri dishes containing distilled water as control, Ce^{3+} solution before adsorption and after adsorption at different concentrations (10-50 mg/L) respectively. Then, Petri dishes containing seeds were kept in dark for 7 days. After 7 days, the seedlings of VM and VR at different concentrations of Ce^{3+} solution were taken out and subjected to phytotoxicity analysis.

4.1.6. Acute fish toxicity experiments

Acute fish toxicity experiments were performed using zebra fish (*Danio rerio*) as the model organism. This test was done as per the test guideline number 203 of OECD. Zebra fishes with similar size and age were selected to carry out this test. Ce^{3+} solution was prepared in two sets for each concentration (1-5 mg/L). One set of Ce^{3+} solutions will be used for before adsorption experiments and another set will be subjected to adsorption process and used for after adsorption experiments. The dissolved oxygen concentration (>75%), pH (6.5-7.5), light period (14 h light: 10 h dark) and temperature (25 °C) were maintained constant throughout the experiments. 10 healthy zebra fishes were taken for each experiment. Totally, 11 experiments including control (only water) were performed. At the end of 96 h the mortality rate and LC_{50} values were calculated to determine the toxicity of Ce^{3+} before and after adsorption (Shahnaz et al., 2021).

4.1.7. Regeneration studies

In short, 0.1 g/L of MCAC was introduced into 100 mg/L of Ce^{3+} solution at pH 6.0, followed by shaking at 150 rpm at 308 K for 90 minutes. After magnetic separation of MCAC from Ce^{3+} solution, the concentration of Ce^{3+} after adsorption was detected using Atomic Emission Spectroscopy. Then, the adsorbed MCAC was collected and subjected to 0.1 M NaOH at 150 rpm at 308 K for 3 h. After NaOH treatment, the MCAC was rinsed with distilled water to remove the residual NaOH. The rinsed MCAC was dried and used for the next cycle of experiments. Similarly, 5 cycles were performed.

4.2. Results and discussion

4.2.1. Characterization studies

The surface morphology, size, topology and roughness of the MCAC was investigated using various microscopy techniques including FESEM, FETEM and AFM. The Fig. 4.1 (a) to (d) represents the FESEM micrographs of MCAC at various magnifications. From the images it is observed that the Fe_3O_4 nanoparticles (Fe_3O_4-NP) are distributed in clusters on the surface of the commercial activated carbon (CAC). The size of the Fe_3O_4-NP was found to be between 30-50 nm. Due to the distribution of Fe_3O_4-NP on the surface of CAC, makes the adsorbent more porous and spongier in structure. The Fig. 4.2 (a), (b) and (c) denotes the FETEM images of MCAC. From the images we can see that the surface of

CAC was occupied with Fe_3O_4-NP, which favours the magnetic property to the CAC promoting easy separation of the adsorbent after the adsorption of Ce^{3+} ions.

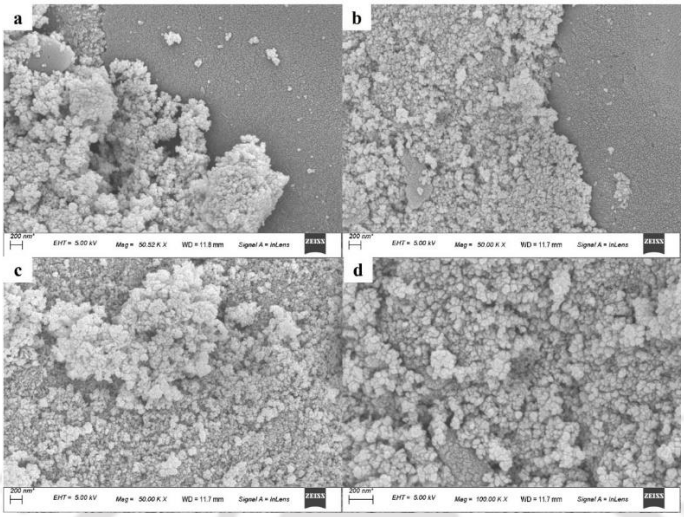

Fig. 4.1. *FESEM micrographs of MCAC at different magnifications* ***a)*** *MCAC (50.52 KX),* ***b)*** *MCAC (50.00 KX),* ***c)*** *MCAC (50.00 KX), and* ***d)*** *MCAC (100.00 KX)*

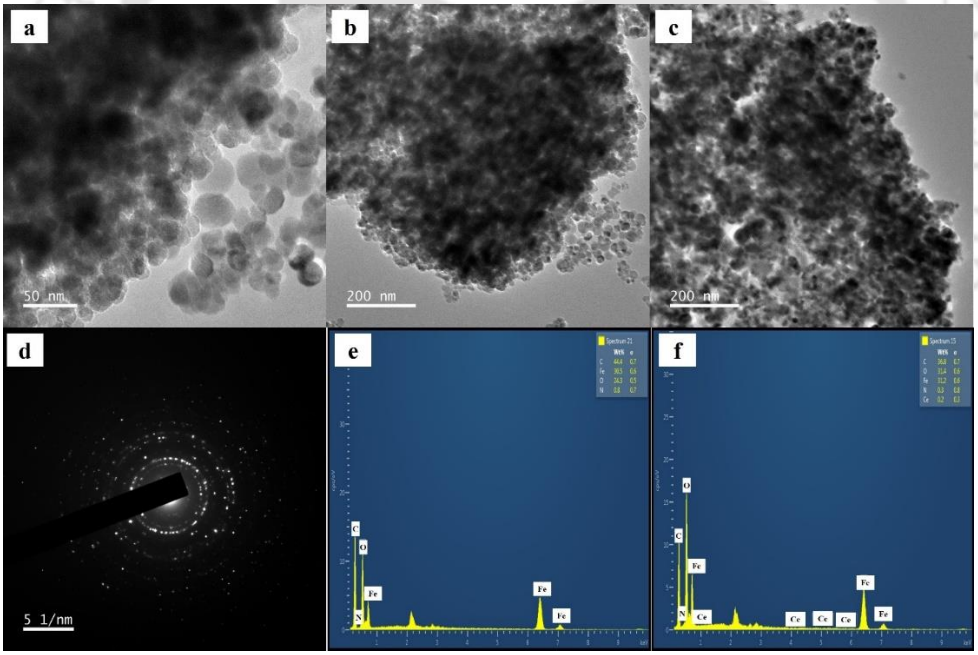

Fig. 4.2. a-c) *FETEM image of MCAC,* ***d)*** *SAED image showing crystallinity of MCAC, EDX spectra of* ***e)*** *MCAC before adsorption of* Ce^{3+} *and* ***f)*** *MCAC after adsorption of* Ce^{3+}

FETEM images confirms that the formed Fe_3O_4-NP are spherical in shape with the size less than 50 nm which is in good agreement with the results of FESEM. The selected area

diffraction pattern (Fig. 4.2 (d)) was done for MCAC and it is found that the adsorbent was contains both crystalline and amorphous regions.

The Fig. 4.2 (e) and (f) represents the EDS spectra of MCAC before and after adsorption of Ce^{3+}. The EDX spectrum of MCAC (Fig. 4.2 (e)) revealed the presence of elements such as carbon (C), oxygen (O), nitrogen (N) and iron (Fe). It is found that the C content was greatest (44.4 wt.%), followed by Fe (30.5 wt.%), O (24.3 wt.%) and N (0.8 wt.%). The carbon peaks were due to the carbon present in the surface CAC. The peaks of Fe were attributed due to the impregnation of Fe_3O_4-NP on the surface of the CAC. Meanwhile, the existence of N (0.8 wt.%) in the sample was due to the presence of a residual nitrogen. The EDS spectrum of MCAC after the adsorption of Ce^{3+} (Fig. 4.2 (f)) revealed the presence of all major elements along with Ce. The weight percentage of the elements was found to be C (36.8 wt.%), Fe (31.2 wt.%), O (31.4 wt.%), N (0.3 wt.%) and Ce (0.2 wt.%). The presence of Ce peaks was attributed by cerium ions after the adsorption process. Weight percentage of the elements present in MCAC before and after adsorption Ce^{3+} ions was tabulated in the Table 4.2.

Table 4.2. *Weight percentage of the elements present in MCAC before and after adsorption*

Sample Name	**Elements (wt. %)**				
	Carbon (C)	**Oxygen (O)**	**Iron (Fe)**	**Nitrogen (N)**	**Cerium (Ce)**
MCAC	44.4	24.3	30.5	0.8	-
MCAC- Ce^{3+}	36.8	31.4	31.2	0.3	0.2

The crystallinity changes of CAC, MCAC before and after adsorption of Ce^{3+} were examined by using XRD (Fig. 4.3 (a)). The diffraction peaks for CAC were seen at 2θ of 12.74°, 24.14°, 35.72°, 43.64°, 52.72°, 67.94° and 76.66° respectively. The XRD peaks at 24.14° and 43.14° of CAC attributed to (002) and (101) planes of graphitic carbon (Hu et al., 2020). In addition, CAC shows some sharp peaks which may be due to the presence of residual ash in CAC. The diffraction peak found at 2θ of 12.74° corresponds to the kaolinite phase of the commercial activated carbon. The sharp peaks in MCAC and MCAC-Ce^{3+} at 2θ of 30.12°, 35.74°, 43.46°, 53.68°, 57.62° and 62.92° represents the crystalline structure of the magnetite (Fe_3O_4) (Danalıoğlu et al., 2017; Feng et al., 2020). The presence of these 6 typical peaks confirms the presence of Fe_3O_4-NP on the surface of CAC. There is no shifting or change in the peak position of MCAC for both before and after adsorption. The

peaks at 35.74°, 57.62° and 62.98° of MCAC-Ce^{3+} can also be due to the presence of Ce in the sample (Hosseynizadeh Khezri et al., 2012).

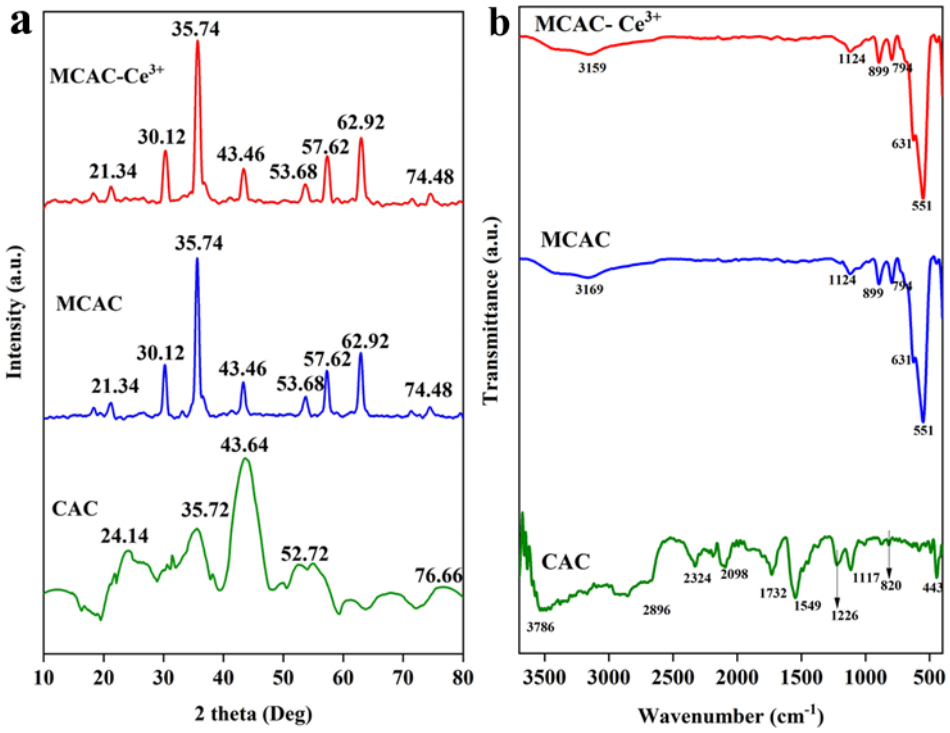

Fig. 4.3. a) *XRD analysis of CAC, MCAC and MCAC- Ce^{3+} showing 2 theta peaks explaining crystallinity, and* ***b)*** *FTIR spectra of CAC, MCAC and MCAC- Ce^{3+}*

The FTIR spectra of CAC, MCAC before and after adsorption was represented in the Fig. 4.3 (b). The bands between 3800-3100 cm^{-1} was typically due to the various vibrational stretching of hydroxyl (OH) and amino (NH) groups. The maximum effect on these stretching vibrations was due to hydrogen bonding (Wang et al., 2020). The observed OH stretch depends upon the strength of the hydrogen bonds. The band at 2896 cm^{-1} corresponds to the vibrations of the methyl (CH_3) group. The peak at 2324 cm^{-1} was attributed by conjugated aromatics and the aliphatic groups (-N=C=O). The band at 2098 cm^{-1} was assigned to C=O stretching vibrations (Ren et al., 2021). The peaks in the region of 1800-1500 cm^{-1} attributed to carbonyl containing species (D'Cruz et al., 2020). The peak at 1732 cm^{-1} was due to anhydride. The C-O stretching vibrations are seen at 1300 – 750 cm^{-1}. The peak at 1226 cm^{-1} assigned to C-C vibration mode. The bands at 877 and 820 cm^{-1} represents the C-O-C stretching vibrations of carbonyl compounds. The band at 1226 and 1117 cm^{-1} was shifted to 899 and 794 cm^{-1} due to bending vibrations in MCAC before and

after adsorption. We can observe the peaks at 631 and 551 cm^{-1} which corresponds to the stretching vibrations of Fe-O bond of Fe_3O_4-NP (Queiroz et al., 2020).

The deformation in the structure of CAC and MCAC was investigated using Raman spectroscopy. From the Fig. 4.4, we can see the unique bands of graphitic carbon at 1332 cm^{-1} and 1595 cm^{-1}. The band at 1332 cm^{-1} and 1595 cm^{-1} corresponds to the D and G band of the graphitic carbon related with the disordered structure of carbon (A_{1g} vibrational mode) due to the presence of the sp^3 hybridization in CAC and MCAC (Rosaiah et al., 2019**;** Nguyen et al., 2020).

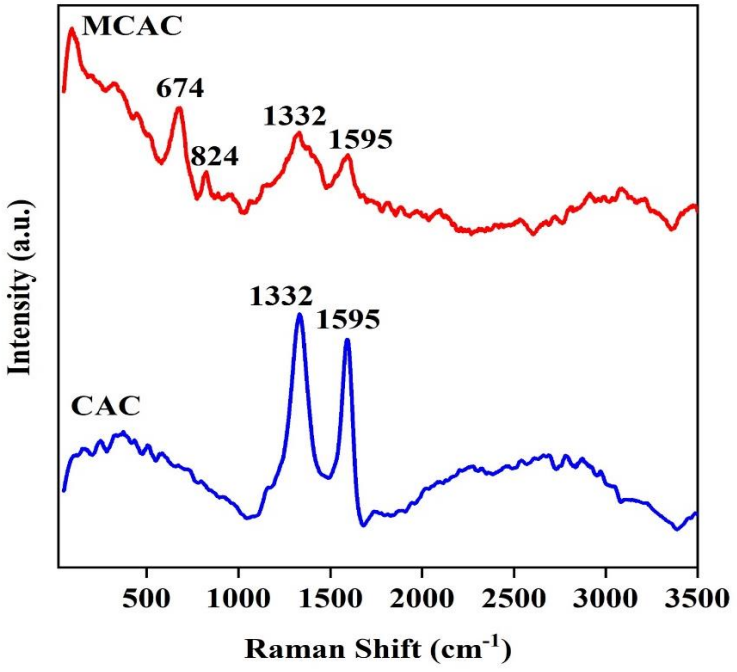

Fig. 4.4. *Raman spectra of CAC and MCAC showing different bands*

In MCAC, these D and G bands are seen with less intensities on compare to the D and G bands of CAC due to the presence of Fe_3O_4 on the surface of MCAC and reduction of lattice carbon. The lower Raman shift peak at 674 cm^{-1} and 824 cm^{-1} corresponds to Fe-O bond of Fe_3O_4 in A_{1g}, E_g and T_{2g}vibration modes (Barmi et al., 2020). This band was not seen in Raman spectra of CAC because of absence of Fe_3O_4 on the surface of CAC.

The magnetic properties of the prepared MCAC were investigated by using vibrating sample magnetometer. Fig. 4.5 depicts the graph plotted between magnetic field (Oe) and moment/mass (emu/g). The maximum magnetic strength (Ms) of the nanocomposite MCAC was found to be 42.256 emu/g. The maximum magnetic strength of the pristine

Fe_3O_4 was 92 emu/g (Gallios et al., 2017). The decrease in the maximum magnetic strength (Ms) of MCAC was due to the presence of graphitic carbon layers on the surface of MCAC (Udhayakumar et al., 2021). Despite the lower Ms value, it is very much sufficient for separating the adsorbent from the aqueous solution after adsorption of Ce^{3+} by the magnet. The coercivity (H_{ci}) and retentivity (Mr) of the MCAC was found to be 55.033 Oe and 3.6386 emu/g.

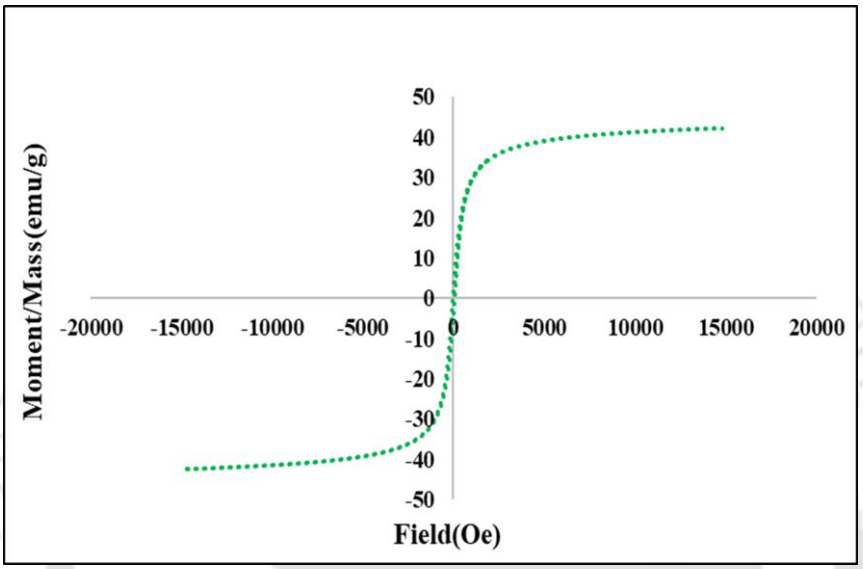

Fig. 4.5. *VSM analysis of MCAC for evaluating the magnetic behaviour*

4.2.2. Effect of various parameters on adsorption

4.2.2.1. Effect of pH on Ce^{3+} adsorption

pH, one of the crucial factors in the adsorption process, play an essential role in achieving maximum adsorption. The MCAC chemical properties and Ce^{3+} are greatly affected by the solution pH; the adsorbent's surface charge ultimately depends on the pH. Similarly, adsorbate functional groups and metal ions have different charge density or charge under different pH values (Vishnu Priyan et al., 2021). The removal efficiency increases from 9.58% to 37.46% as the pH of the cerium solution increases (Fig. 4.6 (a)). The point of zero charge (PZC) was estimated through zeta potential analysis of MCAC at different initial pH (2.0 to 10.0). The pH PZC for MCAC was found to be 5.5. It shows that the surface of adsorbent was positive below pH 5.5 and negative above pH 5.5. The maximum Ce^{3+} adsorption was observed at solution pH 6.0. But after pH 6.0, we noticed the formation of cerium salts in alkaline condition and it get precipitated. So, after pH 6.0 we cannot perform

the batch experiments for optimization due to conversion Ce^{3+} ions into their respective metal hydroxides. The MCAC surface is positive in acidic condition (pH< 5.5) causing electrostatic repulsion between protons (H^+) and cerium (Ce^{3+}) cations. Hence, due to the competition between H^+ and Ce^{3+} we could observe very less adsorption at pH below 5.5. Rodrigues et al. (2020) reported that the PZC for magnetic activated carbon was found to be 3.72. As the pH increases, adsorption increases due to ionization of the functional sites. With increasing pH of solution, the electrostatic repulsion between Ce^{3+} and the surface of the MCAC is decreased. Then, the concentration of OH^- increases on the surface of MCAC allowing more free surface sites to Ce^{3+}, which results in an increase in removal efficiency (Azari et al., 2015).

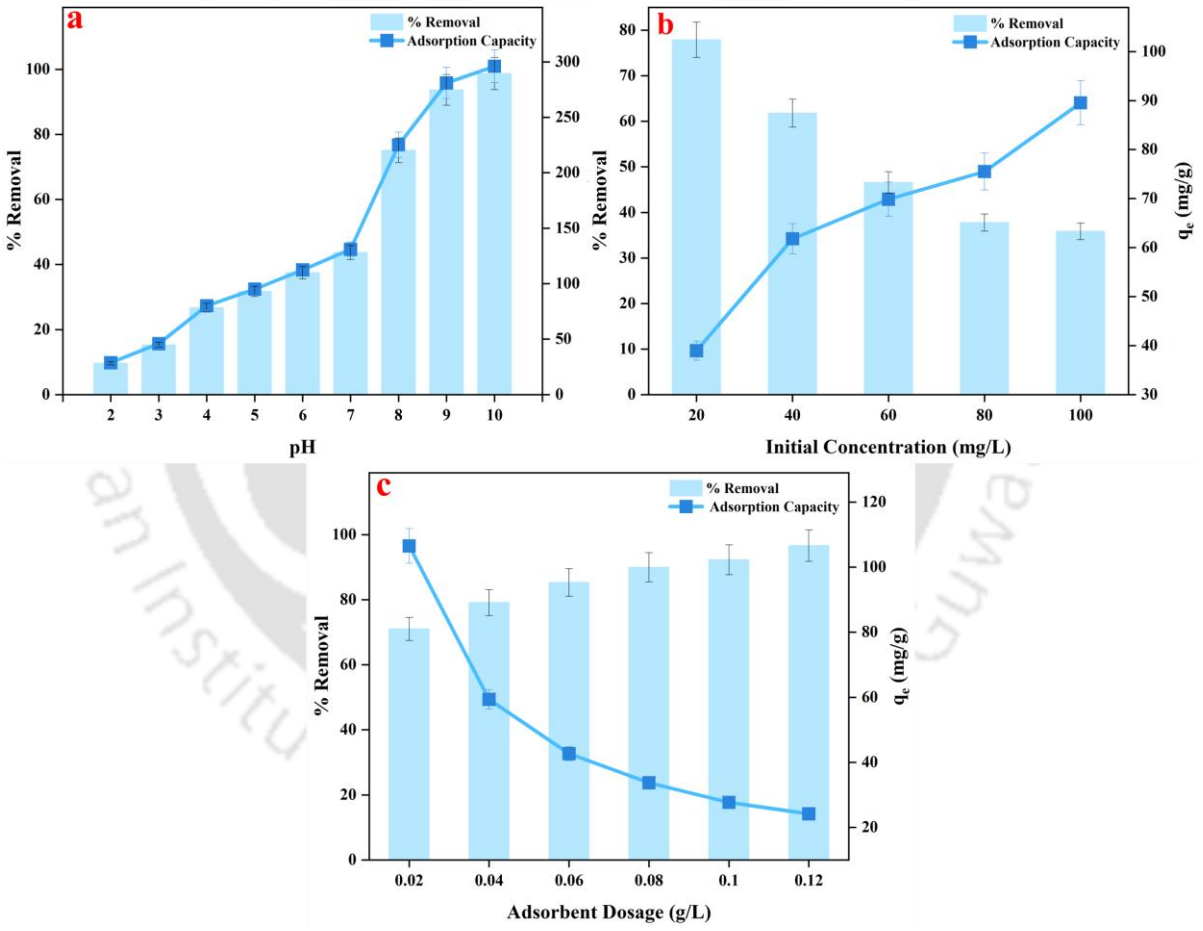

Fig. 4.6. a) *Effect of pH on adsorption of Ce^{3+} by MCAC at various pH ranging from pH 2.0-10.0,* ***b)*** *Effect of initial Ce concentration on adsorption of Ce^{3+} by MCAC at different concentrations of Ce ranging from 20-100 mg/L, and* ***c)*** *Effect of adsorbent dosage on adsorption of Ce^{3+} by MCAC at different dosage of MCAC ranging from 0.02 to 0.12 g/L*

4.2.2.2. Effect of initial Ce^{3+} concentration

The initial concentration of Ce^{3+} affects the removal efficiency as well as the adsorption capacity of the MCAC. As the initial concentration increases, the removal efficiency decreases because, at a lower concentration, MCAC carry more unoccupied active sites relative to Ce^{3+} molecules; thus, high removal efficiency is obtained (Fig. 4.6 (b)). In other words, it can be said that for the available mass of adsorbent, the adsorption amount is fixed (Priyan et al., 2020). Conversely, the adsorption capacity of adsorbent rises with an increase in initial concentration, which is caused by the high driving force for mass transfer between Ce^{3+} and MCAC**.** In the present study, the effect of the initial concentration of Ce^{3+} (20-100 mg/L) was analysed on the fixed mass of MCAC at an optimized pH value.

As the initial concentration rises, the removal efficiency was reached 35.82% from 77.9% gradually, and the adsorption capacity increased from 38.95 to 85.55 mg/g. This behaviour has also been observed in other adsorption studies (Ahsan et al., 2018; Danalıoğlu et al., 2017; Ebadollahzadeh and Zabihi, 2020; Esmaeili and Eslami, 2020) were the initial concentration is an important parameter which provides a driving force for the adsorbate molecules to diffuse from the aqueous phase to the solid phase by overcoming all mass transfer resistances. Moreover, higher concentration of adsorbate molecules leads to more collision, which results in a higher adsorption capacity.

4.2.2.3. Effect of MCAC dosage

Determining the minimum dosage amount of MCAC required to remove the same initial concentration of Ce^{3+} with an increasing dosage amount is imperative because it scales down the overall adsorption process's cost. An increase in the dosage amount affects the adsorption via elevating removal efficiency, which may be due to the availability of many binding sites compared to Ce^{3+} molecules at the higher MCAC concentration for adsorption. However, after a certain dosage amount, there is no increase in removal efficiency even at a higher adsorbent amount, which can be attributed to a lack of adsorbate molecules in the solution in comparison to available binding sites (Fabre et al., 2020). A decrease in adsorbate amount adsorbed per unit mass of adsorbent at a specified volume is obtained, thereby causing a reduction in adsorption capacity (Han et al., 2020). For optimizing MCAC dosage amount, Cerium adsorption was carried out using MCAC at different dosages with a fixed initial concentration of cerium (100 mg/L). It was observed

that removal efficiency increased from 71.01% to 96.61% by increasing the dosage of MCAC, whereas adsorption capacity reduced from 106.53 to 24.1525 mg/g (Fig. 4.6 (c)). Shirsath and Shirivastava (2015) reported that at equilibrium there is a decrease in adsorption capacity with an increase in magnetic nano adsorbent dosage from 0.5 mg/L to 5 mg/L. Similar type of results have been reported by Eslami et al. (2019) narrating that the removal efficiency increases gradually with increasing dosage of adsorbent.

4.2.3. Adsorption isotherms

The adsorption mechanism or interactive behaviour depends on the surface functional groups and porosity of the adsorbent and the nature of adsorbate molecules. Therefore, specific isotherm models such as Freundlich, Langmuir, Dubinin-Radushkevich (D-R), Temkin were brought up to explain the binding mechanism and ability of adsorbate for the adsorbent (Fig. 4.7 (a)). Each model provides physiochemical data to predict the adsorption process and maximum adsorption capacity, which is evaluated using these models' equations Table A1 (Appendix). Maximum adsorption is achieved when adsorption and desorption rate become equal, and it can be easily determined by conducting isotherm experiments using isotherm models subsequently (Patel et al., 2019). The adsorption process parameters of different isotherm models are depicted in Table 4.3.

Langmuir adsorption isotherm model, a non-linear model, assumes that all active sites on adsorbent are identical and that each adsorbate molecules binding energy for active sites is similar. This model also considers no interaction among adsorbate molecules, and only monolayer formation occurs (Ahsan et al., 2018). The values of K_L and Q_0 for Ce^{3+} adsorption was found to be 0.1841 (L/mg) and 86.206 (mg/g). The nature of adsorption process was determined from the value of R_L (separation factor). The favorable adsorption takes place when the R_L value > 0 to < 1, for unfavorable adsorption R_L value > 1, for linear and irreversible adsorption the R_L value = 1 and = 0. The value of R_L is 0.1062 which shows favorable adsorption process. The R^2 value (0.9769) of Ce^{3+} adsorption fit to the Langmuir isotherm model and it is found to be more significant on compare to other isotherm models for Ce^{3+} adsorption.

In contrast, heterogeneous surface and multilayer adsorption is suggested by the Freundlich isotherm model with unequal binding energy distribution and affinity between adsorbent and adsorbate molecules (Kumar et al., 2017). The calculated values of n and K_F are 3.481

and 26.199 (L/g). Unlike other adsorption models, Dubinin-Radushkevich (D-R) model is used to predict the type of adsorption, e.g., chemical or physical adsorption, and it does not assume a homogeneous surface or constant adsorption potential (Kilic et al., 2011).

Table 4.3. *Various isotherm parameters of Ce^{3+} adsorption onto Fe_3O_4/CAC adsorbent*

Isotherm Model	**Ce^{3+} adsorption**
Langmuir Isotherm	
Q_0 (mg/g)	86.206
K_L (L/mg)	0.1841
R^2	0.9769
Freundlich Isotherm	
K_F (L/g)	26.199
n	3.481
R^2	0.9697
Dubinin Radushkevich Isotherm	
q_m (mg/g)	75.452
β (mol^2/J^2)	0.0049
E (kJ/mol)	10.042
R^2	0.8665
Temkin Isotherm	
b_T (kJ/mol)	460.678
K_T (L/mg)	0.7939
R^2	0.9606

The apparent energy (E) depicts the mechanism of adsorption process. If E is between 1 to 16 kJ/mol it favors physisorption and E > 16 kJ/mol it favors chemisorption. In our case it is found to be theoretically physisorption (E=10.042 kJ/mol).

On the other hand, the Temkin isotherm model suggests that binding energy of adsorption, which is a function of temperature, of all molecules in the layer decline linearly rather than logarithmic with a surface coverage of adsorbent (Vishnu Priyan et al., 2021). The values of b_T and K_T was found to be 460.678 kJ/mol and 0.7939 L/mg. The regression value was found to be 0.9606 for Ce^{3+} adsorption.

4.2.4. Adsorption kinetics

Adsorption rate pertaining to the mechanism of adsorption is an essential parameter for determining the amount of Ce^{3+} biosorbed at a particular time interval on a adsorbent (Gao et al., 2021). Various kinetic models such as pseudo 1^{st} order, pseudo 2^{nd} order, Elovich and intra-particle-diffusion (Fig. 4.7 (b)) were investigated in this study to understand the better mechanism of adsorption of Ce^{3+} on MCAC. The various kinetic models and their equations were represented in the Table A2 (Appendix).

The Pseudo-first-order model assumes that the rate of change of adsorption depends on the free active sites available on the MCAC and the concentration of Ce^{3+} in the solution and on the MCAC surface (Patra et al., 2020). This model generally explains the physisorption mechanism and is considered valid for up to a certain interval of time; In other words, it suits the adsorption process only at the initial stage. The regression value is found to be 0.9467, which is comparatively high then pseudo 2^{nd} order (0.8821) and Elovich models (0.9172).

On the other hand, the pseudo 2^{nd} order model is considered to describe the chemisorption mechanism, where Ce^{3+} ions form chemical bonds with MCAC functional groups. Here, the rate-limiting step is the adsorption, which involves chemical interaction.

The nature of chemical adsorption (chemical reaction) mechanism was elucidated by Elovich model (Chandrasekaran et al., 2020). Elovich kinetic model is best applied for the adsorbents with heterogeneous surface.

Adsorption on porous adsorbent is better explained by the intra-particle diffusion model in which diffusibility of adsorbate is the rate-controlling step. The intraparticle diffusion

model removes the diffusion limitation present in the above models. The R^2 value for this model is found to be 0.9792 showing that intraparticle diffusion model was the most significant model to study the kinetics of Ce^{3+} adsorption on MCAC. The various kinetic parameters of these models were tabulated in the Table 4.4.

Table 4.4. *Various kinetic parameters of Ce^{3+} adsorption onto Fe_3O_4/CAC adsorbent*

Kinetics	**Ce^{3+} adsorption**
Pseudo-first-order model	
q_e (mg/g)	20.426
k_1 (1/min)	0.0292
R^2	0.9467
Pseudo-second-order model	
q_e (mg/g)	23.255
k_2 (g/mg min)	0.0016
R^2	0.8821
Elovich model	
α (g/mg min)	2.366
β (mg/g)	0.2271
R^2	0.9172
Intra-particle diffusion model	
k_i (mg/g min $^{1/2}$)	2.116
d	0.4534
R^2	0.9792

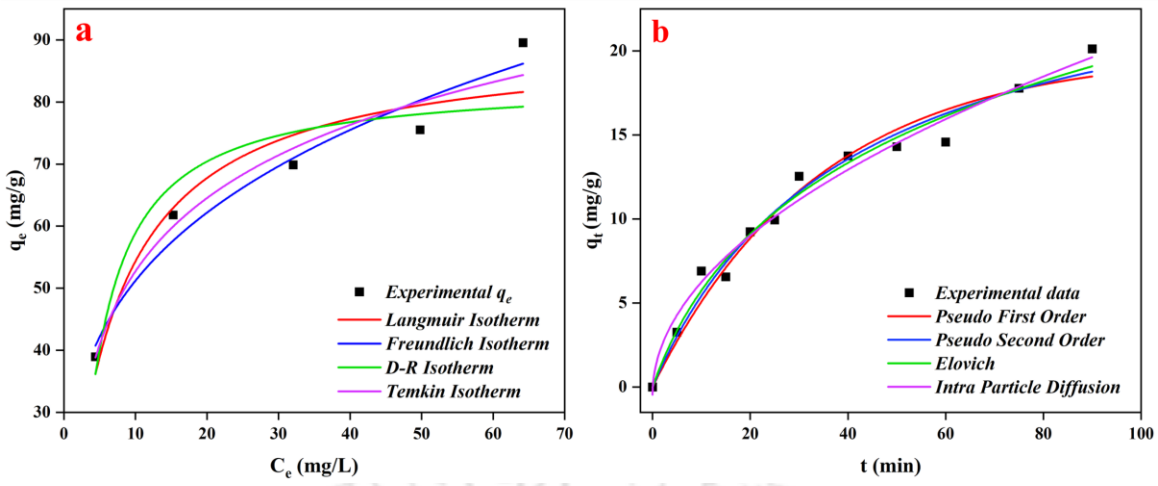

Fig. 4.7. a) *Isotherm models of Ce^{3+} adsorption on MCAC adsorbent and* ***b)*** *Kinetic models of Ce^{3+} adsorption on MCAC adsorbent*

4.2.5. Phytotoxicity studies

The various toxic effects on seeds of *Vigna mungo* (VM) and *Vigna radiata* (VR) before and after Ce^{3+} adsorption on MCAC was investigated in this study. The phytotoxicity was evaluated based on seed germination (%) (Fig. 4.8 (a)) and the growth inhibition of the seedlings (%) (Fig. 4.8 (b)) at 10-50 mg/L initial concentrations of Ce solution. For control, the seeds are soaked in distilled water without any Ce^{3+} ions in it. It is observed that the control groups show 100% germination for seeds of both plant species. The germination rate of seeds before Ce^{3+} adsorption was found to be 100%, 93.33%, 86.66%, 80% and 66.66% for *Vigna radiata* and 100%, 100%, 90%, 83.33% and 73.33% for *Vigna mungo* at different initial concentrations (10, 20, 30 ,40 and 50 mg/L). The reduction in rate of seed germination was due to the inhibition of certain enzymes, closure of stomata, metabolic pathways and damage in outer membrane of seeds by Ce^{3+} ions. After the adsorption process, we can notice that till 30 mg/L the seeds exhibit 100% germination in both plant species. At 40 mg/L and 50 mg/L of Ce initial concentration the rate of seed germination was found to be 96.66% (VR), 96.66% (VM) and 93.33% (VR), 86.66% (VM) respectively. Thus, adsorption removes the Ce^{3+} ions from the water and increases the germination % of seeds by decreasing the toxicity caused by Ce^{3+}. Moreira et al. (2019) reported that cerium exposure on various plant species such as corn, rice, wheat, sorghum, sunflower, radish, soybeans, and beans reduce their germination rate. The lowest observed effective concentration for corn was 144.5 mg Ce kg^{-1}. Cerium NPs exhibit very high toxicity for the

seeds of *Lactuca sativa, Cucumis sativus, Solanum lycopersicum and Spinacia oleracea* tested at the maximum stable concentration of 0.64 mg/mL (García et al., 2011) .

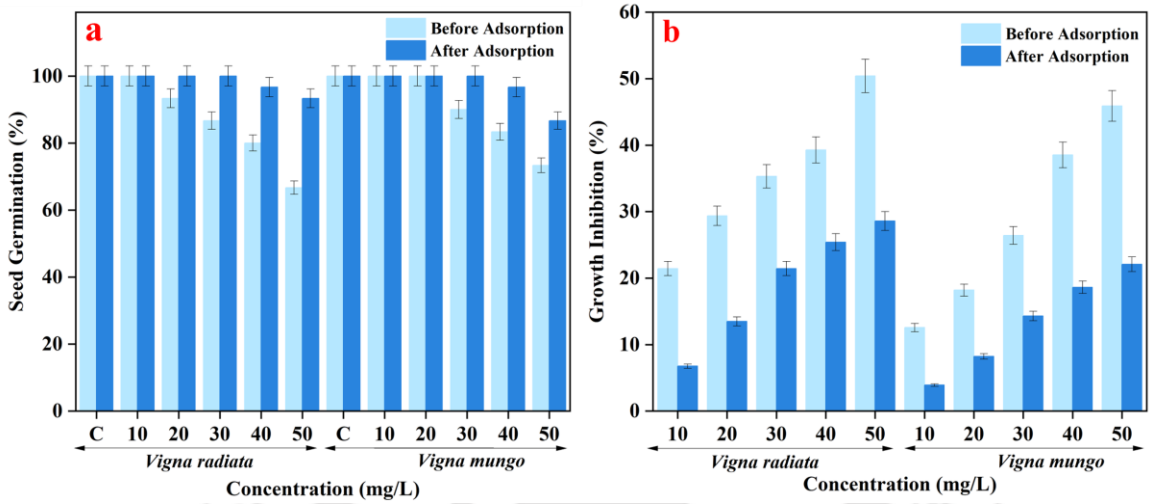

Fig. 4.8. a) *Seed germination (%) of Vigna mungo and Vigna radiata seeds at various concentrations of Cerium before and after adsorption, and* ***b)*** *Inhibition of growth (%) of Vigna mungo and Vigna radiata seeds at various concentrations of Cerium before and after adsorption*

Fig. 4.8 (b) represents growth inhibition (%) of seedlings of *Vigna mungo* and *Vigna radiata*. When the concentration of Ce^{3+} within the plant exceed optimal levels, it adversely affects the plant growth (i.e., it inhibits the growth of the plant). Thus, the high concentration induces the inhibition in growth of the plant by reduction in the length of the shoot and root of the plant. The reduction in the shoot and root length was due to inhibition of cytoplasmic enzymes and damage of cellular structures caused due to oxidative stress. Before adsorption of Ce^{3+} the growth of seedlings decreases as the concentration increases in dependent manner. Before adsorption at 10 to 50 mg/L concentration of Ce, the growth inhibition (%) was found to be 12.55%, 18.18%, 26.40%, 38.52%, 45.88% for VR and 21.42%, 29.36%, 35.31%, 39.28%, 50.39% for VM respectively. Similar results have been reported at 10-50 mg/L Ce concentrations, there is a significant decrease in the root length of *Allium cepa* L. on comparing with control. They also stated that at 5 mg/L concentration and above, the proliferation activity was decreased, leading to high cytotoxic effects on *Allium cepa* L. (Kotelnikova et al., 2019). High Ce^{3+} concentrations lead to ROS production and apoptosis which inhibits the growth of seedlings. However, this toxic effect on the vegetative growth of plants was mostly reported when the plants are exposed to high Ce^{3+}

concentrations, while at lesser concentrations it is beneficial for the growth of plants. The growth rate decreased to 64% compared to control on exposure of *Spirodela polyrhiza* L. at 60 μM Ce solution. It is also found that high Ce concentration will inhibit PS-II photochemical reaction in *S. polyrhiza* L. (Xu et al., 2017). After adsorption process, we can observe the reduction in inhibition of growth. This confirms that MCAC effectively removed the Ce^{3+} ions present in the water.

4.2.6. Acute fish toxicity studies

In this study, the toxicity levels of Ce^{3+} on zebra fish before and after adsorption on MCAC was evaluated through acute toxicity test (Fig. 4.9). For this, 110 healthy zebra fishes were taken and separated into 11 sets in individual fish tanks marking control (without Ce^{3+}), before treatment (Ce^{3+} before adsorption) and after treatment (Ce^{3+} after adsorption). The initial Ce^{3+} concentrations taken from 1mg/L to 5 mg/L in the interval of 1 mg/L. It is noticed that there is no mortality (death) of fishes in the control tank. The fishes in the control tank were active with usual swimming even after 96 h. But we can observe the abnormal behaviour in fish motility at 4 mg/L before treatment tank after 48 h. At the end of 96 h, about 20% of mortality is seen for 4mg/L. At the end of 96 h, 5 mg/L before treatment the mortality rate increases from 30% to 90%. The symptoms such as unusual swimming, rapid moving, lying at bottom were observed in the 5 mg/L tank before treatment. No mortality in zebra fish was observed to the experiment groups after treatment (after adsorption) till 4 mg/L. In 5 mg/L after treatment at 48 h mortality is about 10% and at 96 h the mortality increases to 20%. The concentrations of the pollutant in water that kills 50% of the test animals during the observation period is called as Lethal Concentration 50 (LC_{50}) value. After adsorption of Ce^{3+} by MCAC, the concentration of Ce^{3+} in the water will be low on comparison to the concentration Ce^{3+} in water before adsorption. So, the concentration of Ce^{3+} required to kill 50% of *Danio rerio* (LC_{50}) before adsorption process was 2.44 mg/L. But the LC_{50} value increases to 77.85 mg/L after adsorption because there will be less Ce^{3+} ions in water due to the adsorption of Ce^{3+} on MCAC. So, the required concentration of Ce^{3+} to kill 50% of *Danio rerio* after adsorption will be 77.85 mg/L. After adsorption process once the concentration of Ce^{3+} reaches to 77.85 mg/L, then the 50% of fishes from total population will be die. This confirms that MCAC effectively remove the toxic Ce^{3+} from the water allowing the fishes alive with normal behaviour and swimming. Chandra and Sukumaran (2020) reported that the LC_{50} value for *Cirrhinus mrigala* was

found to be 22 mg/L after 24 h of exposure. The LC_{50} value of cerium exposure on *D. magna* was found to be 0.012 mg/mL which shows even at very low concentrations cerium has great effect on aquatic organisms (García et al., 2011).

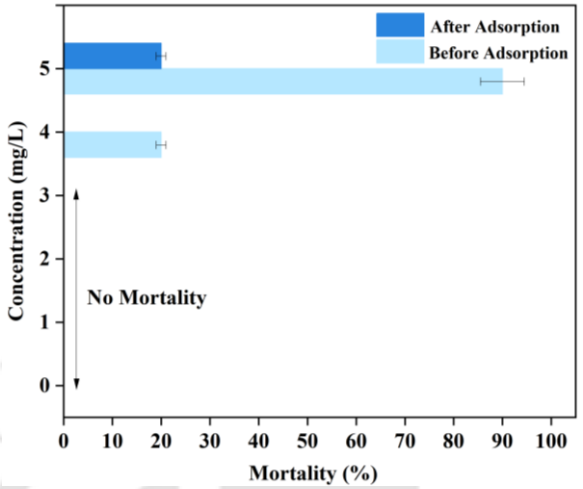

Fig. 4.9. *Mortality (%) of Danio rerio (zebra fish) to various concentrations of Ce before and after adsorption*

4.2.7. Regeneration studies

Regeneration experiments were carried out to determine the potential reusability of MCAC, which makes the adsorption process more economically feasible. Using 0.1 M NaOH as a desorbing agent, MCAC was desorbed after each cycle of adsorption. The removal efficiency at the first, second, third, fourth, and fifth cycles was 93.08%, 88.09%, 81.25%, 68.23% and 43.28% respectively (Fig. 4.10).

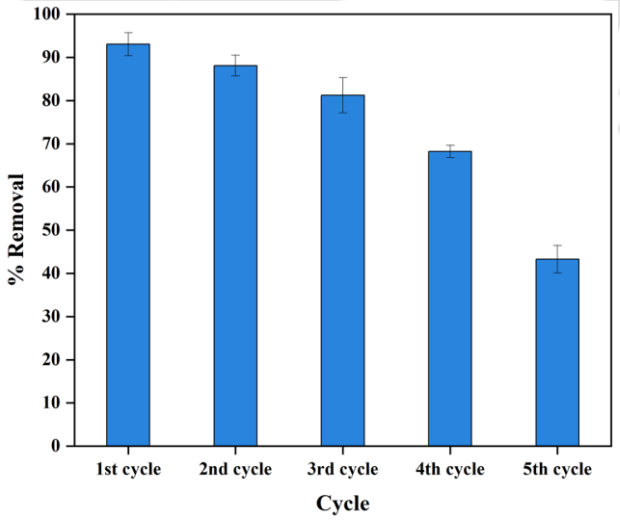

Fig. 4.10. *Regeneration studies of MCAC*

After 3 cycles, the removal efficiency of MCAC was less significant. These consecutive adsorption, desorption, and regeneration studies revealed that MCAC could be effectively reusable for up to 3 cycles. After desorption with 0.1 M NaOH, the presence of Ce^{3+} ion on the surface of MCAC limits this phenomenon. We can observe a gradual decrease in the biosorption capacity, which may be due to the structural change in MCAC. Therefore, we can conclude that MCAC can be effectively reused for series of adsorption-desorption cycles from the regeneration studies.

4.3. Significant findings

MCAC was prepared using coprecipitation of ferric and ferrous salts. The synthesised nanocomposite was subjected to different characterization techniques for determining their shape and size, which shows that MCAC was nano range in size with spherical Fe_3O_4 nanoparticles (30-50 nm) covering the CAC. The crystallinity of MCAC before and after adsorption of Ce^{3+} was found to be semicrystalline in nature containing both amorphous and crystalline regions. The magnetic nature of MCAC helps in the recovery of the adsorbent after adsorption process which plays an important role in separation of MCAC from water. The maximum removal of Ce^{3+} by MCAC was optimized at pH 6.0, initial concentration of 20 mg/L and 0.04 g/L of MCAC with adsorption capacity (Q_0) 86.206 mg/g. The behaviour of $Ce^{3+}$and MCAC were described by Langmuir isotherm and intra-particle diffusion kinetic model. The efficiency of the MCAC on Ce^{3+} removal at 120 mg of adsorbent was found to be 96.61%, which shows that the synthesised adsorbent was more effective in removing the pollutant present in the water. Ecotoxicological assessment was carried out with *Vigna mungo*, *Vigna radiata* and *Danio rerio*. Phytotoxicity studies revealed that before adsorption of Ce^{3+} the percentage of seed germination decreases as the concentration of Ce^{3+}increases. At 50 mg/L, the seed germination rate was found to be 66.66% for *Vigna radiata* and 73.33% for *Vigna mungo*. After adsorption we can observe drastic increase in seed germination % upto 93.33% for *Vigna radiata* and 86.66% for *Vigna mungo.* Acute mortality (%) was determined in *Danio rerio* at various concentrations of Cerium before and after adsorption. At the end of 96 h, 5 mg/L of Ce^{3+} (before adsorption) the mortality rate increases from 30% to 90%. The LC_{50} of Ce^{3+} on *Danio rerio* was found to be 2.44 mg/L. These findings inferred feasibility of the preparation of MCAC nanocomposite for the maximum effective removal (%) of Ce^{3+} from water.

Chapter 5

Toxicological assessment and adsorptive removal of Lead (Pb) and Congo Red (CR) from water by synthesized Iron oxide/Activated Carbon (Fe_3O_4/AC) nanocomposite

The work embodied in this chapter is published in

Vishnu Priyan V, Nitesh Kumar, Selvaraju Narayanasamy, 2022. Toxicological assessment and adsorptive removal of lead (Pb) and Congo red (CR) from water by synthesized iron oxide/activated carbon (Fe_3O_4/AC) nanocomposite. **Chemosphere**, 294, 133758, https://doi.org/10.1016/j.chemosphere.2022.133758 **(Elsevier; SCI IF 2023: 8.8).**

Abstract

Heavy metals and dyes are the persistent pollutants causing harmful effects on living organisms in different ecosystems. In current study, removal of Lead (Pb) and Congo Red (CR) from water was performed using Iron oxide/Activated Carbon (Fe_3O_4/AC) nanocomposite. Ferromagnetic behavior of the nanocomposite is the crucial advantage in separation of nanocomposite after biosorption process. The biosorbent was thermally stable till 800 °C of temperature. The synthesized biosorbent was polycrystalline in nature comprising of elements like C, O, Fe. The influence of various experimental conditions was optimized through batch study with the biosorption capacity of 144.92 mg/g (Pb) and 122.22 mg/g (CR) at pH 5.0-6.0, Fe_3O_4/AC dosage (0.04 g/L) for 40 mg/L of Pb and CR. Toxicological assessment was performed using *Danio rerio* and seeds to evaluate the harmful effects of pollutants on these organisms. The phytotoxicity results revealed that growth inhibition of seeds lies between 85.64% to 55.92% (Pb) and 77.94% to 51.85% (CR). The LC_{50} value of Pb on the *Danio rerio* was found to be 20.98 mg/L. These findings implied feasibility of the preparation of MSD for the efficient removal of DCF from water systems.

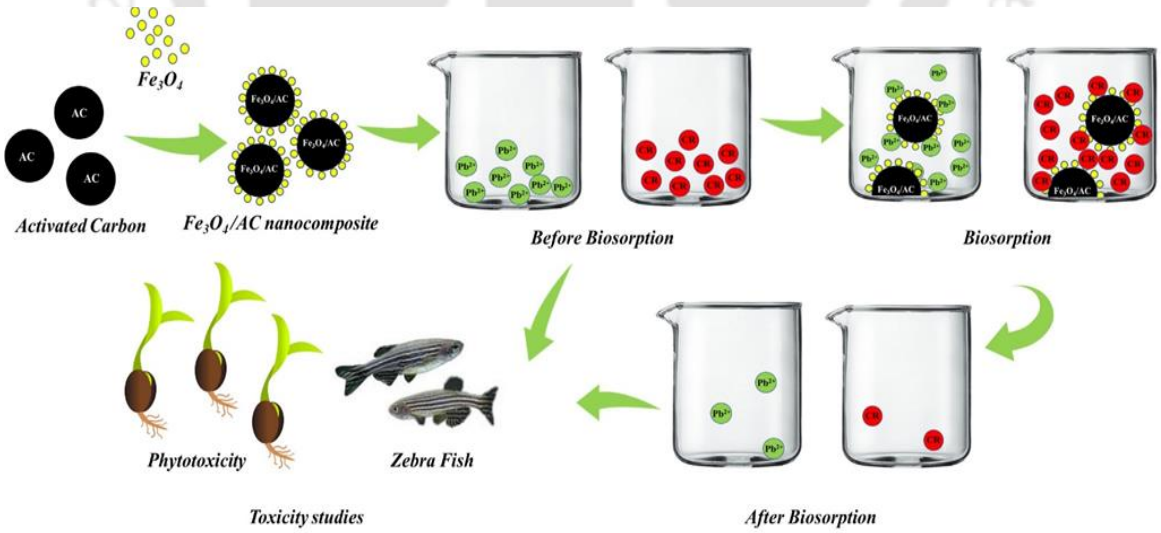

Graphical Abstract

5.1. Materials and methods

5.1.1. Chemicals and materials

To synthesis the Fe_3O_4/AC nanocomposite, the chemicals including $FeCl_3.6H_2O$, $FeSO_4.7H_2O$, NH_3 solution, and ethanol (absolute, ≥ 99.9%) were obtained from HiMedia. The stock solution sorbate was prepared from lead nitrate ($Pb(NO_3)_2$) and congo red dye ($C_{32}H_{22}N_6Na_2O_6S_2$) which was procured from Sigma-Aldrich. To regulate the pH of the solution 0.1 M NaOH (HiMedia) and 0.1 M HCl (SRL) were used.

5.1.2. Synthesis of Fe_3O_4/AC nanocomposite

At the first step of nanocomposite synthesis, biomass of *Prosopis juliflora* was collected from Coimbatore district of Tamil Nadu, India and washed with distilled water to remove all debris and dried at 100 °C for 36 h. The dried biomass was pulverized to fine powder and the powder was subjected to sieve to get uniform particles. Following this, the biomass was carbonized in the muffle furnace at 550 °C for 3 h. The obtained activated carbon (AC) was oven dried at 80 °C for further use.

At second step, $FeCl_3.6H_2O$ and $FeSO_4.7H_2O$ solutions were prepared in the molar ratio of 1:2 and to this, 1 g of AC was added under continuous stirring at the temperature of 80 °C for 3 h. Then, 10% ammonia solution was added drop by drop to the mixture by using a syringe. Then, the synthesized nanocomposite was recovered by magnet and washed with ethanol/distilled water (2:1) to eliminate the unreacted and excess materials. After washing, the obtained Fe_3O_4/AC nanocomposite was oven dried at 100 °C for 36 h and powdered by a mill for further use as biosorbent (Takmil et al., 2020).

5.1.3. Characterization of Fe_3O_4/AC nanocomposite

The detailed characterization of the Fe_3O_4/AC nanocomposite before and after biosorption of Pb and CR were investigated through various techniques provided in the Table A3 (Appendix)

5.1.4. Biosorption experiments

The biosorption of lead (Pb) and congo red dye (CR) were studied through batch experiments under different initial concentrations (20 to 100 mg/L) of the stock solution. 30 mL of stock solution was stirred at 150 rpm in a shaking incubator with the pH range of

2.0-10.0. By using 0.1 M HCl or 0.1 M NaOH the pH of the mixture was altered. To optimize the biosorbent dosage different amount of biosorbent ranging from 0.02-0.12 g/L was used. After biosorption, the residual Pb and CR concentration was determined using AES (405.781 nm), UV visible spectrophotometer (498 nm) (Chen and Qiu, 2021).

The amount of Pb and CR biosorbed per gram of Fe_3O_4/AC nanocomposite was calculated from the following expression

$$q_e = \frac{(C_0 - C_e)}{m} \times V \quad (5.1)$$

The removal efficiency of Pb and CR was determined by following equation

$$Removal\ (\%) = \frac{C_0 - C_e}{C_0} \times 100 \quad (5.2)$$

where q_e is the amount of pollutant biosorbed at equilibrium time (mg/g), C_0 and C_e are the initial and equilibrium pollutant concentrations (mg/L), m and V were the mass of the Fe_3O_4/AC nanocomposite (g) and the volume of Pb and CR solution (L).

5.1.5. Phytotoxicity experiments

The seed toxicity studies of Pb and CR before and after biosorption on Fe_3O_4/AC nanocomposite was investigated using the seeds of *Pennisetum glaucum* (PG), *Cicer arietinum* (CA), *Vigna mungo* (VM) and *Vigna radiata* (VR). The experiments for seed toxicity were done using the protocol of (Vishnu Priyan et al., 2021) with minor modifications. These experiments were carried out in Petri dishes at ambient temperature. The effect of seed toxicity was measured after seven days in terms of growth inhibition (%) and seed germination (%) of the seedlings. By using 0.1% sodium hypochlorite solution and deionized water the seeds were rinsed to avoid the fungal and yeast contamination. The sterilized seeds were subjected to toxicity analysis by adding the seeds to the Petri dishes containing the Pb and CR solutions before and after biosorption process. The Pb and CR solutions were prepared in different concentrations (10, 30 and 50 mg/L) and distilled water is used as control. Then the seeds in Petri dishes were placed in dark for seven days. After seven days, the seedlings were subjected to toxicity analysis.

5.1.6. Acute fish toxicity experiments

Zebra fish (*Danio rerio*) was selected as the model organism to perform acute fish toxicity test. This test as performed as per the test guideline number 203 of OECD. Fishes with

same age and size were selected to perform experiments. Various concentrations of Pb and CR solutions (1, 5, 10, 15, 20, 25, 30, 40, 50 mg/L) were prepared and named as untreated solutions (before biosorption). The oxygen concentration (>75%), pH (6.5-7.5), light period (14 h light: 10 h dark) and temperature (25 °C) were maintained constant throughout the experiments. Ten healthy fishes were taken for each experiment. Totally, 20 experiments were performed with various untreated and treated solutions of Pb and CR. The water without Pb and CR was taken as control. At the end of 96 h total number of alive and dead fishes was recorded and the percentage of mortality was calculated (Shahnaz et al., 2021).

5.1.7. Desorption and reusability studies

In short, 0.1 g of synthesized Iron oxide/Activated Carbon (Fe_3O_4/AC) nanocomposite was added into 100 mg/L of Pb and CR solution and kept in a shaking incubator at 150 rpm at 303 K for 5 h. After 5 h Fe_3O_4/AC nanocomposite was separated using magnet from Pb and CR solutions. The amount of Pb and CR after adsorption onto Fe_3O_4/AC nanocomposite was detected using Atomic Emission Spectroscopy and UV-Visible spectrometer. Then, the collected adsorbent was treated with sodium hydroxide (1 M) for 4 h. After the treatment with NaOH, the Fe_3O_4/AC nanocomposite was rinsed with distilled water for several times to eliminate the residual sodium hydroxide. The rinsed Fe_3O_4/AC nanocomposite was dried in oven and used for further cycle of experiments. 5 cycles of experiments were performed in similar way.

5.2. Results and discussion

5.2.1. Characterization of Fe_3O_4/AC nanocomposite

5.2.1.1. Morphology analysis

The surface morphologies of activated carbon and Fe_3O_4/AC nanocomposite were examined by FESEM and the micrographs were shown in the Fig. 5.1. (a-d). As shown in Fig. 5.1. (a) the surface of the AC is smooth and forms a layered structure. From the Fig. 5.1. (c) and (d) the surface of Fe_3O_4/AC nanocomposite is relatively rough due to the impregnation of iron oxide. The impregnation leads to the formation of spongy pore structure. The size of the formed crystallites of Fe_3O_4/AC nanocomposite was measured lesser than 50 nm. The Fe_3O_4/AC nanocomposite produced by the chemical coprecipitation

method will be in smaller size due to the ferocious agitation by magnetic stirrer, which enhances the distribution of Fe_3O_4 particles onto AC.

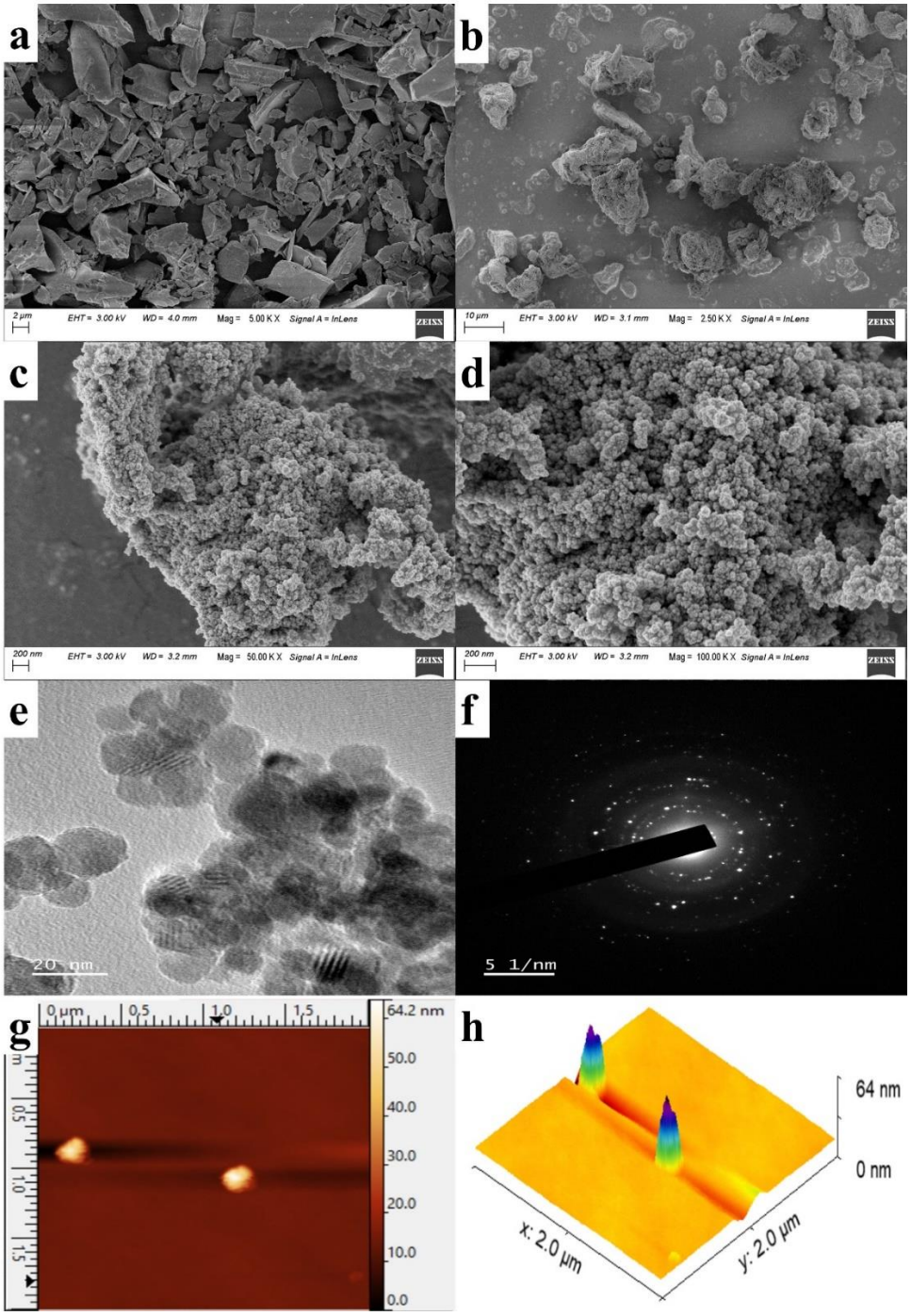

Fig. 5.1. *FESEM micrographs at different magnifications* ***a)*** *AC (5.00 KX),* ***b)*** *Fe_3O_4/AC nanocomposite (2.50 KX),* ***c)*** *Fe_3O_4/AC nanocomposite (50.00 KX),* ***d)*** *Fe_3O_4/AC nanocomposite (100.00 KX),* ***e)*** *FETEM image of Fe_3O_4/AC nanocomposite,* ***f)*** *SAED image of Fe_3O_4/AC, AFM micrographs of Fe_3O_4/AC* ***g)*** *2-Dimensional and* ***h)*** *3-Dimensional image*

FETEM image (Fig. 5.1. (e)) of the synthesized Fe_3O_4/AC nanocomposite depicted that the iron oxide nanoparticles were evenly distributed on the surface of the AC, which favors the magnetism of Fe_3O_4/AC nanocomposite. The FETEM images also showed that the size of Fe_3O_4/AC nanocomposite is less than 30 nm which confirms the results of FESEM. Fig. 5.1. (f) shows the selected area electron diffraction (SAED) pattern of the Fe_3O_4/AC nanocomposite which shows the nanocomposite comprises of both amorphous and crystalline regions in it.

5.2.1.2. AFM analysis

The various characteristics such as shape, size and surface roughness of Fe_3O_4/AC nanocomposite was depicted through AFM. The 2D and 3D images of Fe_3O_4/AC is represented in the Fig. 5.1. (g) and (h). It is seen that brighter peaks represents the nodules which are clear and not merged. The darker depressions represent the pores (Priyan et al., 2020). The difference in height was found to be 64 nm. The different roughness parameters such as average roughness (R_a), RMS roughness (R_q), average maximum height of roughness (R_z), maximum roughness valley depth (R_v) and maximum roughness peak height (R_p) were calculated and found to be 1.038 nm, 3.438 nm, 64.17 nm, 14.33 nm and 49.84 nm respectively.

5.2.1.3. EDX analysis

The chemical characterization of the AC, Fe_3O_4/AC, Fe_3O_4/AC-Pb and Fe_3O_4/AC-CR was determined by using energy dispersive X-ray spectroscopy (EDX), which was coupled with FESEM. A beam of high energized charged particles was irradiated on the surface of the sample which causes excitation of electrons producing characteristic X-rays specific for each element. It is found that AC (Fig. 5.2. (a)) consists of carbon (80.1 wt.%) and oxygen (19.9 wt.%). In Fe_3O_4/AC nearly 37.4 wt.% of Fe and 33.0 wt.% of O were present due to the process of magnetization of AC.

The result of EDX spectra of Fe_3O_4/AC (Fig. 5.2. (b)) reveals that the iron oxide particles are present homogenously on the surface of the AC. The presence of sulphur in the Fig. 5.2. (c) was due to the biosorption of CR upon the Fe_3O_4/AC. We can see Pb (2.5 wt.%) in the EDX spectra (Fig. 5.2. (d)), due to the biosorption of Pb by Fe_3O_4/AC. The peak of Fe, C and O in the EDX spectra of Fe_3O_4/AC, Fe_3O_4/AC-Pb and Fe_3O_4/AC-CR confirms the presence of iron oxide particles on AC to form nanocomposite. The weight percentage of

the elements present in AC, Fe_3O_4/AC, Fe_3O_4/AC-Pb and Fe_3O_4/AC-CR were represented in the Table 5.1.

Table 5.1. *Weight percentage of the elements present in AC, Fe_3O_4/AC, Fe_3O_4/AC-Pb and Fe_3O_4/AC-CR*

Sample Name	Elements (Wt. %)				
	Carbon (C)	Oxygen (O)	Iron (Fe)	Sulphur (S)	Lead (Pb)
AC	80.1	19.9	-	-	-
Fe_3O_4/AC	29.6	33.0	37.4	-	-
Fe_3O_4/AC-Pb	29.6	27.3	40.6	-	2.5
Fe_3O_4/AC-CR	32.8	22.3	44.7	0.2	-

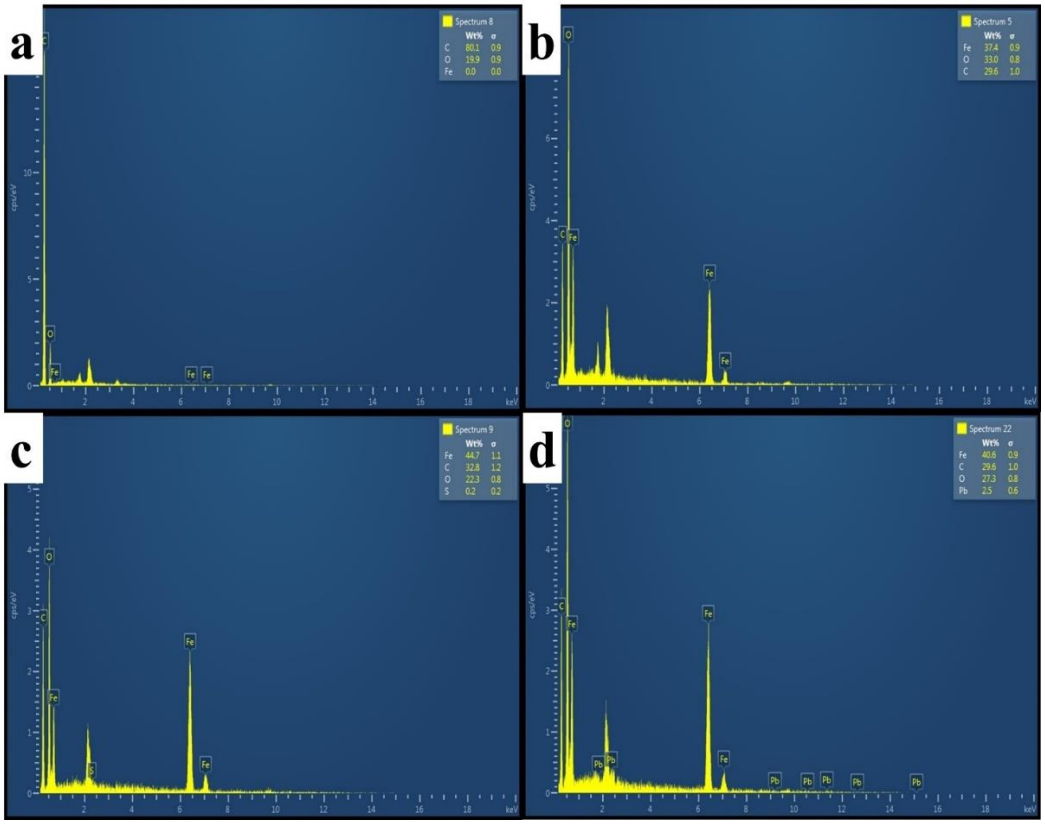

Fig. 5.2. *EDX image of a) AC, b) Fe_3O_4/AC, c) Fe_3O_4/AC-CR and d) Fe_3O_4/AC-Pb*

5.2.1.4. XRD analysis

The phase purity and crystallinity of the AC, Fe_3O_4/AC nanocomposite before and after biosorption of Pb and CR was investigated by XRD. The Fig. 5.3. shows the diffraction

pattern of the samples, in which the peak at 2 theta about 24.2° of AC confirms the amorphous nature of the carbon. Also, the peak at 28° denotes the fluffy structure of the AC. The similar peak at 2 thetas about 24° and 28° was reported by (Feng et al., 2020). We can observe the characteristic peaks of Fe_3O_4 (magnetite) at 30.26°, 35.65°, 43.28°, 53.79°, 57.12°, 62.81°. These six individual peaks agree with 220, 311, 400, 422, 511 and 440 planes of magnetite (Danalıoğlu et al., 2017). In Fe_3O_4/AC nanocomposite, the sharper peaks were formed due to the magnetization process of AC. Higher the intensity of the peaks higher the magnetic strength of the crystallites (Venkateswarlu et al., 2020). The carbon peaks were not found in Fe_3O_4/AC, Fe_3O_4/AC-CR, Fe_3O_4/AC-Pb because of the high crystallinity of the Fe_3O_4 particles on the AC.

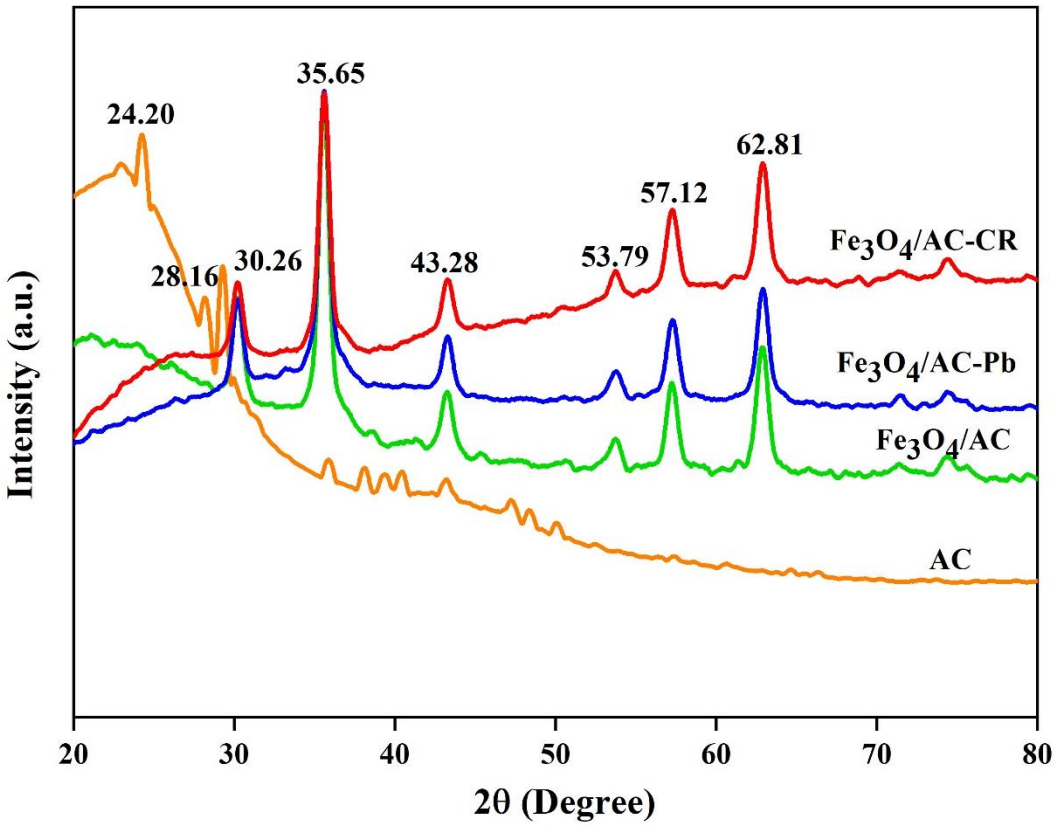

Fig. 5.3. *XRD analysis of AC, Fe_3O_4/AC, Fe_3O_4/AC-CR and Fe_3O_4/AC-Pb showing 2 theta peaks explaining crystallinity*

5.2.1.5. FTIR analysis

The FTIR analysis was done for AC, Fe_3O_4/AC, Fe_3O_4/AC-Pb and Fe_3O_4/AC-CR to determine the functional groups as shown in Fig. 5.4. (a). The weak peak at 3750 cm^{-1}

attributed to NH_2 group due to the presence of small amount of amine compounds in the biomass of *Proposis juliflora*. The broad peak between 3615-3035 cm^{-1} which corresponds to stretching vibrations of O-H group (Wang et al., 2020). In the FTIR spectra of AC we can observe the sharp peaks at 1698, 1588, 1437, 1373, 1213, 871, 807 and 753 cm^{-1} respectively. The band at 1698 cm^{-1}, denotes the C=O bonds of carbonyl compounds such as aldehydes, ketones and carboxylic acids in vibrational stretching mode (Ebadollahzadeh and Zabihi, 2020).

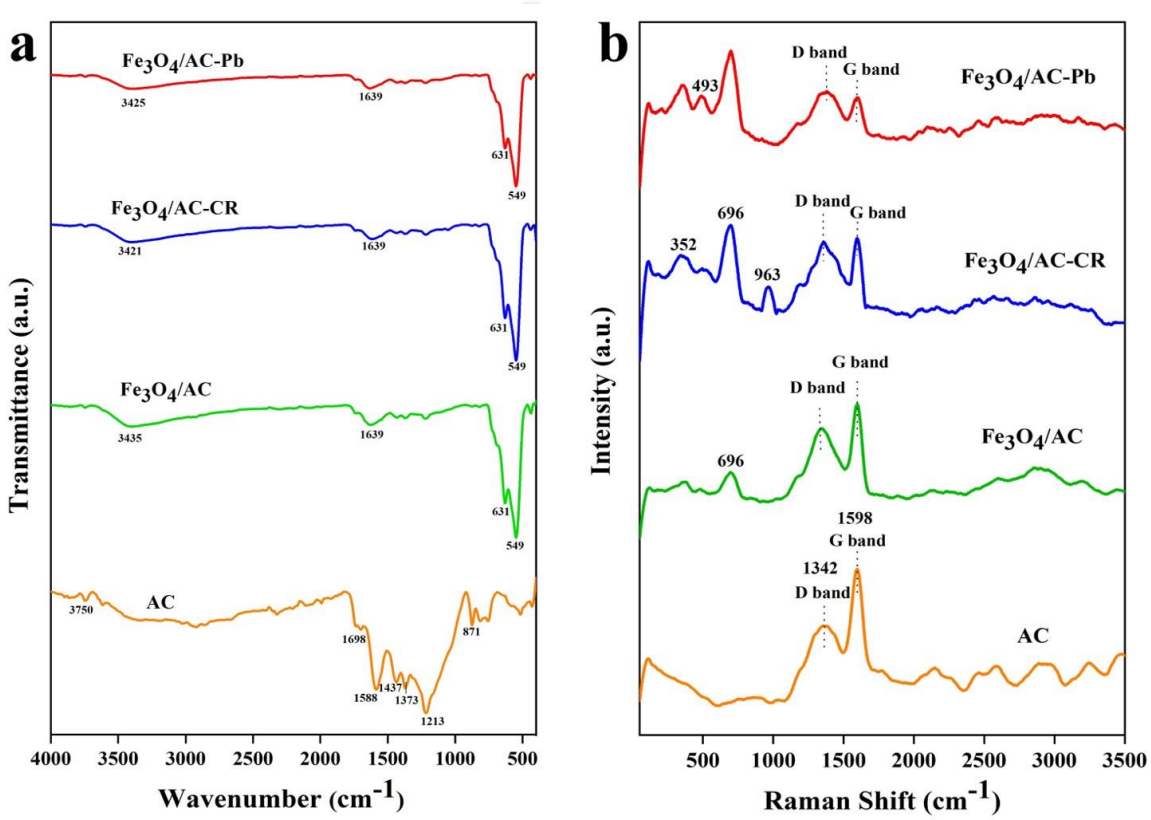

Fig. 5.4. a) *FTIR analysis and* ***b)*** *Raman spectra of AC, Fe_3O_4/AC, Fe_3O_4/AC-CR and Fe_3O_4/AC-Pb*

The bands at 1588 and 1437 cm^{-1} corresponds to the out-phase and in-phase stretching vibrations of CO_2. The peak at 1588 cm^{-1} is very strong than the in-phase band at 1437 cm^{-1}. The medium peak at 1373 cm^{-1} attributed to CH_3 in-phase bending and the peak at 1213 cm^{-1} assigned to C-C vibration mode. The peaks at 871, 807 and 753 cm^{-1} were due to the C-O-C stretching vibrations of carbonyl compounds such as esters and anhydrides (Sharma et al., 2020). The band at 753 cm^{-1} also be due to C-O bond of alcohol. The spectra of Fe_3O_4/AC, Fe_3O_4/AC-Pb and Fe_3O_4/AC-CR showed two strong peaks at 631 and 549 cm^{-1}

^{1}, which corresponds to the stretching vibration of Fe-O bond of Fe_3O_4 (D'Cruz et al., 2020). These characteristic peaks confirm the presence of iron oxide in the composite.

5.2.1.6. Raman analysis

The structural deformations of AC, Fe_3O_4/AC nanocomposite before and after biosorption of Pb and CR was studied using Raman spectroscopy. From the Fig. 5.4. (b) we can observe the two characteristic bands of carbon namely D band at 1342 cm^{-1} and G band at 1598 cm^{-1} (Spessato et al., 2020). The D-band is due to the structural disorder of graphitic domains caused due to the disorder in aromatic rings. The characteristic G-band appears due to the symmetrical nature which occurs in all sp^2 hybridized carbons (Queiroz et al., 2020). These D and G bands were present in AC, Fe_3O_4/AC nanocomposite before and after biosorption of Pb and CR. But it is seen that the intensity of G-band decreases after the biosorption process and there is a slight shift on the D and G bands due to the interactions of Fe on AC. The total number of defective sites in AC is proportional to the I_D/I_G of D and G bands, which reveals that the ratio is high, the degree of graphitization will be low (Abbas et al., 2020). The characteristic bands of Fe-O-Fe bond was observed at 352 cm^{-1}, 493 cm^{-1} and 696 cm^{-1} (D'Cruz et al., 2020). The peak at 963 cm^{-1} for Fe_3O_4/AC-CR was due to the aromatic ring of benzene in the structure of congo red dye.

5.2.1.7. Thermal stability analysis

TGA is used to examine the thermal stability of the synthesized Fe_3O_4/AC nanocomposite. The TGA thermogram (20 °C- 1000 °C) of Fe_3O_4/AC nanocomposite was shown in the Fig. 5.5. (a). In TGA the properties of the sample were altered by heat produced at high temperatures. The process like dehydration, oxidation and decomposition alters the mass of the Fe_3O_4/AC (Vishnu Priyan et al., 2021). From the Fig. 5.5. (a) it is illustrated that the Fe_3O_4/AC shows very good thermal stability at higher temperatures. At the initial stage, a loss of 3.47% of total weight at temperature of 100 °C was due to the humidity present in Fe_3O_4/AC. At a temperature about 250 °C, we can observe a small weight loss (8.17%) due to evaporation of rigidly bound water and thermal degradation of cellulose and hemicellulose from Fe_3O_4/AC (Jain et al., 2018). As the temperature increases the mass of the Fe_3O_4/AC decreases due to gasification of C atoms. At the temperature about 800 °C the decomposition starts to occur rapidly. The DTG peaks at 103 °C, 556 °C and 910 °C illustrates that the degradation occurs in 3 distinct stages. At the temperature of 1000 °C

the residual mass is found be 38.28% which might be due to the presence of non-degraded iron oxide and carbon residues. The surface area of the Fe_3O_4/AC nanocomposite before and after adsorption of Pb and CR was investigated using surface area and pore size analyzer. Results revealed that specific surface area (m^2/g) of Fe_3O_4/AC nanocomposite before adsorption of Pb and CR was found to be 632 m^2/g and after adsorption process the specific surface area of Fe_3O_4/AC nanocomposite reduces to 406 m^2/g (Pb) and 452 m^2/g (CR) adsorption.

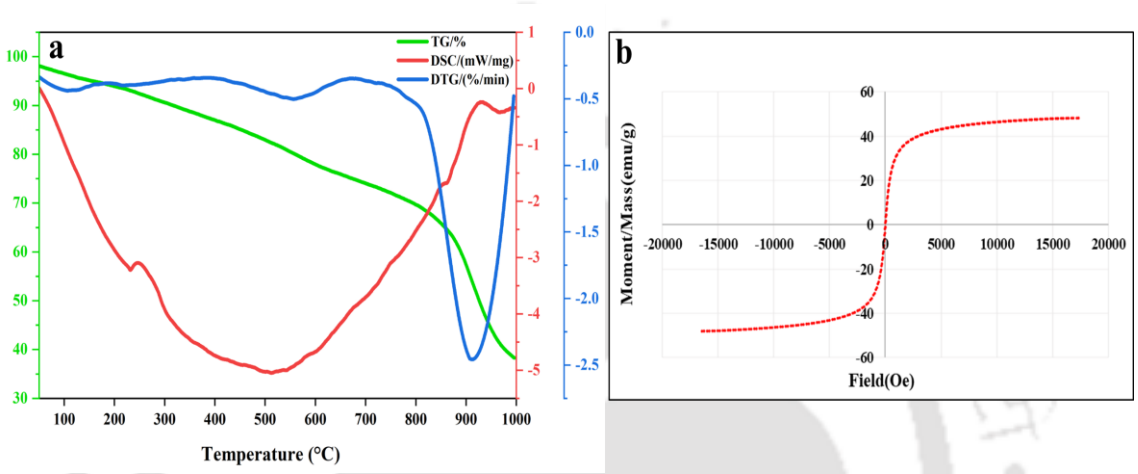

Fig. 5.5. a) *TGA/DSC image of Fe_3O_4/AC nanocomposite,* ***b)*** *VSM analysis of Fe_3O_4/AC nanocomposite for evaluating the magnetic behaviour*

5.2.1.8. VSM analysis

The magnetization of the activated carbon was studied using vibrating sample magnetometer. A graph between Field (Oe) and Moment/mass (emu/g) was plotted as shown in Fig. 5.5. (b). The magnetic saturation (maximum magnetic strength) of Fe_3O_4/AC nanocomposite was found to be 48.098 emu/g, which was in agreement with the values of magnetic saturation of Fe_3O_4/AC (52.2 emu/g) reported by (Jain et al., 2018). The magnetic saturation of the pure Fe_3O_4 was predicted as 92 emu/g. The saturation magnetization of the nanocomposite was quite lesser due to the presence of carbon on comparison with pure Fe_3O_4. The coercivity (H_{ci}) is found to be 18.068 Oe (1.8068 mT) which indicates the ferromagnetic nature of the biosorbent (Fe_3O_4/AC nanocomposite). The retentivity (Mr) is found to be 1.3010 emu/g. The Fe_3O_4/AC nanocomposite have high magnetic saturation value which make them rapid response to external magnetic field, thus helps in fast separation process from the solution (Danalıoğlu et al., 2017).

5.2.2. Effect of various parameters on biosorption

5.2.2.1. Effect of pH on biosorption

A very important parameter which affects the process of biosorption of Pb, CR on Fe_3O_4/AC nanocomposite is pH of the solution as it influences chemical properties of sorbent and sorbate. To study the influence of pH on Pb and CR biosorption, different pH of the solutions (2.0-10.0) was taken. Zeta potential was performed to analyse the PZC (point of zero charge) of Fe_3O_4/AC nanocomposite at various pH 2.0 to 10.0. The pH PZC for Fe_3O_4/AC nanocomposite was found to be 5.7. It illustrates that the Fe_3O_4/AC nanocomposite surface was positive at pH below 5.7 and above pH 5.7 the surface was negative. The surface of Fe_3O_4/AC nanocomposite is positive in acidic condition which leads to the electrostatic repulsion between the Fe_3O_4/AC nanocomposite surface and Pb. At pH above 5.7 the surface of Fe_3O_4/AC nanocomposite is -ve promoting higher adsorption of Pb.

As the pH of the Pb solution increases the removal efficiency of Pb also increases gradually till pH 6.0 and above pH 7.0 the Pb precipitates to its salt form thus the removal efficiency of the biosorbent cannot be predicted. The formation of the salt does not happen at lower pH. So, the pH below 6.0 will be the suitable pH for the biosorption of Pb. In case of CR biosorption the removal efficiency increases as the pH of the CR solution increases. Suddenly, the efficiency decreases at pH 7.0 and we can observe the gradual decrease in the removal efficiency till pH 10.0. At lower pH (4.5-6.0) the colour of CR changes due to amino group protonation. At pH above 6.0, most of the CR molecules are predominantly in deprotonated form. So, due to protonation the CR molecules are more anionic leading to higher adsorption at pH 5.0-6.0. The maximum biosorption capacity about 79.38 mg/g for Pb biosorption at pH 6.0 and 38.60 mg/g for CR biosorption was seen at pH 5.0-6.0 (Fig. 5.6. (a)). The removal efficiency of Pb biosorption increases from 6.58% to 26.46% at pH 6.0. As the pH increases from 2.0 to 6.0 the removal efficiency of CR biosorption also increased and maximum removal efficiency was found at pH 5.0-6.0 with nearly 85.78% removal. The pH of the Pb and CR solution effects the surface charge of Fe_3O_4/AC nanocomposite. At the lower pH, the protonation effect is more, which promotes high biosorption capacity (Sharma et al., 2020).

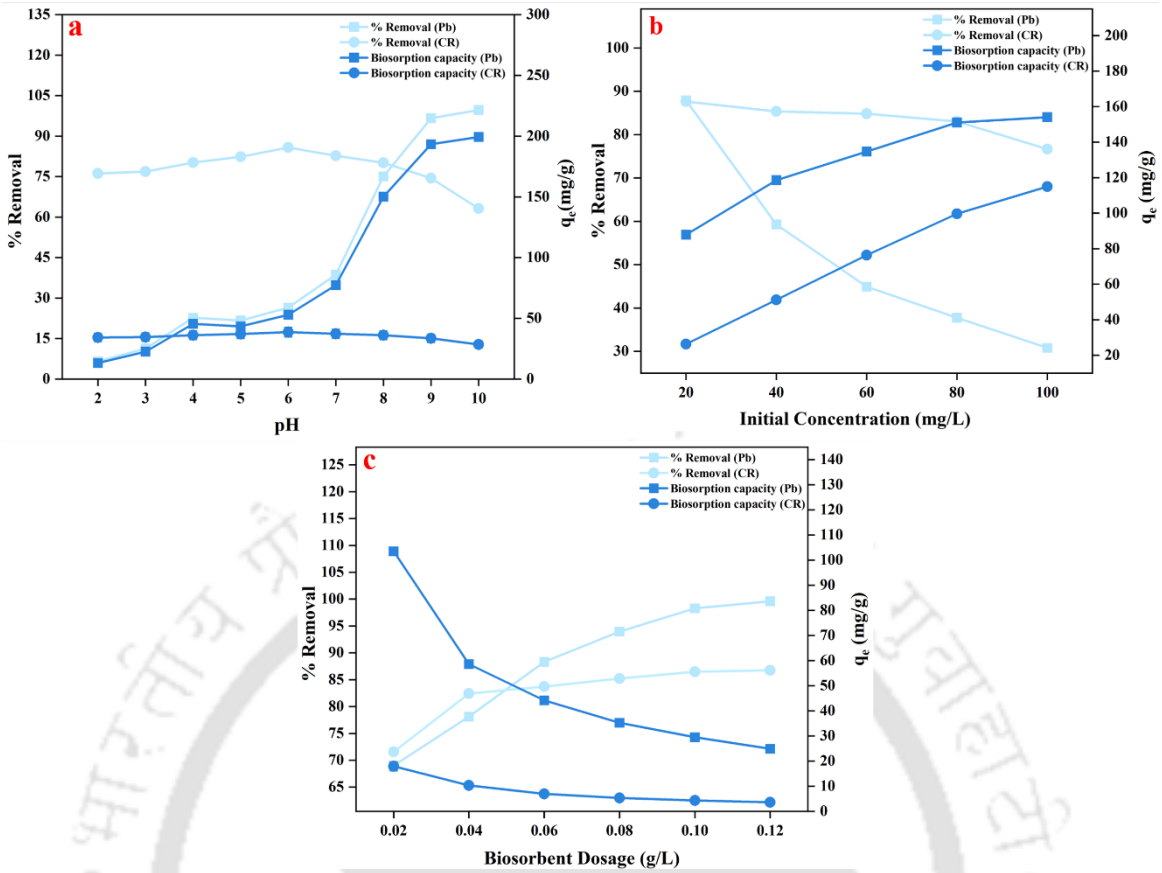

Fig. 5.6. a) *Effect of pH on biosorption of Pb and CR by Fe_3O_4/AC at various pH ranging from pH 2.0-10.0,* ***b)*** *Effect of initial Pb and CR concentration on biosorption of Pb and CR by Fe_3O_4/AC at different concentrations of Pb and CR ranging from 20-100 mg/L and* ***c)*** *Effect of biosorbent dosage on biosorption of Pb and CR by Fe_3O_4/AC at different dosage of Fe_3O_4/AC ranging from 0.02 to 0.12 g/L*

5.2.2.2. Effect of initial concentration of Pb and CR solution

The influence of initial concentration on Pb and CR biosorption (Fig. 5.6. (b)) was performed using Pb and CR solutions of different concentrations (20-100 mg/L). As the concentration of Pb and CR solutions increases, we can observe the increase in biosorption capacity from 87.90 mg/g to 154.10 mg/g for Pb biosorption and 26.28 mg/g to 115.01 mg/g for CR biosorption. The percentage of removal efficiency decreases as the biosorption capacity increases from 87.90% to 30.82% for Pb biosorption and 87.62% to 76.67% for CR biosorption. The initial concentration of the solutions was affected by the dynamic interactions between the sorbate and sorbent. An adequate sorption environment was seen at high initial concentration of Pb, CR solutions and a strong biosorption driving force between the sorbent and sorbate overcomes the mass transfer resistance (Patra et al., 2020).

Higher Pb, CR removal percentage was seen at 20 mg/L initial concentration and lower Pb, CR removal efficiency was observed at 100 mg/L initial concentration of solutions. Due to high amount of sorbate molecules (Pb and CR) than the sorbent (Fe_3O_4/AC nanocomposite) at high initial concentration leads to decrease in efficiency of removal.

5.2.2.3. Effect of Fe_3O_4/AC nanocomposite dosage

The influence of Fe_3O_4/AC nanocomposite dosage on biosorption was performed with different dosage ranging from 0.02 - 0.12 g/L with constant temperature, pH and initial concentration. From the Fig. 5.6. (c) we can observe that as the dosage of Fe_3O_4/AC nanocomposite increases, the efficiency of removal of Pb, CR also increased from 69.02% to 99.61% for Pb and 71.58% to 86.77% for CR. Whereas, we can see the decrease in biosorption capacity (q_e) from 103.53 mg/g to 24.90 mg/g for the Pb biosorption and 17.90 mg/g to 3.62 mg/g for CR biosorption. As the dosage increases, the removal efficiency of Pb and CR also increases because of large number of active sites in biosorbent attracts a greater number of Pb and CR. The attraction between sorbate and sorbent leads to strong sorbent/sorbate interactions, which increases removal efficiency. The maximum biosorption capacity was seen at low biosorbent dosage due to the complete exposure of diffusion sites (Priyan et al., 2020).

5.2.3. Biosorption isotherms

The biosorption process was investigated through theoretical graphs called biosorption isotherms which is the function of increase in pollutant (adsorbate) concentration at a constant temperature. Various parameters including biosorption capacity, nature of biosorption process (physical or chemical) of the Fe_3O_4/AC nanocomposite was determined by various isotherm models (Fig. 5.7 (a) and (b)). The biosorption process parameters of different isotherm models are depicted in Table 5.2.

5.2.3.1. Langmuir isotherm

The Langmuir isotherm model describes the monolayer biosorption of Pb and CR onto the surface of Fe_3O_4/AC nanocomposite which have fixed number of sites for biosorption. In Langmuir model, the process of transmigration of the Pb and CR molecules in the Fe_3O_4/AC nanocomposite surface plane is absent. The maximum sorption capacity of biosorbent is calculated as monolayer coverage in the model. The Q_0 for the biosorption of

Pb and CR was found to be 144.92 and 122.22 (mg/g). The nature of biosorption process was determined from the value of R_L (separation factor). The favorable biosorption takes place when the R_L value > 0 to < 1, for unfavorable biosorption R_L value > 1, for linear and irreversible biosorption the R_L value = 1 and = 0 (Chandrasekaran et al., 2020). The value of R_L is 0.0352 (for Pb biosorption) and 0.2754 (for CR biosorption), which shows favorable biosorption. The R^2 value (0.9971) of CR biosorption fit to the Langmuir isotherm model and it is found to be more significant on compare to other isotherm models for CR biosorption.

5.2.3.2. Freundlich isotherm

Freundlich isotherm model assumes that the biosorption process occurs in a heterogeneous multilayer surface. It also shows the exponential distribution of multilayer biosorption active centers with their energies (Patra et al., 2020). Freundlich isotherm constant (K_F, (L/g)) for biosorption of Pb and CR are 74.900 and 15.125. The value of 1/n is nearly zero for the higher concentration of the Pb and CR. Hence at very high concentration of adsorbate, the biosorbent potential of the biosorbent becomes independent of the biosorbent dosage. The value of n for Pb and CR biosorption was found to be 5.824 and 1.456, which represents the degree to which biosorption deviates from linearity. The regression value (R^2) of Pb and CR biosorption was found to be 0.9925 and 0.9700 respectively. The R^2 value of Pb biosorption fit to the Freundlich model and it is found to be more significant on compare to other isotherm models for Pb biosorption.

5.2.3.3. Dubinin-Radushkevich (D-R) isotherm

D-R isotherm model describes the mechanism of biosorption on heterogeneous surface with Gaussian energy distribution. This model is best suited for intermediate range of adsorbate concentrations due to the exhibition of unrealistic asymptotic behavior and absence to predict the Henry's law at very low pressure (Mate and Mishra, 2020). Here the biosorption process follow the pore filling mechanism. This model is used to predict whether the mechanism of biosorption is physical or chemical. The value of apparent energy (E) depicts the mechanism of Pb and CR biosorption process. If E is between 1 to 16 kJ/mol it favors physisorption and E > 16 kJ/mol it favors chemisorption. The apparent energy (E) for Pb and CR biosorption was found to be 9.559 kJ/mol and 10.042 kJ/mol which favors theoretically physisorption for both Pb and CR.

Table 5.2. *Various isotherm parameters of Pb and CR biosorption onto Fe_3O_4/AC nanocomposite*

Isotherm Model	Pb Biosorption	CR Biosorption
Langmuir Isotherm		
Q_0 (mg/g)	144.92	122.22
K_L (L/mg)	0.6160	0.0540
R^2	0.9165	0.9971
Freundlich Isotherm		
K_F (L/g)	74.900	15.125
n	5.8240	1.456
R^2	0.9925	0.9700
Dubinin Radushkevich Isotherm		
q_m (mg/g)	139.714	94.273
β (mol^2/J^2)	0.0054	0.0049
E (kJ/mol)	9.559	10.042
R^2	0.8121	0.8763
Temkin Isotherm		
b_T (kJ/mol)	574.82	363.61
K_T (L/mg)	1.7847	1.1927
R^2	0.9434	0.9631

5.2.3.4. Temkin isotherm

The indirect biosorbent/adsorbate interactions were depicted by Temkin isotherm model. It assumes that as the surface increases there is a linear decrease in the heat of biosorption

(ΔH) of all the molecules (Abutaleb et al., 2020). This isotherm model is valid only for the intermediate concentration range of the adsorbate solutions. The values b_T for the biosorption of Pb and CR was calculated as 574.82 and 363.61(kJ/mol). The regression value was found to be 0.9434 for Pb and 0.9631 for CR biosorption.

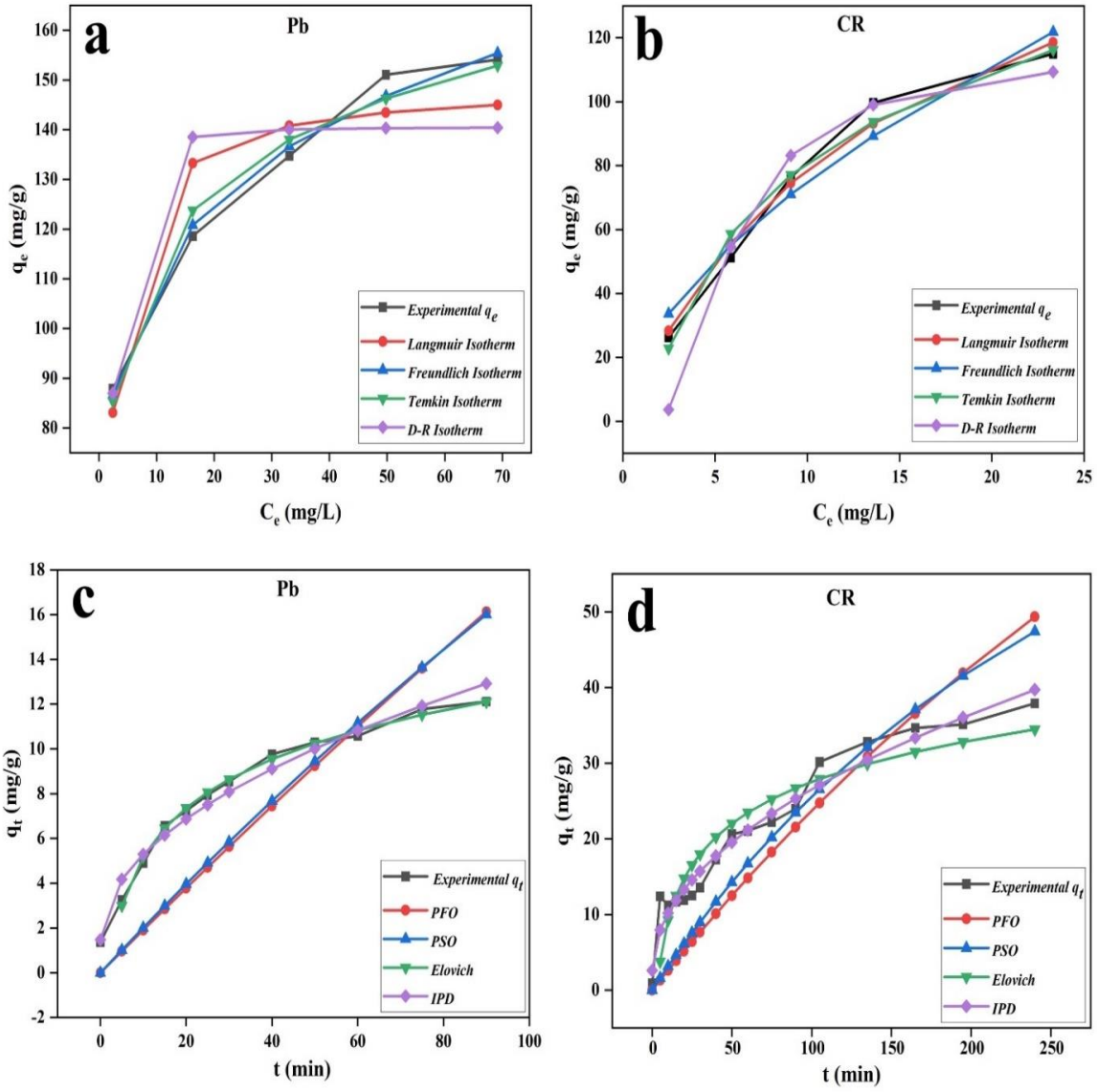

Fig. 5.7. *Isotherm models for* ***a)*** *Pb and* ***b)*** *CR biosorption, Kinetic models for* ***c)*** *Pb and* ***d)*** *CR biosorption on Fe_3O_4/AC biosorbent*

5.2.4. Biosorption kinetics

The rate of uptake of the adsorbate on the biosorbent is investigated through the kinetics study different kinetic models and their equations were used to study the kinetics of

biosorption of Pb and CR on Fe_3O_4/AC nanocomposite (Fig. 5.7 (c) and (d)). Various kinetic models and their calculated parameters are given below in the Table 5.3.

In the pseudo first order kinetics, we assume that the rate of total number of filled biosorption sites to the unfilled biosorption sites in most adsorption process and it is not very much significant for entire contact time. So, this model is only applicable at initial stage of biosorption (Thuyavan et al., 2014). The values of k_1 for Pb and CR was calculated as 0.0329 (min^{-1}) and 0.0256 (min^{-1}). The q_e value (9.605 (mg/g) for Pb and 59.590 (mg/g) for CR) calculated was not significant with the experimental values of q_e, due to boundary layer control of biosorption process. The R^2 value of pseudo first order found to be less on comparison with other kinetic models, which reveal that the biosorption of Pb (0.9512) and CR (0.6967) upon Fe_3O_4/AC nanocomposite is not significant for pseudo first order kinetics.

Pseudo second order kinetic model describes about the action of the adsorption process for the whole time (Rajabi et al., 2019). This model assumes that there is a sharing of electrons between Pb and CR with biosorbent, which forms some valence forces which act as rate limiting step. The value of R^2 (0.9693 for Pb biosorption and 0.9321 for CR biosorption) was found to be less on comparison with intraparticle diffusion model.

The nature of chemical biosorption (chemical reaction) mechanism was elucidated by Elovich model. Elovich kinetic model is best applied for the biosorbents with heterogeneous surface (Gupta et al., 2020). The values of α for Pb and CR biosorption are 2.5570 (g/mg min), 3.5856 (g/mg min). The value of β for Pb and CR biosorption are 0.3888 (mg/g) and 0.1464 (mg/g). The coefficient of correlation for Pb, CR biosorption was found to be 0.9593 and 0.8609. Which reveals the process of biosorption of Pb, CR upon Fe_3O_4/AC nanocomposite does not fit for Elovich kinetic model.

Adsorption, intraparticle diffusion and external mass diffusion are the 3 stages in the process of adsorption on porous material (Vishnu Priyan et al., 2021). The diffusion of sorbate on the sorbent was rate limiting step in the process. Pb biosorption and CR biosorption on Fe_3O_4/AC nanocomposite which shows that diffusion of Pb and CR on Fe_3O_4/AC nanocomposite surface may be the rate controlling step for the sorption process. From the Table 5.3 on seeing the values of R^2 it is found that the Pb biosorption and CR biosorption on Fe_3O_4/AC nanocomposite follows the intraparticle diffusion model.

Table 5.3. *Different Kinetic parameters of Pb and CR biosorption onto Fe_3O_4/AC nanocomposite*

Kinetics	Pb Biosorption	CR Biosorption
Pseudo-first-order model		
q_e (mg/g)	9.6051	59.5901
k_1 (1/min)	0.0329	0.0256
R^2	0.9512	0.6967
Pseudo-second-order model		
q_e (mg/g)	13.5300	42.1903
k_2 (g/mg min)	0.0052	0.0005
R^2	0.9693	0.9321
Elovich model		
α (g/mg min)	2.5570	3.5856
β (mg/g)	0.3888	0.1464
R^2	0.9593	0.8609
Intra-particle diffusion		
k_i (mg/g min $^{1/2}$)	1.2073	2.3959
d	1.4722	2.5830
R^2	0.9766	0.9667

5.2.5. Thermodynamic studies

The influence of temperature on adsorption of Pb and CR onto Fe_3O_4/AC nanocomposite was investigated with temperatures ranging from 293 K to 303 K. The removal % at 293,

298, 303 K for Pb was found to be 41.55%, 66.23%, and 90.60% and for CR it was found to be 55.03%, 62.66%, and 84.44% respectively. As the temperature increases from 293 K to 303 K, the removal % also increases. Different thermodynamic parameters were calculated and mentioned in Table 5.4. ΔG (kJ/ mol) for the adsorption of Pb and CR were negative, which shows that the adsorption process is spontaneous. The values of ΔH (kJ /mol) and ΔS (kJ \mol K) were negative and positive for both Pb and CR biosorption, proving that the Pb and CR biosorption process was exothermic and showed randomness.

Table 5.4. *Different thermodynamic parameters of Pb and CR biosorption onto Fe_3O_4/AC nanocomposite*

Temperature (K)	ΔG (kJ/ mol)		ΔH (kJ /mol)		ΔS (kJ \mol K)	
	Pb	CR	Pb	CR	Pb	CR
293	-1.844	-3.168	-23.112	-13.180	0.0795	0.0461
298	-4.390	-4.004				
303	-8.474	-7.028				

5.2.6. Phytotoxicity studies

The toxic effects of Pb and CR before and after biosorption on Fe_3O_4/AC nanocomposite on seeds of various plant species were studied through germination of seeds (%) and growth inhibition (%). From the Fig. 5.8. (a) and (b), as the concentration of Pb and CR increases there is a decrease in the percentage of seed germination. In the control groups, the seed germination was observed to be 100%. At 50 mg/L of Pb solution we can notice the drastic decrease in germination rate from 86.6% to 70% for *Pennisetum glaucum*, 76.6% to 63.3% for *Cicer arietinum*, 93.3% to 76.6% for *Vigna mungo* and 90% to 86.6% for *Vigna radiata*. The decreased % of seed germination was due to the interference of Pb with some enzymatic activities, closure of stomata and some membranal damages. These damages were caused due to abscisic acid induction and negative correlation of Pb with K in plants (Zulfiqar et al., 2019). In the different concentrations of CR (10, 30, 50 mg/L) the germination (%) is above 90%, which shows the CR is less toxic to the seeds on comparison with Pb. After the removal of Pb and CR through biosorption, we can observe there is increase in the percentage of seed germination at each concentration used in the experiments. *Vigna mungo* and *Vigna radiata* shows the highest percentage of germination

above 93.3% for *Vigna mungo* and 96.6% for *Vigna radiata*. The increase in the rate of germination of seeds was due to the efficient removal of Pb and CR from the water by the biosorbent.

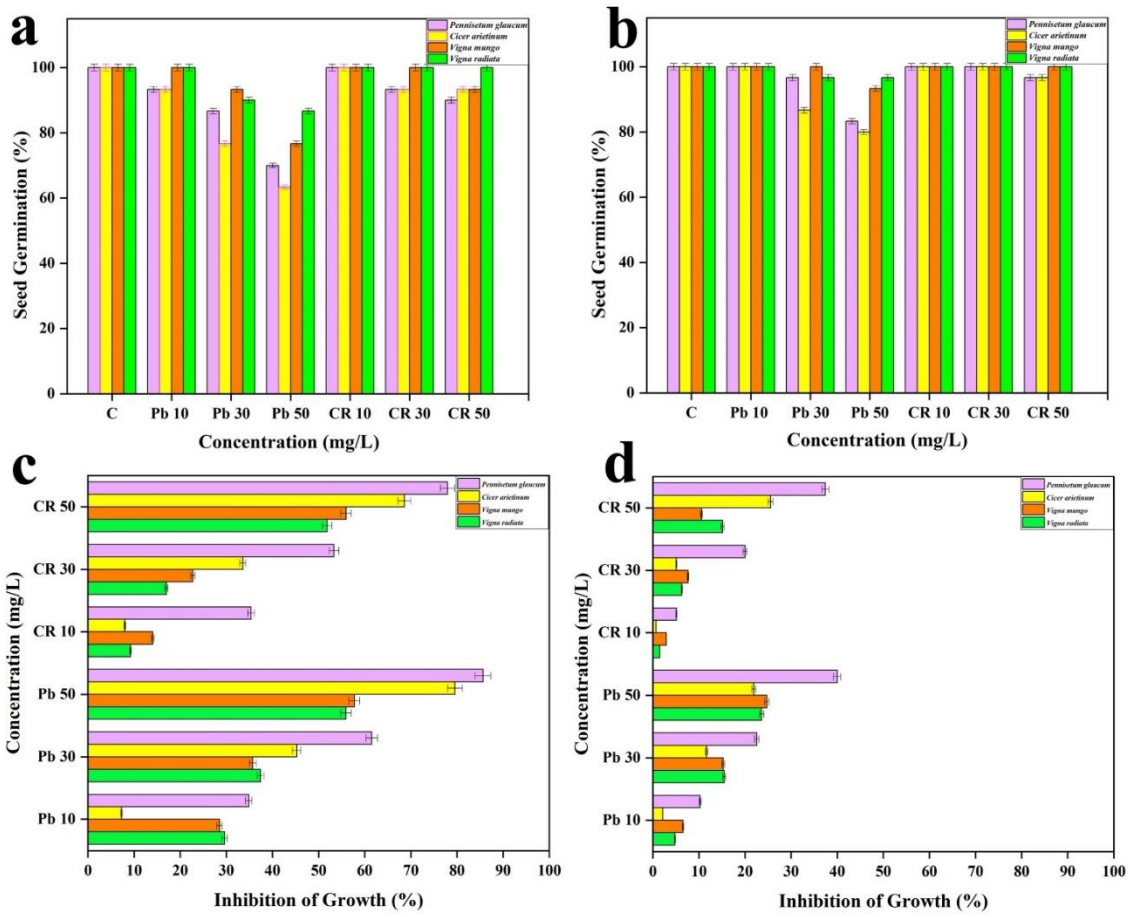

Fig. 5.8. *Seed germination (%) of Pennisetum glaucum, Cicer arietinum, Vigna mungo and Vigna radiata seeds at various concentrations of Pb and CR.* ***a)*** *Before biosorption,* ***b)*** *After biosorption, Inhibition of growth (%) of Pennisetum glaucum, Cicer arietinum, Vigna mungo and Vigna radiata seeds at various concentrations of Pb and CR.* ***c)*** *Before biosorption,* ***d)*** *After biosorption*

Fig. 5.8. (c) and (d) represents the growth inhibition of various seeds to various concentrations of Pb and CR before and after biosorption. As the concentration and time exposure of Pb and CR increases the growth of the seeds decreases due to inhibition in concentration and time dependent manner. The root and shoot length of the seedlings decreases at high concentrations of Pb and CR. At the concentration of 50 mg/L of Pb the growth inhibition of *Pennisetum glaucum, Cicer arietinum, Vigna mungo* and *Vigna radiata* were found to be 85.64%, 79.56%, 57.76% and 55.92% respectively. In case of CR

at 50 mg/L concentration the inhibition of growth was found to be 51.85% (*Vigna radiata*), 55.95% (*Vigna mungo*), 68.61% (*Cicer arietinum*) and 77.94% (*Pennisetum glaucum*). On removal of Pb and CR by biosorption promotes the growth seedlings and reduces the inhibition rate to 40% (Pb), 37.43% (CR) for *Pennisetum glaucum*, 21.89% (Pb) and 25.54% (CR) for *Cicer arietinum*, 24.72% (Pb) and 10.54% (CR) for *Vigna mungo* and 23.61% (Pb), 15.12% (CR) for *Vigna radiata* respectively. The exposure of Pb and CR to the plants at higher rates disturbs nutritional and water relations leading to oxidative damages to the seedlings which affects the growth of the seedlings (Vishnu Priyan et al., 2021b). But, the removal of these pollutants from the water promotes the growth and reduces the oxidative stress in the plants (Tasrin et al., 2021).

5.2.7. Acute fish toxicity studies

In this current study the toxicological effects of Pb and CR before and after biosorption process on zebra fish was investigated. It is found that, the control group fishes were active and alive throughout the study (Fig. 5.9.). There is no abnormal behaviour of *Danio rerio* in the control group. Acute symptoms like fast tumbling, unusual swimming and staying at bottom were observed in the treatment groups (before biosorption) with the Pb concentration above 10 mg/L. The acute symptoms were not seen in the treatment groups with congo red (CR). The mortality percentage of the zebra fish increases as the Pb concentration increases, but there is no mortality in CR till 50 mg/L. The mortality percentage is depending on the concentration of the solution. In the present study, the LC_{50} values were calculated for Pb before and after biosorption due to mortality in the treatment groups. The treatment groups with CR (before and after biosorption) was studied till 50 mg/L initial concentration (50 ppm) there is no mortality of fish. It is found that CR is not acutely toxic to zebra fish, but it can induce deflation in swimming bladder at the concentration above 30 mg/L. (Hernández-Zamora and Martínez-Jerónimo, 2019) reported that the LC_{50} of CR is about 476.84 mg/L to Danio rerio embryos. The CR salt is deposited on the surface of scales of the zebra fish.

The LC_{50} values of Pb before biosorption process at various time intervals of 24 h, 48 h, 72 h and 96 h were calculated as 70.84 mg/L, 58.83 mg/L, 42.04 mg/L and 20.98 mg/L. At the end of 96 h the LC_{50} value was found to be 20.98 mg/L which is in good agreement with the LC_{50} values reported by (Kim et al., 2020). We can also observe from the graph there is no mortality rate for CR (both before and after biosorption) and there is about 100%

mortality of fishes at the concentration of 50 mg/L of Pb. 100% mortality decreased to 60% mortality after the biosorption of Pb on Fe_3O_4/AC nanocomposite. This confirms that the Fe_3O_4/AC nanocomposite removes the Pb from the aqueous solution at highly efficient manner.

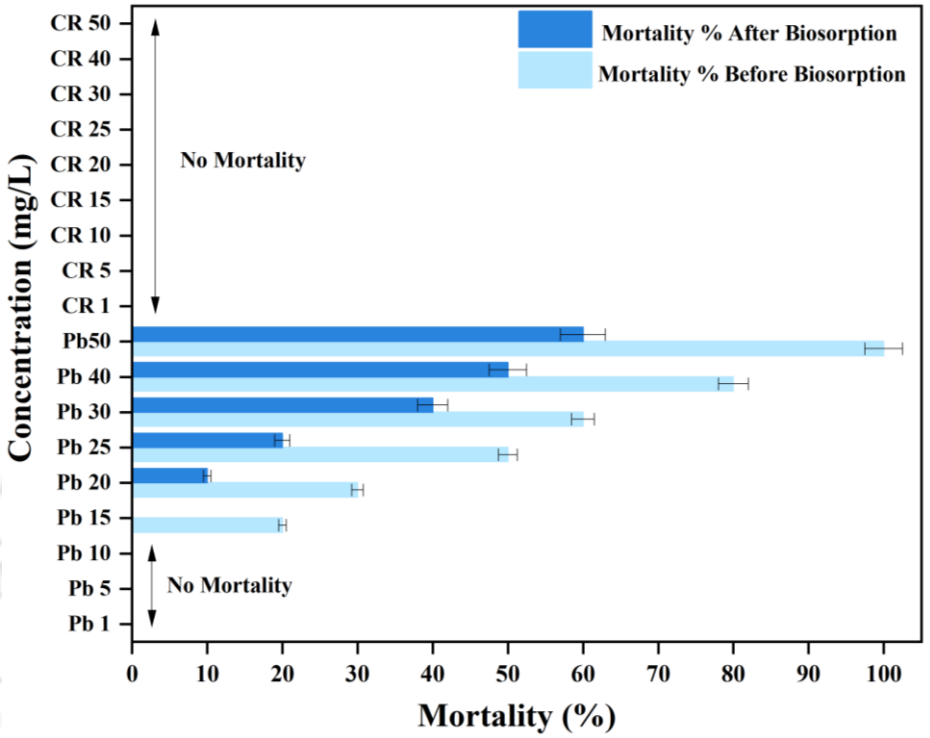

Fig. 5.9. *Mortality (%) of Danio rerio (zebra fish) to various concentrations of Pb and CR before and after biosorption*

5.2.8. Proposed biosorption mechanism

The biosorption of Pb and CR onto Fe_3O_4/AC nanocomposite is dependent on the pH of the solution. The biosorption of Pb^{2+} ions on Fe_3O_4/AC nanocomposite involves surface complexation and electrostatic interaction. The Pb charge is positive and gets attracted to the negatively charged surface as the pH_{ZPC} of Fe_3O_4/AC nanocomposite was found to be 5.7. Above pH 5.7, the surface of Fe_3O_4/AC nanocomposite is negative, and below 5.7, the surface is positive, which results in the repulsion of lead ions. The adsorption of CR molecules on Fe_3O_4/AC nanocomposite involves different mechanisms such as π–π stacking interaction, hydrophobic interactions, hydrogen bond formation, and electrostatic interactions (Fig. 5.10.). π–π stacking interaction occurs between the π electrons of Fe_3O_4/AC nanocomposite and the aromatic ring of Congo red dye molecules, including the

transfer of charges. The hydrophobic part (no charge) of the CR molecules interacts with the hydrophobic surface of the activated carbon. The formation of H bonds occurs between the surface of -OH groups of Fe_3O_4/AC nanocomposite and the -NH_2 group of the CR molecule. As the result of the protonation of oxygen atoms on the surface of Fe_3O_4/AC nanocomposite, electrostatic interaction occurs between -vely charged SO_3^- group of CR dye molecules and the +vely charged Fe_3O_4/AC nanocomposite surface.

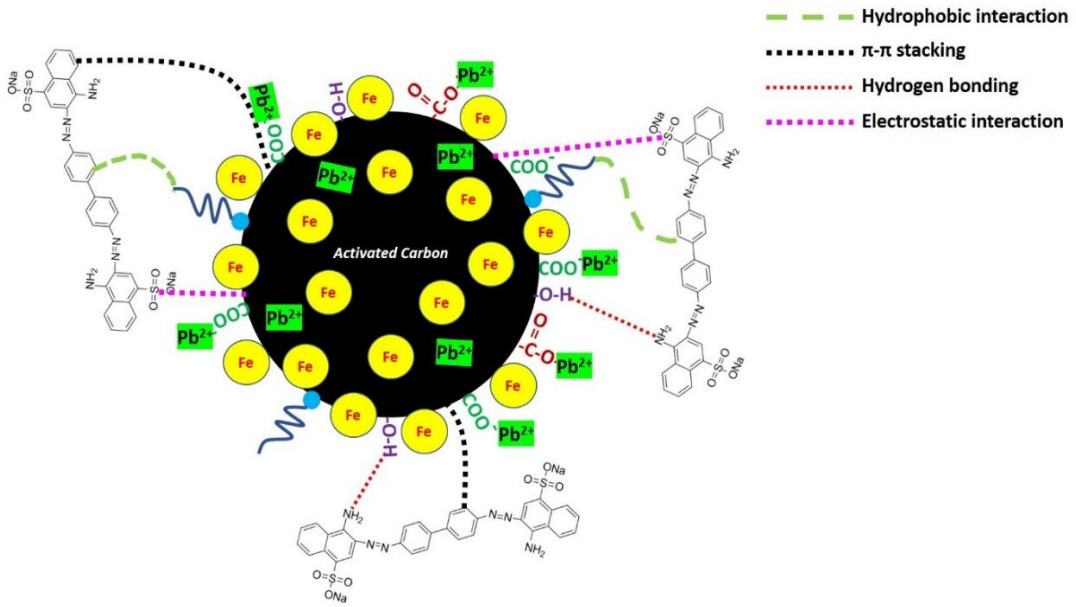

Fig. 5.10. *Proposed biosorption mechanism*

5.2.9. Effect of salts

Ground water contains different kinds of salts such as $MgSO_4$, $Mg(NO_3)_2$, $ZnSO_4$, KH_2PO_4, $CaCl_2$, K_2CO_3, $CuSO_4$, KCl and NaCl which can interfere in the removal of Pb and CR. To check the effects of these salts on adsorption of Pb and CR onto Fe_3O_4/AC nanocomposite 1:1 ratio of pollutant solution and 0.1M salt solution was taken. The results showed that the removal % for Pb and CR was found to be 76.51% and 67.72% without any salts (Fig. 5.11. (a)). On adding these salts in the Pb solution the removal % was found to be $MgSO_4$ (66.75%), $Mg(NO_3)_2$ (73.25%), $ZnSO_4$ (67.05%), KH_2PO_4 (96.30%), $CaCl_2$ (73.2%), K_2CO_3 (88.3%), $CuSO_4$ (63.25%), KCl (85.45%) and NaCl (79%). On addition of potassium and sodium salts the removal efficiency of Pb increases which may be due to the precipitation of lead salts. The removal % of CR on addition of the salts were found to be $MgSO_4$ (49.34%), $Mg(NO_3)_2$ (52.74%), $ZnSO_4$ (52.51%), KH_2PO_4 (47.57%), $CaCl_2$ (44.63%), K_2CO_3 (14.05%), $CuSO_4$ (49.16%), KCl (63.04%) and NaCl (20.02%)

respectively. The adsorption of metal ion on adsorbent is directly correlated with the ionic radius. The decline in the removal percentage of Pb and CR could be due to transformation of the metal ions into its metal hydrate forms in water, specially into its $M(OH)^{+}$ and $M(OH)_X$ forms. Metal ions with higher ionic radii compete with Pb^{2+} and CR showing reduction in the removal % of Pb and CR.

5.2.10. Desorption and reusability studies

Desorption and reusability experiments were performed to determine the regeneration potential of Iron oxide/Activated Carbon (Fe_3O_4/AC) nanocomposite, which makes the process of adsorption economically feasible. 1 M sodium hydroxide is used as desorbing agent, for the desorption of Pb and CR from Fe_3O_4/AC nanocomposite after every adsorption cycle. The % removal of Pb was found to be 97.66% (1st cycle), 91.61% (2nd cycle), 84.69% (3rd cycle), 72.57% (4th cycle) and 56.25% (5th cycle) and for CR 82.77% (1st cycle), 78.91% (2nd cycle), 69.52% (3rd cycle), 55.44% (4th cycle) and 39.29% (5th cycle) respectively (Fig. 5.11. (b)).

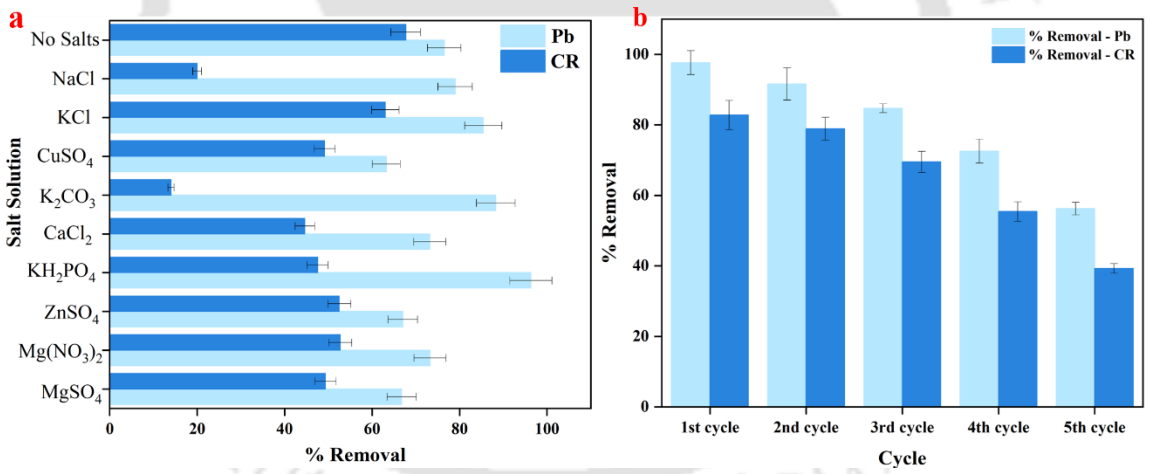

Fig. 5.11. a) *Effects of different salts on adsorption of Pb and CR and* ***b)*** *Desorption and reusability studies*

After three cycles, the adsorption of Pb and CR onto Fe_3O_4/AC nanocomposite was less significant. These repeated adsorption, desorption, and regeneration studies showed that Fe_3O_4/AC nanocomposite could be effectively reusable for up to three cycles of adsorption. After treatment with 1 M sodium hydroxide, the presence of pollutants on Fe_3O_4/AC nanocomposite surface limits this phenomenon. Due to some structural change in Fe_3O_4/AC nanocomposite, we can witness a gradual reduction in the adsorption capacity.

So, from the reusability studies we can conclude that Fe_3O_4/AC nanocomposite can be effectively reused for adsorption of Pb and CR for many cycles.

5.3. Significant findings

Fe_3O_4/AC nanocomposite was synthesised using coprecipitation of ferric chloride and ferrous sulphate. The synthesised nanocomposite was characterized with different microscopic techniques (FESEM, FETEM, AFM) for structural, topological and morphological analysis, which shows that Fe_3O_4/AC nanocomposite was nano range (10-50 nm) in size with Fe_3O_4 nanoparticles covering the AC. The presence of elements like iron, oxygen, carbon, sulphur and lead were determined by EDX analysis of the samples. The crystallinity of the biosorbent before and after biosorption of Pb and CR were analysed using XRD which shows the polycrystalline nature of Fe_3O_4/AC nanocomposite. The XRD peaks at 30.26°, 35.65°, 43.28°, 53.79°, 57.12°, 62.81° proves the presence of magnetite on AC. The FTIR and Raman spectroscopy was done for AC, which predicts the functional groups and their vibrational modes. The thermal stability of the biosorbent was investigated using TGA which shows that the nanocomposite is highly thermal stable till 800 °C. The DTG peaks at 103 °C, 556 °C and 910 °C illustrates that the degradation occurs in 3 distinct stages. VSM was done for Fe_3O_4/AC nanocomposite showing the coercivity (H_{ci}) about 18.068 Oe indicating the ferromagnetic nature of the biosorbent. The maximum removal of Pb and CR by Fe_3O_4/AC nanocomposite was optimized at pH 5.0-6.0, initial concentration of 40 mg/L and 0.04 g/L of Fe_3O_4/AC nanocomposite with biosorption capacity (Q_0) 144.92 mg/g for Pb and 122.22 mg/g for CR. The behaviour of sorbate and sorbent were described by Freundlich isotherm and intra-particle diffusion kinetic model for Pb biosorption, Langmuir isotherm and intra-particle diffusion kinetic model for CR biosorption. Toxicological assessment was carried out with seeds of different plant species for growth inhibition (%) and seed germination (%). Acute mortality (%) was determined in zebra fish at various concentrations of Pb and CR before and after biosorption. These findings inferred feasibility of the preparation of Fe_3O_4/AC nanocomposite for the maximum removal (%) of pollutants (Pb and CR) and decreased toxicity of the treated Pb and CR on model organisms.

Chapter 6

Synthesis, characterization, and application of oxidant-modified biochar prepared from saw-dust for sequestration of Basic Fuchsin: Isotherm, Kinetics, Column and Toxicity studies

The work embodied in this chapter is published in

Vishnu Priyan V., Ramesh, G., Kumar, A., Jeyabalan, J., Narayanasamy, S., 2023. Synthesis, characterization, and application of oxidant-modified biochar prepared from sawdust for sequestration of basic fuchsin: isotherm, kinetics, and toxicity studies. **Biomass Conversion and Biorefinery**, 13, 9525–9536. https://doi.org/10.1007/s13399-023-04210-z **(Springer; SCI IF 2023: 4.05).**

Abstract

Waste re-cycling and up-cycling are important strategies to preserve the sustainability of resources on earth, as water is the key for sustenance of life. In the present study, oxidant-modified biochar (OBC) is used for the adsorptive removal of Basic fuchsin in aqueous system through batch and column studies. Characterization of the adsorbent was done using various analytical techniques. Morphology analysis shows that OBC was irregular in shape with more spongy structure. The adsorbent was thermally stable till 850 °C. Functional groups on OBC before and after adsorption was determined using Raman spectroscopy and FTIR. Through batch investigations, the effect of different experimental factors on the adsorption process, such as pH, adsorbent dosage, and initial concentration of pollutant was optimized. The highest removal efficiency of 98.28% was seen at pH 6.0 with 0.05 g/L adsorbent dosage at the initial concentration of 10 mg/L. Freundlich isotherm and Pseudo-second order kinetics model fits to the adsorption process. The continuous column studies show that at 0.5 cm bed height, 1.5 mL/min flowrate, 50 mg/L initial concentration, Yield % is 79.73. The toxicity of Basic fuchsin before and after adsorption was compared using exposure of *Vigna radiata* seeds to the dye. The growth inhibition reduces to 26.86% from 67.67% after adsorption process. Thus, oxidant-modified Biochar was effective in adsorptive removal of Basic fuchsin from water.

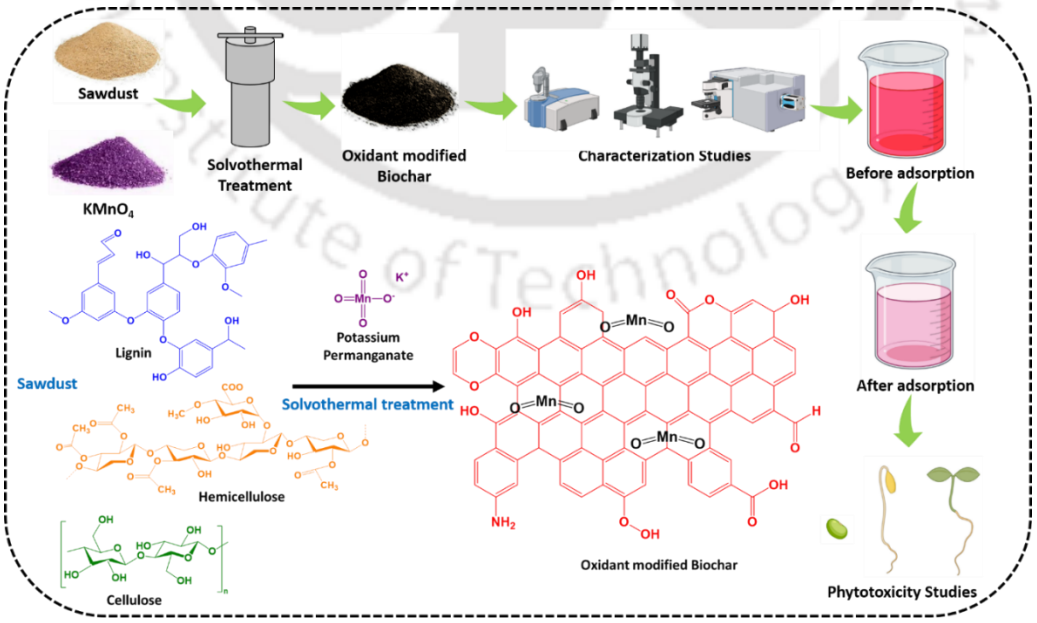

Graphical Abstract

6.1. Materials and methods

6.1.1. Chemicals and materials

The sawdust was procured from a sawmill in Maligaon, Guwahati, Assam, India. Potassium permanganate ($KMnO_4$, Mol. Wt. 158.03, purity >98.0%) was used as an oxidant, and Basic Fuchsin ($C_{20}H_{20}ClN_3$, Mol. Wt. 337.85, purity >99.0%) was used as a pollutant procured from HiMedia. The pH of the pollutant solution for the pH study was adjusted using Hydrochloric acid (purity >99.0%, SRL) and Sodium hydroxide (purity >99.0%, HiMedia). Analytical grade chemicals without further purification were used in this study.

6.1.2. Preparation of oxidant-modified biochar (OBC)

The procured sawdust was grounded using a grinder to get a uniform particle size of 150 BSS mesh. The powdered sawdust was washed with distilled water to remove impurities on the surface and oven dried at 65°C for 24 h. Oxidant-modified biochar (OBC) was synthesized using the solvothermal method. Briefly, to 4:1 of sawdust and $KMnO_4$, 50 mL of distilled water was added and stirred for one hour at 100 rpm in a magnetic stirrer. After stirring, the mixture was dispersed ultrasonically for 3 h. Then the dispersed mixture was placed in a solvothermal autoclave (Teflon-lined stainless steel) followed by heating the autoclave at 200 °C for 12 h. After cooling down, the mixture was taken out, filtered, and washed several times with ethanol and deionized water. Then the prepared OBC was kept at 70 °C for further use as an adsorbent.

6.1.3. Characterization of oxidant-modified biochar (OBC)

The characterization of OBC before and after adsorption of Basic Fuchsin (BF) was carried out using different analytical techniques as stated in the Table A1 (Appendix).

6.1.4. Adsorption experiments

The adsorption parameter optimization was performed using batch experiments under different experimental conditions. Various process parameters such as pH (2.0-12.0), OBC dosage (0.01- 0.05 g/L), temperature (298-328 K) and initial BF concentration (10-100 mg/mL) were optimized for high removal of pollutant. 0.1M NaOH and HCl was used to alter the pH of the BF solution to study the effect of pH on adsorption process. The batch studies were performed in an incubator shaker by adding the required amount of adsorbent (OBC) in pollutant (BF) solution of different concentrations at 100 rpm for 8 h. The residual

BF concentration was found using UV-Vis spectrophotometer (546 nm) (Saood Manzar et al., 2022).

The maximum adsorption capacity and removal efficiency of BF adsorption was calculated from Table 6.1.

Table 6.1. *The maximum adsorption capacity and removal efficiency of BF adsorption*

Parameters	Equation	Description	Equ. No.
Maximum adsorption capacity	$q_e = \frac{(C_0 - C_e)}{m} \times V$	**q_e** is the amount of BF adsorbed at equilibrium time (mg/g), **C_0** and **C_e** are the initial and equilibrium BF concentrations. (mg/L), **m** is the mass of the OBC (g), **V** is the volume of BF solution (L).	(6.1)
Removal efficiency	$Removal\ (\%) = \frac{C_0 - C_e}{C_0} \times 100$		(6.2)

6.1.5. Phytotoxicity experiments

The phytotoxic assessment of BF before and after adsorption was evaluated as the measure of growth inhibition % and germination % of seedlings of *Vigna radiata*. The experiments were conducted as per V. Priyan V *et al.* with minor modifications (Priyan V et al., 2022). The tests were performed at room temperature and in the dark. To prevent fungal infection, the *Vigna* seeds were treated with a 1% NaOCl (sodium hypochlorite) solution and repeatedly washed with water. Ten seeds were distributed on a Petri dish with varying BF solution concentrations before and after adsorption. Water was used as the control. To assess the phytotoxic effects of BF on *Vigna radiata*, the seed germination percentage and seedling growth inhibition were evaluated after seven days of incubation.

6.1.6. Column studies

Continuous column studies were performed to estimate the capacity of the OBC to eliminate Basic Fuchsin (BF) under various conditions in continuous mode. For conducting continuous column studies, glass column of diameter 21 mm with thickness 3 mm and height 150 mm was used. Peristaltic pump (PP-20-EX, Miclins, India) was used to pump the Basic Fuchsin solution into the column. The flow was kept upward to prevent

channelling. Various parameters influencing the adsorption of BF such as bed height, initial BF concentration and flow rate were studied. The effect of bed height was studied by considering bed height 0.25 cm, 0.5 cm, and 1 cm. The influence of flow rate was investigated by using flow rate 1.5 mL/min, 3 mL/min and 6 mL/min. The effect of initial BF concentration was examined by using 10 mg/L, 50 mg/L and 100 mg/L BF dye. Various column adsorption parameters and their equations were given in Appendix A4.

6.2. Results and Discussion

6.2.1. Characterization of OBC

6.2.1.1. Morphology analysis

Surface morphology of SD and OBC was examined using Field Emission Scanning Electron Microscope. From the Fig. 6.1 (a) and (b) it is seen that SD surface is rough with irregular shape and size. The synthesized biochar from SD with $KMnO_4$ (Oxidant) have more cracks and spongy structure as seen in the Fig. 6.1 (c) and (d). The diverse pore structures result in rougher surface and would allow efficient adsorption of Basic Fuchsin than on saw dust (John et al., 2022). Similar structure of biochar was reported by Rashad *et al* (Rashad et al., 2022).

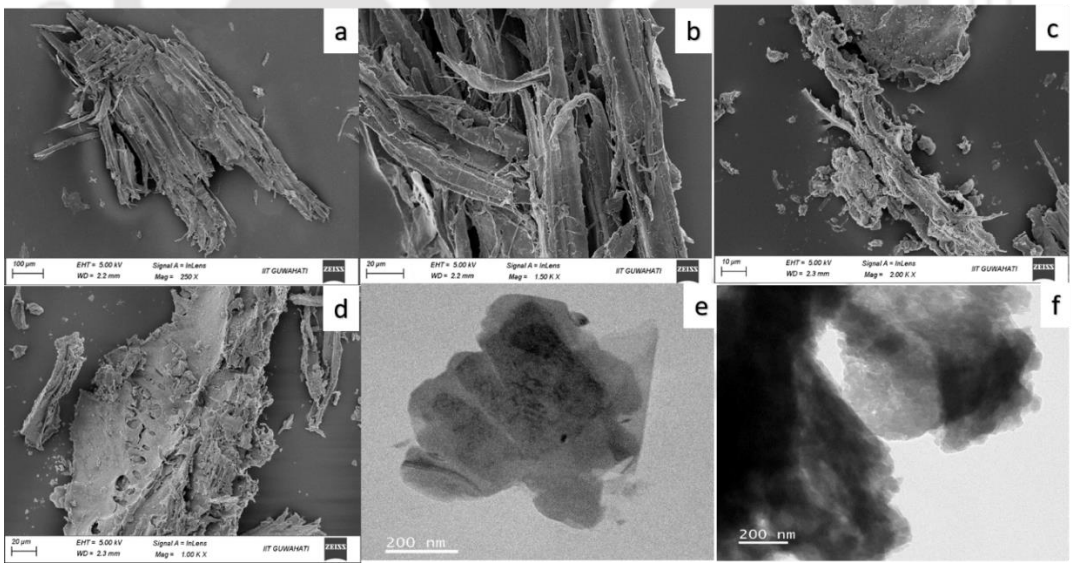

Fig. 6.1. a) & b) *FESEM micrographs of SD at different magnifications,* ***c) & d)*** *FESEM micrographs of OBC at different magnifications and* ***e) & f)*** *FETEM image of OBC*

Fig. 6.1 (e) and (f) represents the Field Emission Transmission Electron Microscope micrograph of OBC confirming the irregular shape and size for aggregates. From the Fig.

6.1 (f) it is seen that the produced biochar was arranged layer-by-layer. These observations were due to the high density of hydroxyl groups on the surface of oxidant modified biochar, which resulted in the formation of hydrogen bonds.

6.2.1.2. Raman and FTIR analysis

The Raman spectra of SD and OBC before and after the adsorption of BF are shown in the Fig. 6.2. The band at 1314 cm^{-1} represents the D-band that occurs due to the disordered graphitic carbon rings. The G-band at 1614 cm^{-1} represents the vibrations of sp^2 hybridized graphitic carbon (Zhou et al., 2022). The band at 882 cm^{-1} was due to the C-O-C skeletal mode of cellulose. All three spectra, SD, OBC, and OBC-BF, have bands at 1080 cm^{-1} corresponding to OC stretching and CH_3 wagging of cellulose (Tasrin et al., 2021). The 2190 cm^{-1} and 2542 cm^{-1} bands correspond to C≡C stretching and methyl CH stretching bands, respectively (Shrestha et al., 2019).

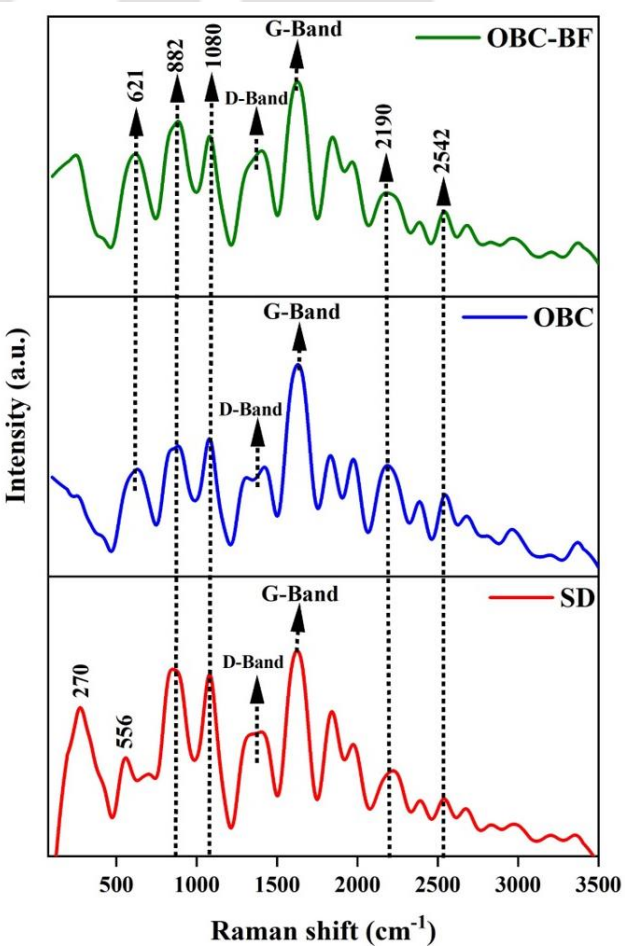

Fig. 6.2. *Raman spectra of SD, OBC and OBC-BF*

The Raman spectra of SD show a band at 556 cm^{-1} corresponding to CCO and CCC in-phase bend of lignin of sawdust. The band at 270 cm^{-1} confirms the C-C aliphatic chains of cellulose. The band at 621 cm^{-1} of OBC and OBC-BF is the characteristic band of the MnO_2 group, which confirms the modification of biochar with $KMnO_4$ (Gao et al., 2009; Lupoi et al., 2015). The oxidant modification can cause more defects in carbon structure in biochar due to alkaline corrosion or metal insert at graphited carbon.

Fig. 6.3 shows the FTIR spectra of SD and OBC before and after BF adsorption. O-H stretching and N-H stretching vibrations were related to the bandwidth between 3700-3040 cm^{-1} (Al-Juboori et al., 2022). The weak peak at 2922 cm^{-1} corresponds to C-H stretching vibrations in sawdust's alkyl groups. The band at 1737 cm^{-1} of SD shows C=O vibration in hemicellulose carbonyl groups (Ghani et al., 2013; Pan et al., 2016). The aromatic stretching vibration caused by the presence of lignin resulted in a peak of around 1594-1584 cm^{-1} in SD, OBC, and OBC-BF. Similar type of peak was also reported by Vishnu Priyan *et al* (Vishnu Priyan et al., 2021b). The C-C-O/C-O-C asymmetric stretching caused a sharp peak of around 1029 cm^{-1}. The peak confirmed O-H out of plane bending at 559 cm^{-1}. A weak peak of about 1425 cm^{-1} was due to the C-H deformation of alkoxy and alkyl groups (Mylarappa et al., 2016).

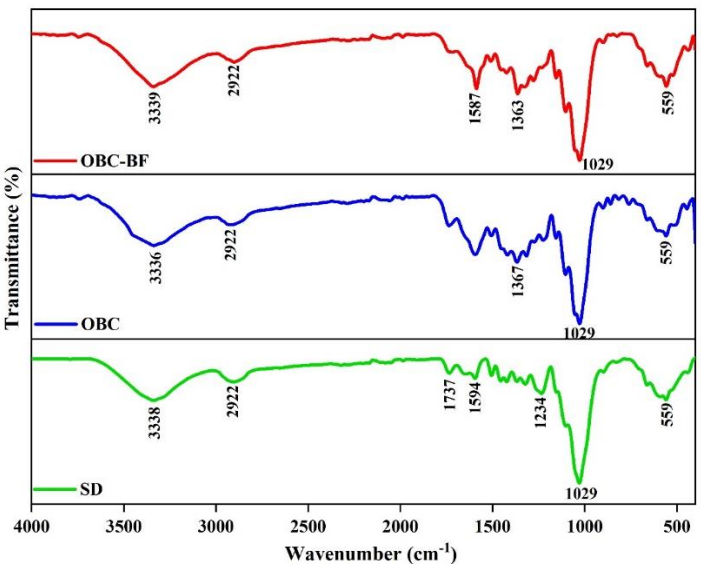

Fig. 6.3. *FTIR spectra of SD, OBC and OBC-BF*

6.2.1.3. XRD analysis

The XRD diffractogram of sawdust (SD) and Oxidant-modified biochar (OBC) before and after adsorption of Basic Fuchsin (BF) was shown in the Fig. 6.4. Sawdust comprises

cellulose, hemicellulose, and lignin. XRD pattern of SD shows a significant peak at 15.52 °, 22.58 °, and 34.34 ° due to the characteristic peak of cellulose in the sawdust (Vishnu Priyan et al., 2021b). Similar peaks were also seen in OBC before and after the adsorption of BF. The diffraction peaks of OBC before and after adsorption of BF at 28.54 °, 31.28 °, and 51.66 ° was due to MnO_2. These results showed that oxidation and reduction reactions between potassium permanganate and biochar exist. Biochar was oxidized to generate high CO groups, and potassium permanganate was reduced to MnO_2 (Chowdhury et al., 2016; Shaheen and Emam, 2018). The peak at 28.51° disappeared at OBC-BF after the adsorption of BF on OBC. Although OBC may exist as compounds with low crystallinity, the material lattice of OBC did not change considerably after BF adsorption, demonstrating that OBC does not form any crystal structures following BF adsorption.

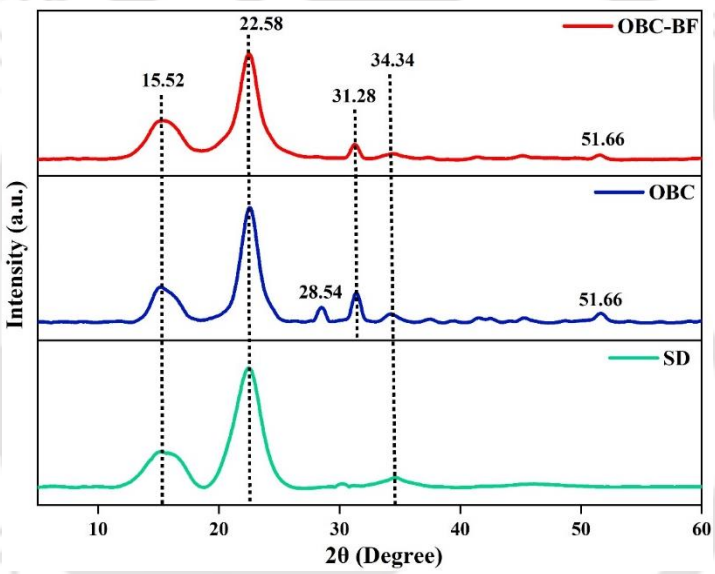

Fig. 6.4. *XRD spectra of SD, OBC and OBC-BF*

6.2.1.4. Thermal stability analysis

The thermal stability of OBC was examined by measuring the change in mass at different temperatures using Thermogravimetric analysis (TGA). Fig. 6.5 represents the thermogram of the OBC in the temperature range of 20℃ to 900℃. There are four stages namely evaporation of water molecules (stage 1), 1st stage decomposition (stage 2), 2nd stage decomposition (stage 3), and final decomposition (stage 4). There is 6.2% decrease in mass between 55℃ to 280℃. This can be attributed to the evaporation of water molecules. There is further decrease of 53% in mass in the temperature range of 280 ℃ to 435 ℃. Earlier reports suggest that the thermal degradation of cellulose and hemicellulose in the SD occurs

in the temperature range of 200 ℃ to 400 ℃ (Shrestha et al., 2019). The mass further decreases by 18.3% in the temperature range of 435 ℃ to 852 ℃. Decomposition of lignin is reported to occur in the third stage (Mishra and Mohanty, 2018). The residual mass of the sample present was 29% and the thermal decomposition occurred till 850 ℃. This shows that the OBC possess high thermal stability.

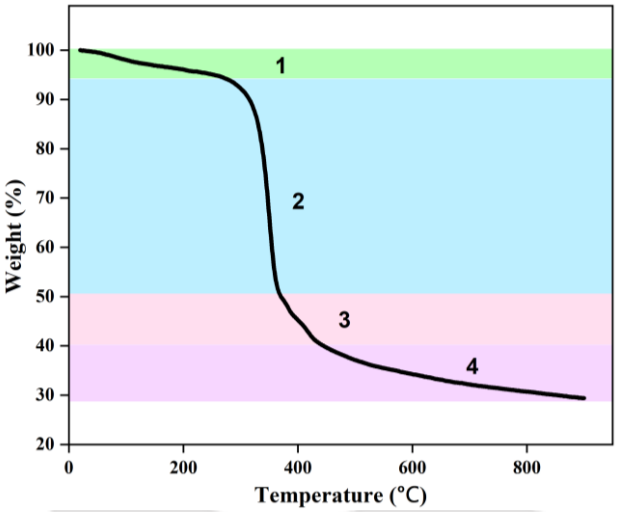

Fig. 6.5. *TGA plot of OBC*

6.2.2. Effects of various parameters on adsorption

6.2.2.1. Effect of pH on adsorption

pH effects the chemical nature and surface charge of the adsorbent and adsorbate in aqueous solutions. So, studying the effect of pH is necessary to optimize any adsorption process. The removal efficiency and adsorption capacity in the range of pH 2.0 to pH 12.0 was studied (Fig. 6.6 (a)). Zeta potential analysis was carried out and point of zero charge aka pZC of OBC was evaluated to be 1.9. At pH below 1.9, OBC surface would possess a positive charge and a negative charge at pH above 1.9. The removal efficiency increases till pH 6.0, reaches a maximum with 91.11% removal and then decreases to 70.04% at pH 12.0. Basic fuchsin is a cationic dye which will be in positive state in aqueous solution. pH is adjusted to acidic values by the addition of protons and the adsorbent is negatively charged. Therefore, protons could compete with the dye molecules for adsorption sites leading to decreased removal % (El Haddad, 2016). Also at basic pH, the addition of hydroxyl ions leads to change in dye conformation and discoloration (Huang et al., 2012). Therefore, at pH 6.0 the cationic dye could possibly out-compete the protons showing a higher adsorption efficiency. The adsorption capacity increases as the pH increases and a

maximum of 49.77 mg/g was observed at pH 12.0. Since the adsorbate possesses a negative surface at all the experiment condition (pH > pZC) considered here, the capacity of the adsorbate it can hold increases with increase in pH.

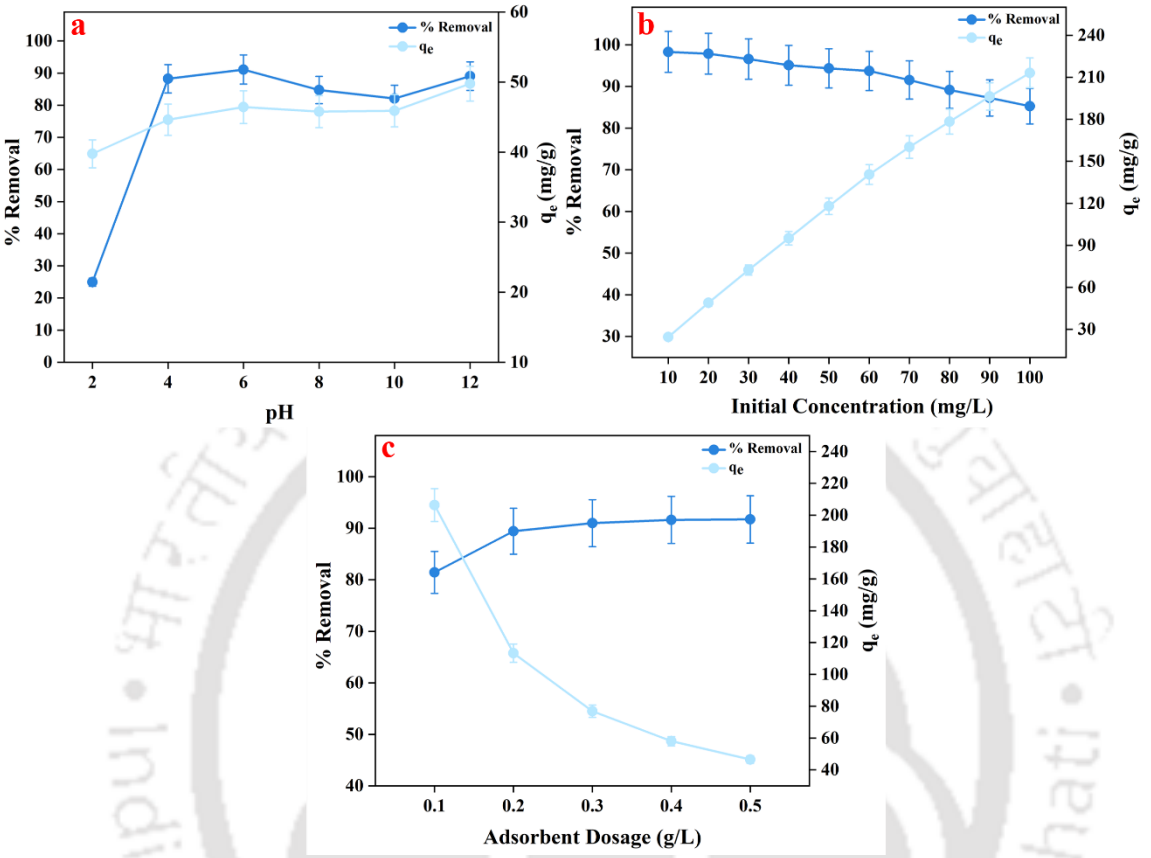

Fig. 6.6. a) *Effect of pH on adsorption of BF by OBC at various pH ranging from pH 2.0-12.0,* ***b)*** *Effect of initial BF concentration on adsorption of BF by OBC at different concentrations of BF ranging from 10-100 mg/L, and* ***c)*** *Effect of adsorbent dosage on adsorption of BF by OBC at different dosage of OBC ranging from 0.01 to 0.05 g/L*

6.2.2.2. Effect of initial BF concentration

Initial concentration of BF is another influential parameter on the adsorption process. Its effect was studied using 10 mg/L to 100 mg/L solutions of Basic fuchsin (Fig. 6.6 (b)). The removal efficiency is maximum with 98.29% at 10 mg/L initial concentration. Further, the removal % decreases as initial concentration increases. A minimum of 85.26% was observed at an initial concentration of 100 mg/L. In this experiment, the adsorbent dosage is fixed. Hence, at lower initial concentration, there will be less number of BF molecules and so the number of unoccupied adsorption sites in the OBC will also be more, than at

higher initial concentration (Kannan and Sundaram, 2001). As the initial dye concentration increases the residual dye concentration after adsorption also increases, thereby showing lower removal efficiency. The adsorption capacity increases with the increasing initial concentration. Maximum and minimum adsorption capacity of 213.14 g/mg and 24.57 mg/g was observed at the initial concentration of 100 mg/L and 10 mg/L respectively. As there are higher number of BF molecules in solution, greater adsorption capacity is observed to bring about the equilibrium in the adsorption process (Gorzin and Bahri Rasht Abadi, 2018). Also, at high initial concentration, BF molecules overcomes the mass transfer resistance.

6.2.2.3. Effect of OBC dosage

The dosage of adsorbent also influences the adsorption process. To study its effect, dosage is varied from 0.01 to 0.05 g/L. Minimum and maximum removal efficiency of 81.45% and 91.74% was observed at 0.01 and 0.05 g/L adsorbent dosage (Fig. 6.6 (c)), respectively. The number of active adsorption sites increases with increasing dosage (Vishnu Priyan et al., 2021a). The OBC-BF interaction is hence strong and this attributes to the increasing trend of removal efficiency. At 0.01 and 0.05 g/L adsorbent dosage, adsorption capacity of 206.41 and 46.49 mg/g was observed respectively, with a decreasing trend. There is higher exposure of adsorption sites at lower adsorbent dosage, leading to higher amount of BF adsorption per unit mass of adsorbent at a specified volume and vice versa.

6.2.3. Adsorption isotherms

The functional groups on OBC surface influences the adsorption of BF on OBC. The interaction of BF with OBC and binding mechanism were determined using various isotherm models (Fig.6.7 (a)). Adsorption isotherms are theoretical graphs that allow the study of the adsorption process in relation to an increase in concentration of adsorbate at constant temperature. Maximum adsorption capacity and mechanism of adsorption were predicted using physiochemical data which is calculated from specific equations for specific isotherms (Tasrin et al., 2021; Vishnu Priyan et al., 2021b). The Table 6.2 displays the various isotherm model process parameters.

The Langmuir isotherm model considers identicality of OBC active sites, and that the binding energies of BF molecules at each active site are equivalent. This model states the monolayer adsorption of BF onto the OBC surface. The Q_0 was found to be 241.19 mg/g

for BF adsorption. The R^2 and χ^2 for Langmuir isotherm model is estimated to be 0.9812 and 76.496, respectively.

Table 6.2. *Various isotherm parameters of BF adsorption onto OBC adsorbent*

Isotherm Model	BF adsorption
Langmuir Isotherm	
K_L (L/mg)	0.3696
Q_0 (mg/g)	241.19
R^2	0.9812
χ^2	76.496
Freundlich Isotherm	
n	2.4890
K_F (L/g)	74.749
R^2	0.9847
χ^2	62.289
Temkin Isotherm	
K_T (L/mg)	6.9030
b_T (kJ/mol)	59.231
R^2	0.9659
χ^2	139.25
Jovanovic Isotherm	
K_J (L/g)	0.3357
q_m (mg/g)	199.19
R^2	0.9579
χ^2	171.96

In contrast, multilayer and heterogeneous surface adsorption was explained by Freundlich isotherm model. In this model, unequal affinity and binding energy distribution occurs between OBC and BF molecules. Non-linear equation was used to calculate the value of

K_F and n which is found to be 74.749 (L/g) and 2.4890. The R^2 and χ^2 value is estimated to be 0.9847 and 62.2894, respectively. Temkin isotherm model assumes that as the surface of OBC increases, the heat of adsorption of molecules of BF linearly decreases. The b_T and k_T values is calculated from non-linear Temkin equation and was 59.2312 KJ/mol and 6.9030 L/mg. The R^2 and χ^2 is found to be 0.9659 and 139.257 respectively. The assumption of Jovanovic model is based on Langmuir model with inclusion of mechanical contact between adsorbing and desorbing molecules. The R^2 and χ^2 of Jovanovic isotherm model was found to be 0.9579 and 171.9621 which was found to be non-significant than other isotherm models. The R^2 of Freundlich isotherm model was found to be higher than all other isotherm models and it has lower the χ^2 value, which shows that adsorption of BF onto OBC theoretically fits into Freundlich isotherm model showing multilayer and heterogeneous surface adsorption.

6.2.4. Adsorption kinetics

The rate of adsorption is an important parameter to calculate the amount of BF adsorbed on the OBC at specific time interval. The mechanism of adsorption can also be determined using various kinetic models such as Elovich, Intraparticle diffusion (IPD), pseudo first order (PFO) and pseudo second order (PSO) (Kannan and Sundaram, 2001). The Table 6.3 represents the process parameters of various kinetic models.

Rate of adsorption in the PFO kinetic model depends on the BF molecules concentration in the solution and availability of free active sites on the surface of OBC. This model demonstrates the mechanism of adsorption to be physisorption with the limitation that this model valid for initial time of the process of adsorption. The q_e and k_1 is estimated to be 179.38 mg/g and 0.0244 min^{-1}. The R^2 and χ^2 value for the PFO is estimated to be 0.9455 and 141.90, respectively.

The behaviour of the adsorption process for the entire time was stated by PSO kinetic model, which assumes that the electrons are shared between BF and OBC involving valence forces with rate limiting step. This model explains about chemical adsorption process. The R^2 and χ^2 value for PSO is estimated to be 0.9730 and 70.214, respectively. The heterogenous surface adsorption was elucidated by Elovich kinetic model. The R^2 value is estimated to be 0.9580 which is not significant compared to other R^2 values. The R^2 value of IPD is 0.7830 which is very lesser compared to all other R^2 values of kinetic models.

The IPD has higher χ^2 value which shows that this model is not suited for adsorption of BF onto OBC. Based on the higher R^2 and lower χ^2 values the PSO kinetic model is the best fitted model for BF adsorption process (Fig. 6.7 (b)).

Table 6.3. *Various kinetic parameters of BF biosorption onto OBC adsorbent*

Kinetics	BF adsorption
Pseudo-first-order model	
k_1 (1/min)	0.0244
q_e (mg/g)	179.38
R^2	0.9455
χ^2	141.90
Pseudo-second-order model	
k_2 (g/mg min)	0.0001
q_e (mg/g)	197.71
R^2	0.9730
χ^2	70.214
Elovich model	
β (mg/g)	0.0302
α (g/mg min)	24.349
R^2	0.9580
χ^2	109.37
Intra-particle diffusion	
d	64.454
k_i (mg/g min $^{1/2}$)	6.3261
R^2	0.7830
χ^2	565.55

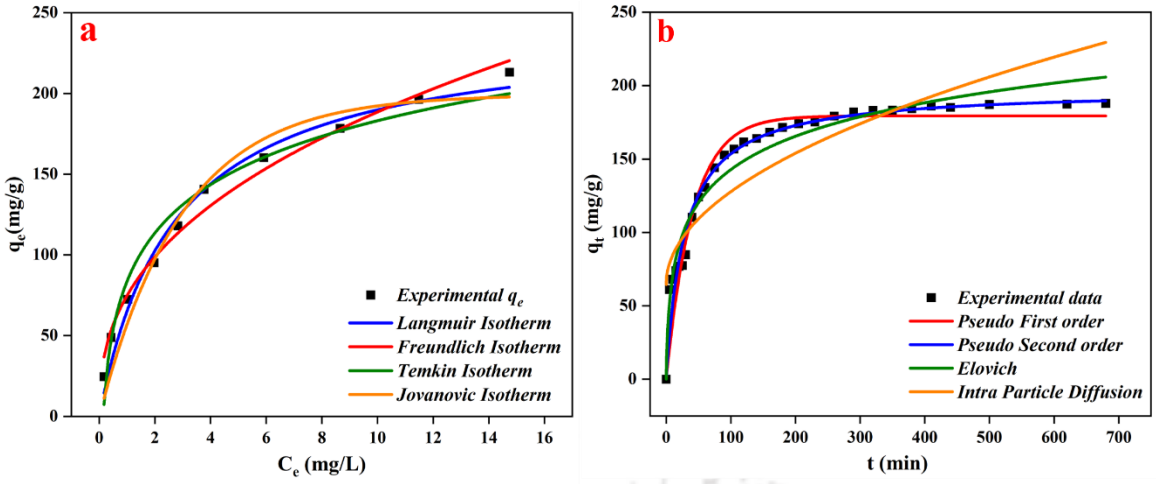

Fig. 6.7. a) *Isotherm models of BF adsorption onto OBC adsorbent and* ***b)*** *Kinetic models of BF adsorption onto OBC adsorbent*

6.2.5. Phytotoxicity studies

The phytotoxic effects of BF before and after treatment with OBC were assessed using growth inhibition % and germination % of *Vigna radiata* seedlings. According to the Fig. 6.8 (a), the seed germination percentage decreased as the BF concentration increased. Seed germination was observed to be 100% in groups that just received water without BF (control). The seed germination rate was lowered to 60% before adsorption with a BF solution at a 200 mg/L concentration. The seed germination % till 100 mg/L concentration was about 80%. The interference of BF molecules with enzymes in the cell system caused membranous damage and stomatal closure in *Vigna* seedlings, decreasing seed germination percentage (Vishnu Priyan et al., 2021b). Later, BF molecules were removed from the water by adsorption; we can detect an increase in seed germination percentage at every concentration.

The Fig. 6.8 (b) depicts the percentage of growth inhibition of *Vigna radiata* at BF concentrations ranging from 5 to 200 mg/L before and after adsorption. The growth of the *Vigna* seedlings is inhibited as the concentration of BF rises. The percentage of growth inhibition was determined to be 10.27%, 16.37%, and 20% at 5, 10, and 20 mg/L of BF before adsorption, respectively. After adsorption, it was reduced to 2.16%, 2.21%, and 4.86%. Adsorption of BF onto OBC promotes seedling development and reduces the inhibition rate to 26.86% for 200 mg/L. The disturbance of nutritional and water balance relations was induced by the increased rates of BF exposure to the *Vigna* seedlings, which

resulted in oxidative stress and injury to the seedlings, impacting their growth of the seedlings.

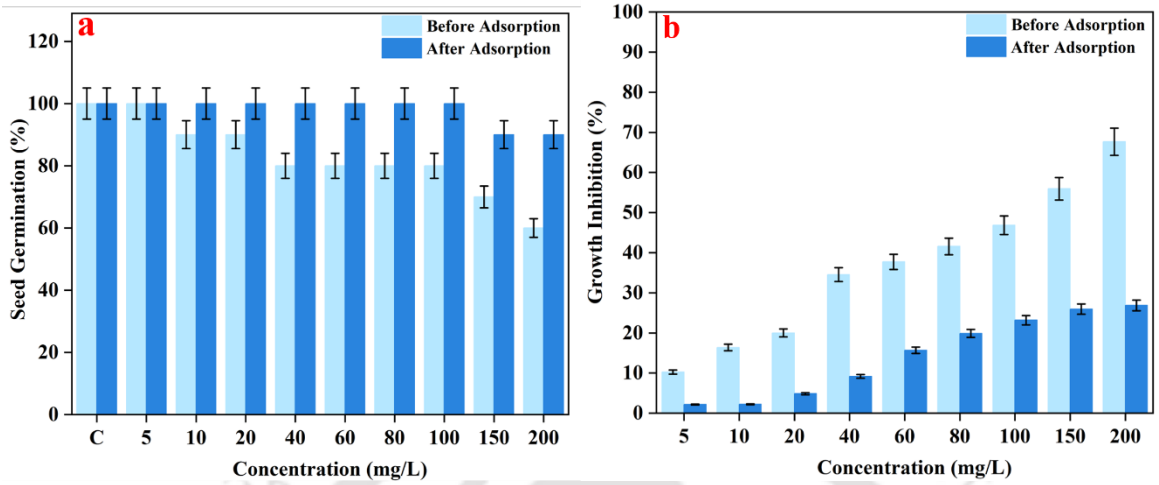

Fig. 6.8. a) *Seed germination (%) and* ***b)*** *Growth inhibition (%) of Vigna radiata seeds to various concentrations of BF before and after adsorption*

6.2.6. Proposed adsorption mechanism

The BF adsorption on OBC involves different mechanisms such as π–π interactions, covalent bonding, and hydrogen bonding (Fig. 6.9).

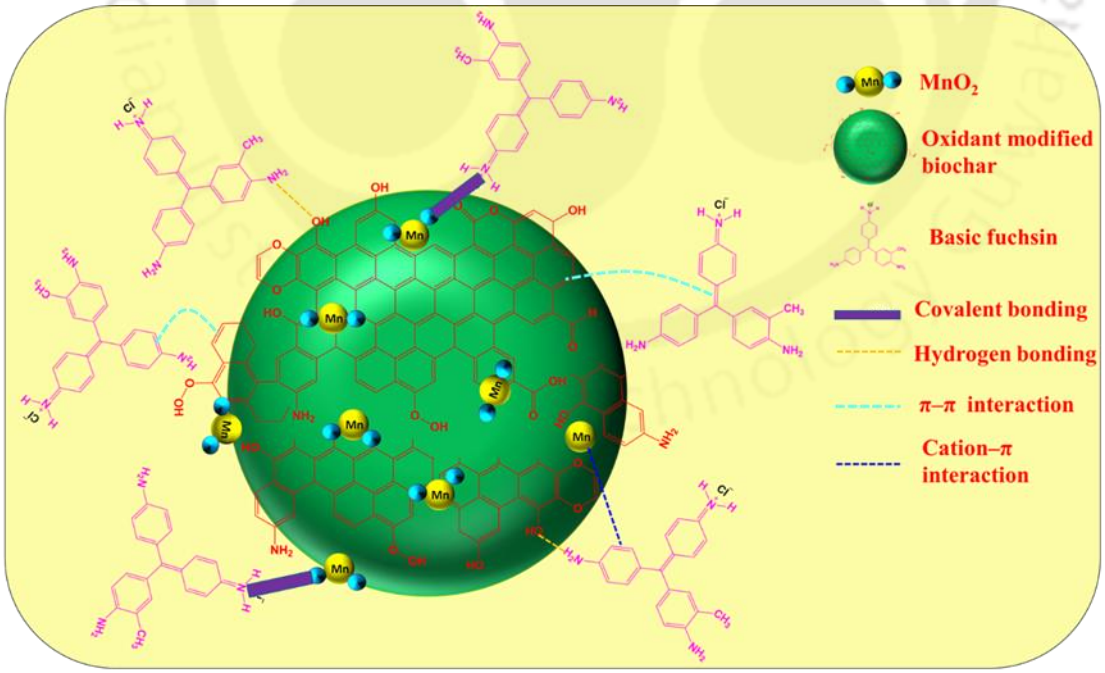

Fig. 6.9. *Proposed adsorption mechanism of BF adsorption onto OBC*

π–π interactions takes place when one aromatic π system binds face-to-face to the another π system. π–π interactions occur between π-system of Basic fuchsin dye (10 pi bonds) and π system of oxidant modified biochar. The H bonds are formed between the surface -OH groups of OBC and :NH_2 group of BF. The covalent bonding occurs between O^- group of Biochar and N^+ group of BF. These were the possible mechanism for the adsorption of BF onto OBC.

6.2.7. Continuous column studies

In this study a fixed-bed column is packed with OBC (adsorbent material), and a liquid containing the BF (pollutant) to be adsorbed is passed through the column. Various parameters influencing the adsorption of BF such as bed height, initial BF concentration and flow rate were studied. The diagrammatic representation of the packed bed column is shown in the Fig. 6.10 (a-c). The effect of bed height was studied by considering bed height 0.25 cm, 0.5 cm, and 1 cm. The influence of flow rate was investigated by using flow rate 1.5 mL/min, 3 mL/min and 6 mL/min. The effect of initial BF concentration was examined by using 10 mg/L, 50 mg/L and 100 mg/L BF dye. The experimental parameters such as ttotal (min), qtotal (mg), mtotal (g), Veff (mL) and Y (%) are tabulated in the Table 6.4.

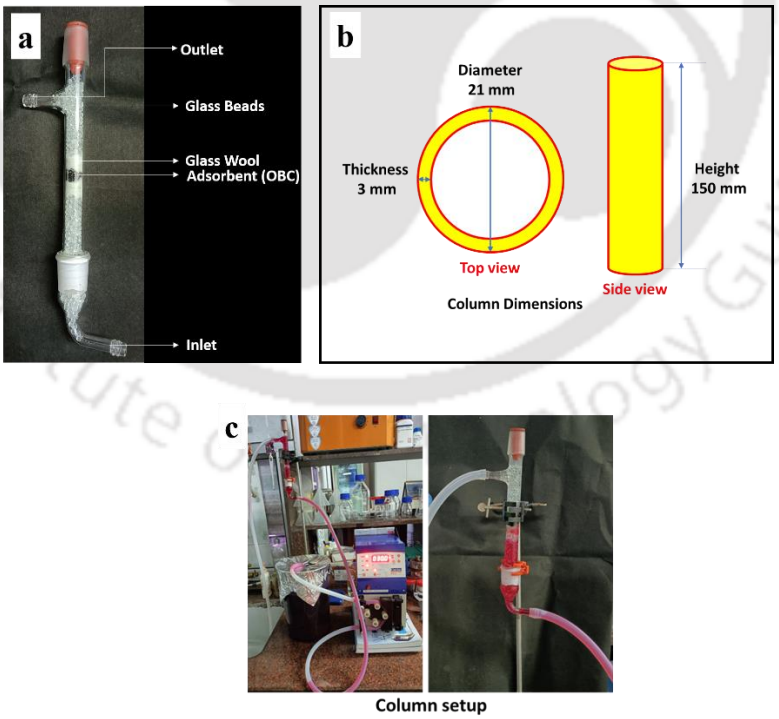

Fig. 6.10. *Diagrammatic representation of the packed bed column* ***a)*** *Column packed with OBC,* ***b)*** *Column dimensions, and* ***c)*** *Laboratory column setup*

Table 6.4. *Various column parameters of BF biosorption onto OBC adsorbent*

Z (cm)	F (mL/min)	C_0 (mg/mL)	t_{total} (min)	m_{total} (g)	q_{total} (mg)	$q_{e(exp)}$ (mg/g)	V_{eff} (mL)	Y (%)
0.25	3	50	1860	279	168.06	168.06	5580	60.23
0.5	3	50	3000	450	322.80	146.73	9000	71.73
1	3	50	4180	627	491.51	109.22	12540	78.39
0.5	1.5	50	3940	296	235.61	107.09	5910	79.73
0.5	3	50	3000	450	322.80	146.73	9000	71.73
0.5	6	50	2400	720	524.97	238.62	14400	72.91
0.5	3	10	4300	129	99.76	45.34	12900	77.33
0.5	3	50	3000	450	322.80	146.73	9000	71.73
0.5	3	100	2100	630	412.16	187.35	6300	65.42

6.2.7.1. Effect of bed height

The effect of bed height for the adsorption of BF onto OBC was carried out at different bed heights of 0.25 cm, 0.5 cm, and 1 cm at a fixed initial BF concentration of 50 mg/L and flow rate of 3 mL/min. As the bed height increases, the volume of BF solution required for saturation of the bed and the time required for breakthrough increases Fig. 6.11 (a) Additionally, a rise in total time was seen along with a rise in bed height. BF removal percentage increased from 60.23% to 78.39% with an increase in bed height from 0.25 to 1 cm. It could be because more dye species can diffuse and adsorb onto OBC due to the increased time an adsorbate (BF dye) spends in contact with an adsorbent (OBC) due to increased bed height. However, a higher surface area from the raised bed height meant that more active sites on the adsorbent surface were available for the adsorption of BF dye species.

6.2.7.2. Effect of flow rate

The effect of flow rate was investigated for the adsorption of BF dye at 1.5 mL/min, 3 mL/min, and 6 mL/min with a fixed bed height of 0.5 cm and initial BF concentration of 50 mg/L. It was seen that when the flow rate increased, the breakthrough time and overall time decreased Fig. 6.11 (b). Additionally, less BF solution was needed to completely saturate the bed as the flow rate increased. With an increase in flow rate, the percentage of

BF removal also reduced. With an increase in flow rate from 1.5 mL/min to 6 mL/min, the adsorption capacity for BF adsorption increased from 107.09 mg/g to 238.62 mg/g, and the removal % decreased from 79.73% to 72.91% respectively. The sorbate-sorbent contact time decreased with an increased influent rate, and the external film mass resistance decreased. Decreased saturation time resulted from dye species leaving the adsorbent without being absorbed in a column from the effluent. Similar results have been reported by Tasrin et al.

6.2.7.3. Effect of initial dye concentration

The effect of initial dye concentration was performed for 10 mg/L, 50 mg/L, and 100 mg/L keeping bed height and flow rate constant at 0.5 cm and 3 mL/min, respectively. With an increase in initial BF concentration from 10 mg/L to 100 mg/L, total time, and breakthrough time it has decreased Fig. 6.11 (c). The adsorption capacity increased with an increase in the initial BF concentration from 45.34 mg/g to 187.35 mg/g, and the % removal decreased from 77.33% to 65.42%, respectively. This may be due to the greater driving force between the functional groups on the surface of the adsorbent and the BF molecules due to the higher initial BF concentration.

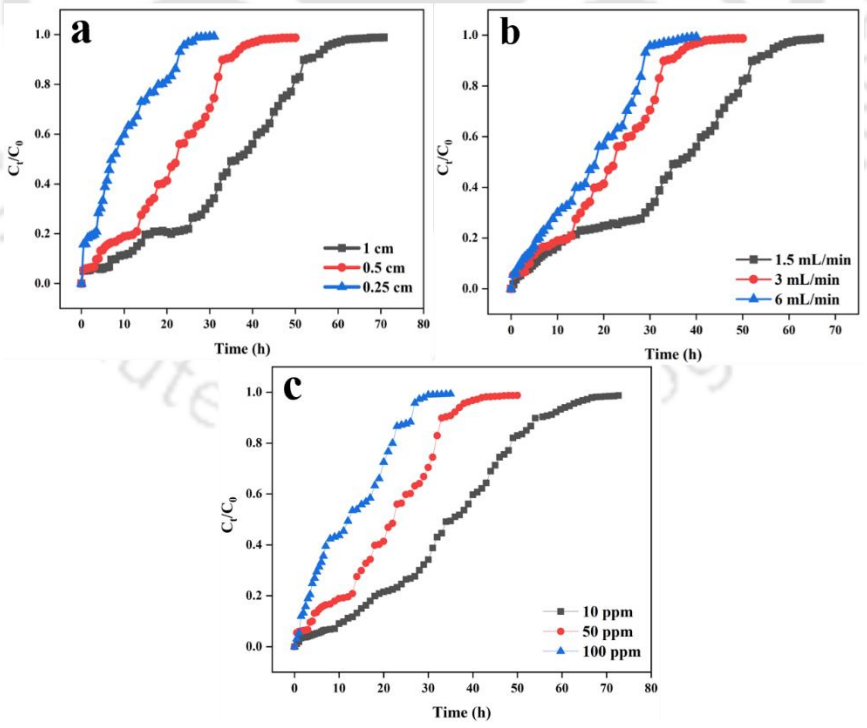

Fig. 6.11. a) *Effect of bed height* ***b)*** *Effect of flow rate, and* ***c)*** *Effect of initial BF concentration*

6.2.8. Breakthrough curve and modelling

Thomas model assumes that the adsorption of solutes occurs on a surface with a finite capacity, and that the driving force for adsorption is the concentration difference between the bulk liquid phase and the adsorbent surface. The data were fitted to Thomas model to determine the values of both adsorption capacity (q_0, mg/g) and rate constant (k_{TH}, mL/mg min) which were calculated from the intercept and slope of a plot of ln [C_o C_t −1] against time. From the Table 6.5, as the initial concentration of BF increases, the adsorption capacity increases from 271.48 to 987.89 mg/g. The value of k_{TH} decreases from 0.0180 to 0.0033 mL/mg/min. As bed height increases from 0.25 to 1.0 cm, the values of both k_{TH} and q_0 decreases. However, as the flow rate increases from 1.5 to 6 mL/min the values of k_{TH} also increases from 0.0034 to 0.0060 mL/mg/min.

The Adams-Bohart model assumes that the adsorption process is a combination of external mass transfer and intraparticle diffusion. The values of saturation constant (N_{AB}, mg/L) and kinetic constant (K_{AB}, mL/mg min) were determined from the intercept and slope of Adams-Bohart plot at different initial dye concentrations, bed height, and flow rates as shown in Tables 6.5.

The values of k_{AB} decreases as the initial concentration of dye and bed height increases indicating that the overall system kinetics was not dominated by external mass transfer. As the bed height increases the value of N_{AB} decreases from 5065.61 to 2928.49 mg/L. Of all the models used, it has the poorest fittings with R^2 values ranging from 0.7389 to 0.9359 indicating that the model has less applicability.

The Yoon-Nelson model is based on the concept of a two-phase flow, where the fluid is treated as one phase and the particles are treated as another phase. The model uses equations that describe the motion and behavior of the particles and the fluid, and includes terms that account for the interactions between the particles and the fluid. The values of rate constant (k_{YN}, 1/min), τ (time required for 50% BF breakthrough) were estimated from the slope and intercept of Yoon-Nelson plot at different concentrations, bed height, and flow rates as shown in Tables 6.5. The values of k_{YN} were found to increases with increases in concentration from 0.0018 to 0.0033 1/min and flow rate from 0.0017 to 0.0030 1/min but decreases with increases in bed height. The well-fitting of the experimental data with the Thomas model indicated that the external and internal diffusion is not the limiting step.

Table 6.5. *Parameters of different models for BF adsorption in packed bed at various conditions*

Column parameters			Thomas Model			Adams-Bohart Model			Yoon-Nelson Model		
Z (cm)	**F (mL/min)**	**C_0 (mg/mL)**	**q_0 (mg/g)**	**k_{TH} (mL/mg min)**	**R^2**	**N_{AB} (mg/L)**	**k_{AB} (mL/mg min)**	**R^2**	**k_{YN} (1/min)**	**τ (min)**	**R^2**
0.5	3	10	271.48	0.0180	0.9904	1285.81	0.0080	0.8802	0.0018	199.08	0.9904
0.5	3	50	822.05	0.0050	0.9817	4109.11	0.0020	0.8935	0.0025	120.57	0.9817
0.5	3	100	987.89	0.0033	0.9447	5770.60	0.0011	0.7389	0.0033	72.45	0.9447
0.5	1.5	50	624.26	0.0034	0.9409	3139.57	0.0014	0.8960	0.0017	183.12	0.9409
0.5	3	50	822.05	0.0050	0.9817	4109.11	0.0020	0.8935	0.0025	120.57	0.9817
0.5	6	50	1261.05	0.0060	0.9616	6777.27	0.0022	0.8967	0.0030	92.48	0.9616
0.25	3	50	828.65	0.0068	0.9662	5065.61	0.0020	0.9359	0.0034	54.58	0.9648
0.5	3	50	822.05	0.0050	0.9817	4109.11	0.0020	0.8935	0.0025	120.57	0.9817
1.0	3	50	630.39	0.0036	0.9648	2928.49	0.0016	0.8159	0.0018	189.12	0.9662

6.3. Significant findings

In the current research, Oxidant-modified Biochar (OBC) was prepared using SD for the removal of BF dye from aqueous system. The synthesized adsorbent was characterized using various analytical techniques like FESEM, FETEM, TGA, XRD, Raman spectroscopy and FTIR. It was found that OBC showed enhanced surface properties than raw SD. The TGA analysis showed that OBC is thermally stable over 850 °C. The XRD peaks at 28.54º, 31.28º and 51.66º in OBC confirms the presence of MnO_2 groups. The FTIR and Raman spectroscopic data presents the changes in function groups and vibrational modes confirming the modification of adsorbent before and after adsorption of BF. Batch adsorption studies were carried out to optimize process parameters like pH of BF solution, initial concentration of BF and OBC dosage. At pH 6.0, 10 mg/L initial concentration of BF and 0.05 g/L OBC dosage maximum removal efficiency of 98.28% was obtained. The isotherm and kinetic model fitting were done and the results showed that the adsorption of BF onto OBC follows Freundlich isotherm and pseudo second order kinetics. The phytotoxicity studies revealed that before adsorption process, BF was more toxic to the seeds of *Vigna* and after adsorption the toxicity level decreases due to the removal of BF from water by OBC. The continuous column studies show that at 0.5 cm bed height, 1.5 mL/min flowrate, 50 mg/L initial concentration, Yield % is 79.73. Thus, oxidant-modified biochar serves as an effective adsorbent for the removal of basic fuchsin dye from aqueous system.

6.4. APPLICATION OF ADSORBENTS ON REAL-TIME WASTEWATER

6.4.1. Collection of wastewater samples

Real-time wastewater samples used for the research work was collected from five different spots (**Spot 1**- 26°14'00.6"N, 91°42'19.2"E; **Spot 2**- 26°13'24.4"N, 91°42'41.0"E; **Spot 3**- 26°13'26.5"N, 91°42'55.5"E; **Spot 4**- 26°13'16.7"N, 91°42'32.3"E; **Spot 5**- 26°13'10.4"N, 91°42'38.1"E) of Brahmaputra Industrial Park, Gauripur, Assam as per the standard wastewater sampling protocol. Then the collected wastewater was examined for various physico-chemical parameters including biochemical oxygen demand (BOD, mg/L), chemical oxygen demand (COD, mg/L), total dissolved solids (TDS, mg/L), pH, conductivity (µs/cm), turbidity (NTU), salinity (%), and heavy metals (Cr, Ni, Zn, Cd, Cu, Ce, Mn, Co, and Pb) in (mg/L) before and after adsorption process.

6.4.2. Adsorption studies

All the adsorbents prepared for this research work were subjected to real-time analysis. Equal amount (0.01g) of Magnetic Sawdust (MSD), Corn starch nanoparticles (CSNP), Fe_3O_4/CAC nanocomposite (MCAC), Fe_3O_4/AC nanocomposite, and Oxidant-modified biochar (OBC) were mixed properly. Then it was added to the 1L of collected wastewater and kept at 35 °C for 4h under continuous shaking at 100 rpm. After 4h the adsorbents were recovered from the wastewater and the wastewater was analysed for the various physico-chemical parameters (after adsorption) using standard procedures.

6.4.3. Results and discussion

The various physico-chemical parameters of real-time wastewater before and after the adsorption process provide valuable insights into the effectiveness of the synthesized adsorbents via the adsorption process. Before the adsorption process, the collected wastewater exhibited higher levels of various pollutants, as indicated by parameters. These parameters are indicative of organic and inorganic contaminants, as well as the overall quality of the water. Following the adsorption process, a significant reduction in BOD, COD, TDS, pH, conductivity, and turbidity was observed, suggesting the successful removal of pollutants by adsorbents. The various physico-chemical parameters of real-time wastewater before and after the adsorption process were tabulated in the Table. 6.6. It is found that the pH of the wastewater before adsorption process was found between 5.72 to

8.01 which falls in the permissible pH given by World Health Organization (WHO) and Central Pollution Control Board (CPCB). The adsorption process proved effective in neutralizing the pH, indicating the method's capacity to mitigate acidity or alkalinity in the wastewater. Initially, the BOD levels were notably high, ranging from 4 to 23.4 mg/L. After the adsorption process, a remarkable reduction in BOD was observed, with values ranging from 0.8 to 8.3 mg/L. The BOD level of spot 5 is comparatively very low than other spots. This substantial decrease indicates the efficient removal of organic pollutants, demonstrating the adsorbent's capacity to mitigate the biodegradable organic matter in the wastewater. Similarly, the COD levels, initially ranging from 32 to 293 mg/L, experienced a substantial reduction after adsorption process, with values ranging from 4.4 to 57.5 mg/L. This signifies effective removal of both biodegradable and non-biodegradable organic pollutants. The conductivity levels, initially ranging from 137.4 to 470.1 µs/cm, witnessed a considerable decrease in post-adsorption, further indicating the removal of dissolved salts and ions. Initially, the concentrations of these heavy metals were varied, with values exceeding permissible limits in some spots. But after adsorption these values gets rapidly reduced to negligible values.

Overall, these results suggest that the adsorption of pollutants by synthesised adsorbents effectively improved the physico-chemical parameters of the wastewater, rendering it more compliant with environmental standards and demonstrating the potential for the use of these adsorbents in wastewater treatment.

Fig. 6.12. *Location spots for real-time water sample collection*

Table 6.6. *Physico-chemical parameters of real-time wastewater before and after adsorption process*

Indicators	WHO/EPA Standard	CPCB	Spot 1 26°14'00.6"N 91°42'19.2"E		Spot 2 26°13'24.4"N 91°42'41.0"E		Spot 3 26°13'26.5"N 91°42'55.5"E		Spot 4 26°13'16.7"N 91°42'32.3"E		Spot 5 26°13'10.4"N 91°42'38.1"E	
			BA	**AA**	**BA**	**AA**	**BA**	**AA**	**BA**	**AA**	**BA**	**AA**
BOD (mg/L)	**nil/ 5.0-7.0**	**30**	23.4	8.3	16	3.7	4.7	1.1	20	4.6	4	0.8
COD (mg/L)	**nil/ 40**	**250**	288	57.5	172	22.2	40	7.9	293	28.6	32	4.4
TDS (mg/L)	**1000/ nil**	**nil**	234.3	89.6	194.6	71.1	68.7	17.3	206.2	76.4	43.2	13.6
pH	**6.0-8.5/ 6.0-9.5**	**5.5-9.0**	5.72	7.34	6.47	6.91	8.01	7.2	6.23	6.56	7.2	7.31
Conductivity (µs/cm)	**nil/ 1000**	**nil**	470.1	186.2	398.9	127	121.7	33.9	452.3	159.3	137.4	42.4
Turbidity (NTU)	**5**	**nil**	33.64	5.42	26.42	3.96	4.18	1.12	41.67	7.83	2.16	1.75

Salinity (%)	**nil**	**3.5**	0.9	0.4	0.8	0.4	0.3	0.2	0.9	0.5	0.2	0.2
Cr (mg/L)	**0.05**	**0.1**	1.6	0.06	0.07	0.02	0.02	0	2.1	0.18	0	0
Ni (mg/L)	**0.07/ 0.02**	**3**	1.2	0.02	0.02	0	0	0	1.5	0.09	0	0
Zn (mg/L)	**nil/ 3**	**5**	0.08	0	0.03	0	0.12	0.03	2.7	0.56	0.01	0
Cd (mg/L)	**0.003**	**2**	0.02	0	0.02	0	0	0	0.01	0	0	0
Cu (mg/L)	**2.0 / 1.0**	**3**	1.2	0.05	0.81	0.07	0.05	0	0.24	0.04	0	0
Ce (mg/L)	**nil**	**nil**	0.8	0	0.12	0	0	0	0.8	0	0	0
Mn (mg/L)	**nil / 0.2**	**2**	0	0	0	0	0.04	0	0	0	0	0
Co (mg/L)	**0.01**	**0.1**	0.01	0	0.03	0.02	0	0	0.7	0.6	0	0
Pb (mg/L)	**0.01**	**0.1**	0.56	0.01	0.33	0	0.02	0	1.2	0.01	0	0

BA- Before Adsorption; AA- After Adsorption

Chapter 7

Summary and Overall Conclusion

7.1. Overall Summary

The Chapter 1 begins with a broad introduction to the global concern of water quality degradation, highlighting the rise of contaminants of emerging concern and their potential impacts on human health and the environment. It emphasizes the urgency of addressing these issues and introduces the thesis's central focus on utilizing bio-based engineered adsorbents for the removal of these contaminants. It also emphasizes various theoretical aspects in modelling studies. Moreover, this chapter briefly introduces the specific problem statements and the outline of the thesis.

In the Chapter 2, the saw dust which is a by-product of wood processing was made magnetic, since magnetic sawdust (MSD) can be separated easily from the water after biosorption. MSD can be effectively used for the removal of diclofenac (DCF). The effect of experimental parameters was optimized in batch mode with evaluated maximum efficiency of 86.12% at pH 6.0, biosorbent dosage 0.025 g/L for 50 mg/L of DCF. Various ecotoxicological effects such as phytotoxicity using plant seeds of *Vigna mungo* (black gram), *Macrotyloma uniflorum* (horse gram), *Cicer arietinum* (Bengal gram), *Vigna radiata* (green gram), *Pennisetum glaucum* (pearl millet), microbial toxicity using *E. coli* and *B. subtilis* were studied and their inhibition concentration (IC_{50}) values were determined before and after DCF biosorption. Moreover, acute fish toxicity on exposure of DCF, on *Danio rerio* (zebra fish) were performed and (lethal concentration) LC_{50} values were evaluated in this chapter.

In the Chapter 3, corn starch nanoparticles (CSNP) were synthesised using acid hydrolysis for the removal of two anionic pharmaceuticals ibuprofen (IBU) and sulfamethoxazole (SUL) from the water. The efficiency of IBU and SUL removal was determined as a function of concentration in the experiments. The rate and mechanism of IBU and SUL biosorption using CSNP was studied by performing kinetic modelling. Two and three parameter isotherm models were used to study the biosorption equilibrium. Various seed toxicity assessment including inhibition of seedling growth (%) and germination (%) of the seedlings using plant seeds of *Vigna mungo* (VM) and *Vigna radiata* (VR) were studied. Acute fish toxicity on exposure of pharmaceuticals IBU and SUL at different concentrations before and after biosorption process by CSNP, on *Danio rerio* (zebra fish) were done and LC_{50} values for IBU and SUL exposure were calculated in this study.

In Chapter 4, Fe_3O_4/CAC nanocomposite was synthesised via a simple co-precipitation method and used to adsorb cerium (Ce^{3+}). In this study, commercial activated carbon (CAC) was impregnated with iron oxide (Fe_3O_4) particles, which adds desired characteristics to the biosorbent, thereby making the surface more active to contaminants. The maximum removal of Ce^{3+} by MCAC was optimized at pH 6.0, initial concentration of 20 mg/L and 0.04 g/L of MCAC with adsorption capacity (Q_0) 86.206 mg/g. To assess the biosorption capacity of MCAC nanocomposite different kinetic models were discussed in the treatment of water containing Ce^{3+}. Different ecotoxicological assessments including seed toxicity using plant seeds of *Vigna mungo* and *Vigna radiata* were studied. Acute fish toxicity on exposure of Ce^{3+} at various concentrations before and after biosorption process, on *Danio rerio* (zebra fish) were done and LC_{50} values were calculated in this study.

In the Chapter 5, the magsorbent of Iron oxide/Activated Carbon (Fe_3O_4/AC) nanocomposite was synthesized by incorporating iron oxide (Fe_3O_4) on the surface of activated carbon (AC). The incorporation of iron oxide on activated carbon provides the ferromagnetic property to Fe_3O_4/AC nanocomposite, which helps the magsorbent for rapid and easy separation from the aqueous solution after the biosorption of Pb and CR. Fe_3O_4/AC nanocomposite was efficiently used to remove Pb and CR from the water. Different toxicological assessments including seed toxicity, seed germination (%), and growth inhibition (%) using plant seeds of *Pennisetum glaucum, Cicer arietinum, Vigna mungo,* and *Vigna radiata* were studied. Acute fish toxicity on exposure of Pb and CR at various concentrations before and after the biosorption process on *Danio rerio* (zebrafish) was done, and LC_{50} values were calculated in this study.

In the Chapter 6, sawdust is modified into biochar in presence of potassium permanganate ($KMnO_4$) and thus the oxidant-modified biochar (OBC) was used as the adsorbent. The treatment with oxidizing agent could enhance the functional groups like carboxylic, phenolic, hydroxyl and amide groups in the surface of OBC and hence leads to effective Basic Fuchsin (BF) dye removal. At pH 6.0, 10 mg/L initial concentration of BF and 0.05 g/L OBC dosage maximum removal efficiency of 98.28% was obtained. Toxicity before and after adsorption process were evaluated using *Vigna radiata.* The regeneration studies were performed to determine the re-usability of OBC. Moreover, continuous column experiments were performed to study the process of adsorption in industrial and laboratory

setup. Various parameters influencing the adsorption of BF such as bed height, initial BF concentration and flow rate were studied in this chapter.

The comparison table of various bio-based engineered adsorbents and the model pollutants used in the entire thesis work along with their various adsorption parameters were tabulated in the Table 7.1.

7.2. Significance of thesis work

- ✓ This work will contribute to sustainable engineering practices.
- ✓ The synthesized bio-based engineered adsorbents will act as an alternative to activated carbon filters in water purification systems.
- ✓ The synthesized magnetic adsorbents have advantages in terms of selectivity, regeneration, and separation from water systems after adsorption process.
- ✓ Used adsorbents can be converted in to fertilizers.

7.3. Future perspectives

- ✓ The integration of adsorption by bio-based engineered adsorbents with other water treatment technologies.
- ✓ Expanding toxicological evaluations to encompass long-term and cumulative effects on various model organisms.
- ✓ Laboratory-scale studies to practical applications.
- ✓ Formulating the regulatory frameworks to incorporate bio-based engineered adsorbents in water quality standards.

Table 7.1. *Adsorption parameters of various bio-based engineered adsorbents and the model pollutants used in the entire thesis work*

Adsorbent	Pollutant	pH	Adsorbent Dosage (g/L)	Initial Concentration (mg/L)	Temp. (°C)	Isotherm	Kinetics	Reusability (Cycles)	Adsorption Capacity (mg/g)	% Removal
MSD	DCF	6.0	0.025	50	25	Freundlich	IPD	5	107.52	86.12
MCAC	Ce^{3+}	6.0	0.04	20	35	Langmuir	IPD	3	86.21	77.90
Fe_3O_4/AC	Pb	6.0	0.04	40	30	Freundlich	IPD	3	144.92	78.17
	CR	6.0	0.04	40	30	Langmuir	IPD	3	122.22	82.41
CSNP	IBU	2.0	0.01	10	35	Temkin	PSO	5	65.35	86.33
	SUL	3.0	0.01	10	35	Langmuir	PSO	5	96.15	85.80
OBC	BF	6.0	0.05	10	35	Freundlich	PSO	5	241.19	91.74

7.4. Overall Conclusion

In conclusion, this research has undertaken a comprehensive exploration into the realm of water quality enhancement through the application of bio-based engineered adsorbents for the adsorptive removal of contaminants of emerging concern (CECs). Through a combination of sophisticated modeling techniques and rigorous toxicological evaluations, the research has made significant contributions to our understanding of the effectiveness and implications of utilizing these innovative bio-based adsorbents. The key findings of this study underscore the potential of bio-based engineered adsorbents as a viable and sustainable solution for the removal of CECs from water sources. The predicted models, grounded in fundamental principles of adsorption, provide valuable insights into the mechanisms governing the adsorption process and offer a predictive tool for optimizing system parameters.

Furthermore, the toxicological evaluations conducted as part of this research shed light on the environmental implications of CEC removal. The assessment of pollutants and the overall impact on aquatic ecosystems contribute to a more holistic understanding of the trade-offs involved in water treatment strategies. While the results demonstrate promising outcomes, it is essential to acknowledge the limitations inherent in any scientific inquiry. Variabilities in real-world conditions, the dynamic nature of water matrices, and the potential long-term effects of continuous adsorption processes necessitate ongoing research in this field. Addressing these challenges will not only refine the proposed models but also pave the way for the practical implementation of bio-based engineered adsorbents on a larger scale. Looking ahead, this research provides a foundation for future research endeavours. The identified research gaps and limitations present opportunities for further exploration, including the refinement of adsorbent materials, optimization of operational parameters, and the development of more comprehensive toxicity assessments. In essence, the work presented in this report contributes to the evolving landscape of water quality management by offering a sustainable approach to addressing contaminants of emerging concern. By combining scientific rigor with a commitment to environmental stewardship, this research marks a significant step toward ensuring the availability of clean and safe water resources for present and future generations.

Bibliography

- Abbas, Q., Mirzaeian, M., Ogwu, A.A., Mazur, M., Gibson, D., 2020. Effect of physical activation/surface functional groups on wettability and electrochemical performance of carbon/activated carbon aerogels based electrode materials for electrochemical capacitors. Int. J. Hydrogen Energy 45, 13586–13595. https://doi.org/https://doi.org/10.1016/j.ijhydene.2018.04.099
- Abutaleb, A., Tayeb, A.M., Mahmoud, M.A., Daher, A.M., Desouky, O.A., Bakather, O.Y., Farouq, R., 2020. Removal and recovery of U(VI) from aqueous effluents by flax fiber: Adsorption, desorption and batch adsorber proposal. J. Adv. Res. 22, 153–162. https://doi.org/https://doi.org/10.1016/j.jare.2019.10.011
- Ahmed, S.F., Mofijur, M., Nuzhat, S., Chowdhury, A.T., Rafa, N., Uddin, M.A., Inayat, A., Mahlia, T.M.I., Ong, H.C., Chia, W.Y., Show, P.L., 2021. Recent developments in physical, biological, chemical, and hybrid treatment techniques for removing emerging contaminants from wastewater. J. Hazard. Mater. 416, 125912. https://doi.org/https://doi.org/10.1016/j.jhazmat.2021.125912
- Ahsan, Md Ariful, Islam, M.T., Hernandez, C., Kim, H., Lin, Y., Curry, M.L., Gardea-Torresdey, J., Noveron, J.C., 2018. Adsorptive Removal of Sulfamethoxazole and Bisphenol A from Contaminated Water using Functionalized Carbonaceous Material Derived from Tea Leaves. J. Environ. Chem. Eng. 6, 4215–4225. https://doi.org/https://doi.org/10.1016/j.jece.2018.06.022
- Ahsan, Md. Ariful, Islam, M.T., Imam, M.A., Hyder, A.H.M.G., Jabbari, V., Dominguez, N., Noveron, J.C., 2018. Biosorption of bisphenol A and sulfamethoxazole from water using sulfonated coffee waste: Isotherm, kinetic and thermodynamic studies. J. Environ. Chem. Eng. 6, 6602–6611. https://doi.org/https://doi.org/10.1016/j.jece.2018.10.004
- Al-Juboori, R.A., Bakly, S., Bowtell, L., Alkurdi, S.S.A., Altaee, A., 2022. Innovative capacitive deionization-degaussing approach for improving adsorption/desorption for macadamia nutshell biochar. J. Water Process Eng. 47, 102786. https://doi.org/https://doi.org/10.1016/j.jwpe.2022.102786
- Allahkarami, E., Rezai, B., 2019. Removal of cerium from different aqueous solutions using different adsorbents: A review. Process Saf. Environ. Prot. 124, 345–362. https://doi.org/https://doi.org/10.1016/j.psep.2019.03.002

- Aluko, O.A., Osei Opoku, E.E., Ibrahim, M., 2021. Investigating the environmental effect of globalization: Insights from selected industrialized countries. J. Environ. Manage. 281, 111892. https://doi.org/https://doi.org/10.1016/j.jenvman.2020.111892
- Amdany, R., Chimuka, L., Cukrowska, E., 2014. Determination of naproxen, ibuprofen and triclosan in wastewater using the polar organic chemical integrative sampler (POCIS): A laboratory calibration and field application. Water SA 40, 407. https://doi.org/10.4314/wsa.v40i3.3
- Amusat, S.O., Kebede, T.G., Dube, S., Nindi, M.M., 2021. Ball-milling synthesis of biochar and biochar–based nanocomposites and prospects for removal of emerging contaminants: A review. J. Water Process Eng. 41, 101993. https://doi.org/https://doi.org/10.1016/j.jwpe.2021.101993
- Anastopoulos, I., Bhatnagar, A., Lima, E.C., 2016. Adsorption of rare earth metals: A review of recent literature. J. Mol. Liq. 221, 954–962. https://doi.org/10.1016/j.molliq.2016.06.076
- Anwar, H., Shahid, M., Natasha, Niazi, N.K., Khalid, S., Tariq, T.Z., Ahmad, S., Nadeem, M., Abbas, G., 2021. Risk assessment of potentially toxic metal(loid)s in Vigna radiata L. under wastewater and freshwater irrigation. Chemosphere 265, 129124. https://doi.org/https://doi.org/10.1016/j.chemosphere.2020.129124
- Aoopngan, C., Nonkumwong, J., Phumying, S., Promjantuek, W., Maensiri, S., Noisa, P., Pinitsoontorn, S., Ananta, S., Srisombat, L., 2019. Amine-Functionalized and Hydroxyl-Functionalized Magnesium Ferrite Nanoparticles for Congo Red Adsorption. ACS Appl. Nano Mater. 2, 5329–5341. https://doi.org/10.1021/acsanm.9b01305
- Awokoya, K.N., Oninla, V.O., Bello, D.J., 2021. Corrigendum to "Synthesis of oxidized Dioscorea dumentorum starch nanoparticles for the adsorption of lead(II) and cadmium(II) ions from wastewater" [Environ. Nanotechnol. Monit. Manage. 15 (May) (2021) 100440]. Environ. Nanotechnology, Monit. Manag. 16, 100489. https://doi.org/https://doi.org/10.1016/j.enmm.2021.100489
- Azari, A., Kakavandi, B., Kalantary, R.R., Ahmadi, E., Gholami, M., Torkshavand, Z., Azizi, M., 2015. Rapid and efficient magnetically removal of heavy metals by magnetite-activated carbon composite: a statistical design approach. J. Porous Mater. 22, 1083–1096. https://doi.org/10.1007/s10934-015-9983-z
- Azizian, S., 2004. Kinetic models of sorption: a theoretical analysis. J. Colloid Interface Sci. 276, 47–52. https://doi.org/https://doi.org/10.1016/j.jcis.2004.03.048

- Ba Mohammed, B., Hsini, A., Abdellaoui, Y., Abou Oualid, H., Laabd, M., El Ouardi, M., Ait Addi, A., Yamni, K., Tijani, N., 2020. Fe-ZSM-5 zeolite for efficient removal of basic Fuchsin dye from aqueous solutions: Synthesis, characterization and adsorption process optimization using BBD-RSM modeling. J. Environ. Chem. Eng. 8, 104419. https://doi.org/https://doi.org/10.1016/j.jece.2020.104419
- Balakrishna, K., Praveenkumarreddy, Y., Nishitha, D., Gopal, C.M., Shenoy, J.K., Bhat, K., Khare, N., Dhangar, K., Kumar, M., 2023. Occurrences of UV filters, endocrine disruptive chemicals, alkyl phenolic compounds, fragrances, and hormones in the wastewater and coastal waters of the Antarctica. Environ. Res. 222, 115327. https://doi.org/10.1016/j.envres.2023.115327
- Barmi, A.-A.M., Aghazadeh, M., Moosavian, M.A., Golikand, A.N., 2020. Binder-free high-performance Fe3O4 fine particles in situ grown onto N-doped porous graphene layers co-embedded into porous substrate as supercapacitor electrode. J. Mater. Sci. Mater. Electron. 31, 15198–15217. https://doi.org/10.1007/s10854-020-04085-0
- Belachew, N., Bekele, G., 2020. Synergy of Magnetite Intercalated Bentonite for Enhanced Adsorption of Congo Red Dye. Silicon 12, 603–612. https://doi.org/10.1007/s12633-019-00152-2
- Bunluesin, S., Kruatrachue, M., Pokethitiyook, P., Upatham, S., Lanza, G.R., 2007. Batch and continuous packed column studies of cadmium biosorption by Hydrilla verticillata biomass. J. Biosci. Bioeng. 103, 509–513. https://doi.org/10.1263/jbb.103.509
- Calero, M., Hernáinz, F., Blázquez, G., Tenorio, G., Martín-Lara, M.A., 2009. Study of Cr (III) biosorption in a fixed-bed column. J. Hazard. Mater. 171, 886–893. https://doi.org/10.1016/j.jhazmat.2009.06.082
- Çalik, S., Sözüdoğru, O., Massara, T.M., Yılmaz, A.E., Bakırdere, S., Katsou, E., Komesli, O.T., 2021. Removal of Heavy Metals by a Membrane Bioreactor Combined with Activated Carbon. Anal. Lett. 54, 1616–1626. https://doi.org/10.1080/00032719.2020.1818089
- Carvalho Costa, A.W.M., Guerhardt, F., Ribeiro Júnior, S.E.R., Cânovas, G., Vanale, R.M., de Freitas Coelho, D., Ehrhardt, D.D., Rosa, J.M., BasileTambourgi, E., Curvelo Santana, J.C., de Souza, R.R., 2020. Biosorption of Cr(VI) using coconut fibers from agro-industrial waste magnetized using magnetite nanoparticles. Environ. Technol. 1–12. https://doi.org/10.1080/09593330.2020.1752812

- Chabani, M., Amrane, A., Bensmaili, A., 2006. Kinetic modelling of the adsorption of nitrates by ion exchange resin. Chem. Eng. J. 125, 111–117. https://doi.org/10.1016/j.cej.2006.08.014
- Chandra, S., Sukumaran, S., 2020. Physiological, Biochemical and Neurochemical responses of Cirrhinus mrigala upon short term exposure to Cerium oxide. Int. J. Aquat. Biol. 7, 368–373.
- Chandrasekaran, A., Patra, C., Narayanasamy, S., Subbiah, S., 2020. Adsorptive removal of Ciprofloxacin and Amoxicillin from single and binary aqueous systems using acid-activated carbon from Prosopis juliflora. Environ. Res. 188, 109825. https://doi.org/https://doi.org/10.1016/j.envres.2020.109825
- Chen, C., Qiu, M., 2021. High efficiency removal of Pb(ii) in aqueous solution by a biochar-supported nanoscale ferrous sulfide composite. RSC Adv. 11, 953–959. https://doi.org/10.1039/D0RA08055A
- Chen, H., Gao, Y., Li, J., Fang, Z., Bolan, N., Bhatnagar, A., Gao, B., Hou, D., Wang, S., Song, H., Yang, X., Shaheen, S.M., Meng, J., Chen, W., Rinklebe, J., Wang, H., 2022. Engineered biochar for environmental decontamination in aquatic and soil systems: a review. Carbon Res. 1, 4. https://doi.org/10.1007/s44246-022-00005-5
- Chen, M.-J., Liu, Y.-T., Lin, C.-W., Ponnusamy, V.K., Jen, J.-F., 2013. Rapid determination of triclosan in personal care products using new in-tube based ultrasound-assisted salt-induced liquid–liquid microextraction coupled with high performance liquid chromatography-ultraviolet detection. Anal. Chim. Acta 767, 81–87. https://doi.org/10.1016/j.aca.2013.01.014
- Chen, X., Wang, Y., Lv, J., Feng, Z., Liu, Yuting, Xia, H., Li, Y., Wang, C., Zeng, K., Liu, Yan, 2022. Simple one-pot synthesis of manganese dioxide modified bamboo-derived biochar composites for uranium (vi) removal. New J. Chem. 46, 14427–14438.
- Cheng, N., Wang, B., Wu, P., Lee, X., Xing, Y., Chen, M., Gao, B., 2021. Adsorption of emerging contaminants from water and wastewater by modified biochar: A review. Environ. Pollut. 273, 116448. https://doi.org/https://doi.org/10.1016/j.envpol.2021.116448
- Chikri, R., Elhadiri, N., Benchanaa, M., El maguana, Y., 2020. Efficiency of Sawdust as Low-Cost Adsorbent for Dyes Removal. J. Chem. 2020, 8813420. https://doi.org/10.1155/2020/8813420

- Chowdhury, Z.Z., Karim, M.Z., Ashraf, M.A., Khalid, K., 2016. Influence of carbonization temperature on physicochemical properties of biochar derived from slow pyrolysis of durian wood (Durio zibethinus) sawdust. BioResources 11, 3356–3372.
- Chu, K.H., 2020. Breakthrough curve analysis by simplistic models of fixed bed adsorption: In defense of the century-old Bohart-Adams model. Chem. Eng. J. 380, 122513. https://doi.org/10.1016/j.cej.2019.122513
- Chu, K.H., Hashim, M.A., Debord, J., Harel, M., Salvestrini, S., Bollinger, J.-C., 2023. The Jovanović adsorption isotherm in water contaminant research: Unmasking spurious versions and spotlighting the real thing. Chem. Eng. Sci. 281, 119127. https://doi.org/10.1016/j.ces.2023.119127
- D'Cruz, B., Madkour, M., Amin, M.O., Al-Hetlani, E., 2020. Efficient and recoverable magnetic AC-Fe3O4 nanocomposite for rapid removal of promazine from wastewater. Mater. Chem. Phys. 240, 122109. https://doi.org/https://doi.org/10.1016/j.matchemphys.2019.122109
- Dai, Y., Zhang, N., Xing, C., Cui, Q., Sun, Q., 2019. The adsorption, regeneration and engineering applications of biochar for removal organic pollutants: A review. Chemosphere 223, 12–27. https://doi.org/10.1016/j.chemosphere.2019.01.161
- Danalıoğlu, S.T., Bayazit, Ş.S., Kerkez Kuyumcu, Ö., Salam, M.A., 2017. Efficient removal of antibiotics by a novel magnetic adsorbent: Magnetic activated carbon/chitosan (MACC) nanocomposite. J. Mol. Liq. 240, 589–596. https://doi.org/https://doi.org/10.1016/j.molliq.2017.05.131
- Dashtian, K., Zare-Dorabei, R., 2017. Synthesis and characterization of functionalized mesoprous SBA-15 decorated with Fe3O4 nanoparticles for removal of Ce(III) ions from aqueous solution: ICP–OES detection and central composite design optimization. J. Colloid Interface Sci. 494, 114–123. https://doi.org/https://doi.org/10.1016/j.jcis.2017.01.072
- Delgado-Moreno, L., Bazhari, S., Gasco, G., Méndez, A., El Azzouzi, M., Romero, E., 2021. New insights into the efficient removal of emerging contaminants by biochars and hydrochars derived from olive oil wastes. Sci. Total Environ. 752, 141838. https://doi.org/https://doi.org/10.1016/j.scitotenv.2020.141838
- Demarchi, C.A., Michel, B.S., Nedelko, N., Ślawska-Waniewska, A., Dłużewski, P., Kaleta, A., Minikayev, R., Strachowski, T., Lipińska, L., Dal Magro, J., Rodrigues, C.A., 2019. Preparation, characterization, and application of magnetic activated carbon

from termite feces for the adsorption of Cr(VI) from aqueous solutions. Powder Technol. 354, 432–441. https://doi.org/https://doi.org/10.1016/j.powtec.2019.06.020

- Deng, H., Zhang, J., Huang, R., Wang, W., Meng, M., Hu, L., Gan, W., 2022. Adsorption of Malachite Green and Pb2+ by KMnO4-Modified Biochar: Insights and Mechanisms. Sustainability. https://doi.org/10.3390/su14042040
- Diatloff, E., Smith, F.W., Asher, C.J., 2008. Effects of Lanthanum and Cerium on the Growth and Mineral Nutrition of Corn and Mungbean. Ann. Bot. 101, 971–982. https://doi.org/10.1093/aob/mcn021
- Dubinin, M.M., 1947. The equation of the characteristic curve of activated charcoal, in: Dokl. Akad. Nauk. SSSR. pp. 327–329.
- Dutta, S., Gupta, B., Srivastava, S.K., Gupta, A.K., 2021. Recent advances on the removal of dyes from wastewater using various adsorbents: a critical review. Mater. Adv. 2, 4497–4531. https://doi.org/10.1039/D1MA00354B
- Ebadollahzadeh, H., Zabihi, M., 2020. Competitive adsorption of methylene blue and Pb (II) ions on the nano-magnetic activated carbon and alumina. Mater. Chem. Phys. 248, 122893. https://doi.org/https://doi.org/10.1016/j.matchemphys.2020.122893
- El-Azazy, M., El-Shafie, A.S., Ashraf, A., Issa, A.A., 2019. Eco-Structured Biosorptive Removal of Basic Fuchsin Using Pistachio Nutshells: A Definitive Screening Design—Based Approach. Appl. Sci. https://doi.org/10.3390/app9224855
- El-Khaiary, M.I., Malash, G.F., Ho, Y.-S., 2010. On the use of linearized pseudo-second-order kinetic equations for modeling adsorption systems. Desalination 257, 93–101. https://doi.org/10.1016/j.desal.2010.02.041
- El-Naggar, A., Shaheen, S.M., Ok, Y.S., Rinklebe, J., 2018. Biochar affects the dissolved and colloidal concentrations of Cd, Cu, Ni, and Zn and their phytoavailability and potential mobility in a mining soil under dynamic redox-conditions. Sci. Total Environ. 624, 1059–1071. https://doi.org/https://doi.org/10.1016/j.scitotenv.2017.12.190
- El Haddad, M., 2016. Removal of Basic Fuchsin dye from water using mussel shell biomass waste as an adsorbent: Equilibrium, kinetics, and thermodynamics. J. Taibah Univ. Sci. 10, 664–674. https://doi.org/10.1016/j.jtusci.2015.08.007
- Emnet, P., Mahaliyana, A.S., Northcott, G., Gaw, S., 2020. Organic Micropollutants in Wastewater Effluents and the Receiving Coastal Waters, Sediments, and Biota of

Lyttelton Harbour (Te Whakaraupō), New Zealand. Arch. Environ. Contam. Toxicol. 79, 461–477. https://doi.org/10.1007/s00244-020-00760-9

- Eslami, H., Ehrampoush, M.H., Esmaeili, A., Salmani, M.H., Ebrahimi, A.A., Ghaneian, M.T., Falahzadeh, H., Fard, R.F., 2019. Enhanced coagulation process by Fe-Mn bimetal nano-oxides in combination with inorganic polymer coagulants for improving As(V) removal from contaminated water. J. Clean. Prod. 208, 384–392. https://doi.org/https://doi.org/10.1016/j.jclepro.2018.10.142
- Esmaeili, A., Eslami, H., 2020. Adsorption of Pb (II) and Zn (II) ions from aqueous solutions by Red Earth. MethodsX 7, 100804. https://doi.org/https://doi.org/10.1016/j.mex.2020.100804
- Fabre, E., Lopes, C.B., Vale, C., Pereira, E., Silva, C.M., 2020. Valuation of banana peels as an effective biosorbent for mercury removal under low environmental concentrations. Sci. Total Environ. 709, 135883. https://doi.org/https://doi.org/10.1016/j.scitotenv.2019.135883
- Fang, Z., Gao, Y., Bolan, N., Shaheen, S.M., Xu, S., Wu, X., Xu, X., Hu, H., Lin, J., Zhang, F., Li, J., Rinklebe, J., Wang, H., 2020. Conversion of biological solid waste to graphene-containing biochar for water remediation: A critical review. Chem. Eng. J. 390, 124611. https://doi.org/https://doi.org/10.1016/j.cej.2020.124611
- Feng, Z., Chen, H., Li, H., Yuan, R., Wang, F., Chen, Z., Zhou, B., 2020. Preparation, characterization, and application of magnetic activated carbon for treatment of biologically treated papermaking wastewater. Sci. Total Environ. 713, 136423. https://doi.org/https://doi.org/10.1016/j.scitotenv.2019.136423
- Forgionny, A., Acelas, N.Y., Ocampo-Pérez, R., Padilla-Ortega, E., Leyva-Ramos, R., Flórez, E., 2021. Understanding mechanisms in the adsorption of lead and copper ions on chili seed waste in single and multicomponent systems: a combined experimental and computational study. Environ. Sci. Pollut. Res. https://doi.org/10.1007/s11356-020-11721-z
- Foroughi-dahr, M., Esmaieli, M., Abolghasemi, H., Shojamoradi, A., Sadeghi Pouya, E., 2016. Continuous adsorption study of congo red using tea waste in a fixed-bed column. Desalin. Water Treat. 57, 8437–8446. https://doi.org/10.1080/19443994.2015.1021849
- Freundlich, H., 1907. Über die Adsorption in Lösungen. Zeitschrift für Phys. Chemie 57U, 385–470. https://doi.org/10.1515/zpch-1907-5723

- Frîncu, R.-M., 2021. Long-Term Trends in Water Quality Indices in the Lower Danube and Tributaries in Romania (1996–2017). Int. J. Environ. Res. Public Health 18, 1665. https://doi.org/10.3390/ijerph18041665
- Gallios, G.P., Tolkou, A.K., Katsoyiannis, I.A., Stefusova, K., Vaclavikova, M., Deliyanni, E.A., 2017. Adsorption of Arsenate by Nano Scaled Activated Carbon Modified by Iron and Manganese Oxides. Sustain. . https://doi.org/10.3390/su9101684
- Gao, M., Wang, X., Xia, C., Song, N., Ma, Y., Wang, Q., Yang, T., Ge, S., Wu, C., Lam, S.S., 2021. Phenol removal via activated carbon from co-pyrolysis of waste coal tar pitch and vinasse. Korean J. Chem. Eng. 38, 64–71. https://doi.org/10.1007/s11814-020-0676-1
- Gao, T., Fjellvåg, H., Norby, P., 2009. A comparison study on Raman scattering properties of α- and β-MnO2. Anal. Chim. Acta 648, 235–239. https://doi.org/https://doi.org/10.1016/j.aca.2009.06.059
- García, A., Espinosa, R., Delgado, L., Casals, E., González, E., Puntes, V., Barata, C., Font, X., Sánchez, A., 2011. Acute toxicity of cerium oxide, titanium oxide and iron oxide nanoparticles using standardized tests. Desalination 269, 136–141. https://doi.org/https://doi.org/10.1016/j.desal.2010.10.052
- Ghanbarlou, H., Nasernejad, B., Nikbakht Fini, M., Simonsen, M.E., Muff, J., 2020. Synthesis of an iron-graphene based particle electrode for pesticide removal in three-dimensional heterogeneous electro-Fenton water treatment system. Chem. Eng. J. 395, 125025. https://doi.org/10.1016/j.cej.2020.125025
- Ghani, W.A.W.A.K., Mohd, A., da Silva, G., Bachmann, R.T., Taufiq-Yap, Y.H., Rashid, U., Al-Muhtaseb, A.H., 2013. Biochar production from waste rubber-wood-sawdust and its potential use in C sequestration: Chemical and physical characterization. Ind. Crops Prod. 44, 18–24. https://doi.org/https://doi.org/10.1016/j.indcrop.2012.10.017
- Gogoi, A., Mazumder, P., Tyagi, V.K., Tushara Chaminda, G.G., An, A.K., Kumar, M., 2018. Occurrence and fate of emerging contaminants in water environment: A review. Groundw. Sustain. Dev. 6, 169–180. https://doi.org/10.1016/j.gsd.2017.12.009
- Gorzin, F., Bahri Rasht Abadi, M.M., 2018. Adsorption of Cr (VI) from aqueous solution by adsorbent prepared from paper mill sludge: Kinetics and thermodynamics studies. Adsorpt. Sci. Technol. 36, 149–169.

- Guedidi, H., Reinert, L., Soneda, Y., Bellakhal, N., Duclaux, L., 2017. Adsorption of ibuprofen from aqueous solution on chemically surface-modified activated carbon cloths. Arab. J. Chem. 10, S3584–S3594. https://doi.org/https://doi.org/10.1016/j.arabjc.2014.03.007
- Guillossou, R., Le Roux, J., Mailler, R., Pereira-Derome, C.S., Varrault, G., Bressy, A., Vulliet, E., Morlay, C., Nauleau, F., Rocher, V., 2020. Influence of dissolved organic matter on the removal of 12 organic micropollutants from wastewater effluent by powdered activated carbon adsorption. Water Res. 115487.
- Guo, S., Gao, M., Shen, T., Xiang, Y., Cao, G., 2019. Effective adsorption of sulfamethoxazole by novel Organo-Vts and their mechanistic insights. Microporous Mesoporous Mater. 286, 36–44. https://doi.org/https://doi.org/10.1016/j.micromeso.2019.05.032
- Guo, X., Liu, Y., Wang, J., 2019. Sorption of sulfamethazine onto different types of microplastics: A combined experimental and molecular dynamics simulation study. Mar. Pollut. Bull. 145, 547–554. https://doi.org/10.1016/j.marpolbul.2019.06.063
- Gupta, V.K., Agarwal, S., Ahmad, R., Mirza, A., Mittal, J., 2020. Sequestration of toxic congo red dye from aqueous solution using ecofriendly guar gum/ activated carbon nanocomposite. Int. J. Biol. Macromol. 158, 1310–1318. https://doi.org/https://doi.org/10.1016/j.ijbiomac.2020.05.025
- Gupta, V.K., Mittal, A., Gajbe, V., Mittal, J., 2008. Adsorption of basic fuchsin using waste materials—bottom ash and deoiled soya—as adsorbents. J. Colloid Interface Sci. 319, 30–39. https://doi.org/https://doi.org/10.1016/j.jcis.2007.09.091
- Han, Q., Du, M., Guan, Y., Luo, G., Zhang, Z., Li, T., Ji, Y., 2020. Removal of simulated radioactive cerium (III) based on innovative magnetic trioctylamine-polystyrene composite microspheres. Chem. Phys. Lett. 741, 137092. https://doi.org/https://doi.org/10.1016/j.cplett.2020.137092
- Haroon, M., Wang, L., Yu, H., Abbasi, N.M., Zain-ul-Abdin, Saleem, M., Khan, R.U., Ullah, R.S., Chen, Q., Wu, J., 2016. Chemical modification of starch and its application as an adsorbent material. RSC Adv. 6, 78264–78285. https://doi.org/10.1039/C6RA16795K
- Heo, J., Kim, S., Her, N., Park, C.M., Yu, M., Yoon, Y., 2020. Removal of contaminants of emerging concern by FO, RO, and UF membranes in water and wastewater, in:

Contaminants of Emerging Concern in Water and Wastewater. Elsevier, pp. 139–176. https://doi.org/10.1016/B978-0-12-813561-7.00005-5

- Hernández-Zamora, M., Martínez-Jerónimo, F., 2019. Congo red dye diversely affects organisms of different trophic levels: a comparative study with microalgae, cladocerans, and zebrafish embryos. Environ. Sci. Pollut. Res. 26, 11743–11755. https://doi.org/10.1007/s11356-019-04589-1
- Hoslett, J., Ghazal, H., Ahmad, D., Jouhara, H., 2019. Removal of copper ions from aqueous solution using low temperature biochar derived from the pyrolysis of municipal solid waste. Sci. Total Environ. 673, 777–789. https://doi.org/https://doi.org/10.1016/j.scitotenv.2019.04.085
- Hoslett, J., Ghazal, H., Katsou, E., Jouhara, H., 2021. The removal of tetracycline from water using biochar produced from agricultural discarded material. Sci. Total Environ. 751, 141755. https://doi.org/https://doi.org/10.1016/j.scitotenv.2020.141755
- Hoslett, J., Ghazal, H., Mohamad, N., Jouhara, H., 2020. Removal of methylene blue from aqueous solutions by biochar prepared from the pyrolysis of mixed municipal discarded material. Sci. Total Environ. 714, 136832. https://doi.org/https://doi.org/10.1016/j.scitotenv.2020.136832
- Hosseynizadeh Khezri, S., Yazdani, A., Khordad, R., 2012. Pure iron nanoparticles prepared by electric arc discharge method in ethylene glycol. Eur. Phys. J. Appl. Phys. 59.
- Hu, Q., Liu, H., Zhang, Z., Xie, Y., 2020. Nitrate removal from aqueous solution using polyaniline modified activated carbon: Optimization and characterization. J. Mol. Liq. 309, 113057. https://doi.org/https://doi.org/10.1016/j.molliq.2020.113057
- Hu, Q., Zhang, Z., 2019. Application of Dubinin–Radushkevich isotherm model at the solid/solution interface: A theoretical analysis. J. Mol. Liq. 277, 646–648. https://doi.org/https://doi.org/10.1016/j.molliq.2019.01.005
- Huang, L., Kong, J., Wang, W., Zhang, C., Niu, S., Gao, B., 2012. Study on Fe (III) and Mn (II) modified activated carbons derived from Zizania latifolia to removal basic fuchsin. Desalination 286, 268–276.
- Huang, Y., Xiao, L., Li, F., Xiao, M., Lin, D., Long, X., Wu, Z., 2018. Microbial Degradation of Pesticide Residues and an Emphasis on the Degradation of Cypermethrin and 3-phenoxy Benzoic Acid: A Review. Molecules 23, 2313. https://doi.org/10.3390/molecules23092313

- Jain, M., Yadav, M., Kohout, T., Lahtinen, M., Garg, V.K., Sillanpää, M., 2018. Development of iron oxide/activated carbon nanoparticle composite for the removal of Cr(VI), Cu(II) and Cd(II) ions from aqueous solution. Water Resour. Ind. 20, 54–74. https://doi.org/https://doi.org/10.1016/j.wri.2018.10.001
- Jeyabalan, J., Veluchamy, A., V, V.P., Kumar, A., Chandrasekar, R., Narayanasamy, S., 2023. A review on the laccase assisted decolourization of dyes: Recent trends and research progress. J. Taiwan Inst. Chem. Eng. 151, 105081. https://doi.org/10.1016/j.jtice.2023.105081
- John, J., Gandhimathi, R., Sillanpää, M., Chellam, P.V., 2022. Fe3O4-functionalised biochar for persulphate systems towards the removal of Remazol Brilliant Orange 3R: machine learning–based approach and toxicity analysis. Biomass Convers. Biorefinery. https://doi.org/10.1007/s13399-022-03056-1
- Kannan, N., Sundaram, M.M., 2001. Kinetics and mechanism of removal of methylene blue by adsorption on various carbons—a comparative study. Dye. Pigment. 51, 25–40. https://doi.org/https://doi.org/10.1016/S0143-7208(01)00056-0
- Kasonga, T.K., Coetzee, M.A.A., Kamika, I., Ngole-Jeme, V.M., Benteke Momba, M.N., 2021. Endocrine-disruptive chemicals as contaminants of emerging concern in wastewater and surface water: A review. J. Environ. Manage. 277, 111485. https://doi.org/10.1016/j.jenvman.2020.111485
- Khadir, A., Motamedi, M., Negarestani, M., Sillanpää, M., Sasani, M., 2020. Preparation of a nano bio-composite based on cellulosic biomass and conducting polymeric nanoparticles for ibuprofen removal: Kinetics, isotherms, and energy site distribution. Int. J. Biol. Macromol. 162, 663–677. https://doi.org/https://doi.org/10.1016/j.ijbiomac.2020.06.095
- Khan, S., Naushad, M., Govarthanan, M., Iqbal, J., Alfadul, S.M., 2022. Emerging contaminants of high concern for the environment: Current trends and future research. Environ. Res. 207, 112609. https://doi.org/10.1016/j.envres.2021.112609
- Khedr, T.M., El-Sheikh, S.M., Hakki, A., Ismail, A.A., Badawy, W.A., Bahnemann, D.W., 2017. Highly active non-metals doped mixed-phase TiO2 for photocatalytic oxidation of ibuprofen under visible light. J. Photochem. Photobiol. A Chem. 346, 530–540. https://doi.org/https://doi.org/10.1016/j.jphotochem.2017.07.004
- Kilic, M., Apaydin-Varol, E., Pütün, A.E., 2011. Adsorptive removal of phenol from aqueous solutions on activated carbon prepared from tobacco residues: Equilibrium,

kinetics and thermodynamics. J. Hazard. Mater. 189, 397–403. https://doi.org/https://doi.org/10.1016/j.jhazmat.2011.02.051

- Kim, H.-J., Mahboob, S., Viayaraghavan, P., Abdullah Al-Ghanim, K., Al-Misned, F., Ock Kim, Y., Ahmed, Z., 2020. Determination of toxic effects of lead acetate on different sizes of zebra fish (Danio rerio) in soft and hard water. J. King Saud Univ. - Sci. 32, 1390–1394. https://doi.org/https://doi.org/10.1016/j.jksus.2019.11.032
- Kim, S., Chu, K.H., Al-Hamadani, Y.A.J., Park, C.M., Jang, M., Kim, D.-H., Yu, M., Heo, J., Yoon, Y., 2018. Removal of contaminants of emerging concern by membranes in water and wastewater: A review. Chem. Eng. J. 335, 896–914. https://doi.org/10.1016/j.cej.2017.11.044
- Kotelnikova, A., Fastovets, I., Rogova, O., Volkov, D.S., Stolbova, V., 2019. Toxicity assay of lanthanum and cerium in solutions and soil. Ecotoxicol. Environ. Saf. 167, 20–28. https://doi.org/https://doi.org/10.1016/j.ecoenv.2018.09.117
- Kumar, R., Sharma, R.K., Singh, A.P., 2017. Cellulose based grafted biosorbents - Journey from lignocellulose biomass to toxic metal ions sorption applications - A review. J. Mol. Liq. 232, 62–93. https://doi.org/https://doi.org/10.1016/j.molliq.2017.02.050
- Kütahyalı, C., Sert, Ş., Çetinkaya, B., Yalçıntaş, E., Bahadır Acar, M., 2012. Biosorption of Ce(III) onto modified Pinus brutia leaf powder using central composite design. Wood Sci. Technol. 46, 721–736. https://doi.org/10.1007/s00226-011-0437-8
- Lindsey, G., Irene, C., Pablo, C., Ana, S., 2018. Treatment Options for Reclaiming Wastewater Produced by the Pesticide Industry. Int. J. Water Wastewater Treat. 4. https://doi.org/10.16966/2381-5299.149
- Langmuir, I., 1918. THE ADSORPTION OF GASES ON PLANE SURFACES OF GLASS, MICA AND PLATINUM. J. Am. Chem. Soc. 40, 1361–1403. https://doi.org/10.1021/ja02242a004
- Larous, S., Meniai, A.-H., 2016. Adsorption of Diclofenac from aqueous solution using activated carbon prepared from olive stones. Int. J. Hydrogen Energy 41, 10380–10390. https://doi.org/https://doi.org/10.1016/j.ijhydene.2016.01.096
- Lee, S.C., Lintang, H.O., Yuliati, L., 2017. High photocatalytic activity of Fe 2 O 3 /TiO 2 nanocomposites prepared by photodeposition for degradation of 2,4-dichlorophenoxyacetic acid. Beilstein J. Nanotechnol. 8, 915–926. https://doi.org/10.3762/bjnano.8.93

- Lehutso, R.F., Daso, A.P., Okonkwo, J.O., 2017. Occurrence and environmental levels of triclosan and triclocarban in selected wastewater treatment plants in Gauteng Province, South Africa. Emerg. Contam. 3, 107–114. https://doi.org/10.1016/j.emcon.2017.07.001
- Lellis, B., Fávaro-Polonio, C.Z., Pamphile, J.A., Polonio, J.C., 2019. Effects of textile dyes on health and the environment and bioremediation potential of living organisms. Biotechnol. Res. Innov. 3, 275–290. https://doi.org/https://doi.org/10.1016/j.biori.2019.09.001
- Li, W., Li, X., Tong, J., Xiong, W., Zhu, Z., Gao, X., Li, S., Jia, M., Yang, Z., Liang, J., 2023. Effects of environmental and anthropogenic factors on the distribution and abundance of microplastics in freshwater ecosystems. Sci. Total Environ. 856, 159030. https://doi.org/10.1016/j.scitotenv.2022.159030
- Lim, A.P., Aris, A.Z., 2014. Continuous fixed-bed column study and adsorption modeling: Removal of cadmium (II) and lead (II) ions in aqueous solution by dead calcareous skeletons. Biochem. Eng. J. 87, 50–61. https://doi.org/10.1016/j.bej.2014.03.019
- Lin, Z., Li, J., Luan, Y., Dai, W., 2020. Application of algae for heavy metal adsorption: A 20-year meta-analysis. Ecotoxicol. Environ. Saf. 190, 110089. https://doi.org/https://doi.org/10.1016/j.ecoenv.2019.110089
- Lingamdinne, L.P., Chang, Y.-Y., Yang, J.-K., Singh, J., Choi, E.-H., Shiratani, M., Koduru, J.R., Attri, P., 2017. Biogenic reductive preparation of magnetic inverse spinel iron oxide nanoparticles for the adsorption removal of heavy metals. Chem. Eng. J. 307, 74–84. https://doi.org/https://doi.org/10.1016/j.cej.2016.08.067
- Lingamdinne, L.P., Choi, J.-S., Angaru, G.K.R., Karri, R.R., Yang, J.-K., Chang, Y.-Y., Koduru, J.R., 2022. Magnetic-watermelon rinds biochar for uranium-contaminated water treatment using an electromagnetic semi-batch column with removal mechanistic investigations. Chemosphere 286, 131776. https://doi.org/https://doi.org/10.1016/j.chemosphere.2021.131776
- Lingamdinne, L.P., Yang, J.-K., Chang, Y.-Y., Koduru, J.R., 2016. Low-cost magnetized Lonicera japonica flower biomass for the sorption removal of heavy metals. Hydrometallurgy 165, 81–89. https://doi.org/https://doi.org/10.1016/j.hydromet.2015.10.022

- Lupoi, J.S., Gjersing, E., Davis, M.F., 2015. Evaluating lignocellulosic biomass, its derivatives, and downstream products with Raman spectroscopy. Front. Bioeng. Biotechnol. 3, 50.
- Madikizela, L.M., Ncube, S., Chimuka, L., 2020. Analysis, occurrence and removal of pharmaceuticals in African water resources: A current status. J. Environ. Manage. 253, 109741. https://doi.org/10.1016/j.jenvman.2019.109741
- Marican, A., Durán-Lara, E.F., 2018. A review on pesticide removal through different processes. Environ. Sci. Pollut. Res. 25, 2051–2064. https://doi.org/10.1007/s11356-017-0796-2
- Mate, C.J., Mishra, S., 2020. Synthesis of borax cross-linked Jhingan gum hydrogel for remediation of Remazol Brilliant Blue R (RBBR) dye from water: Adsorption isotherm, kinetic, thermodynamic and biodegradation studies. Int. J. Biol. Macromol. 151, 677–690. https://doi.org/https://doi.org/10.1016/j.ijbiomac.2020.02.192
- Mathias, F.T., Fockink, D.H., Disner, G.R., Prodocimo, V., Ribas, J.L.C., Ramos, L.P., Cestari, M.M., Silva de Assis, H.C., 2018. Effects of low concentrations of ibuprofen on freshwater fish Rhamdia quelen. Environ. Toxicol. Pharmacol. 59, 105–113. https://doi.org/https://doi.org/10.1016/j.etap.2018.03.008
- Matongo, S., Birungi, G., Moodley, B., Ndungu, P., 2015. Pharmaceutical residues in water and sediment of Msunduzi River, KwaZulu-Natal, South Africa. Chemosphere 134, 133–140. https://doi.org/10.1016/j.chemosphere.2015.03.093
- Meng, M., Meng, X., Liu, Y., Liu, Z., Han, J., Wang, Y., Luo, M., Chen, R., Ni, L., Yan, Y., 2014. An ion-imprinted functionalized SBA-15 adsorbent synthesized by surface imprinting technique via reversible addition–fragmentation chain transfer polymerization for selective removal of Ce(III) from aqueous solution. J. Hazard. Mater. 278, 134–143. https://doi.org/https://doi.org/10.1016/j.jhazmat.2014.06.002
- Mishra, A.K., Mohanty, B., 2008. Acute toxicity impacts of hexavalent chromium on behavior and histopathology of gill, kidney and liver of the freshwater fish, Channa punctatus (Bloch). Environ. Toxicol. Pharmacol. 26, 136–141. https://doi.org/https://doi.org/10.1016/j.etap.2008.02.010
- Mishra, B., Aggarwal, M., Remya, N., 2022. Application of Biochar for Removal of Emerging Contaminants BT - New Trends in Emerging Environmental Contaminants, in: P. Singh, S., Agarwal, A.K., Gupta, T., Maliyekkal, S.M. (Eds.), . Springer Singapore, Singapore, pp. 211–224. https://doi.org/10.1007/978-981-16-8367-1_10

- Mishra, R.K., Mohanty, K., 2018. Pyrolysis kinetics and thermal behavior of waste sawdust biomass using thermogravimetric analysis. Bioresour. Technol. 251, 63–74. https://doi.org/https://doi.org/10.1016/j.biortech.2017.12.029
- Miskeen, S., Hong, J.S., Choi, H.-D., Kim, J.-Y., 2021. Fabrication of citric acid-modified starch nanoparticles to improve their thermal stability and hydrophobicity. Carbohydr. Polym. 253, 117242. https://doi.org/https://doi.org/10.1016/j.carbpol.2020.117242
- Moldoveanu, G.A., Papangelakis, V.G., 2012. Recovery of rare earth elements adsorbed on clay minerals: I. Desorption mechanism. Hydrometallurgy 117–118, 71–78. https://doi.org/10.1016/j.hydromet.2012.02.007
- Moreira, C.G., Carvalho, T.S. de, de Oliveira, C., Abreu, L.B. de, Castro, A.C.S. de, Ribeiro, P.G., Bispo, F.H.A., Boutin, C., Guilherme, L.R.G., 2019. Ecological risk assessment of cerium for tropical agroecosystems. Chemosphere 221, 124–131. https://doi.org/https://doi.org/10.1016/j.chemosphere.2018.12.195
- Mwandira, W., Nakashima, K., Togo, Y., Sato, T., Kawasaki, S., 2020. Cellulose-metallothionein biosorbent for removal of Pb(II) and Zn(II) from polluted water. Chemosphere 246, 125733. https://doi.org/https://doi.org/10.1016/j.chemosphere.2019.125733
- Myers, A.L., Monson, P.A., 2014. Physical adsorption of gases: the case for absolute adsorption as the basis for thermodynamic analysis. Adsorption 20, 591–622. https://doi.org/10.1007/s10450-014-9604-1
- Mylarappa, M., Lakshmi, V.V., Mahesh, K.R.V., Nagaswarupa, H.P., Raghavendra, N., 2016. A facile hydrothermal recovery of nano sealed MnO2 particle from waste batteries: An advanced material for electrochemical and environmental applications, in: IOP Conference Series: Materials Science and Engineering. IOP Publishing, p. 12178.
- Narayana, P.L., Lingamdinne, L.P., Karri, R.R., Devanesan, S., AlSalhi, M.S., Reddy, N.S., Chang, Y.-Y., Koduru, J.R., 2022. Predictive capability evaluation and optimization of Pb(II) removal by reduced graphene oxide-based inverse spinel nickel ferrite nanocomposite. Environ. Res. 204, 112029. https://doi.org/https://doi.org/10.1016/j.envres.2021.112029
- Navaratna, D., Shu, L., Jegatheesan, V., 2016. Evaluation of herbicide (persistent pollutant) removal mechanisms through hybrid membrane bioreactors. Bioresour. Technol. 200, 795–803. https://doi.org/10.1016/j.biortech.2015.10.041

- Ncibi, M.C., Mahjoub, B., Mahjoub, O., Sillanpää, M., 2017. Remediation of Emerging Pollutants in Contaminated Wastewater and Aquatic Environments: Biomass-Based Technologies. CLEAN – Soil, Air, Water 45, 1700101. https://doi.org/10.1002/clen.201700101
- Neha, S., Remya, N., 2022. Thermochemical conversion of comingled food waste to bio-oil through microwave copyrolysis using different susceptors. Biomass Convers. Biorefinery. https://doi.org/10.1007/s13399-022-02449-6
- Nejadshafiee, V., Islami, M.R., 2020. Intelligent-activated carbon prepared from pistachio shells precursor for effective adsorption of heavy metals from industrial waste of copper mine. Environ. Sci. Pollut. Res. 27, 1625–1639. https://doi.org/10.1007/s11356-019-06732-4
- Nguyen, V.H., Van, H.T., Nguyen, V.Q., Dam, X. Van, Hoang, L.P., Ha, L.T., 2020. Magnetic Fe_3O_4 Nanoparticle Biochar Derived from Pomelo Peel for Reactive Red 21 Adsorption from Aqueous Solution. J. Chem. 2020, 3080612. https://doi.org/10.1155/2020/3080612
- Nika, M.C., Ntaiou, K., Elytis, K., Thomaidi, V.S., Gatidou, G., Kalantzi, O.I., Thomaidis, N.S., Stasinakis, A.S., 2020. Wide-scope target analysis of emerging contaminants in landfill leachates and risk assessment using Risk Quotient methodology. J. Hazard. Mater. 394, 122493. https://doi.org/10.1016/j.jhazmat.2020.122493
- Nilsen, E., Smalling, K.L., Ahrens, L., Gros, M., Miglioranza, K.S.B., Picó, Y., Schoenfuss, H.L., 2019. Critical review: Grand challenges in assessing the adverse effects of contaminants of emerging concern on aquatic food webs. Environ. Toxicol. Chem. 38, 46–60. https://doi.org/10.1002/etc.4290
- Oba, S.N., Ighalo, J.O., Aniagor, C.O., Igwegbe, C.A., 2021. Removal of ibuprofen from aqueous media by adsorption: A comprehensive review. Sci. Total Environ. 780, 146608. https://doi.org/https://doi.org/10.1016/j.scitotenv.2021.146608
- Ogueji, E.O., Nwani, C.D., Iheanacho, S.C., Mbah, C.E., Okeke, C.O., Yaji, A., 2018. Acute toxicity effects of ibuprofen on behaviour and haematological parameters of African catfish Clarias gariepinus (Burchell, 1822). African J. Aquat. Sci. 43, 293–303. https://doi.org/10.2989/16085914.2018.1465393
- Oliveira, L.C.A., Rios, R.V.R.A., Fabris, J.D., Garg, V., Sapag, K., Lago, R.M., 2002. Activated carbon/iron oxide magnetic composites for the adsorption of contaminants in

water. Carbon N. Y. 40, 2177–2183. https://doi.org/https://doi.org/10.1016/S0008-6223(02)00076-3

- Osuoha, J.O., Anyanwu, B.O., Ejileugha, C., 2023. Pharmaceuticals and personal care products as emerging contaminants: Need for combined treatment strategy. J. Hazard. Mater. Adv. 9, 100206. https://doi.org/10.1016/j.hazadv.2022.100206
- Pai, S., M Kini, S., Selvaraj, R., Pugazhendhi, A., 2020. A review on the synthesis of hydroxyapatite, its composites and adsorptive removal of pollutants from wastewater. J. Water Process Eng. 38, 101574. https://doi.org/10.1016/j.jwpe.2020.101574
- Pan, N., Li, L., Ding, J., Li, S., Wang, R., Jin, Y., Wang, X., Xia, C., 2016. Preparation of graphene oxide-manganese dioxide for highly efficient adsorption and separation of Th(IV)/U(VI). J. Hazard. Mater. 309, 107–115. https://doi.org/https://doi.org/10.1016/j.jhazmat.2016.02.012
- Pan, X., Liu, P., Wang, Y., Yi, Y., Zhang, H., Qian, D.-W., Xiao, P., Shang, E., Duan, J.-A., 2021. Synthesis of starch nanoparticles with controlled morphology and various adsorption rate for urea. Food Chem. 130882. https://doi.org/https://doi.org/10.1016/j.foodchem.2021.130882
- Panthi, S., Sapkota, A.R., Raspanti, G., Allard, S.M., Bui, A., Craddock, H.A., Murray, R., Zhu, L., East, C., Handy, E., Callahan, M.T., Haymaker, J., Kulkarni, P., Anderson, B., Craighead, S., Gartley, S., Vanore, A., Betancourt, W.Q., Duncan, R., Foust, D., Sharma, M., Micallef, S.A., Gerba, C., Parveen, S., Hashem, F., May, E., Kniel, K., Pop, M., Ravishankar, S., Sapkota, A., 2019. Pharmaceuticals, herbicides, and disinfectants in agricultural water sources. Environ. Res. 174, 1–8. https://doi.org/10.1016/j.envres.2019.04.011
- Patel, M., Kumar, R., Kishor, K., Mlsna, T., Pittman, C.U., Mohan, D., 2019. Pharmaceuticals of Emerging Concern in Aquatic Systems: Chemistry, Occurrence, Effects, and Removal Methods. Chem. Rev. 119, 3510–3673. https://doi.org/10.1021/acs.chemrev.8b00299
- Patra, C., Shahnaz, T., Subbiah, S., Narayanasamy, S., 2020. Comparative assessment of raw and acid-activated preparations of novel Pongamia pinnata shells for adsorption of hexavalent chromium from simulated wastewater. Environ. Sci. Pollut. Res. https://doi.org/10.1007/s11356-020-07979-y
- Pérez-Lucas, G., Aliste, M., Vela, N., Garrido, I., Fenoll, J., Navarro, S., 2020. Decline of fluroxypyr and triclopyr residues from pure, drinking and leaching water by photo-

assisted peroxonation. Process Saf. Environ. Prot. 137, 358–365. https://doi.org/10.1016/j.psep.2020.02.039

- Podio, N.S., Bertrand, L., Wunderlin, D.A., Santiago, A.N., 2020. Assessment of phytotoxic effects, uptake and translocation of diclofenac in chicory (Cichorium intybus). Chemosphere 241, 125057. https://doi.org/10.1016/j.chemosphere.2019.125057
- Priyan, V.V., Shahnaz, T., Kunnumakkara, A.B., Rana, V., Saravanan, M., Narayanasamy, S., 2021. Antioxidant, Anti-inflammatory and Biosorption Properties of Starch Nanocrystals In Vitro Study: Cytotoxic and Phytotoxic Evaluation. J. Clust. Sci. 32, 1419–1430. https://doi.org/10.1007/s10876-020-01905-5
- Priyan, V.V., Shahnaz, T., Kunnumakkara, A.B., Rana, V., Saravanan, M., Narayanasamy, S., 2020. Antioxidant, Anti-inflammatory and Biosorption Properties of Starch Nanocrystals In Vitro Study: Cytotoxic and Phytotoxic Evaluation. J. Clust. Sci. https://doi.org/10.1007/s10876-020-01905-5
- Priyan V, V., Kumar, N., Narayanasamy, S., 2022. Toxicological assessment and adsorptive removal of lead (Pb) and Congo red (CR) from water by synthesized iron oxide/activated carbon (Fe3O4/AC) nanocomposite. Chemosphere 294, 133758. https://doi.org/https://doi.org/10.1016/j.chemosphere.2022.133758
- Priyan V, V., Narayanasamy, S., 2022. Effective removal of pharmaceutical contaminants ibuprofen and sulfamethoxazole from water by Corn starch nanoparticles: An ecotoxicological assessment. Environ. Toxicol. Pharmacol. 94, 103930. https://doi.org/https://doi.org/10.1016/j.etap.2022.103930
- Queiroz, L.S., de Souza, L.K.C., Thomaz, K.T.C., Leite Lima, E.T., da Rocha Filho, G.N., do Nascimento, L.A.S., de Oliveira Pires, L.H., Faial, K. do C.F., da Costa, C.E.F., 2020. Activated carbon obtained from amazonian biomass tailings (acai seed): Modification, characterization, and use for removal of metal ions from water. J. Environ. Manage. 270, 110868. https://doi.org/https://doi.org/10.1016/j.jenvman.2020.110868
- Rahman, M.F., Peldszus, S., Anderson, W.B., 2014. Behaviour and fate of perfluoroalkyl and polyfluoroalkyl substances (PFASs) in drinking water treatment: A review. Water Res. 50, 318–340. https://doi.org/10.1016/j.watres.2013.10.045
- Rajabi, M., Moradi, O., Sillanpää, M., Zare, K., Asiri, A.M., Agarwal, S., Gupta, V.K., 2019. Removal of toxic chemical ethidium monoazide bromide using graphene oxide:

Thermodynamic and kinetics study. J. Mol. Liq. 293, 111484. https://doi.org/https://doi.org/10.1016/j.molliq.2019.111484

- Ramalingam, B., Parandhaman, T., Choudhary, P., Das, S.K., 2018. Biomaterial Functionalized Graphene-Magnetite Nanocomposite: A Novel Approach for Simultaneous Removal of Anionic Dyes and Heavy-Metal Ions. ACS Sustain. Chem. Eng. 6, 6328–6341. https://doi.org/10.1021/acssuschemeng.8b00139
- Rangabhashiyam, S., Selvaraju, N., 2015. Evaluation of the biosorption potential of a novel Caryota urens inflorescence waste biomass for the removal of hexavalent chromium from aqueous solutions. J. Taiwan Inst. Chem. Eng. 47, 59–70. https://doi.org/https://doi.org/10.1016/j.jtice.2014.09.034
- Rashad, E., Saleh, H.N., Eltaweil, A.S., Saleh, M.E., Sillanpaa, M., Mostafa, A.R., 2022. Pinewood sawdust biochar as an effective biosorbent for PAHs removal from wastewater. Biomass Convers. Biorefinery. https://doi.org/10.1007/s13399-021-02181-7
- Rathi, B.S., Kumar, P.S., Show, P.-L., 2021. A review on effective removal of emerging contaminants from aquatic systems: Current trends and scope for further research. J. Hazard. Mater. 409, 124413. https://doi.org/https://doi.org/10.1016/j.jhazmat.2020.124413
- Remanan, M.K., Zhu, F., 2021. Encapsulation of rutin using quinoa and maize starch nanoparticles. Food Chem. 353, 128534. https://doi.org/https://doi.org/10.1016/j.foodchem.2020.128534
- Ren, T., Chen, N., Wan Mahari, W.A., Xu, C., Feng, H., Ji, X., Yin, Q., Chen, P., Zhu, S., Liu, H., Liu, G., Li, L., Lam, S.S., 2021. Biochar for cadmium pollution mitigation and stress resistance in tobacco growth. Environ. Res. 192, 110273. https://doi.org/https://doi.org/10.1016/j.envres.2020.110273
- REN, Y., NAKANO, K., NOMURA, M., CHIBA, N., NISHIMURA, O., 2007. A thermodynamic analysis on adsorption of estrogens in activated sludge process. Water Res. 41, 2341–2348. https://doi.org/10.1016/j.watres.2007.01.058
- Richardson, S.D., Kimura, S.Y., 2017. Emerging environmental contaminants: Challenges facing our next generation and potential engineering solutions. Environ. Technol. Innov. 8, 40–56. https://doi.org/10.1016/j.eti.2017.04.002
- Rodrigues, S.C., Silva, M.C., Torres, J.A., Bianchi, M.L., 2020. Use of Magnetic Activated Carbon in a Solid Phase Extraction Procedure for Analysis of 2,4-

dichlorophenol in Water Samples. Water, Air, Soil Pollut. 231, 294. https://doi.org/10.1007/s11270-020-04610-1

- Roh, J., Cheng, H., 2022. Ultraviolet filter, fragrance and preservative allergens in New Zealand sunscreens. Australas. J. Dermatol. 63. https://doi.org/10.1111/ajd.13748
- Rosaiah, P., Zhu, J., Hussain, O.M., Qiu, Y., 2019. Facile and cost-effective synthesis of flower-like RGO/Fe3O4 nanocomposites with ultra-long cycling stability for supercapacitors. Ionics (Kiel). 25, 655–664. https://doi.org/10.1007/s11581-018-2669-1
- Rout, P.R., Zhang, T.C., Bhunia, P., Surampalli, R.Y., 2021. Treatment technologies for emerging contaminants in wastewater treatment plants: A review. Sci. Total Environ. 753, 141990. https://doi.org/10.1016/j.scitotenv.2020.141990
- Saidulu, D., Gupta, B., Gupta, A.K., Ghosal, P.S., 2021. A review on occurrences, eco-toxic effects, and remediation of emerging contaminants from wastewater: Special emphasis on biological treatment based hybrid systems. J. Environ. Chem. Eng. 9, 105282. https://doi.org/https://doi.org/10.1016/j.jece.2021.105282
- Saleem, S., Kannan, R.R., 2018. Zebrafish: an emerging real-time model system to study Alzheimer's disease and neurospecific drug discovery. Cell Death Discov. 4, 45. https://doi.org/10.1038/s41420-018-0109-7
- Saleh, I.A., Zouari, N., Al-Ghouti, M.A., 2020. Removal of pesticides from water and wastewater: Chemical, physical and biological treatment approaches. Environ. Technol. Innov. 19, 101026. https://doi.org/10.1016/j.eti.2020.101026
- Salimi, M., Esrafili, A., Gholami, M., Jonidi Jafari, A., Rezaei Kalantary, R., Farzadkia, M., Kermani, M., Sobhi, H.R., 2017. Contaminants of emerging concern: a review of new approach in AOP technologies. Environ. Monit. Assess. 189, 414. https://doi.org/10.1007/s10661-017-6097-x
- Saood Manzar, M., Ahmad, T., Ullah, N., Velayudhaperumal Chellam, P., John, J., Zubair, M., Brandão, R.J., Meili, L., Alagha, O., Çevik, E., 2022. Comparative adsorption of Eriochrome Black T and Tetracycline by NaOH-modified steel dust: Kinetic and process modeling. Sep. Purif. Technol. 287, 120559. https://doi.org/https://doi.org/10.1016/j.seppur.2022.120559
- Shafeeyan, M.S., Daud, W.M.A.W., Houshmand, A., Shamiri, A., 2010. A review on surface modification of activated carbon for carbon dioxide adsorption. J. Anal. Appl. Pyrolysis 89, 143–151. https://doi.org/https://doi.org/10.1016/j.jaap.2010.07.006

- Shaheen, T.I., Emam, H.E., 2018. Sono-chemical synthesis of cellulose nanocrystals from wood sawdust using Acid hydrolysis. Int. J. Biol. Macromol. 107, 1599–1606. https://doi.org/https://doi.org/10.1016/j.ijbiomac.2017.10.028
- Shahid, M.K., Kashif, A., Fuwad, A., Choi, Y., 2021. Current advances in treatment technologies for removal of emerging contaminants from water – A critical review. Coord. Chem. Rev. 442, 213993. https://doi.org/https://doi.org/10.1016/j.ccr.2021.213993
- Shahnaz, T., Vishnu Priyan, V., Anjali, J., Selvaraju, N., 2021a. Magnetic nanocellulose from Cyperus rotundas grass in the absorptive removal of rare earth element cerium (III): Toxicity studies and interpretation. Chemosphere 131912. https://doi.org/https://doi.org/10.1016/j.chemosphere.2021.131912
- Shahnaz, T., Vishnu Priyan, V., Pandian, S., Narayanasamy, S., 2021b. Use of Nanocellulose extracted from grass for adsorption abatement of Ciprofloxacin and Diclofenac removal with phyto, and fish toxicity studies. Environ. Pollut. 268, 115494. https://doi.org/https://doi.org/10.1016/j.envpol.2020.115494
- Sharma, H.R., Malan, A., 2017. Effect of paracetamol and ibuprofen on morphological parameters and chlorophyll content of Vigna radiata (Green Gram). Environ. We Int. J. Sci. Tech 12, 99–108.
- Sharma, V., Shahnaz, T., Subbiah, S., Narayanasamy, S., 2020. New Insights into the Remediation of Water Pollutants using Nanobentonite Incorporated Nanocellulose Chitosan Based Aerogel. J. Polym. Environ. 28, 2008–2019. https://doi.org/10.1007/s10924-020-01740-9
- Shirsath, D.S., Shirivastava, V.S., 2015. Adsorptive removal of heavy metals by magnetic nanoadsorbent: an equilibrium and thermodynamic study. Appl. Nanosci. 5, 927–935. https://doi.org/10.1007/s13204-014-0390-6
- Shrestha, D., Maensiri, S., Wongpratat, U., Lee, S.W., Nyachhyon, A.R., 2019. Shorea robusta derived activated carbon decorated with manganese dioxide hybrid composite for improved capacitive behaviors. J. Environ. Chem. Eng. 7, 103227. https://doi.org/https://doi.org/10.1016/j.jece.2019.103227
- Soetaredjo, F.E., Kurniawan, A., Ong, L.K., Widagdyo, D.R., Ismadji, S., 2014. Investigation of the continuous flow sorption of heavy metals in a biomass-packed column: revisiting the Thomas design model for correlation of binary component systems. RSC Adv. 4, 52856–52870. https://doi.org/10.1039/C4RA06425A

- Somsesta, N., Sricharoenchaikul, V., Aht-Ong, D., 2020. Adsorption removal of methylene blue onto activated carbon/cellulose biocomposite films: Equilibrium and kinetic studies. Mater. Chem. Phys. 240, 122221. https://doi.org/https://doi.org/10.1016/j.matchemphys.2019.122221
- Sophia A., C., Lima, E.C., 2018. Removal of emerging contaminants from the environment by adsorption. Ecotoxicol. Environ. Saf. 150, 1–17. https://doi.org/https://doi.org/10.1016/j.ecoenv.2017.12.026
- Sotto, R.B.D., Medriano, C.D., Cho, Y., Kim, H., Chung, I.Y., Seok, K.S., Song, K.G., Hong, S.W., Park, Y., Kim, S., 2017. Sub-lethal pharmaceutical hazard tracking in adult zebrafish using untargeted LC–MS environmental metabolomics. J. Hazard. Mater. 339, 63–72. https://doi.org/10.1016/j.jhazmat.2017.06.009
- Spessato, L., Cazetta, A.L., Melo, S., Pezoti, O., Tami, J., Ronix, A., Fonseca, J.M., Martins, A.F., Silva, T.L., Almeida, V.C., 2020. Synthesis of superparamagnetic activated carbon for paracetamol removal from aqueous solution. J. Mol. Liq. 300, 112282. https://doi.org/https://doi.org/10.1016/j.molliq.2019.112282
- Su, H., Zhang, D., Antwi, P., Xiao, L., Deng, X., Liu, Z., Long, B., Shi, M., Manefield, M.J., Ngo, H.H., 2021. Exploring potential impact(s) of cerium in mining wastewater on the performance of partial-nitrification process and nitrogen conversion microflora. Ecotoxicol. Environ. Saf. 209, 111796. https://doi.org/https://doi.org/10.1016/j.ecoenv.2020.111796
- Takmil, F., Esmaeili, H., Mousavi, S.M., Hashemi, S.A., 2020. Nano-magnetically modified activated carbon prepared by oak shell for treatment of wastewater containing fluoride ion. Adv. Powder Technol. 31, 3236–3245. https://doi.org/https://doi.org/10.1016/j.apt.2020.06.015
- Tasrin, S., Mohamed Madhar Fazil, S., Senthilmurugan, S., Selvaraju, N., 2021. Facile preparation of nanocellulose embedded polypyrrole for dye removal: unary and binary process optimization and seed toxicity. Int. J. Environ. Sci. Technol. 18, 365–378. https://doi.org/10.1007/s13762-020-02814-w
- Tejaswini, E.S.S., Panjwani, S., Seshagiri Rao, A., 2020. Design of hierarchical control strategies for biological wastewater treatment plants to reduce operational costs. Chem. Eng. Res. Des. 161, 197–205. https://doi.org/https://doi.org/10.1016/j.cherd.2020.07.003

- Temkin, M.I., 1940. Kinetics of ammonia synthesis on promoted iron catalysts. Acta physiochim. URSS 12, 327–356.
- Thuyavan, Y.L., Anantharaman, N., Arthanareeswaran, G., Ismail, A.F., 2014. Adsorptive Removal of Humic Acid by Zirconia Embedded in a Poly(ether sulfone) Membrane. Ind. Eng. Chem. Res. 53, 11355–11364. https://doi.org/10.1021/ie5015712
- Tian, L., Chang, H., Tang, P., Li, T., Zhang, X., Liu, S., He, Q., Wang, T., Yang, J., Bai, Y., Vidic, R.D., Crittenden, J.C., Liu, B., 2020. Rare Earth Elements Occurrence and Economical Recovery Strategy from Shale Gas Wastewater in the Sichuan Basin, China. ACS Sustain. Chem. Eng. 8, 11914–11920. https://doi.org/10.1021/acssuschemeng.0c04971
- Udhayakumar, S., Kumar, G.J., Kumar, E.S., Navaneethan, M., Bharathi, K.K., 2021. Magnetic anomalies, chemical and magnetic properties at wide temperature range (15–1000 K) in LiSrxFe5-xO8 (x = 0, 0.025, 0.05). J. Alloys Compd. 859, 158290. https://doi.org/https://doi.org/10.1016/j.jallcom.2020.158290
- Varadharaj, V., Ramaswamy, A., Sakthivel, R., Subbaiya, R., Barabadi, H., Chandrasekaran, M., Saravanan, M., 2020. Antidiabetic and Antioxidant Activity of Green Synthesized Starch Nanoparticles: An In Vitro Study. J. Clust. Sci. 31, 1257–1266. https://doi.org/10.1007/s10876-019-01732-3
- Velásquez-Castillo, L.E., Leite, M.A., Ditchfield, C., Sobral, P.J. do A., Moraes, I.C.F., 2020. Quinoa starch nanocrystals production by acid hydrolysis: Kinetics and properties. Int. J. Biol. Macromol. 143, 93–101. https://doi.org/10.1016/j.ijbiomac.2019.12.011
- Venkateswarlu, S., Mahajan, H., Panda, A., Lee, J., Govindaraju, S., Yun, K., Yoon, M., 2020. Fe3O4 nano assembly embedded in 2D-crumpled porous carbon sheets for high energy density supercapacitor. Chem. Eng. J. 127584. https://doi.org/https://doi.org/10.1016/j.cej.2020.127584
- Vikrant, K., Giri, B.S., Raza, N., Roy, K., Kim, K.-H., Rai, B.N., Singh, R.S., 2018. Recent advancements in bioremediation of dye: Current status and challenges. Bioresour. Technol. 253, 355–367. https://doi.org/https://doi.org/10.1016/j.biortech.2018.01.029
- Vishnu Priyan, V, Kumar, N., Narayanasamy, S., 2021a. Development of Fe3O4/CAC nanocomposite for the effective removal of contaminants of emerging concerns (Ce3+)

from water: An ecotoxicological assessment. Environ. Pollut. 285, 117326. https://doi.org/https://doi.org/10.1016/j.envpol.2021.117326

- Vishnu Priyan, V, Shahnaz, T., Suganya, E., Sivaprakasam, S., Narayanasamy, S., 2021b. Ecotoxicological assessment of micropollutant Diclofenac biosorption on magnetic sawdust: Phyto, Microbial and Fish toxicity studies. J. Hazard. Mater. 403, 123532. https://doi.org/https://doi.org/10.1016/j.jhazmat.2020.123532
- Vishnu Priyan, V., Shahnaz, T., Suganya, E., Sivaprakasam, S., Narayanasamy, S., 2021. Ecotoxicological assessment of micropollutant Diclofenac biosorption on magnetic sawdust: Phyto, Microbial and Fish toxicity studies. J. Hazard. Mater. 403, 123532. https://doi.org/10.1016/j.jhazmat.2020.123532
- Wang, B., Lin, X., Zheng, Y., Zeng, M., Huang, M., Guo, Z., 2021. Effect of homogenization-pressure-assisted enzymatic hydrolysis on the structural and physicochemical properties of lotus-seed starch nanoparticles. Int. J. Biol. Macromol. 167, 1579–1586. https://doi.org/https://doi.org/10.1016/j.ijbiomac.2020.11.113
- Wang, C., Yang, H., Li, F., Jin, P., Zhu, W., Fan, J., 2024. Efficient adsorption of fluorescent whitening agent 351 from high salinity environmental water by polymer supported hydroxyl functional ionic liquid. Sep. Purif. Technol. 334, 125901. https://doi.org/10.1016/j.seppur.2023.125901
- Wang, J., Cahyadi, A., Wu, B., Pee, W., Fane, A.G., Chew, J.W., 2020. The roles of particles in enhancing membrane filtration: A review. J. Memb. Sci. 595, 117570. https://doi.org/10.1016/j.memsci.2019.117570
- Wang, J., Guo, X., 2022. Rethinking of the intraparticle diffusion adsorption kinetics model: Interpretation, solving methods and applications. Chemosphere 309, 136732. https://doi.org/10.1016/j.chemosphere.2022.136732
- Wang, J., Guo, X., 2020. Adsorption kinetic models: Physical meanings, applications, and solving methods. J. Hazard. Mater. 390, 122156. https://doi.org/10.1016/j.jhazmat.2020.122156
- Wang, J., Zhuan, R., 2020. Degradation of antibiotics by advanced oxidation processes: An overview. Sci. Total Environ. 701, 135023. https://doi.org/10.1016/j.scitotenv.2019.135023
- Wang, L., O'Connor, D., Rinklebe, J., Ok, Y.S., Tsang, D.C.W., Shen, Z., Hou, D., 2020. Biochar Aging: Mechanisms, Physicochemical Changes, Assessment, And Implications

for Field Applications. Environ. Sci. Technol. 54, 14797–14814. https://doi.org/10.1021/acs.est.0c04033

- Wang, Zhanghui, Guo, S., Zhang, B., Fang, J., Zhu, L., 2020. Interfacially crosslinked β-cyclodextrin polymer composite porous membranes for fast removal of organic micropollutants from water by flow-through adsorption. J. Hazard. Mater. 384, 121187.
- Wang, Zongwu, Zhang, J., Wu, Q., Han, X., Zhang, M., Liu, W., Yao, X., Feng, J., Dong, S., Sun, J., 2020. Magnetic supramolecular polymer: Ultrahigh and highly selective Pb(II) capture from aqueous solution and battery wastewater. Chemosphere 248, 126042. https://doi.org/https://doi.org/10.1016/j.chemosphere.2020.126042
- Wei, X., Wang, Y., Chen, J., Xu, F., Liu, Z., He, X., Li, H., Zhou, Y., 2020. Adsorption of pharmaceuticals and personal care products by deep eutectic solvents-regulated magnetic metal-organic framework adsorbents: performance and mechanism. Chem. Eng. J. 124808.
- Wen, Y., Zheng, Z., Wang, S., Han, T., Yang, W., Jönsson, P.G., 2021. Magnetic bio-activated carbons production using different process parameters for phosphorus removal from artificially prepared phosphorus-rich and domestic wastewater. Chemosphere 271, 129561. https://doi.org/https://doi.org/10.1016/j.chemosphere.2021.129561
- Wijaya, L., Alyemeni, M., Ahmad, P., Alfarhan, A., Barcelo, D., El-Sheikh, M.A., Pico, Y., 2020. Ecotoxicological Effects of Ibuprofen on Plant Growth of Vigna unguiculata L. Plants . https://doi.org/10.3390/plants9111473
- Wu, F.-C., Tseng, R.-L., Juang, R.-S., 2009. Characteristics of Elovich equation used for the analysis of adsorption kinetics in dye-chitosan systems. Chem. Eng. J. 150, 366–373. https://doi.org/10.1016/j.cej.2009.01.014
- Xu, Q., Jiang, Y., Chu, W., Su, C., Hu, D., Lu, Q., Zhang, T., 2017. Response of Spirodela polyrhiza to cerium: subcellular distribution, growth and biochemical changes. Ecotoxicol. Environ. Saf. 139, 56–64. https://doi.org/https://doi.org/10.1016/j.ecoenv.2017.01.012
- Yahya, M.A., Al-Qodah, Z., Ngah, C.W.Z., 2015. Agricultural bio-waste materials as potential sustainable precursors used for activated carbon production: A review. Renew. Sustain. Energy Rev. 46, 218–235. https://doi.org/https://doi.org/10.1016/j.rser.2015.02.051

- Yan, Z., Lu, G., Ye, Q., Liu, J., 2016. Long-term effects of antibiotics, norfloxacin, and sulfamethoxazole, in a partial life-cycle study with zebrafish (Danio rerio): effects on growth, development, and reproduction. Environ. Sci. Pollut. Res. 23, 18222–18228. https://doi.org/10.1007/s11356-016-7018-1
- Yang, C., 1993. Statistical mechanical aspects of adsorption systems obeying the Temkin isotherm. J. Phys. Chem. 97, 7097–7101. https://doi.org/10.1021/j100129a029
- Yin, K., Wang, J., Zhai, S., Xu, X., Li, T., Sun, S., Xu, S., Zhang, X., Wang, C., Hao, Y., 2022. Adsorption mechanisms for cadmium from aqueous solutions by oxidant-modified biochar derived from Platanus orientalis Linn leaves. J. Hazard. Mater. 428, 128261. https://doi.org/https://doi.org/10.1016/j.jhazmat.2022.128261
- Yu, Z., Qi, T., Qu, J., Guo, Y., 2015. Application of mathematical models for ion-exchange removal of calcium ions from potassium chromate solutions by Amberlite IRC 748 resin in a continuous fixed bed column. Hydrometallurgy 158, 165–171. https://doi.org/10.1016/j.hydromet.2015.10.015
- Zaheer, Z., AL-Asfar, A., Aazam, E.S., 2019. Adsorption of methyl red on biogenic Ag@Fe nanocomposite adsorbent: Isotherms, kinetics and mechanisms. J. Mol. Liq. 283, 287–298. https://doi.org/10.1016/j.molliq.2019.03.030
- Zhang, F., Tang, X., Lan, J., Huang, Y., 2019. Successive removal of Pb2+ and Congo red by magnetic phosphate nanocomposites from aqueous solution. Sci. Total Environ. 658, 1139–1149. https://doi.org/https://doi.org/10.1016/j.scitotenv.2018.12.291
- Zhang, H., Ma, J., Wang, F., Chu, Y., Yang, L., Xia, M., 2020. Mechanism of carboxymethyl chitosan hybrid montmorillonite and adsorption of Pb(II) and Congo red by CMC-MMT organic-inorganic hybrid composite. Int. J. Biol. Macromol. 149, 1161–1169. https://doi.org/https://doi.org/10.1016/j.ijbiomac.2020.01.201
- Zhao, R., Li, X., Hu, M., Li, S., Zhai, Q., Jiang, Y., 2017. Efficient enzymatic degradation used as pre-stage treatment for norfloxacin removal by activated sludge. Bioprocess Biosyst. Eng. 40, 1261–1270. https://doi.org/10.1007/s00449-017-1786-y
- Zhou, L., Limbu, S.M., Shen, M., Zhai, W., Qiao, F., He, A., Du, Z.-Y., Zhang, M., 2018. Environmental concentrations of antibiotics impair zebrafish gut health. Environ. Pollut. 235, 245–254. https://doi.org/https://doi.org/10.1016/j.envpol.2017.12.073
- Zhou, L., Tang, S., Yang, L., Huang, X., Zou, L., Huang, Y., Dong, S., Zhou, X., Yang, X., 2019. Cerium ion promotes the osteoclastogenesis through the induction of reactive

oxygen species. J. Trace Elem. Med. Biol. 52, 126–135. https://doi.org/https://doi.org/10.1016/j.jtemb.2018.12.006

- Zhou, Y., Li, J., Hu, S., Qian, G., Shi, J., Zhao, S., Wang, Y., Wang, C., Lian, J., 2022. Sawdust-Derived Activated Carbon with Hierarchical Pores for High-Performance Symmetric Supercapacitors. Nanomaterials 12, 810.
- Zhuang, S., Chen, R., Liu, Y., Wang, J., 2020. Magnetic COFs for the adsorptive removal of diclofenac and sulfamethazine from aqueous solution: Adsorption kinetics, isotherms study and DFT calculation. J. Hazard. Mater. 385, 121596.
- Zulfiqar, U., Farooq, M., Hussain, S., Maqsood, M., Hussain, M., Ishfaq, M., Ahmad, M., Anjum, M.Z., 2019. Lead toxicity in plants: Impacts and remediation. J. Environ. Manage. 250, 109557. https://doi.org/https://doi.org/10.1016/j.jenvman.2019.109557.

Appendix

Table A1. *Various isotherm models with their linear and non-linear equations*

Isotherm Model	Linear equation	Non-linear equation	Description
Langmuir Isotherm	$\frac{C_e}{q_e} = \frac{1}{K_L Q_0} + \frac{C_e}{Q_0}$	$q_e = \frac{Q_0 K_L C_e}{1 + K_L C_e}$	**q_e** is the quantity of adsorbate adsorbed (mg/g), **Q_0** denotes the amount of adsorbate adsorbed monolayer capacity (mg/g), **C_e** is the adsorbate equilibrium concentration (mg/L), **K_L** is the Langmuir isotherm constant (L/mg).
Freundlich Isotherm	$\log q_e = \log K_F + \frac{1}{n} \log C_e$	$q_e = K_F C_e^{1/n}$	**K_F** is the Freundlich isotherm constant (L/g), **n** represents the exponent of Freundlich constant.
Dubinin-Radushkevich Isotherm	$\ln q_e = \ln q_m - \beta\, \varepsilon^2$	$q_e = q_m e^{-\beta \varepsilon^2}$	**q_m** is the maximum adsorption capacity (mg/g), **β** corresponds to the activity coefficient (mol^2/J^2), **ε** represents the Polanyi potential.
Temkin Isotherm	$q_e = \frac{RT}{b_T} \ln K_T + \frac{RT}{b_T} \ln C_e$	$q_e = \frac{RT}{b_T} ln(K_T C_e)$	**K_T** is the equilibrium binding constant (L/g), **b_T** is Temkin constant for the heat of adsorption (kJ/mol).
Jovanovic Isotherm	$ln\, q_e = ln\, q_m - K_J C_e$	$q_e = q_m(1 - e^{K_J C_e})$	**K_J** is Jovanovic isotherm constant (L/g).

Table A2. *Various kinetic models with their equations*

Kinetic Model	Equation	Description
Pseudo-first-order model	$log(q_e - q_t) = log\, q_e - k_1 t/2.303$	$\mathbf{q_e}$ and $\mathbf{q_t}$ represents the equilibrium adsorption capacity and adsorption capacity at time t (mg/g), $\mathbf{k_1}$ is the pseudo-first-order rate constant (min^{-1}).
Pseudo-second-order model	$\frac{t}{q_t} = \frac{1}{k_2 q_e^2} + \frac{t}{q_e}$	$\mathbf{k_2}$ is the pseudo-second-order rate constant (g/mg min).
Elovich model	$q_t = \frac{1}{\beta} ln\, \alpha\beta + \frac{1}{\beta} ln\, t$	**α** (g/mg min) and **β** (mg/g) corresponds to the Elovich constants.
Intra-particle diffusion model	$q_t = K_{ID}\sqrt{t} + c$	$\mathbf{K_{ID}}$ (mg/g $min^{1/2}$) is the rate constant, **c** is the intra-particle diffusion model constant.

Table A3. *Various characterization techniques*

Analysis	Characterization techniques	Make and Model
Morphological, topological, and surface analysis	Field Emission Scanning Electron Microscopy, FESEM	Zeiss-Gemini
	Field Emission Transmission Electron Microscopy, FETEM	JEOL-2100F
	Atomic Force Microscopy, AFM	Oxford-Cypher
Elemental analysis	Energy Dispersive X-Ray Analysis, EDX	Zeiss-Sigma
	Atomic Emission Spectroscopy, AES	Agilent-4210 MP
Functional group determination	Fourier Transform Infrared Spectroscopy, FTIR	PerkinElmer- Spectrum 2
	Raman Spectroscopy, RS	Horiba Jobin Vyon-LabRam HR
Nature of crystallinity	X-ray powder Diffraction, XRD	Rigaku- Micromax-007HF
Magnetic nature	Vibrating Sample Magnetometer, VSM	Lakeshore-7410 series
To measure the absorbance	UV–Visible Spectrophotometry	Tecan-Infinite M200 PRO

A4. Packed bed column parameters

Various column adsorption parameters and their equations are as follows as:

$$m_{total} = \frac{FC_0 t_{total}}{1000} \quad \text{(A.1)}$$

$$q_{total} = \frac{C_0 F}{1000} \times \left(t_{total} - \int_{t=0}^{t=t_{total}} \frac{C_t}{C_0} dt \right) \quad \text{(A.2)}$$

$$V_{eff} = Q \times t_{total} \quad \text{(A.3)}$$

$$q_{e(exp)} = \frac{Q_{total}}{w} \quad \text{(A.4)}$$

$$\text{Y \%} = \frac{q_{total}}{m_{total}} \times 100 \quad \text{(A.5)}$$

Were,

F (mL/h): Flow rate

C_0 (mg/L): Initial dye concentration

C_t (mg/L): Dye concentration at time t

t_{total} (min): Total time for column saturation

m_{total} (mg): Total amount of dye introduced into the column

Q_{total} (mg): amount of dye molecules adsorbed by OBC in the column experiment

$q_{e(exp)}$ (mg/g): Maximum adsorption capacity in column studies

V_{eff} (mL): Total volume of the effluent

Y (%): Removal percentage of dye

List of Publications and Conferences

A. LIST OF PUBLICATIONS FROM THESIS WORK

1. **Vishnu Priyan V**., Ramesh, G., Kumar, A., Jeyabalan, J., Narayanasamy, S., 2023. Synthesis, characterization, and application of oxidant-modified biochar prepared from sawdust for sequestration of basic fuchsin: isotherm, kinetics, and toxicity studies. **Biomass Conversion and Biorefinery**, 13, 9525–9536. https://doi.org/10.1007/s13399-023-04210-z **(Springer; SCI IF 2023: 4.05).**

2. **Vishnu Priyan V**., Kumar, N., Rajendran, Harish. Kumar., Ray, J., Narayanasamy, Selvaraju., 2022. Sequestration and toxicological assessment of emerging contaminants with polypyrrole modified carboxymethyl cellulose (CMC/PPY): Case of ibuprofen pharmaceutical drug. **International Journal of Biological Macromolecules**, 221, 547–557. https://doi.org/https://doi.org/10.1016/j.ijbiomac.2022.09.046 **(Elsevier; SCI IF 2023: 8.2).**

3. **Vishnu Priyan V**. and Selvaraju Narayanasamy, 2022. Effective removal of Pharmaceutical Contaminants Ibuprofen and Sulfamethoxazole from water by Corn starch nanoparticles: An ecotoxicological assessment, **Environmental Toxicology and Pharmacology**, 103930. https://doi.org/10.1016/j.etap.2022.103930 **(Elsevier; SCI IF 2023: 4.3).**

4. **Vishnu Priyan V,** Nitesh Kumar, Selvaraju Narayanasamy, 2022. Toxicological assessment and adsorptive removal of lead (Pb) and Congo red (CR) from water by synthesized iron oxide/activated carbon (Fe_3O_4/AC) nanocomposite. **Chemosphere**, 294, 133758, https://doi.org/10.1016/j.chemosphere.2022.133758 **(Elsevier; SCI IF 2023: 8.8).**

5. **Vishnu Priyan V**., Nitesh Kumar, Selvaraju Narayanasamy**,** 2021. Development of Fe_3O_4/CAC nanocomposite for the effective removal of contaminants of emerging concerns (Ce^{3+}) from water: An ecotoxicological assessment, **Environmental Pollution**, 285, 117326. https://doi.org/10.1016/j.envpol.2021.117326 **(Elsevier; SCI IF 2023: 8.9).**

6. **Vishnu Priyan V**., Tasrin Shahnaz, Ajaikumar B Kunnumakkara, Varsha Rana, Muthupandian Saravanan, Selvaraju Narayanasamy, 2021. Antioxidant, anti-inflammatory and biosorption properties of starch nanocrystals in vitro study: Cytotoxic and Phytotoxic Evaluation, **Journal of Cluster Science**, 32, 1419-1430, https://doi.org/10.1007/s10876-020-01905-5 **(Springer; SCI IF 2023: 3.4).**

7. **Vishnu Priyan V**., Shahnaz, T., Suganya, E., Sivaprakasam, S., Narayanasamy, S., 2020. Ecotoxicological assessment of micropollutant Diclofenac biosorption on magnetic sawdust: Phyto, Microbial and Fish toxicity studies. **Journal of Hazardous Materials**, 403,123532. https://doi.org/10.1016/j.jhazmat.2020.123532 **(Elsevier; SCI IF 2023: 13.6).**

B. LIST OF PUBLICATIONS FROM COLLABORATIVE WORK

1. Chandrasekar, R, Harish Kumar Rajendran, **Vishnu Priyan V**. and Selvaraju Narayanasamy, 2022. Valorization of sawdust by mineral acid assisted hydrothermal carbonization for the adsorptive removal of bisphenol A: Greener approach. **Chemosphere**,135171, https://doi.org/10.1016/j.chemosphere.2022.135171 **(Elsevier; SCI IF 2023: 8.8).**

2. Tasrin Shahnaz, **Vishnu Priyan V**., Anjali Ajaykumar, Selvaraju N, 2021. Magnetic nanocellulose from Cyperus rotundas grass in the absorptive removal of rare earth element Cerium (III): toxicity studies and interpretation, **Chemosphere,** 287, 131912, https://doi.org/10.1016/j.chemosphere.2021.131912 **(Elsevier; SCI IF 2023: 8.8).**

3. Shahnaz, T., **Vishnu Priyan V.**, Sivakumar, P. and Narayanasamy, S**.,** 2021. Nanocellulose extracted from grass for adsorption abatement of Ciprofloxacin and Diclofenac removal with Phyto, and fish toxicity studies. **Environmental Pollution**, 268, 115494. https://doi.org/10.1016/j.envpol.2020.115494 **(Elsevier; SCI IF 2023: 8.9).**

4. Jeyabalan, J., Veluchamy, A., **Vishnu Priyan V.,** Kumar, A., Chandrasekar, R., Narayanasamy, S., 2023. A review on the laccase assisted decolourization of dyes: Recent trends and research progress. **Journal of the Taiwan Institute of Chemical Engineers**, 151, 105081. https://doi.org/https://doi.org/10.1016/j.jtice.2023.105081 **(Elsevier; SCI IF 2023: 5.7).**

5. Kumar, A., Jeyabalan, J., **Vishnu Priyan V.,** Charan Patra, C., Narayanasamy, S., 2023. Fabrication of a novel bio-polymer adsorbent with high adsorptive capacity towards organic dyes. **Industrial Crops and Products**, 203, 117166. https://doi.org/10.1016/j.indcrop.2023.117166 **(Elsevier; SCI IF 2023: 5.9).**

C. LIST OF CONFERENCES

1. **Vishnu Priyan V**. and Selvaraju Narayanasamy, 2021. "Development of Fe_3O_4/CAC nanocomposite for the effective removal of Contaminants of emerging concerns from water: An ecotoxicological assessment." ICONN 2021, SRM Institute of Science and Technology, February 1-3, 2021. **(BEST POSTER PRESENTATION AWARD)**

2. **Vishnu Priyan V**. and Selvaraju Narayanasamy, 2022. "Elimination of pharmaceutical drug Ibuprofen by Polypyrrole modified Carboxymethylcellulose (CMC/PPY): Evaluation and Toxicological assessment." ICSW 2022, KPR Institute of Engineering and Technology, March 22-23, 2022.

3. **Vishnu Priyan V**. and Selvaraju Narayanasamy, 2022. "Removal of pharmaceutical drugs from water by tailored nano polysaccharide: Adsorption mechanism and Toxicity assessment." ACBMT 2022, Hindusthan College of Engineering & Technology, May 6, 2022. **(BEST PAPER AWARD)**

4. **Vishnu Priyan V**., Ghurupreya R., and Selvaraju Narayanasamy, 2022. "Sequestration of Endocrine disruptor Bisphenol A from water by modified Hydrophobic Chitosan and its ecotoxicological assessment via Phyto and Fish

Toxicity studies." ETBCT 2022, Shri Mata Vaishno Devi University, December 3-5, 2022. **(BEST ORAL PRESENTATION AWARD)**

5. **Vishnu Priyan V**. and Selvaraju Narayanasamy, 2023. "Sequestration of Micropollutants by Oxidant-Modified Biochar prepared from Sawdust: Insights into Mechanism and Toxicity studies." CHEM-TECHNOVA 2023, Harcourt Butler Technical University, May 26-27, 2023. **(FIRST PLACE IN ORAL PRESENTATION)**

6. **Vishnu Priyan V**. and Selvaraju Narayanasamy, 2023. "Removal of basic fushin by modified Biochar prepared from Sawdust: Mechanism and Toxicity studies." RIC 2023, Indian Institute of Technology Guwahati, May 14-16, 2023. **(SECOND PLACE IN POSTER PRESENTATION)**

7. **Vishnu Priyan V**., Ghurupreya R., and Selvaraju Narayanasamy, 2023. "Engineered Nanopolysaccharides for the sequestration of Endocrine disruptor from water systems and its Ecotoxicological Assessment via Phyto and Fish Toxicity studies." ICWEE 2023, Sathyabama Institute of Science and Technology, July 5-7, 2023. **(BEST ORAL PRESENTATION AWARD)**